New mathematical models for splash dynamics

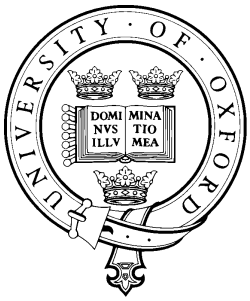

Matthew Moore

Jesus College

University of Oxford

A thesis submitted for the degree of

Doctor of Philosophy

Trinity 2014

For my parents.

Abstract

In this thesis, we derive, extend and generalise various aspects of impact theory and splash dynamics. Our methods throughout will involve isolating small parameters in our models, which we can utilise using the language of matched asymptotics.

In Chapter 1 we briefly motivate the field of impact theory and outline the structure of the thesis. In Chapter 2, we give a detailed review of classical small-deadrise water entry, *Wagner theory*, in both two and three dimensions, highlighting the key results that we will use in our extensions of the theory. We study oblique water entry in Chapter 3, in which we use a novel transformation to relate an oblique impact with its normal-impact counterpart. This allows us to derive a wide range of solutions to both two- and three-dimensional oblique impacts, as well as discuss the limitations and breakdown of Wagner theory. We return to vertical water-entry in Chapter 4, but introduce the air layer trapped between the impacting body and the liquid it is entering. We extend the classical theory to include this air layer and in the limit in which the density ratio between the air and liquid is sufficiently small, we derive the first-order correction to the Wagner solution due to the presence of the surrounding air. The model is presented in both two dimensions and axisymmetric geometries. In Chapter 5 we move away from Wagner theory and systematically derive a series of splash jet models in order to find possible mechanisms for phenomena seen in droplet impact and droplet spreading experiments. Our canonical model is a thin jet of liquid shot over a substrate with a thin air layer trapped between the jet and the substrate. We consider a variety of parameter regimes and investigate the stability of the jet in each regime. We then use this model as part of a growing-jet problem, in which we attempt to include effects due to the jet tip. In the final chapter we summarise the main results of the thesis and outline directions for future work.

Acknowledgements

This thesis would not have been possible without the advice, support and guidance of my supervisors Dr. Jim Oliver, Prof. John Ockendon and Prof. Sam Howison. I would like to thank Dr. Jon Whiteley for the finite-element code he developed for our investigations on splash jets. I have also had several useful discussions with Prof. Siggi Thoroddsen and Dr. Marie-Jean Thoraval at KAUST, particularly in regard to the work on splash jets.

Outside of academia, I would like to thank my family, particularly my parents, for their support throughout my D.Phil. I would like to thank my friends for making the past three-and-a-half years so enjoyable and for being there when it was not so enjoyable. In particular, I would like to thank Claire Davison, Michael Blatherwick, Ben Winter, Hannah Christensen, Duncan Hardy and Simon May.

I would like to acknowledge the EPSRC for providing part of the financial support I received for the duration of my D.Phil. and I would also like to note that this thesis was based on work supported by Award No. KUK-C1-013-04, made by King Abdullah University of Science and Technology (KAUST).

Contents

Chapter 1

Introduction

Splashing is a phenomenon that we can all relate to, whether it be through skipping a stone on the sea during a casual stroll on the beach, raindrops pelting down as we dash inside out of inclement weather, or spray coming up over the side of a ferry in choppy waters. It is ubiquitous in situations where two liquids or a solid and a liquid collide, and as such has been of interest to a wealth of scientists, engineers and mathematicians over the decades.

Viewed as a physical or mathematical problem, impacts and splash dynamics are quite tricky to handle. There are a huge variety of scales over which impacts can be considered: on the large scale, a battleship crashing back down into the water after riding a particularly large wave, on a smaller scale an Olympic diver trying to minimise the splash as she completes her routine, and on the microscale a droplet of ink hitting the paper in a printer in the office. Furthermore, we might be interested in a different aspect of the splash in each of these examples. If you were on the battleship, you would probably be most interested in knowing whether the ship's hull can withstand the force of the impact. If you were designing the printer you might want to minimise the size of the microdroplets that form when the ink splashes on the paper. The diver might be most interested in how she can change her entry to minimise the amount of splash she produces.

Despite these differences, all of these events are characterised by the short, rapid behaviour just after the solid and liquid come into contact, in which the bulk of fluid is violently disturbed and a spray or jet is produced. Much of this interesting behaviour happens over a very short time period, so experimentalists are at their limit to view what is happening; Thoroddsen et al. (2008) need cameras capable of capturing one million frames per second to catch some of the small-time and small-scale phenomena seen in droplet impacts. Computers and numerical analysts also struggle as there is a distinct and sudden topological change just after the collision in which the jets of fluid

are formed. Theoreticians and mathematicians do not have things any easier, as even with the simplest possible model, splashing is a highly nonlinear problem and much of the theory is limited to very shallow bodies, Wagner (1932) and Howison et al. (1991), or for small-times after impact, for example Korobkin (1985) and Korobkin and Pukhnachov (1985). Only a marriage of all three approaches is able to fully understand the problem: asymptotic theory to give numerical analysts an initial configuration to run their code, with experimental results to compare the resulting solutions with.

So why does this thesis exist? There is certainly a lot of literature on splashing: why do we need new mathematical models for splash dynamics? Although there is certainly a solid groundwork of theory, it is by no means comprehensive. Several simplifying assumptions have been made in the existing literature which require further consideration. Despite Clanet et al. (2004) and their revelations about the secrets of skimming stones, angled impact problems are not well-understood in theory, although it is a relatively straightforward job to extend the classical model to incorporate them. Moreover, in the last decade, the surrounding air or gas in an impact has been shown to have a key influence on whether a splash actually occurs, see Xu et al. (2005) for the original experiments, or Quéré (2005) and the suppression of splashing on Mount Everest. This is completely ignored in the classical theory and most attempts to incorporate it are interested in what happens before impact as opposed to its role in the splash. Even further effects could be considered, such as surface tension or compressibility, or we could look at the splash jets themselves and ask if current jet models can explain some of the incredible pictures in Thoroddsen et al. (2011) or Thoraval et al. (2012).

Splashing is anything but a closed field. In this thesis we will attempt to address some of the issues we have outlined here. Although we cannot provide a comprehensive theory incorporating all of these physical effects and situations, we can certainly augment and extend the existing theory.

1.1 Aim and structure of thesis

The thesis naturally splits into three parts. We have not provided a comprehensive literature review in this introduction because it makes more sense to attach a literature review to each of the sections individually: although they are interlinked and arc towards a common goal, they stand sufficiently alone in order for this to be the best option. The same is true of the modelling assumptions we make.

The first part includes Chapters 2 and 3, which deal with the classical Wagner the-

ory of ideal, incompressible water-entry in the absence of gravity, surface tension and an ambient gas. In Chapter 2, we recap Wagner theory for normal water-entry, which provides a basis for not only the extension to non-normal impacts in Chapter 3 but also the work in Chapter 4. Our first novel work is in Chapter 3, in which we consider both two- and three-dimensional oblique impacts within the asymptotic structure of Wagner theory. We consider a wide variety of examples and look extensively into the validity of the model.

In the second part of the thesis, which is contained entirely in Chapter 4, we consider the role of the surrounding gas, which is neglected in Wagner theory. In particular, we consider its influence post-impact, modelling it as a small perturbation to the classical solution presented in Chapter 2. The main motivation behind considering the ambient gas, as opposed to some of the other neglected physics, is that the gas is known to play a pivotal role in whether or not a splash actually occurs, and is moreover viewed as the key mechanism behind some of the dynamics of the splash jets themselves. Understanding the role of the gas on the bulk of the impact is therefore a stepping-stone to understanding its wider role in splashing generally. In Chapter 4 we propose an extension of the Wagner asymptotic structure to incorporate the surrounding air, identifying the key parameters. We apply our theory to examples in both two and three dimensions, and in particular investigate its role on the force exerted on an impacting body.

In Chapter 5, the third and final part, we move on to the splash itself. Existing jet models do not encapsulate the defining physics behind splash jets- that is thin, fast-moving jets of fluid, typically riding on a very thin gas layer. We aim to develop a model which couples the jet and air flow, looking at its stability to small disturbances. We adapt the model to describe the growth of a jet as it is shot into a surrounding gas. Initially, we concentrate on a two-dimensional model and identify various regimes based on the size of the splash jet and the underlying gas layer. We present both asymptotic and numerical solutions to the growing jet problem and conjecture on the possibility of the jet touching down, rupturing the air layer.

Finally, in Chapter 6 we summarise our findings and discuss the open questions arising from our work.

1.2 Statement of originality

The matching between the inner and outer Wagner solutions using an intermediate variable in §2.2.6 is, as far as we are aware, original. While the use of the displacement potential to transform the problem in Chapter 3 is not original, the following

transformation into a fixed frame in §3.1.2.2 and all the results derived from the discovered symmetries is original. The majority of the novel work in Chapter 3 is published in Moore et al. (2012) and Moore et al. (2013a). All the modelling and analysis in Chapters 4 and 5 is original unless otherwise indicated in the text. The work in Chapter 4 has been published in Moore et al. (2013b) and Moore and Oliver (2014). Any figures that are based on figures in these published papers are cited and referenced in the text.

Chapter 2

Classical water-entry

2.1 Introduction

2.1.1 Wedge and cone impacts

The foundations for the theory of water-entry were first discussed by von Kármán (1929) and Wagner (1932), who were both concerned with the hydrodynamics of an alighting seaplane. Even neglecting physical effects such as the influence of gravity, the surrounding gas, surface tension, viscosity and compressibility, the normal impact of a rigid body into a liquid is a highly nonlinear problem and analytic progress is far from simple. Part of the difficulty arises from the formation of splash jets or splash sheets when the surface of the liquid is violently disturbed. Due to these difficulties, much early work concentrates on the constant-velocity, normal impact of a two-dimensional, rigid, symmetric wedge into a half-plane of initially-quiescent, ideal fluid. The lack of a lengthscale means there is a similarity solution to this problem in which distances are scaled with time. However, even with this simplification of physics and geometry, no closed form solution exists, with most approaches to solving the wedge-impact problem being approximate or numerical.

Dobrovol'skaya (1969) uses a complex variable transformation of the problem to map the flow domain to one in which the fluid is bounded by straight lines. She reduces the problem to a nonlinear singular integral equation, which she solves numerically. Mackie (1969) and Hughes (1972) refine and adapt Dobrovol'skaya's ideas. The similar problem of a water wedge impacting a flat solid surface is considered in Cumberbatch (1960). Cumberbatch considers an outer flow away from the wall, where the flow is determined as a perturbation to the initial wedge shape, and an inner region close to the wall, where the flow evolves from the initial wedge apex. He attempts to match between the two regions, by maintaining conservation of mass,

and solves the resulting integral equations numerically.

Greenhow (1987) solves the wedge impact problem numerically using a boundary integral method, although his solution is limited by not being able to resolve the splash jet for particularly flat wedge profiles. His numerical results predict that the jet can separate from the wedge, which breaks the similarity of the problem. These results are supported with experiments in which a triangular prism is dropped into a pool of water. Greenhow (1987) also performs an analysis to establish when gravity might become important in a wedge impact. He concludes that, aside from in the jets, provided the impact time is smaller than the impact velocity divided by twice the acceleration due to gravity, gravity is negligible.

There are more recent numerical simulations of the wedge-entry problem, see, for example, Zhao and Faltinsen (1993), Zhao et al. (1997), Keady and Fowkes (1998), Faltinsen (2002) or Semenov and Yoon (2009). However, despite these analytical and numerical analyses, it was not until Fraenkel and McLeod (1997) that the existence of a solution to the wedge impact problem was proved. Fraenkel and McLeod (1997) also derive some asymptotic solutions when the wedge angle is very large.

The equivalent three-dimensional impact is the constant-speed impact of a cone in the absence of viscosity, surface tension, air-cushioning and gravity. However, despite the self-similarity in the cone impact problem, less progress has been made and much of the work is based on approximations inspired by Wagner (1932). One of the earliest is by Shiffman and Spencer (1951), where the similarity form is exploited to derive an integral equation for the force on the cone, which they then compare to numerical simulations and experimental results obtained by Watanabe (1930). Shiffman and Spencer (1951) approximate the impact by fitting an ellipse to simulate the normally impacting cone, with the ellipse dimensions approximated by equating the penetration depth and the free surface displacement. A similar idea is adopted by Fabula (1957), who approximates cone impacts by considering flow past a diamond-shaped body.

2.1.2 Wagner theory

Unfortunately, similarity approaches do not extend to more general impactor profiles, whereas the ideas of von Kármán (1929) and Wagner (1932) have been successfully adapted. Von Kármán (1929) essentially replaces the two-dimensional impactor with a flat plate of the size of the body cross-section at the instantaneous waterline and neglects deformations of the free surface. The plate is given a normal impact velocity equal to the impact velocity and the force on the plate is calculated by considerations of conservation of momentum. Wagner (1932) presents a much more refined model in which the free surface is allowed to rise and the flat plate width is determined by

demanding that the free surface meets the plate at its tips. Wagner recognised that the flow breaks down close to these tips and proposed a local flow which forces fluid into a splash jet. Schmieden (1953) extended the flat-plate approach of Wagner to axisymmetric body profiles.

The flat-plate assumption is based on the idea that in the early stage of many impacts, and particularly in the cases of interest for von Kármán and Wagner, the impactor is nearly flat as it enters the liquid. That is to say, the *deadrise angle*, which is the angle between the outward-pointing normal of the impactor and the negative vertical axis, is small. It was not until the late 1980s that the first ideas of formalizing this approach using the method of matched asymptotic expansions came to the fore. The pioneers in this field were Armand and Cointe (1987), Cointe (1989), Wilson (1989) and Howison et al. (1991). The outer flow is given by Wagner's expanding flat plate, which is a high pressure region between the two *turnover points* where the free surface 'turns over'. Locally, these turnover regions admit Helmholtz flows and the fluid is forced into a splash jet on the body. The location of these turnover regions is derived from the so-called Wagner condition, which requires the free surface to meet the impactor in the outer flow. We shall be considering the asymptotics in detail in this chapter, so we shall not go into any more detail here. It suffices to say that these works generalise the method to any two-dimensional, symmetric, convex impactor with small deadrise angle. Howison et al. (1991) perform a local stability analysis of the jet-roots that shows that Wagner theory is stable to small perturbations provided the jet-roots are advancing. This instability has been cited as being one of the difficulties in formulating the related water-exit problem, as discussed in Wilson (1989), Gillow (1998) and Oliver (2002). In light of this, Korobkin (2013) proposes a different condition at the tips of the high-pressure region in a linearised, inviscid model for small-time water exit: he demands that the contact points have speed that is proportional to the local velocity of the flow.

More recently, Oliver (2007) found the first-order correction to two-dimensional Wagner theory and in particular used this analysis to compare the asymptotic results to the numerics of Zhao and Faltinsen (1993). Oliver found that with the correction, Wagner theory provided a reliable estimation of the force on the impactor for deadrise angles of up to twenty degrees, which is remarkable for a theory based on the smallness of this angle.

Wilson (1989) and Howison et al. (1991) extend the asymptotic analysis of small-deadrise impact to three-dimensional bodies, although analytical progress is restricted to axisymmetric profiles. Miloh (1991b) considers the specific example of spherical impactors, in which he uses toroidal coordinates based on the penetration depth of

the sphere to solve for the Stokes stream function. Miloh calculates the early-time forces on the sphere and compares his results to experiments in Shiffman and Spencer (1945) and Moghisi and Squire (1981). Scolan and Korobkin (2001) and Korobkin and Scolan (2006) take a different approach to the Wagner idea and attempt to construct solutions to impact problems by solving the so-called inverse Wagner problem. They prescribe a turnover curve and then work backwards, deriving a method which finds the impactor that produces this turnover curve. In particular, they use this method to describe Wagner theory for the impact of elliptic paraboloids. There are also several numerical investigations of three-dimensional impacts: see, for example, Zhao et al. (1997), Battistin and Iafrati (2003), Peseux et al. (2005) or Xu et al. (2011).

Independent of the development of Wagner theory, much progress on fluid impact problems was made by Pukhnachov and Korobkin (1981) and Korobkin and Pukhnachov (1985). They formulate a linearised problem in Lagrangian coordinates assuming small fluid displacement. They apply this to two-dimensional impacts and Korobkin (1985) generalises the approach to three-dimensional normal impacts, including those with an elliptic cross-section. A paper of particular note in regards to this thesis is that of Korobkin (1982), which first introduces the idea of using a Baiocchi-type transformation to reformulate the mixed boundary value problem for the potential flow as a variational inequality. This transformation is via the *displacement potential*, which is defined as the time integral of the velocity potential in the fluid. The displacement potential approach will have several intriguing benefits in our study of oblique impacts and air-cushioning.

2.1.3 Extensions to Wagner theory

With the exception of the discussion of gravity in Greenhow (1987), these papers have all been concerned with normal impacts of two- or three-dimensional bodies onto a half-space of liquid neglecting the influence of air-cushioning, surface tension, viscosity, compressibility and gravity.

Korobkin (1995) looks at impacts in a finite depth of water. To leading-order he assumes that penetrations are of the same order as the liquid depth, giving an entirely different decomposition of the problem to infinite-depth theory. Howison et al. (2002) attempt to reconcile the later-time model of Korobkin with the small-time Wagner theory, and they find that there are four distinct regimes depending on the relative sizes of the contact set, the penetration depth and the depth of the fluid layer. Howison and Oliver (2004) look at one of these stages, in which the contact set is much larger than the fluid depth, but the penetration depth is still much smaller than the fluid depth. Their resulting model is compared to a viscous squeeze flow.

Howison et al. (2005) extend this theory to droplet impacts onto a thin layer of fluid.

When the body has a flat, finite-width bottom, for example a box, the modelling is a little different and the resulting structure with a free jet is considered in Howison et al. (2004). Ermanyuk and Ohkusu (2005) and Ermanyuk and Gavrilov (2011) perform experiments on circular disk impacts, although they are primarily concerned with the added mass coefficient and the air layer trapped before impact. Tkacheva (2013) introduces a small body rotation to the impact of a flat-bottomed box and notes that the resulting asymmetry can lead to a negative pressure on the impactor.

At early impact times, the compressibility of the liquid is important, particularly for impactors of small or zero deadrise angle. Among the authors to consider this are Korobkin (1996a,b, 1997) and Campana et al. (1998), the latter of which is particularly interested in the transition from the supersonic to subsonic stage. Once the velocity of the liquid particles reduces to that associated with the subsonic stage, compressibility is not important. In the particular example of a circular cylinder, Campana et al. (1998) deduce that the maximum force on the impactor occurs in the subsonic stage, suggesting that Wagner theory provides an excellent approximation to the forces felt on the impactor during water-entry. For this reason, compressibility of the liquid is something that is not considered in most analyses of water-entry where the penetration depth is a lot smaller than the depth of the fluid.

Muzaferija et al. (1998) solve the water-entry problem with the full Navier-Stokes equations in order to investigate the importance of viscosity. They conclude that the forces and pressures on the impactor are described almost entirely by the inviscid theory.

Of particular interest to the present study are the extensions of Wagner theory to *oblique* impacts of bodies with small deadrise angle. Early experimental studies by Birkhoff and Caywood (1949) and May (1968, 1975) look at the impact of a bullet or missile in water, examining both the small-time splash behaviour as well as the long-time cavity formation behind the impacting body. Limitations in experimental equipment mean that their results for the initial stages of oblique water-impact lack the resolution to explain and study the early formation of the splash jets.

Although most literature concentrates on the vertical entry case, there are several theoretical investigations of oblique impact that we mention here. Two-dimensional oblique impacts follow a similar history to normal impacts. Garabedian (1953) performs one of the first analytical approaches to solving the oblique impact of a wedge by exploiting the inbuilt similarity of the problem. Garabedian uses hodograph techniques to tackle the problem but only makes progress by assuming that the free surface leaves the wedge either tangentially or perpendicularly. He concludes that

the only way in which the free surface can separate from the vertex of the wedge is if the motion is purely horizontal. Chekin (1989) extends the similarity analysis of Dobrovol'skaya (1969) to the oblique impact of a wedge and utilises more general separation conditions. For a given wedge angle, Chekin finds that there is only one entry angle for which separation does *not* occur; radically different to Garabedian's conclusions. Chekin concludes that either one side of the wedge must be dewetted so that the impact is essentially that of an angled semi-infinite plate or that a cavity forms on the impactor. We shall see evidence of the possibility of cavity formation in Chapter 3.

Iafrati (2000) and de Divitiis and de Socio (2002) both present numerical schemes for solving the oblique entry problem and Judge et al. (2004) use a two-dimensional vortex distribution model to address the vertex-separation problem. Judge et al. (2004) test their model by performing several experiments for wedges of various deadrise angle and orientation as well as performing numerical simulations. Their model is characterised by two points of zero pressure on the impactor and ventilation is assumed to occur when the point of zero pressure on the trailing side of the impactor reaches the wedge apex. They conclude that for a symmetric wedge, the horizontal component of impact velocity needs to be much larger than the vertical component of impact velocity for ventilation to occur. More recent works on the wedge impact problem by Semenov and Iafrati (2006) and Semenov and Yoon (2009) use advanced complex variable techniques to formulate a set of nonlinear integro-differential equations for any deadrise angle and any wedge orientation. Semenov and Yoon (2009) link the onset of ventilation at the wedge apex to the vanishing of the pressure at a contact point, but point out that negative forces on one side of the wedge can occur prior to this ventilation.

Korobkin (1988) moves away from classical wedge entry to discuss the oblique impact of a parabola. For small times, Korobkin finds that, provided the horizontal component of the entry velocity is not substantially larger than the normal component, the vertical component of force on the impactor does not change from the normal-impact problem at leading-order. Miloh (1991a) generalises Korobkin's approach to the three-dimensional inclined entry of a sphere. He draws similar conclusions regarding the vertical component of impact force for small times and moderate impact angles. In Chapter 3 we will consider this phenomenon in more detail and show that it remains true even for much larger angles of incidence.

That the vertical component of force is the same for oblique impact as for normal impact within Wagner theory is related to the so-called Trefethen paradox, see Trefethen and Panton (1990), which asks why the splash of an impacting body appears

to be symmetric even if the entry is non-vertical. Oliver (2002) and Howison et al. (2004) discuss this for bodies of small deadrise angle in relation to Wagner theory. They conclude that if the ratio of the horizontal to vertical components of impact velocity has magnitude smaller than the inverse of the deadrise angle, the horizontal component of impact does not enter the leading-order problem and hence the solution is the same as in normal impact. Their analysis of the case where the ratio reaches this critical magnitude concludes that the symmetry breaks down, and in the particular example of wedge impact they find a critical value of 0.4853 for the speed ratio (scaled by the deadrise angle) at which Wagner theory is no longer applicable; at this value the trailing jet-root stops advancing, resulting in the instability described by Howison et al. (1991). Semenov and Yoon (2009) claim to see breakdown at this speed ratio in their numerical solutions for wedge impact.

Much of the work in Chapter 3 is built upon an algebraic error in Howison et al. (2004) that leads to a correction of this critical value and unearths a surprising wealth of results from the symmetry still ingrained in the problem in spite of the horizontal component of entry velocity. Moore et al. (2012) and Moore et al. (2013a) use the displacement potential to reformulate the leading-order Wagner problem in terms of its normal-impact counterpart. As a result, they are able to simply write down the solution to an oblique impact from the corresponding normal-impact problem. They find the location of the turnover points to be symmetric about the impactor apex in the outer region, and for a wedge, they find a corrected value of $\pi/2$ for the critical value of the ratio of impact speeds at which Wagner theory breaks down. This is in fact exactly what Semenov and Yoon (2009) find in their numerical results. The utility of the displacement potential transformation goes much further than this, in both two- and three-dimensions, which will become apparent in Chapter 3.

Scolan and Korobkin (2012) use Galin's theorem to relate the oblique impact of an elliptic paraboloid in terms of its normal-impact counterpart, supporting the results in Moore et al. (2012). Their method has the benefits of allowing rotation of the impactor, but the drawback of only being applicable to a particular body profile. Recent numerical work on three-dimensional oblique water entry in Sun and Wu (2013a,b) also confirms the findings for small deadrise impactors in Moore et al. (2012). However, these numerical schemes also apply for a wider variety of impacts at larger deadrise angles.

An experimental paper that is of interest to the results in Chapter 3 is that of Bird et al. (2009). They look at the problem of oblique droplet impact onto a solid surface, for which the leading-order theory is readily derived from Wagner theory. In their experiments they introduce an oblique component of impact velocity, either by

inclining or moving the solid surface. They conclude that this component of velocity acts to inhibit the splash of the droplets in the direction opposite the oblique velocity while accentuating the splash in the direction of oblique velocity. This corroborates with the findings of Judge et al. (2004), Semenov and Yoon (2009) and Moore et al. (2012, 2013a), who all state that giving the impactor an oblique velocity component reduces the amount of liquid that can enter the trailing splash jet/sheet, eventually leading to detachment of the jet/sheet when ventilation occurs.

Reinhard et al. (2012) present several possible models for the evolution of the impact after the breakdown of oblique Wagner theory. Their models are based on different conditions for where the liquid free surface detaches from the impactor. They consider three different possibilities: separation of the free surface over the region of negative pressure on the impactor (this is equivalent to the Brillouin-Villat condition, see Birkhoff and Zarantonello (1957)); separation at the shoulder of the body; and separation at the point which minimises the kinetic energy of the fluid. In all three of these cases, motion in the post-Wagner regime induces bouncing of the impactor. Khabakhpasheva and Korobkin (2013) use the Brillouin-Villat separation condition in their model of shallow-water oblique impact. Their impactors are allowed to rotate and the influence of the body mass is taken into account: lighter bodies bounce, while heavy bodies collide with the bottom of the shallow liquid layer, and intermediate masses can interact for extended periods with the liquid, with oscillations in the body orientation.

The theory of bouncing is closely linked with the field of planing and skimming, which Oliver (2002) views as the limit in which the ratio of the horizontal to the vertical components of the impact velocity is much larger than the inverse of the deadrise angle. We will not discuss planing regimes in this thesis, but typical references include Clanet et al. (2004), Rosellini et al. (2005), Hewitt et al. (2011), Hicks and Smith (2011) and Reinhard et al. (2013).

One important physical effect that is neglected in classical Wagner theory is that of the surrounding gas. This can be important both pre- and post-impact. We shall move on to air-cushioning models in Chapters 4–5. Although still in the Wagner regime, these chapters are markedly different to the work on normal and oblique water entry in Chapters 2–3. On this basis, we will leave a discussion of air-cushioning literature until the beginning of Chapter 4.

Before we move on to oblique water entry in Chapter 3, it seems prudent to present a run-through of classical Wagner theory, as it provides the backbone of the work in the remainder of this thesis. Chapter 2 will cover the asymptotic structure of small-deadrise impacts in both two- and three-dimensions, concentrating in particular on

the results which will be of use in the original work in Chapters 3–5.

2.2 Two-dimensional Wagner theory

We consider the vertical impact of a rigid, symmetric, convex, smooth (except possibly at the point of impact) body onto a half-plane of liquid. We assume that the body is moving vertically through a vacuum and that the fluid is initially at rest.

Define (x^*, z^*)-axes so that the body is moving in the negative z^*-direction and such that the impact initially occurs at time $t^* = 0$ at the origin in this plane. Here and hereafter, an asterisk indicates a dimensional quantity. The body profile at time t^* is defined by

$$\frac{z^*}{L} = f\left(\frac{\varepsilon x^*}{L}\right) - s\left(\frac{t^*}{T}\right), \tag{2.1}$$

where $(L/T)\dot{s}$ is the impact speed, Ls is a typical penetration depth and T is a typical impact timescale. We require that the function f be even and monotonically increasing in $|x^*|$, continuously differentiable except possibly at its apex, and $f(0) = s(0) = 0$. Any profile of the form $f(x^*) = |x^*|^n$ satisfies these conditions for $n \geq 1$. The parameter ε measures the shallowness of the impactor. Our assumption of small *deadrise angle*, the angle between the outward-pointing normal to the impactor and the negative z^*-direction, reduces to $0 < \varepsilon \ll 1$, as stated in Howison et al. (1991).

We nondimensionalise the problem using L, T, L/T, L^2/T, $\rho_l L^2/T^2$ as our length, time, velocity, velocity potential and pressure scales respectively, where ρ_l is the constant liquid density. In dimensionless variables, the body profile is given by $z = f(\varepsilon x) - s(t)$. At times $t > 0$, the impactor penetrates the fluid, violently disturbing the free surface, which forms two jets along the impactor. This post-impact configuration is shown for $x > 0$ in Figure 2.1. We define the *turnover points*, where the tangent to the free surface is vertical, as $x = \pm d(t)$, and the two tips of the splash jets as $x = \pm c(t)$. Note that we assume the jet does not detach from the impactor between these points. The multivalued free surface is defined by $z = h(x, t)$.

2.2.1 Modelling assumptions

Throughout our analysis, we will neglect the viscosity and compressibility of the liquid, surface tension at the free surface and the influence of gravity. These physical effects are governed by the Reynolds, Mach, Weber and Froude numbers, which are defined in terms of our nondimensionalisation by

$$\mathrm{Re}_l = \frac{L^2}{T\nu_l}, \quad \mathrm{Ma}_l = \frac{L}{Tc_l}, \quad \mathrm{We} = \frac{\rho_l L^3}{T^2\sigma}, \quad \mathrm{Fr}^2 = \frac{L}{T^2 g}, \tag{2.2}$$

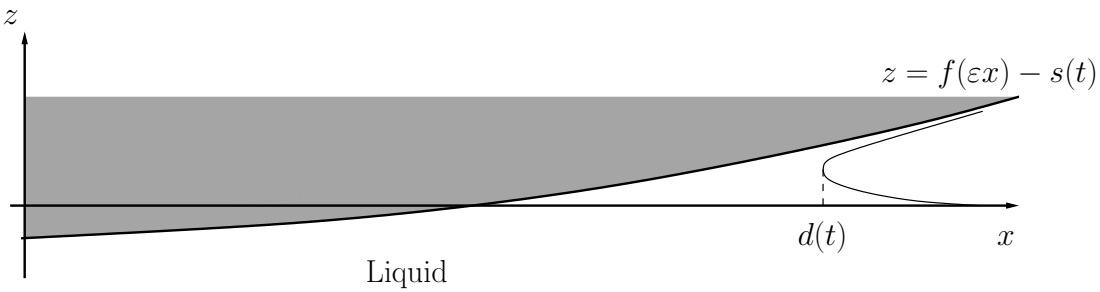

Figure 2.1: Dimensionless splashing configuration for time $t > 0$ for $x > 0$. See text for details.

where ν_l is the kinematic viscosity of the liquid, c_l is the speed of sound in the liquid, σ is the surface tension coefficient and $g \approx 9.8$ ms^{-2} is the acceleration due to gravity. Our modelling assumptions require the Reynolds, Weber and Froude numbers to be large, while we need the Mach number to be small.

We consider two typical impact scenarios to illustrate the applicability of our assumptions. Consider a ship slamming into the ocean. A typical modern destroyer can travel at speeds of up to 20 ms^{-1}, and we might be interested at penetration depths on the order of 1 m. Given that $\nu_l \approx 10^{-6}$ m^2s^{-1}, $c_l = 1.4 \times 10^3$ ms^{-1}, $\rho_l \approx 10^3$ kgm^{-3} and $\sigma = 7.5 \times 10^{-4}$ Nm^{-1} for water, this gives

$$\text{Re}_l \approx 10^7, \quad \text{Ma}_l \approx 10^{-2}, \quad \text{We} \approx 10^9, \quad \text{Fr}^2 \approx 40, \tag{2.3}$$

which gives good grounds for neglecting viscosity, compressibility, surface tension and gravity.

At a much smaller scale, we consider the impact of a water-glycerol droplet as presented in Figure S3 of Thoraval et al. (2012). The droplet is falling with velocity 3.54 ms^{-1} and the first shots captured in their experiments are at time 3×10^{-5} s, so that the penetration depth is approximately 10^{-4} m. The liquid has density $\rho_l \approx 1.12 \times 10^3$ kgm^{-3}, kinematic viscosity $\nu_l \approx 3 \times 10^{-6}$ m^2s^{-1}, surface tension coefficient $\sigma \approx 6.74 \times 10^{-2}$ Nm^{-1} and the speed of sound, although not explicitly given, will be approximately $c_l \approx 1.5 - 2 \times 10^3$ ms^{-1} based on the values for pure water and glycerol respectively. Therefore,

$$\text{Re}_l \approx 3 \times 10^2, \quad \text{Ma}_l \approx 10^{-3}, \quad \text{We} \approx 20, \quad \text{Fr}^2 \approx 10^4, \tag{2.4}$$

so that again, we have solid reasons for neglecting viscosity, compressibility, surface tension and gravity.

We delay a discussion of the effect of an air-cushioning layer on the impact until Chapter 4.

2.2.2 Problem formulation

Based on these parameter estimates, we shall assume that the half-space of liquid is incompressible and inviscid. Since the liquid is initially at rest, its flow is irrotational by Kelvin's theorem. Hence, there exists a velocity potential of the liquid, $\phi(x, z, t)$, which satisfies

$$\frac{\partial^2 \phi}{\partial x^2} + \frac{\partial^2 \phi}{\partial z^2} = 0 \tag{2.5}$$

in the fluid. The kinematic condition on the body is given by

$$\varepsilon f'(\varepsilon x)\frac{\partial \phi}{\partial x} - \frac{\partial \phi}{\partial z} = \dot{s}(t) \quad \text{on} \quad z = f(\varepsilon x) - s(t),\ |x| < c(t), \tag{2.6}$$

where, here and hereafter, a prime indicates differentiation with respect to the argument and a dot indicates differentiation with respect to time, t. On the free surface, the kinematic and dynamic boundary conditions are given by

$$\frac{\partial \phi}{\partial z} = \frac{\partial h}{\partial t} + \frac{\partial \phi}{\partial x}\frac{\partial h}{\partial x} \quad \text{on} \quad z = h(x, t),\ |x| > d(t), \tag{2.7}$$

$$p = 0 \quad \text{on} \quad z = h(x, t),\ |x| > d(t), \tag{2.8}$$

where the fluid pressure $p(x, z, t)$ is given by Bernoulli's equation,

$$p + \frac{\partial \phi}{\partial t} + \frac{1}{2}|\nabla \phi|^2 = 0; \tag{2.9}$$

here $\nabla = \mathbf{i}\partial/\partial x + \mathbf{k}\partial/\partial z$, where $\mathbf{i}$ and $\mathbf{k}$ are the unit vectors in the x- and z-directions, respectively.

Finally, since the fluid is at rest and the free surface is planar prior to impact, the initial and far-field conditions are given by

$$\phi(x, z, 0) = 0 \quad \text{for} \quad -\infty < x < \infty, z \leq 0, \tag{2.10}$$

$$h(x, 0) = 0 \quad \text{for} \quad -\infty < x < \infty, \tag{2.11}$$

$$\phi = O\left(1/r\right) \quad \text{as} \quad r = \sqrt{x^2 + z^2} \to \infty, \tag{2.12}$$

$$h = O\left(1/x^2\right) \quad \text{as} \quad |x| \to \infty, \tag{2.13}$$

where the rates of decay in (2.12)–(2.13) follow from demanding the spatially integrated kinetic energy of the liquid be finite. Moreover, we enforce that $d(0) = 0$.

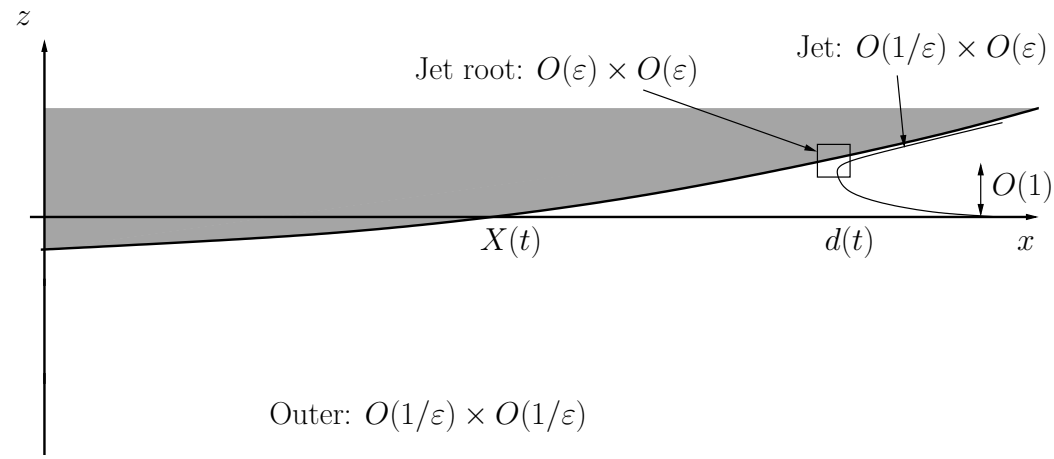

Figure 2.2: Asymptotic structure for small deadrise impact shown for $x > 0$. See text for details.

2.2.3 Asymptotic structure

As the impactor hits the liquid, the free surface is violently disturbed. The distance between the turnover points, at which the tangent to the free surface is vertical, increases in size as the impactor penetrates further into the fluid. Between the turnover points there is a region of high pressure on the body, which Wagner (1932) used as the basis for his model of the impact as a liquid being loaded by an expanding flat plate. At each end of this high pressure region, a jet is formed. This jet initiates from a region in the neighbourhood of the turnover points.

In order to analyse the asymptotic solution for small deadrise angles, we consider the structure of the flow field after impact as described in Armand and Cointe (1987) and Howison et al. (1991). Thus, we look at the flow in an outer region based on the size of the high-pressure region between the two turnover points at $x = \pm d(t)$. This outer region is of size of $O(1/\varepsilon) \times O(1/\varepsilon)$ and the free surface displacement in the outer region is of $O(1)$. Local to the turnover points, there is an inner turnover region on the body whose size we state *a priori* to be of $O(\varepsilon) \times O(\varepsilon)$: we will deduce this explicitly in §2.2.6. A jet region emanates from the turnover region. The thickness of the jet is of $O(\varepsilon)$ and this thickness varies over distances of $O(1/\varepsilon)$. This flow configuration is displayed for $x > 0$ in Figure 2.2.

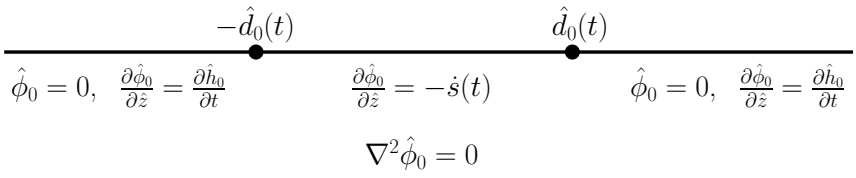

Figure 2.3: The linearised leading-order-outer problem where a subscript zero indicates a leading-order variable. In addition, we have the far-field condition that $\hat{\phi}_0 = O(1/\hat{r})$ as $\hat{r} = \sqrt{\hat{x}^2 + \hat{z}^2} \to \infty$. The velocity potential has square-root singularities at the turnover points. The initial conditions are $\hat{h}_{\hat{x},0}(0) = \hat{d}_0(0) = 0$. As described in the text, this problem is not closed as it requires a condition to determine $\hat{d}_0(t)$.

2.2.4 Leading-order-outer region

Assuming that the penetration depth $s = O(1)$, the x-coordinate of the intersection of the body profile with the undisturbed free surface, denoted by $X(t)$ in Figure 2.2, is of $O(1/\varepsilon)$ as $\varepsilon \downarrow 0$. This is consistent with the size of the outer region being of $O(1/\varepsilon)$, the distance between the turnover points also being of $O(1/\varepsilon)$.

Therefore, in the outer region, we neglect the jets on the body and rescale x, z, ϕ, p, h, d in (2.5)-(2.13) by setting

$$(x, z) = \frac{1}{\varepsilon}(\hat{x}, \hat{z}) \quad \phi = \frac{\hat{\phi}}{\varepsilon}, \quad p = \frac{\hat{p}}{\varepsilon}, \quad h = \hat{h}, \quad d = \frac{\hat{d}}{\varepsilon}.$$

Thus, the impactor is given by $\hat{z} = \varepsilon(f(\hat{x}) - s(t))$, the positions of the turnover points are given by $\hat{x} = \pm\hat{d}(t)$, and the free surface is given by $\hat{z} = \varepsilon\hat{h}(\hat{x}, t)$.

We perform regular perturbation expansions for $\hat{\phi}$, $\hat{p}$, $\hat{h}$, $\hat{d}$ in powers of ε and linearise the boundary conditions (2.6), (2.7) and (2.8) onto $\hat{z} = 0$ to obtain the leading-order-outer problem displayed in Figure 2.3. The leading-order variables are denoted by a subscript zero. Note that the kinematic boundary condition on the impactor, (2.6), is applied on the contact set $\hat{z} = 0$, $|\hat{x}| < \hat{d}_0(t)$, while the kinematic and dynamic boundary conditions on the free surfaces, (2.7) and (2.8), are applied on the non-contact set, $\hat{z} = 0$, $|\hat{x}| > \hat{d}_0(t)$. Note that the leading-order form of (2.8) is equivalent to

$$\frac{\partial \hat{\phi}_0}{\partial t} = 0 \quad \text{on} \quad \hat{z} = 0, |\hat{x}| > \hat{d}_0(t), \tag{2.14}$$

where we have used the leading-order Bernoulli equation (2.9). This can be integrated with respect to time, and along with (2.10), we deduce that $\hat{\phi}_0 = 0$ on the free surface.

The leading-order problem is supplemented by assigning the behaviour of $\hat{\phi}_0$ at the leading-order turnover points $\pm\hat{d}_0(t)$. Gillow (1998) performed a local analysis at a

turnover point to deduce that the least-singular behaviour of the velocity is an inverse square-root singularity at these points. Moreover, given the change from Dirichlet to Neumann boundary data for $\hat{\phi}_0$ at the free points, Howison et al. (1997) argue that this form of the singularity coupled with the far-field condition for $\hat{\phi}_0$ gives a unique solution to the codimension-two free boundary problem[1] depicted in Figure 2.3. The form of the singularity can only be verified by matching with the inner jet-root region, something we check *a posteriori*. Thus, we have

$$\hat{\phi}_0 = O(\hat{r}_\pm^{1/2}) \quad \text{as} \quad \hat{r}_\pm = \sqrt{(\hat{x} \mp \hat{d}_0(t))^2 + \hat{z}^2} \to \pm 0. \tag{2.15}$$

Finally, we note that the problem in Figure 2.3 is not closed as we require a condition to solve for $\hat{d}_0(t)$, which we will determine in §2.2.6.

2.2.4.1 Reduction to the canonical problem

In Figure 2.3, we note that time appears as a parameter in the leading-order problem, except in the kinematic boundary condition. Therefore, if $s(t)$ is monotonically increasing with t, we can make the change of variables

$$\hat{\phi}_0(x, z, t) = \dot{s}\tilde{\phi}_0(\hat{x}, \hat{z}, s), \quad \hat{h}_0(\hat{x}, t) = \tilde{h}_0(\hat{x}, s),$$

which reduces the problem to the constant-speed impact problem, in which $s(t) = t$. Thus, henceforth we shall assume $s(t) = t$ and note that the above change of variables allows us to consider variable impact speeds.

2.2.4.2 Solution of the leading-order-outer problem

The potential problem in Figure 2.3 can be formulated as a Riemann-Hilbert problem for the complex potential, $\hat{w}_0 = \hat{\phi}_0 + \mathrm{i}\hat{\psi}_0$, where $\hat{\psi}_0$ is the leading-order streamfunction. As described in Howison et al. (1991), the solution is given by

$$\hat{w}_0(\hat{\zeta}, t) = \mathrm{i}\left(\hat{\zeta} - \sqrt{\hat{\zeta}^2 - \hat{d}_0(t)^2}\right), \tag{2.16}$$

where $\hat{\zeta} = \hat{x} + \mathrm{i}\hat{z}$ and the square root is defined such that it has a branch cut on the contour $\Gamma = \{\hat{x} + \mathrm{i}\hat{z} | -\hat{d}_0(t) < \hat{x} < \hat{d}_0(t), \hat{z} = 0\}$, and is real and positive on the positive real axis for $\hat{x} > \hat{d}_0(t)$.

[1]The problem is a codimension-two free boundary problem as we must solve for the unknown free points $\pm\hat{d}_0(t)$ as part of the problem, and they have dimension 0 compared to the dimension of the problem, namely 2.

It follows from the leading-order kinematic condition on the free surface in Figure 2.3 that the free surface profile is given by

$$\hat{h}_0(\hat{x},t) = -t + \int_0^t \frac{\hat{x}}{\sqrt{\hat{x}^2 - \hat{d}_0(\tau)^2}}\,\mathrm{d}\tau \quad \text{on} \quad |\hat{x}| > \hat{d}_0(t). \tag{2.17}$$

A local analysis at the right-hand turnover point gives the local expansion

$$\hat{h}_0(\hat{x},t) = \hat{h}_0(\hat{d}_0(t),t) - \frac{\sqrt{2\hat{d}_0(t)(\hat{x}-\hat{d}_0(t))}}{\dot{\hat{d}}_0(t)} + O(x-\hat{d}_0(t)) \quad \text{as} \quad \hat{x} \downarrow \hat{d}_0(t). \tag{2.18}$$

Note that due to the symmetry of the problem, a similar expression holds near to the left-hand turnover point.

Using Bernoulli's equation, the leading-order-outer pressure is given by

$$\hat{p}_0(\hat{x},\hat{z},t) = -\frac{\partial\hat{\phi}_0}{\partial t} = -\frac{\partial}{\partial t}\left[-\hat{z} - \mathrm{Re}\left(\sqrt{\hat{d}_0(t)^2 - (\hat{x}+\mathrm{i}\hat{z})^2}\right)\right], \tag{2.19}$$

so that the pressure on the impactor for $|\hat{x}| < \hat{d}_0(t)$ is given by

$$\hat{p}_0(\hat{x},0,t) = \frac{\hat{d}_0(t)\dot{\hat{d}}_0(t)}{\sqrt{\hat{d}_0(t)^2 - \hat{x}^2}}. \tag{2.20}$$

Provided that $\dot{\hat{d}}_0(t) > 0$, the pressure is positive with a minimum on the line of symmetry of the impactor. Furthermore, the pressure is unbounded at the turnover points. We remark that for more complicated $s(t)$, the rescaled Bernoulli equation gives $\hat{p}(\hat{x},0,t) = -\partial/\partial t(\dot{s}\tilde{\phi}_0)$.

Since both the velocity and the pressure are singular at $x = \pm\hat{d}_0(t)$, we need to match to the inner region solution to describe the local flow near to the turnover points. Moreover, we need another condition to determine the leading-order locations of the turnover points.

2.2.5 Leading-order-inner problem

To investigate the flow near to the turnover points we return to the original nondimensional variables introduced in §2.2.2. The symmetry of the problem necessitates that we only need to solve the inner problem in the neighbourhood of the right-hand turnover point at $x = d(t)$ and for simplicity we present the details for $s(t) = t$ only, more general impact velocity being readily accounted for because the inner problem is quasi-steady at leading order.

We introduce the inner variables

$$x - d(t) = \varepsilon^n X, \quad z - (f(\varepsilon d(t)) - t) = \varepsilon^n Z,$$

where again $d(t) = \hat{d}(t)/\varepsilon$ and the exponent, $n > 0$, which dictates the size of the inner region, is to be determined. This is a travelling-wave frame moving with the turnover point. We know that the inner region moves with speed of $O(1/\varepsilon)$ in the x-direction, suggesting that we must rescale the velocity potential by

$$\phi = \varepsilon^{n-1}\left(\Phi + \varepsilon\dot{d}(t)X\right),$$

where on the right-hand side we have accounted for the velocity due to the moving frame. The multivalued free surface is defined as $Z = H(X,t)$, where

$$h - (f(\varepsilon d(t)) - t) = \varepsilon^n H.$$

Finally, from Bernoulli's equation, we deduce that the pressure is scaled by

$$p = \frac{1}{\varepsilon^2}P.$$

Expanding the inner region variables in powers of ε, we deduce that the leading-order-inner problem is as illustrated in Figure 2.4. Note that $\partial/\partial N$ denotes the outward normal derivative in the inner region and that $X = X_s, Z = 0$ denote the leading-order coordinates of the relative stagnation point on the body, corresponding to the point where the dividing (dashed) streamline meets the impacting body. The unknown leading-order jet thickness is denoted by $J(t)$.

The problem is closed by the far-field matching condition that

$$\Phi_0 = -\dot{\hat{d}}_0(t)X + O(R^{1/2}) \quad \text{as} \quad R = \sqrt{X^2 + Z^2} \to \infty. \tag{2.21}$$

The potential problem in Figure 2.4 is readily solved using the hodograph method, see Carrier et al. (1966), which we do not reproduce here. As shown in Howison et al. (1991), the solution can be defined implicitly, viz.

$$W_0 = -\frac{J(t)}{\pi}\left[\frac{4W_0'}{(W_0'+1)^2} + 2\log\left(\frac{W_0'-1}{W_0'+1}\right)\right] + k(t), \tag{2.22}$$

where $\dot{\hat{d}}_0(t)W_0(\zeta,t) = \Phi_0(X,Z,t) + \mathrm{i}\Psi_0(X,Z,t)$ is the leading-order-inner complex potential, $\Psi_0(X,Z,t)$ is the leading-order-inner streamfunction, $\zeta = X + \mathrm{i}Z$, and the unknown function of time $k(t)$ is defined as the value of $\Phi_0/\dot{\hat{d}}_0$ at the stagnation point. As noted by Oliver (2002), a higher-order analysis is required to determine $k(t)$. In the far-field (not in the jet), the complex potential has the expansion

$$W_0 \sim -\zeta - 4\mathrm{i}\sqrt{\frac{J(t)}{\pi}}\zeta \quad \text{as} \quad \zeta \to \infty, \tag{2.23}$$

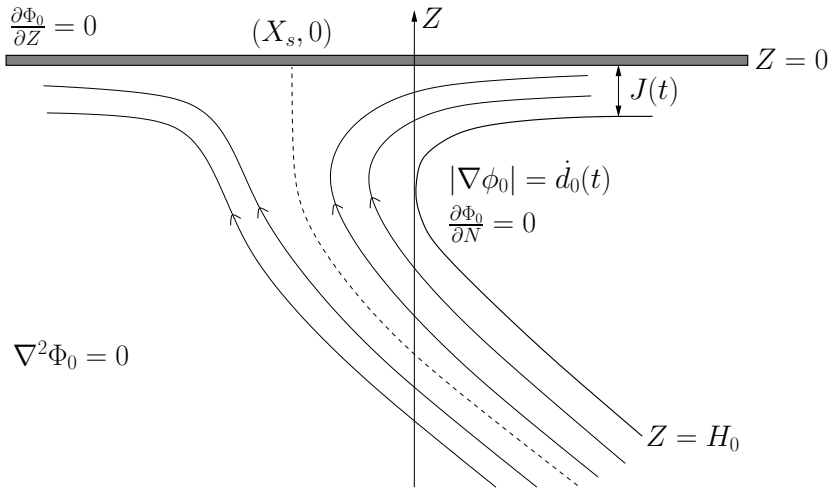

Figure 2.4: The leading-order-inner problem in the right-hand jet-root region. We have included several streamlines to help visualise the flow. The dashed line indicates the dividing streamline: flow on the right-hand side of this goes into the jet, flow to the left goes back into the main body of the fluid. See text for details.

and in the jet, the complex potential has the expansion

$$W_0 \sim \zeta \quad \text{as} \quad \zeta \to \infty. \tag{2.24}$$

The free surface $Z = H_0(X, t)$ is given parametrically by

$$X = -\frac{J(t)}{\pi}\left(\log\left|\frac{\xi - 1}{\xi + 1}\right| + \frac{2\xi}{\xi + 1}\right), \tag{2.25}$$

$$H_0(X, t) = Z_D - \frac{4J(t)}{\pi}\left(\sqrt{\frac{1 - \xi}{1 + \xi}} - 1\right), \tag{2.26}$$

where $\xi \in (-1, 1)$ and $X = 0, Z = Z_D$ is the location of the turnover point in the local coordinate frame.

We note that the upper free surface asymptotes to $H_0 \sim Z_D + 4J(t)/\pi$ as $X \to \infty$, so that $Z_D = -J(t) - 4J(t)/\pi$. Similarly, the lower free surface asymptotes to

$$H_0 \sim -4\sqrt{\frac{J(t)}{\pi}X} \quad \text{as} \quad X \to \infty. \tag{2.27}$$

2.2.5.1 Inner region pressure

In order to consider the pressure in the inner region, it is useful to write the complex potential in a more malleable form. Fortunately, such a form exists in the guise of the parametric solution to a similar cavity flow by Tuck (1994) and applied to the

water-entry scenario by Oliver (2002). The complex potential can be expressed in the form:

$$\dot{\hat{d}}_0(t)W_0 = \frac{\dot{\hat{d}}_0(t)J(t)}{\pi}\mathcal{G}(s) \tag{2.28}$$

where the function $\mathcal{G}(s)$ is given by

$$\mathcal{G}(s) = s - \log s, \quad X + \mathrm{i}Z = X_0 - \frac{J(t)}{\pi}(s + 4\sqrt{s} + \log s) \tag{2.29}$$

such that the fluid domain corresponds to $\mathrm{Im}(s) < 0$. Here X_0 is an arbitrary real constant. We take the principal branches of the logarithm and square root in (2.29).

Substituting the inner region scalings into Bernoulli's equation (2.9) and utilising (2.28) and (2.29), we find that the leading-order-inner pressure on the impactor is given by

$$P_0(X, 0, t) = \frac{\dot{\hat{d}}_0(t)^2}{2}\left[1 - \left(\frac{1-\sqrt{s}}{1+\sqrt{s}}\right)^2\right], \tag{2.30}$$

where $s > 0$ and X is defined by (2.29).

We note that although the leading-order-inner pressure on the impactor is an order of magnitude larger than the leading-order-outer pressure on the impactor, it is acting over a region that is two orders of magnitude smaller and therefore does not contribute to the leading-order force on the impactor, as we shall describe shortly.

2.2.6 Matching conditions

To complete the inner and outer solutions, we need to match them. The outer variables can be expressed in terms of the inner variables, viz.

$$\hat{x} = \varepsilon d + \varepsilon^{n+1}X,\ \hat{z} = \varepsilon\left(f\left(\varepsilon d\right) - t\right) + \varepsilon^{n+1}Z,\ \phi = \varepsilon^n\varphi,\ \hat{h} = f\left(\varepsilon d\right) - t + \varepsilon^n H,\ d = \frac{\hat{d}}{\varepsilon},$$

where $\varphi = \Phi + \varepsilon\dot{d}X$. Now, using a tilde to denote an intermediate variable, we define

$$\hat{x} = \varepsilon d + \varepsilon^\alpha\tilde{x}, \quad \hat{z} = \varepsilon\left(f(\varepsilon d) - t\right) + \varepsilon^\alpha\tilde{z}, \quad \hat{\phi} = \varepsilon^{\alpha-1}\tilde{\varphi}, \quad \hat{h} = f\left(\varepsilon d\right) - t + \varepsilon^{\alpha-1}\tilde{h},$$

where $0 < \alpha < n + 1$.

We can write (2.16), (2.23), (2.18) and (2.27) in intermediate variables, to find that

$$\tilde{\varphi} \sim -\frac{1}{\varepsilon^{\alpha-1}}\mathrm{Re}\left(\mathrm{i}\sqrt{2\hat{d}_0}\sqrt{\varepsilon^\alpha(\tilde{x} + \mathrm{i}\tilde{z}) + \mathrm{i}\varepsilon\left(f(\hat{d}_0) - t\right)}\right), \tag{2.31}$$

is the expansion local to the right-hand turnover point of the leading-order-outer potential solution, (2.16);

$$\tilde{\varphi} \sim -\frac{1}{\varepsilon^{\alpha-n-1}}\mathrm{Re}\left(4\mathrm{i}\sqrt{\frac{J}{\pi}}\sqrt{\varepsilon^{\alpha-n-1}(\tilde{x} + \mathrm{i}\tilde{z})}\right), \tag{2.32}$$

is the far-field expansion of the leading-order-inner solution, (2.23);

$$\tilde{h} \sim \frac{1}{\varepsilon^{\alpha-1}}\left[\hat{h}_0(\hat{d}_0,t) - f(\hat{d}_0) + t\right] - \frac{1}{\varepsilon^{\alpha/2-1}}\frac{\sqrt{2\hat{d}_0}}{\dot{\hat{d}}_0}\sqrt{\tilde{x}}, \tag{2.33}$$

is the expansion local to the right-hand turnover point of the leading-order-outer free surface profile, (2.18); and

$$\tilde{h} \sim -\frac{4}{\varepsilon^{(\alpha-n-1)/2}}\sqrt{\frac{J}{\pi}}\sqrt{\tilde{x}} \tag{2.34}$$

is the far-field asymptote of the leading-order-inner free surface. We seek to use (2.31)-(2.34) to deduce n, $J(t)$ and a condition for $\hat{d}_0(t)$, the leading-order location of the turnover point.

If we assume that $\alpha > 1$, we quickly reach a contradiction in matching between (2.31)–(2.32), so we force $0 < \alpha \leq 1$. Then the leading-order term in (2.31) is of $O(1/\varepsilon^{\alpha/2-1})$. Thus, as the leading-order term in (2.32) is of $O(1/\varepsilon^{(\alpha-n-1)/2})$, we deduce that

$$\frac{2-\alpha}{2} = \frac{n+1-\alpha}{2}, \tag{2.35}$$

giving $n = 1$.

As the leading-order term on the right-hand side of (2.33) is of $O(1/\varepsilon^{\alpha-1})$ compared to $O(1/\varepsilon^{\alpha/2-1})$ in (2.34), we must also have

$$\hat{h}_0\left(\hat{d}_0(t),t\right) = f\left(\hat{d}_0(t)\right) - t. \tag{2.36}$$

This matching condition is called the *Wagner condition*. Physically, it says that the leading-order-outer free surface meets the impactor at the turnover points. We note that (2.36) could also be derived on the basis of global conservation of mass at leading order, as in Wilson (1989).

Finally, we can deduce from matching the coefficients of the leading-order terms of (2.31) and (2.32) that the leading-order jet thickness, $J(t)$, is given by

$$J(t) = \frac{\pi\hat{d}_0(t)}{8\dot{\hat{d}}_0(t)^2}. \tag{2.37}$$

2.2.7 Motion of the free point

We can use the Wagner condition (2.36) in conjunction with (2.17) to find that the turnover point is given implicitly by

$$f(\hat{d}_0(t)) = \int_0^t \frac{\hat{d}_0(t)}{(\hat{d}_0(t)^2 - \hat{d}_0(\tau)^2)^{1/2}}\mathrm{d}\tau. \tag{2.38}$$

We assume that $x = \hat{d}_0(t)$ is invertible and denote its inverse by $t = \omega_0(x)$. Then (2.38) can be transformed into an Abel integral equation by making the change of variables $\tau = \omega_0(\sigma)$. Following the approach of Sneddon (1966), we can solve the resulting integral equation and use the initial condition $\hat{d}_0(0) = 0$ to deduce that $\hat{d}_0(t)$ is given implicitly by

$$\frac{\pi t}{2} = \int_0^{\hat{d}_0} \frac{f(\sigma)}{(\hat{d}_0^2 - \sigma^2)^{1/2}} \mathrm{d}\sigma = \int_0^{\pi/2} f(\hat{d}_0 \sin\theta)\, \mathrm{d}\theta. \tag{2.39}$$

2.2.8 Jet regions

Upon impact, the free surface is violently disturbed, and jets of fluid shoot from $x = \pm d(t)$ away from the large body of fluid in the outer region. By symmetry, we shall only consider the right-hand jet here. The right-hand jet is ejected along the impactor from the jet root at $x = d(t)$ with thickness $\varepsilon J(t)$ and speed $2\dot{d}(t)$ relative to the original dimensionless coordinates. Hence, recalling that $d = O(1/\varepsilon)$, the jet has velocity of $O(1/\varepsilon)$, thickness of $O(\varepsilon)$ and thickness variations over distances of $O(1/\varepsilon)$. Note that in the case of an impacting wedge, the arc length preservation property of the free surface, which was first proved by Garabedian (1953), requires the jet to have a length of $O(1/\varepsilon)$.

We have assumed that the jet is attached to the impactor; thus, in order to investigate its evolution, we move to a curvilinear coordinate system based on the impactor, say $(\bar{x}, \bar{z})$, where $\bar{x}$ parametrises distance along the body and $\bar{z}$ parametrises distance normal to the body. A full derivation of the leading-order jet problem can be found in Wilson (1989), so we do not go into detail here. In short, the jet variables $\bar{x}$, $\bar{z}$, $\bar{\phi}$, $\bar{h}$ and $\bar{p}$ are rescaled with $1/\varepsilon$, ε, $1/\varepsilon^2$, ε and $1/\varepsilon^2$ respectively. Here $\bar{h}$ represents the *thickness* of the jet.

To leading-order, as the length of the jet is much smaller than the radius of curvature of the impactor, the leading-order governing equations for $\bar{h}(\bar{x}, t)$ and $\bar{u}(\bar{x}, t) = \partial\bar{\phi}(\bar{x}, t)/\partial\bar{x}$ are the zero-gravity shallow water equations, as shown in Wilson (1989). Moreover, at leading order we can replace $\bar{x}$ with $\hat{x}$ because the impactor is flat. Thus, after performing an expansion in powers of ε, the leading-order equations of motion are given by

$$\frac{\partial \bar{h}_0}{\partial t} + \frac{\partial}{\partial \hat{x}}\left(\bar{h}_0 \bar{u}_0\right) = 0, \tag{2.40}$$

$$\frac{\partial \bar{u}_0}{\partial t} + \bar{u}_0 \frac{\partial \bar{u}_0}{\partial \hat{x}} = 0. \tag{2.41}$$

The leading-order boundary data at the jet-root are given by

$$\bar{u}_0 = 2\dot{\hat{d}}_0(t), \quad \bar{h}_0 = \frac{\pi \hat{d}_0(t)}{8\dot{\hat{d}}_0(t)^2} \quad \text{at} \quad \hat{x} = \hat{d}_0(t) \quad \text{for} \quad t > 0. \tag{2.42}$$

The shallow water equations with this boundary data are readily solved using the method of characteristics. Firstly, we parametrise the boundary data with s and let τ be the parameter along a characteristic. The solution is given parametrically for $s, \tau > 0$ by

$$t = \tau + s, \quad \hat{x} = 2\dot{\hat{d}}_0(s)\tau + \hat{d}_0(s), \quad \bar{u}_0 = 2\dot{\hat{d}}_0(s), \quad \bar{h}_0 = \frac{\pi \hat{d}_0(s)}{8}\dot{\hat{d}}_0(s)^{-2}\frac{\mathrm{J}(0,s)}{\mathrm{J}(\tau,s)}, \tag{2.43}$$

where the Jacobian of the problem is

$$\mathrm{J}(\tau, s) = -2\ddot{\hat{d}}_0(s)\tau + \dot{\hat{d}}_0(s). \tag{2.44}$$

Our solution exists provided this Jacobian is bounded and nonzero, and provided that the jet thickness $\bar{h}_0$ is nonzero. In particular, we note that for an advancing but decelerating turnover point, the Jacobian always satisfies these conditions. We shall consider whether the thickness condition holds for some specific examples shortly.

2.2.8.1 Pressure in the jet region

To leading-order, the jet solution is only influenced by the body through $\hat{d}_0(t)$. However, by proceeding to the fourth-order analysis as in Wilson (1989), we can show that the body shape also influences the pressure exerted by the liquid in the jet on the body. Recall that we scaled the pressure by $1/\varepsilon^2$ in the jet region. Expanding the jet pressure

$$\bar{p} \sim \bar{p}_0 + \varepsilon\bar{p}_1 + \varepsilon^2\bar{p}_2 + \varepsilon^3\bar{p}_3,$$

we find that $\bar{p}_i = 0$ for $i = 0, 1, 2$ and

$$\bar{p}_3 = -\kappa\bar{u}_0^2\bar{h}_0, \tag{2.45}$$

where $\kappa = f''(\bar{x})$ is the leading-order curvature of the impactor. Hence the leading-order jet pressure is $O(\varepsilon)$, which suggests that our scaling of $1/\varepsilon^2$ was incorrect. However, in other scenarios where other physical effects come into play, for example air-cushioning, which we shall consider in Chapter 4, $1/\varepsilon^2$ is the appropriate pressure scaling in the jet region, so we have used it here for the sake of consistency. Note that, since $\kappa > 0$ for our convex impactor, the leading-order pressure in the jet is negative, which may indicate separation of the jet. However, Vanden-Broeck and Keller (1989)

show that even a small amount of surface tension can greatly affect the location of any separation point, so using (2.45) to make any such predictions is unreliable.

This pressure is two orders of magnitude smaller than the leading-order-outer pressure, so that, although it is acting over an $O(1/\varepsilon)$ section of the impactor, it has no influence on the leading-order force on the body.

2.2.9 Leading-order force on the body

The vertical component of the hydrodynamic force on the body is found by integrating the liquid pressure over the wetted extent of the body profile. In order to do this formally, we would need to formulate the composite pressure expansion valid in the outer, inner and jet regions, as discussed in Wilson (1989) and Oliver (2002). However, we note that the leading-order-outer pressure is of magnitude $O(1/\varepsilon)$ and acts over a region of size $O(1/\varepsilon)$. Thus the leading-order contribution to the vertical force on the body from the outer region is of $O(1/\varepsilon^2)$. Similarly, the leading-order contributions from the jet root and jet regions are of size of $O(1/\varepsilon)$ and of $O(1)$ respectively. Therefore, clearly, if we expand the force on the body using the series

$$F(t) = \frac{1}{\varepsilon^2}F_0(t) + \frac{1}{\varepsilon}F_1(t) + F_2(t) + ...$$

the leading-order contribution to the force on the body is from the outer region only. It is trivially evaluated using (2.20) as follows

$$F_0(t) = \int_{-\hat{d}_0(t)}^{\hat{d}_0(t)} \hat{p}_0(\hat{x}, 0, t)\mathrm{d}\hat{x} = \pi \hat{d}_0(t)\dot{\hat{d}}_0(t). \tag{2.46}$$

Wagner (1932) derived this expression directly from the outer solution without any comment on his result. It is only by considering the asymptotics of the problem that we can show that this is indeed the correct leading-order force on the body.

2.2.10 Examples

We conclude this section by looking at two different examples of normal impacts at small deadrise angles. We will consider the entry of a wedge defined in dimensionless variables by $z = \varepsilon|x| - t$ and a blunt impactor $z = |\varepsilon x|^n - t$, for $n > 1$.

2.2.10.1 Wedge impact

The leading-order-outer solution is given by

$$\hat{\phi}_0(\hat{x},\hat{z},t) = -\hat{z} - \mathrm{Re}\left(\mathrm{i}\sqrt{(\hat{x}+\mathrm{i}\hat{z})^2 - \left(\frac{\pi t}{2}\right)^2}\right), \tag{2.47}$$

$$\hat{d}_0(t) = \frac{\pi t}{2}, \tag{2.48}$$

$$\hat{h}_0(\hat{x},t) = -t + \frac{2\hat{x}}{\pi}\arcsin\frac{\pi t}{2\hat{x}} \quad \text{for} \quad |\hat{x}| > \frac{\pi t}{2}, \tag{2.49}$$

$$\hat{p}_0(\hat{x},0,t) = \frac{\pi^2 t}{4\sqrt{(\pi t/2)^2 - \hat{x}^2}} \quad \text{for} \quad |\hat{x}| < \frac{\pi t}{2}. \tag{2.50}$$

Since $\ddot{\hat{d}}_0 \equiv 0, \dot{\hat{d}} > 0$, for a wedge impact, the Jacobian (2.44) for the jet solution as defined in §2.2.8 is always nonzero and bounded. Hence the solution exists for all $t > 0$. The jet thickness is given by

$$\bar{h}_0(\hat{x},t) = \frac{1}{2}\left(t - \frac{\hat{x}}{\pi}\right) \tag{2.51}$$

for $\hat{d}_0(t) < \hat{x} < 2\hat{d}_0(t)$, so that the jet terminates on the impactor at $\hat{x} = 2\hat{d}_0(t) = \pi t$. Clearly, the jet has length $\hat{d}_0(t)$.

2.2.10.2 Blunt impactor

The leading-order-outer solution is given by

$$\hat{\phi}_0(\hat{x},\hat{z},t) = -\hat{z} - \mathrm{Re}\left(\mathrm{i}\sqrt{(\hat{x}+\mathrm{i}\hat{z})^2 - \hat{d}_0(t)^2}\right), \tag{2.52}$$

$$\hat{d}_0(t) = \left(\frac{\pi t}{2^n \mathrm{B}((n+1)/2,(n+1)/2)}\right)^{1/n}, \tag{2.53}$$

where $\mathrm{B}(\cdot,\cdot)$ is the beta function. The leading-order-outer free surface and pressure on the impactor do not have as clean a closed form as for a wedge, but they can be found from (2.17) and (2.20) respectively.

For $n > 1$, it is clear that $\ddot{\hat{d}} < 0$ and $\dot{\hat{d}} > 0$, so that the Jacobian (2.44) in the jet solution is negative and bounded for all τ, s. Thus the solution is well-defined for all τ, s, and hence for all $\hat{x}, t$. Since

$$\bar{h}_0 = -\frac{\pi s}{8n}\frac{1}{\mathrm{J}(\tau,s)},$$

we deduce that $\bar{h}_0 > 0$ for all $\tau, s > 0$ and thus as

$$\hat{x} = \left(\frac{2\tau}{ns} + 1\right)\left(\frac{\pi s}{2^n \mathrm{B}((n+1)/2,(n+1)/2)}\right)^{1/n},$$

the jet is of infinite extent. Oliver (2002) showed this explicitly for a parabola.

Clearly, this means that defining $x = c(t)$, as we did at the start of the section, is somewhat misleading. In reality, the jet is not infinitely long and we expect there to be an inner region near the jet tip where we can resolve this problem. In such a region, surface tension and the liquid/solid contact angle are likely to be important. This is an unresolved problem in Wagner theory and we do not go any further into it here since determining $c(t)$ does not add anything further to our outer analysis or, indeed, the force on the impactor. We remark that neglecting this tip region is only reasonable assuming that the jet does not separate from the impactor, since in such situations the jet may impact back into the bulk fluid, cf. Thoroddsen et al. (2011).

2.2.11 Summary and extensions

In this section, we described classical two-dimensional Wagner theory for impact problems. The analysis is based on the assumption that in a wide-range of impacts, the body profile is approximately flat. The assumption of small deadrise angle means that the bulk of the liquid sees the impact as an expanding flat plate on its free surface. We derived the well-known asymptotic structure of Armand and Cointe (1987) and Howison et al. (1991). The flow breaks down into three distinct regions: the outer region of size of $O(1/\varepsilon) \times O(1/\varepsilon)$ sees the impact as the aforementioned flat plate; two inner regions of size of $O(\varepsilon) \times O(\varepsilon)$ local to the turnover points, where the free surface is multivalued; and two splash jets of thickness of $O(\varepsilon)$ and extent of $O(1/\varepsilon)$ emanating from the turnover regions.

After discussing the leading-order theory for constant-speed impacts in each of the three regions, we derived the Wagner condition by matching the outer and inner solutions. This condition states that the leading-order-outer free surface meets the impactor at the leading-order turnover points.

Wagner theory will form the foundation of the next few chapters of this thesis. The theory is readily generalised to other impact scenarios. We have already shown that we can apply our leading-order solution to variable impact speeds by means of a simple change of variables. It is also simple to extend the theory to non-symmetric impactors. As we shall see presently, the generality of the inner region, and thus the generality of the Wagner condition, will allow us to cope with a number of other scenarios.

2.2.11.1 The displacement potential

In conclusion to this overview of the classical theory, we define the *displacement potential*, which will be useful in our considerations of three-dimensional and oblique impacts, as well as our considerations of air-cushioning. The displacement potential, $\hat{\Upsilon}$, was first introduced in impact theory by Korobkin (1982), and is given by

$$\hat{\Upsilon}_0 = -\int_0^t \hat{\phi}_0(\hat{x}, \hat{z}, \tau)\,\mathrm{d}\tau. \tag{2.54}$$

Note that this transformation only makes sense if $\hat{\phi}_0(\hat{x}, \hat{z}, 0) = 0$ and $\hat{d}_0(0) = 0$.

Under this integral transformation, the leading-order-outer problem can be simplified. We assume that we can invert $\hat{x} = \hat{d}_0(t)$ and that its inverse is given by $t = \hat{\omega}_0(\hat{x})$. Therefore, the contact set is given by $t > \hat{\omega}_0(\hat{x})$ and the non-contact set is given by $t < \hat{\omega}_0(\hat{x})$.

It follows that the leading-order kinematic boundary condition on the free surface is given by

$$\begin{aligned}\frac{\partial \hat{\Upsilon}_0}{\partial \hat{z}} &= -\int_0^t \frac{\partial \hat{h}_0}{\partial t}(\hat{x}, \hat{z}, \tau)\,\mathrm{d}\tau \\ &= -\hat{h}_0(\hat{x}, \hat{z}, t) + \hat{h}_0(\hat{x}, \hat{z}, 0) \\ &= -\hat{h}_0\end{aligned}$$

on $\hat{z} = 0$, $|\hat{x}| > \hat{d}_0(t)$, where we have applied the initial condition on the free surface, (2.11). Similarly, the kinematic condition on the body is given by

$$\begin{aligned}\frac{\partial \hat{\Upsilon}_0}{\partial \hat{z}} &= -\int_0^{\hat{\omega}_0} \frac{\partial \hat{h}_0}{\partial t}(\hat{x}, \hat{z}, \tau)\,\mathrm{d}\tau + \int_{\hat{\omega}_0}^t \mathrm{d}\tau \\ &= -h(x, z, \hat{\omega}_0) + (t - \hat{\omega}_0) \\ &= t - f(\hat{d}(t)),\end{aligned}$$

on $\hat{z} = 0$, $|\hat{x}| < \hat{d}_0(t)$, where we have applied the Wagner condition (2.36) to deduce the final expression.

The remaining transformation of the problem displayed in Figure 2.3 is straightforward, and we deduce the leading-order displacement potential problem for classical Wagner theory as shown in Figure 2.5. This can be solved using similar Riemann-Hilbert techniques to those in the velocity potential problem and we do not consider this any further here. However, it is worth noting that the leading-order problem does not contain any time derivatives. This will become useful in our analysis of oblique impacts in §§3.1–3.2.

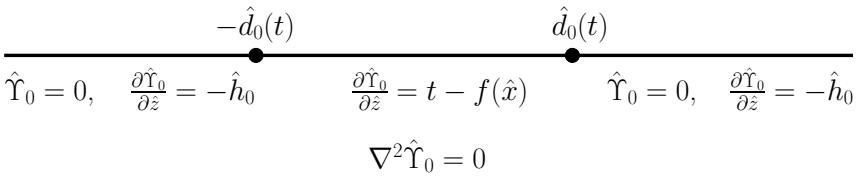

Figure 2.5: The linearised leading-order-outer problem for the displacement potential, $\hat{\Upsilon}_0$. Additionally, we require $\hat{\Upsilon}_0 = O(1/\hat{r})$ as $\hat{r} = \sqrt{\hat{x}^2 + \hat{z}^2} \to \infty$. The smoothing effect of the integral transform means that the displacement potential has (3/2)-power behaviour at the turnover points.

2.2.11.2 Droplet impact and fluid-fluid impact

The initial stages of droplet impact onto a solid surface are well characterised by Wagner theory provided that the local approximation of the droplet at the point of impact has a small deadrise angle. It is also simple to extend Wagner theory to fluid-fluid impact. This is tackled in Wilson (1989) and Howison et al. (1991). The small-deadrise requirement is extended to both fluid bodies and an interface representing a vortex sheet at $z = \eta(x, t)$ is introduced between the fluids after impact. The normal velocity and pressures of the fluids must balance across this interface. There are two turnover regions and the jet will typically make a nonzero, but $O(\varepsilon)$, angle with the horizontal axis. However, under the assumption that the ratio of the radii of curvature of the two bodies and the ratio of impact velocities are approximately order unity, the locations of the upper and lower turnover points at each jet root lie at the same horizontal location in the outer region to leading order, and the boundary conditions on the free surfaces and interface linearise onto the horizontal axis. The resulting problem can then be solved in a similar manner to the outer region in Wagner theory, as shown in Wilson (1989).

2.2.11.3 Stability of the water-entry problem

Howison et al. (1991) and Gillow (1998) perform a local-in-space-and-time stability analysis of the two-dimensional leading-order-outer problem presented in Figure 2.3, where a small perturbation in the out-of-plane $\hat{y}$-direction to the location of the free boundary $\hat{x} = \hat{d}(t)$ is introduced. We will not repeat the full analysis here, but in essence, the two-dimensional solution is a solution of the fully three-dimensional leading-order Wagner problem when the body is still given by $\hat{z} = f(\hat{x})$. At a given point in time, $t = t_0$, the solution local to $\hat{x} = \hat{d}(t_0)$, takes the form of a travelling wave. Perturbing about this local solution, matched asymptotic expansions in the

regions where $\hat{y} = O(1)$ are used to determine a dispersion relation that links the growth of the perturbations to the speed of the turnover point, $\dot{\hat{d}}(t_0)$. Gillow (1998) states that the growth rate of the perturbations, σ, is related to the turnover point speed by

$$\sigma \leq -n\dot{\hat{d}}(t_0) \tag{2.55}$$

where n is a positive constant. Clearly, for the growth of any perturbations to decay, $\dot{\hat{d}}(t_0)$ must be positive. When the turnover point is retreating, perturbations can grow and the problem is unstable. This means that the time-reversed problem of water exit is unstable to small perturbations.

In addition to the instability, if the turnover point is retreating, there is a change in sign in the leading-order-outer pressure on the body (2.20), which may lead to cavitation on the impactor. This is not accounted for in the model we have presented and would require more detailed thought, perhaps including a patch cavity as in, for example, Howison et al. (1994) and Korobkin (2003).

Furthermore, in the time-reversed problem we can no longer solve for the leading-order-outer free surface, $\hat{h}$, from the kinematic boundary conditions since the characteristics, given by $\hat{x} = 2\dot{\hat{d}}(s)\tau + d(s)$, where s parametrises the initial data on the turnover curve in $(\hat{x}, t)$-space and τ parametrises along a characteristic, enter the turnover curve rather than exit it. This means we lose causality in the system.

Since this stability analysis is local-in-space-and-time, it will also apply to an amalgam of other scenarios we consider in this thesis. In particular, to three dimensional impacts, where we require the outward normal speed of the turnover curve to be positive, and in oblique impacts. In the latter case, the oblique velocity will sometimes cause instability and breakdown even if the impactor is entering the fluid. We will consider this in detail in §§3.1–3.2.

2.3 Three-dimensional Wagner theory

Much of the analysis in §2.2 for two-dimensional, incompressible, normal impacts at small deadrise angles can be extended to three-dimensional, normal impacts. Indeed, Wilson (1989), Oliver (2002) and Korobkin and Scolan (2006) consider this exact problem. We will draw on all of these in the following section, in particular concentrating on axisymmetric impacts. Furthermore, much of our analysis will concentrate on the displacement potential form of the problem, so as to make extensions to oblique impacts much simpler. Moreover, we will also give more attention to the *splash sheet*, the three-dimensional generalisation of the splash jets.

We consider the impact of a rigid, smooth (except possibly at the point of impact), convex body onto an initially-quiescent half-space of fluid occupying $z^* \leq 0$ in three-dimensional Euclidean space, with axes denoted by (x^*, y^*, z^*). The impact begins at time $t^* = 0$ at the origin in this space. We assume that the fluid is incompressible and ideal, and that the region not occupied by the impactor or the fluid is a vacuum. We assume that the impactor moves downward with constant speed (L/T), where $(L/T)t^*$ is a typical penetration depth, and T is a typical impact timescale. Note that we could use $(L/T)\dot{s}(t^*/T)$ as a more general impact speed, but as in §2.2.4.1, we would again find a simple rescaling to the constant-speed problem. The location of the impactor profile is given by

$$\frac{z^*}{L} = f\left(\frac{\varepsilon x^*}{L}, \frac{\varepsilon y^*}{L}\right) - \frac{t^*}{T}, \tag{2.56}$$

where f is smooth except possibly at the initial point of impact, $f(0,0) = 0$, f has a unique minimum at its apex and f is increasing with distance from the origin. Throughout this chapter we shall again assume that the deadrise angle is small, which corresponds to $0 < \varepsilon \ll 1$.

The location of the multivalued free surface is denoted by $z^* = h^*(x^*, y^*, t^*)$. The set of points at which this surface is vertical is called the turnover curve, which we denote by $\partial\Omega(t^*)$, with projection $t^* = \omega^*(\varepsilon x^*/L, \varepsilon y^*/L)$ in the (x^*, y^*)-plane[2]. We saw in two dimensions that in some examples, the splash jets were of infinite extent for all times $t^* > 0$. Although this is non-physical, it did not influence our leading-order analysis provided that the jets did not separate from the impactor. It is possible we will see similar behaviour in three-dimensions for the splash sheet. Nevertheless, for notational convenience, we shall define a wetted extent of the impactor given by the curve $\partial C(t^*)$ with projection $t^* = c^*(\varepsilon x^*/L, \varepsilon y^*/L)$ in the (x^*, y^*)-plane. We display the problem configuration for $t^* > 0$ in Figure 2.6

The derivation of the problem follows as in two-dimensional Wagner theory, and we do not reproduce all of the details here. We will state the equations of motion, boundary, initial and far-field conditions in dimensionless form.

2.3.1 Dimensionless problem

As in §2.2, we scale distances, time, velocities, velocity potential and pressure by L, T, L/T, L^2/T and $\rho_l L^2/T^2$ respectively. Therefore, the body is given by $z = f(\varepsilon x, \varepsilon y) - t$. The equation of motion in the fluid is given by

$$\frac{\partial^2\phi}{\partial x^2} + \frac{\partial^2\phi}{\partial y^2} + \frac{\partial^2\phi}{\partial z^2} = 0. \tag{2.57}$$

[2]We shall sometimes lapse into referring to ω^* as the 'turnover curve location'.

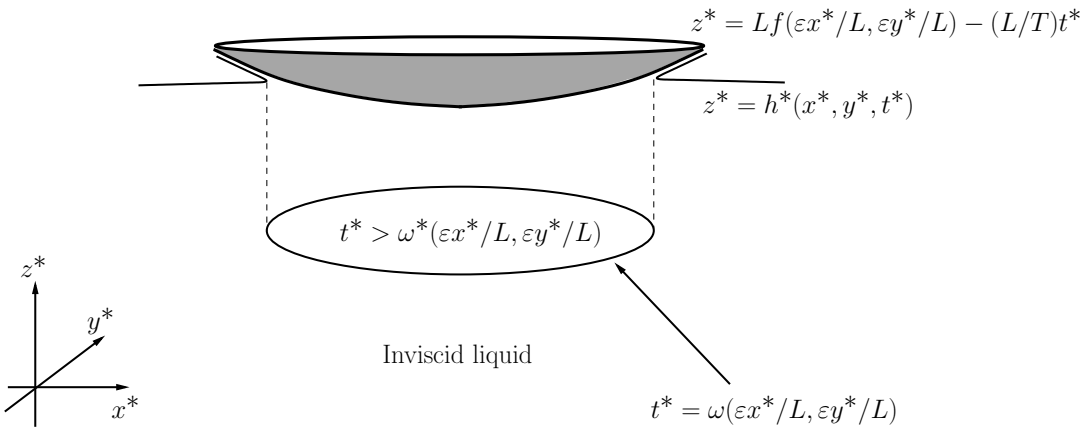

Figure 2.6: Problem configuration for $t^* > 0$.

On the body, the kinematic condition is given by

$$\varepsilon f_{,1}\frac{\partial \phi}{\partial x} + \varepsilon f_{,2}\frac{\partial \phi}{\partial y} - \frac{\partial \phi}{\partial z} = 1 \quad \text{on} \quad z = f(\varepsilon x, \varepsilon y) - t, t > c(\varepsilon x, \varepsilon y), \tag{2.58}$$

where $f_{,i}$ represents differentiation with respect to the i^{th} argument of f. On the multivalued free surface, $z = h(x, y, t)$, the kinematic condition is given by

$$\frac{\partial \phi}{\partial z} = \frac{\partial h}{\partial t} + \frac{\partial \phi}{\partial x}\frac{\partial h}{\partial x} + \frac{\partial \phi}{\partial y}\frac{\partial h}{\partial y} \quad \text{on} \quad z = h(x, y, t), t < \omega(\varepsilon x, \varepsilon y). \tag{2.59}$$

while the dynamic boundary condition is given by

$$p = 0 \quad \text{on} \quad z = h(x, y, t), t < \omega(\varepsilon x, \varepsilon y), \tag{2.60}$$

where the fluid pressure $p(x, y, z, t)$ satisfies the Bernoulli equation

$$p + \frac{\partial \phi}{\partial t} + \frac{1}{2}|\nabla \phi|^2 = 0 \tag{2.61}$$

in the fluid.

Finally, the initial and far-field conditions are given by

$$\phi(x, y, z, 0) = 0 \qquad \text{for} \quad -\infty < x, y < \infty, z \leq 0 \tag{2.62}$$

$$h(x, y, 0) = 0 \qquad \text{for} \quad -\infty < x, y < \infty, \tag{2.63}$$

$$\phi = O\left(1/R^2\right) \quad \text{as} \quad R = \sqrt{x^2 + y^2 + z^2} \to \infty, \tag{2.64}$$

$$h = O\left(1/r^3\right) \quad \text{as} \quad r = \sqrt{x^2 + y^2} \to \infty. \tag{2.65}$$

The far-field conditions guarantee bounded spatially integrated kinetic energy. We must also have $\omega(0, 0) = 0$.

2.3.2 Asymptotic structure

As discussed by Howison et al. (1991), the asymptotic structure for two-dimensional impact problems at small deadrise angles generalises directly to the three-dimensional case. The turnover points become a turnover curve, which we have denoted by $\partial\Omega(t)$ and the splash jets become a splash sheet.

Thus we consider three regions: an outer region of size of $O(1/\varepsilon)$, an inner region of size of $O(\varepsilon)$ in each plane perpendicular to the turnover curve, and a slender, long splash sheet that emanates from the inner region. The splash sheet has thickness of $O(\varepsilon)$, with thickness variations over distances of $O(1/\varepsilon)$.

2.3.3 Leading-order-inner problem

We will now outline the analysis of Wilson (1989) to show that the leading-order-inner problem is in fact quasi-two-dimensional, so we can directly use the results of §2.2.5 in our solution of the leading-order-outer problem.

Let $\xi(x,y,t), \eta(x,y,t)$ be curvilinear coordinates based on the moving turnover curve projection $t = \omega(\varepsilon x, \varepsilon y)$, with η measuring arc length along the turnover curve and ξ measuring distance in the outward normal direction, $\mathbf{n}$. Therefore, curves of constant ξ are concentric with the turnover curve at each time t. We denote the curvature of the turnover curve by $\kappa(\eta)$. Due to our assumption of small deadrise angle, the arc length of the turnover curve is large and the curvature is small, specifically, $\eta = O(1/\varepsilon)$ and $\kappa(\eta) = O(\varepsilon)$. Now, the turnover curve velocity is of $O(1/\varepsilon)$, so that the terms due to the moving frame – ξ_t, η_t – are at most $O(1/\varepsilon)$. Furthermore, on $\xi = 0$, ξ_t is equal to $-v_n(\eta,t) = O(1/\varepsilon)$, where $v_n(\eta,t)$ is the outward normal speed of the turnover curve.

As an example, suppose that the impactor is axisymmetric and the turnover curve is given in dimensionless variables by $\sqrt{x^2+y^2} = a(t)/\varepsilon$. Then the outward normal speed of this curve is simply $a'(t)/\varepsilon$, and the curvilinear coordinate system is

$$\xi = \sqrt{x^2+y^2} - \frac{a(t)}{\varepsilon}, \ \eta = \frac{a(t)}{\varepsilon} \arctan\left(\frac{y}{x}\right). \tag{2.66}$$

Then, $\xi_t = -a'(t)/\varepsilon = -v_n(t) = O(1/\varepsilon)$, $\eta_t = (a'(t)/a(t))\eta = O(1/\varepsilon)$ as $\eta = O(1/\varepsilon)$ and $\kappa(\eta) = \varepsilon/t = O(\varepsilon)$, as expected.

We now state (2.57)-(2.60) in inner variables. Variables in the inner region are denoted with a tilde. The velocity potential $\tilde{\phi}(\xi,\eta,z,t)$ must satisfy

$$\frac{1}{1+\kappa(\eta)\xi}\left[\frac{\partial}{\partial\xi}\left((1+\kappa(\eta)\xi)\frac{\partial}{\partial\xi}\right) + \frac{\partial}{\partial\eta}\left(\frac{1}{1+\kappa(\eta)\xi}\frac{\partial}{\partial\eta}\right) + (1+\kappa(\eta)\xi)\frac{\partial^2}{\partial z^2}\right]\tilde{\phi} = 0. \tag{2.67}$$

There are no time derivatives in the kinematic condition on the impactor, (2.58), so we do not expect to pick up additional terms due to the frame moving with the turnover curve. However, it is nontrivial to rewrite the terms involving $f_{,i}$ in the new coordinates. Hence, in a slight abuse of notation, the kinematic condition on the body is given by

$$\frac{\partial\tilde{\phi}}{\partial z} = -1 + \varepsilon f_{,1}\frac{\partial\tilde{\phi}}{\partial\xi} + \frac{\varepsilon f_{,2}}{1+\kappa(\eta)\xi}\frac{\partial\tilde{\phi}}{\partial\eta} \quad \text{on} \quad z = f(\varepsilon x, \varepsilon y) - t, \tag{2.68}$$

where $f(\varepsilon x, \varepsilon y)$ is the body profile and we can in theory write x, y in terms of ξ, η.

Suppose that the free surface $h(x, y, t) = \tilde{h}(\xi, \eta, t)$. In making the change of variables to a frame that moves with the turnover curve, we expect to pick up additional terms from the $\partial h/\partial t$ term in (2.59) and from the $\partial\phi/\partial t$ term in (2.60)–(2.61). Then, the kinematic condition on the free surface is given by

$$\frac{\partial\tilde{\phi}}{\partial z} = \frac{\partial\tilde{h}}{\partial t} + \frac{\partial\xi}{\partial t}\frac{\partial\tilde{h}}{\partial\xi} + \frac{\partial\eta}{\partial t}\frac{\partial\tilde{h}}{\partial\eta} + \frac{1}{(1+\kappa(\eta)\xi)^2}\frac{\partial\tilde{\phi}}{\partial\eta}\frac{\partial\tilde{h}}{\partial\eta} + \frac{\partial\tilde{\phi}}{\partial\xi}\frac{\partial\tilde{h}}{\partial\xi} \tag{2.69}$$

on $z = \tilde{h}(\xi, \eta, t)$, and the dynamic boundary condition is given by

$$\frac{\partial\tilde{\phi}}{\partial t} + \frac{\partial\xi}{\partial t}\frac{\partial\tilde{\phi}}{\partial\xi} + \frac{\partial\eta}{\partial t}\frac{\partial\tilde{\phi}}{\partial\eta} + \frac{1}{2}\left[\left(\frac{\partial\tilde{\phi}}{\partial\xi}\right)^2 + \frac{1}{(1+\kappa(\eta)\xi)^2}\left(\frac{\partial\tilde{\phi}}{\partial\eta}\right)^2 + \left(\frac{\partial\tilde{\phi}}{\partial z}\right)^2\right] = 0 \tag{2.70}$$

on $z = \tilde{h}(\xi, \eta, t)$.

As we stated previously, in general, we expect the turnover curve speed, and thus the speed of this moving frame, to be of $O(1/\varepsilon)$. Furthermore, we expect the arc length to be of $O(1/\varepsilon)$, the curvature of the turnover curve to be of $O(\varepsilon)$, and as in §2.2.5, the size of the normal coordinate, ξ, is of $O(\varepsilon)$. Therefore, in the inner region we set

$$\xi = \varepsilon\bar{\xi}, \quad \eta = \frac{\bar{\eta}}{\varepsilon}, \quad z = \lambda(t) - t + \varepsilon\bar{z}, \quad \kappa = \varepsilon\bar{\kappa}, \quad \tilde{h} = \lambda(t) - t + \varepsilon\bar{h}, \tag{2.71}$$

where $\lambda(t)$ is the value of $f(\varepsilon x, \varepsilon y)$ on the turnover curve (cf. §2.2.5 where $\lambda(t) = f(d(t))$ in two dimensions). Note that the above change of variables means that the impactor is of $O(\varepsilon)$ in the inner region, so we introduce the notation $\bar{z} = \varepsilon\bar{f}(\bar{\xi}, \bar{\eta}, t)$ to denote the body profile (cf. §2.2.5 where $\bar{z} = \varepsilon\bar{x}f'(d(t)) = \varepsilon\bar{f}(\bar{x}, t)$ in two dimensions). Therefore, the boundary condition (2.68) is applied on $\bar{z} = \varepsilon\bar{f}(\bar{\xi}, \bar{\eta}, t)$.

Now, since we have scaled ξ by ε, the functions due to the moving frame ξ_t and η_t can be approximated to leading-order in ε by their values on the turnover curve, that is

$$\xi_t \sim \frac{-\bar{v}_n(\bar{\eta}, t)}{\varepsilon}, \quad \eta_t \sim \frac{\bar{w}(0, \bar{\eta}, t)}{\varepsilon} \quad \text{as} \quad \varepsilon \to 0, \tag{2.72}$$

where $\bar{v}_n(\bar{\eta}, t)$ is the scaled outward normal speed of the turnover curve. Due to the different scales for ξ and η, the contribution from the $\eta_t \partial/\partial\eta$ terms in (2.69)–(2.70) comes in at lower order and, therefore, we can account for the leading-order velocity due to the moving frame by writing

$$\tilde{\bar{\phi}} = \bar{v}_n(\bar{\eta}, t)\xi + \bar{\phi}, \tag{2.73}$$

which also forces the local velocity to be of $O(1/\varepsilon)$.

Hence, provided that the terms involving $f_{,i}$ in (2.68) are at most $O(1)$ in the inner region, to leading order in ε, (2.67)–(2.70) reduce to

$$\frac{\partial^2\bar{\phi}}{\partial\bar{\xi}^2} + \frac{\partial^2\bar{\phi}}{\partial\bar{z}^2} = 0 \quad \text{in the fluid,} \tag{2.74}$$

$$\frac{\partial\bar{\phi}}{\partial\bar{z}} = 0 \quad \text{on} \quad \bar{z} = 0, \tag{2.75}$$

$$\frac{\partial\bar{\phi}}{\partial\bar{\xi}}\frac{\partial\bar{h}}{\partial\bar{\xi}} - \frac{\partial\bar{\phi}}{\partial\bar{z}} = 0 \quad \text{on} \quad \bar{z} = \bar{h}, \tag{2.76}$$

$$\left(\frac{\partial\bar{\phi}}{\partial\bar{\xi}}\right)^2 + \left(\frac{\partial\bar{\phi}}{\partial\bar{z}}\right)^2 = \bar{v}_n^2 \quad \text{on} \quad \bar{z} = \bar{h}. \tag{2.77}$$

The problem is completed with the inclusion of matching conditions to the splash sheet and the outer region.

Thus, (2.74)–(2.77) is exactly the same form as the leading-order two-dimensional inner problem displayed in §2.2.5, with the turnover point velocity, $\dot{d}(t)$ replaced by the outward normal speed of the turnover curve, $\bar{v}_n(\bar{\eta}, t)$. Hence, for each $\bar{\eta}$, the solution is therefore given by (2.28)-(2.29) replacing $\dot{d}(t)$ with $\bar{v}_n(\bar{\eta}, t)$.

Therefore, a similar matching argument means that the leading-order-outer velocity potential must have square-root behaviour as we approach the turnover curve in any plane perpendicular to it and that the Wagner condition

$$\hat{h}(\hat{x}, \hat{y}, t) = f(\hat{x}, \hat{y}) - t \quad \text{on} \quad t = \omega(\hat{x}, \hat{y}), \tag{2.78}$$

pertains, where $(\hat{x}, \hat{y})$ are outer coordinates. Furthermore, if the splash sheet thickness is again denoted by $J(t)$, matching enforces

$$J(t) = \frac{\pi S^2}{16\bar{v}_n^2}, \tag{2.79}$$

where S is the coefficient of the square-root term as we approach the turnover curve in the leading-order-outer velocity potential as derived in Oliver (2002).

2.3.4 Leading-order-outer problem

As in the two dimensional problem, the impactor penetrates the undisturbed fluid by a distance of order unity as we increase x, y by an $O(1/\varepsilon)$ amount for $t = O(1)$. Hence, we scale x, y, z, ϕ, p, h in (2.57)-(2.61) by

$$x = \frac{\hat{x}}{\varepsilon}, \quad y = \frac{\hat{y}}{\varepsilon}, \quad z = \frac{\hat{z}}{\varepsilon}, \quad \phi = \frac{\hat{\phi}}{\varepsilon}, \quad p = \frac{\hat{p}}{\varepsilon}, \quad h = \hat{h}.$$

Dropping the caret notation, the impactor is now given by $z = \varepsilon(f(x, y) - t)$. The projection of turnover curve into the (x, y)-plane is defined by $t = \omega(x, y)$ and the free surface by $z = \varepsilon h(x, y, t)$. As in the two-dimensional case, we proceed by neglecting the splash sheet on the impactor, expanding ϕ, h, p and ω in powers of ε and linearising the boundary conditions (2.58), (2.59) and (2.60) onto $z = 0$. Hence, at leading order, with a subscript zero indicating a leading-order variable, we derive

$$\frac{\partial^2 \phi_0}{\partial x^2} + \frac{\partial^2 \phi_0}{\partial y^2} + \frac{\partial^2 \phi_0}{\partial z^2} = 0 \qquad \text{in} \quad z \leq 0, \tag{2.80}$$

$$\frac{\partial \phi_0}{\partial z} = -1 \qquad \text{on} \quad z = 0, t > \omega_0(x, y), \tag{2.81}$$

$$\frac{\partial \phi_0}{\partial z} = \frac{\partial h_0}{\partial t} \qquad \text{on} \quad z = 0, t < \omega_0(x, y), \tag{2.82}$$

$$\frac{\partial \phi_0}{\partial t} = 0 \qquad \text{on} \quad z = 0, t < \omega_0(x, y), \tag{2.83}$$

where (2.83) is derived from the leading-order form of the dynamic condition condition (2.60). These are supplemented with the initial and far-field conditions given by

$$\phi_0(x, y, z, 0) = 0 \qquad \text{for} \quad -\infty < x, y < \infty, z \leq 0, \tag{2.84}$$

$$h_0(x, y, 0) = 0 \qquad \text{for} \quad -\infty < x, y < \infty, \tag{2.85}$$

$$\phi_0 = O\left(1/R^2\right) \quad \text{as} \quad R \to \infty, \tag{2.86}$$

$$h_0 = O\left(1/r^3\right) \quad \text{as} \quad r \to \infty. \tag{2.87}$$

We also require that $\omega_0(0, 0) = 0$. It is simple to note that (2.83) can be integrated with respect to time. Upon applying (2.85), we deduce that

$$\phi_0 = 0 \quad \text{on} \quad z = 0, t < \omega_0(x, y). \tag{2.88}$$

Finally, we close the problem by prescribing the Wagner condition, (2.78) and describing the behaviour of ϕ_0 as we approach the turnover curve. As we showed in §2.3.3, since the inner region is quasi-two-dimensional, we require the velocity potential to have square-root behaviour as we approach the turnover curve, $t = \omega_0(x, y)$, in any plane perpendicular to it.

2.3.4.1 Displacement potential formulation

It is easier to make analytic progress in the leading-order three-dimensional outer problem by reformulating the problem using the displacement potential. Recall that this is defined by

$$\Upsilon_0 = -\int_0^t \phi_0(x, y, z, \tau)\mathrm{d}\tau. \tag{2.89}$$

The boundary conditions transform in exactly the same way as in the two-dimensional theory, so we simply state the leading-order displacement potential problem, namely

$$\frac{\partial^2 \Upsilon_0}{\partial x^2} + \frac{\partial^2 \Upsilon_0}{\partial y^2} + \frac{\partial^2 \Upsilon_0}{\partial z^2} = 0 \qquad \text{in} \quad z \leq 0, \tag{2.90}$$

$$\frac{\partial \Upsilon_0}{\partial z} = t - f(x, y) \quad \text{on} \quad z = 0, t > \omega_0(x, y), \tag{2.91}$$

$$\frac{\partial \Upsilon_0}{\partial z} = -h_0 \qquad \text{on} \quad z = 0, t < \omega_0(x, y), \tag{2.92}$$

$$\Upsilon_0 = 0 \qquad \text{on} \quad z = 0, t < \omega_0(x, y), \tag{2.93}$$

subject to

$$\Upsilon_0 = O\left(1/R^2\right) \quad \text{as} \quad R \to \infty, \tag{2.94}$$

$$h_0 = O\left(1/r^3\right) \quad \text{as} \quad r \to \infty. \tag{2.95}$$

Note that there are no time derivatives in this problem, so we do note require any initial conditions to solve it. The initial conditions on ϕ_0 and ω_0 are required for this transformation to make sense, whereas the initial condition on h_0 is used in the transformation of the boundary conditions. The smoothing effect of the integral transformation (2.89) means that we require Υ_0 to have 3/2-power behaviour in distance from the turnover curve, $t = \omega_0(x, y), z = 0$, as we approach it in any plane perpendicular to it. We display the leading-order displacement potential problem in Figure 2.7.

2.3.4.2 Axisymmetric impact

We can make significant analytical progress by making the simplifying assumption that the body profile is axisymmetric. In this section, it is most appropriate to follow the analysis of Korobkin and Scolan (2006) (see §4 and Appendix A in that paper). We make a change to cylindrical polar coordinates defined by

$$x = r\cos\theta, \quad y = r\sin\theta, \quad \Upsilon_0(x, y, z, t) = \Upsilon_0(r, z, t).$$

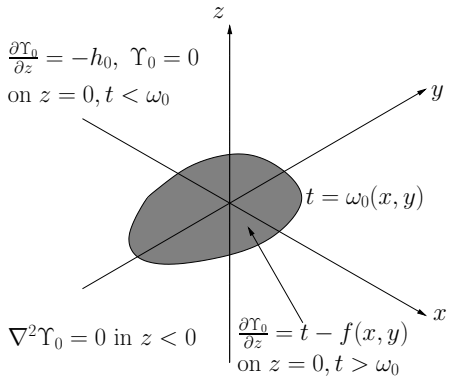

Figure 2.7: The leading-order-outer problem for the displacement potential, Υ_0. Additionally, we require $\Upsilon_0 = O(1/R^2)$ as $R \to \infty$. The smoothing effect of the integral transform means that the displacement potential has (3/2)-power behaviour at the turnover curve.

The leading-order axisymmetric projection of the turnover curve location is defined by $r = d_0(t)$. After this transformation, (2.90) is given by

$$\frac{1}{r}\frac{\partial}{\partial r}\left(r\frac{\partial \Upsilon_0}{\partial r}\right) + \frac{\partial^2 \Upsilon_0}{\partial z^2} = 0 \quad \text{in} \quad z \leq 0. \tag{2.96}$$

The boundary conditions reduce to

$$\frac{\partial \Upsilon_0}{\partial z} = t - f(r) \quad \text{on} \quad z = 0, r < d_0(t), \tag{2.97}$$

$$\frac{\partial \Upsilon_0}{\partial z} = -h_0 \quad \text{on} \quad z = 0, r > d_0(t), \tag{2.98}$$

$$\Upsilon_0 = 0 \quad \text{on} \quad z = 0, r > d_0(t). \tag{2.99}$$

These are subject to the far-field conditions

$$\Upsilon_0 = O\left(1/R^2\right) \quad \text{as} \quad R \to \infty, \tag{2.100}$$

$$h_0 = O\left(1/r^3\right) \quad \text{as} \quad r \to \infty. \tag{2.101}$$

We look for separable solutions to the axisymmetric displacement potential problem of the form $\Upsilon_0 = F(r)G(z)$, which we require to be bounded as $r^2 + z^2 \to \infty$ and also as $r \to 0$. The general solution is given by a superposition of these of the form:

$$\Upsilon_0 = \int_0^\infty \alpha(\lambda, t) e^{\lambda z} \mathrm{J}_0(\lambda r) \mathrm{d}\lambda, \tag{2.102}$$

where $\mathrm{J}_0(\lambda r)$ is the Bessel function of the first kind of order zero and the unknown coefficient $\alpha(\lambda, t)$ can be determined by applying (2.97) and (2.99) to (2.102). We

deduce the following pair of integral equations:

$$0 = \int_0^\infty \alpha(\lambda, t) \mathrm{J}_0(\lambda r)\, \mathrm{d}\lambda \qquad \text{for} \quad r > d_0(t), \tag{2.103}$$

$$t - f(r) = \int_0^\infty \lambda\alpha(\lambda, t) \mathrm{J}_0(\lambda r)\, \mathrm{d}\lambda \quad \text{for} \quad r < d_0(t). \tag{2.104}$$

This is a pair of Titchmarsh-type dual integral equations and we solve for $\alpha(\lambda, t)$ by adapting the method of Sneddon (1966). Consider the representation

$$\alpha(\lambda, t) = \int_0^{d_0(t)} \chi(\sigma, t) \sin\lambda\sigma\, \mathrm{d}\sigma, \quad \chi(0, t) = 0. \tag{2.105}$$

It is well-known that

$$\int_0^\infty \mathrm{J}_0(\lambda r) \sin\lambda\sigma \mathrm{d}\lambda = \begin{cases} 0 & \text{for} \quad r > \sigma, \\ \left(\sigma^2 - r^2\right)^{-1/2} & \text{for} \quad 0 \le r < \sigma, \end{cases} \tag{2.106}$$

and

$$\int_0^\infty \mathrm{J}_0(\lambda r) \cos\lambda\sigma \mathrm{d}\lambda = \begin{cases} 0 & \text{for} \quad 0 \le r < \sigma, \\ \left(r^2 - \sigma^2\right)^{-1/2} & \text{for} \quad r > \sigma. \end{cases} \tag{2.107}$$

Therefore, under (2.105), we can see that (2.103) holds trivially. Applying integration by parts on (2.104) and utilising (2.107) we deduce that

$$t - f(r) = \int_0^{d_0(t)} \chi'(\sigma, t) \int_0^\infty \mathrm{J}_0(\lambda r) \cos\lambda\sigma\, \mathrm{d}\lambda\, \mathrm{d}\sigma,$$

where a prime indicates differentiation with respect to σ. Hence, we can use (2.107) to deduce that

$$t - f(r) = \int_0^r \frac{\chi'(\sigma, t)}{\sqrt{r^2 - \sigma^2}} \mathrm{d}\sigma \tag{2.108}$$

for $0 < r < d(t)$.

This is an Abel integral equation similar to that for the turnover point in two-dimensional Wagner impact in §2.2.7. We can invert to deduce that

$$\chi'(\sigma, t) = \frac{2}{\pi} \frac{\mathrm{d}}{\mathrm{d}\sigma} \int_0^\sigma \frac{\rho(t - f(\rho))}{\sqrt{\sigma^2 - \rho^2}}\, \mathrm{d}\rho, \tag{2.109}$$

This is easily integrated and recalling our choice of $\chi(0, t) = 0$, we find

$$\chi(\sigma, t) = \frac{2}{\pi} \int_0^\sigma \frac{\rho(t - f(\rho))}{\sqrt{\sigma^2 - \rho^2}}\, \mathrm{d}\rho, \tag{2.110}$$

and hence that

$$\alpha(\lambda, t) = \frac{2}{\pi} \int_0^{d_0(t)} \sin\lambda\sigma \int_0^\sigma \frac{\rho(t - f(\rho))}{\sqrt{\sigma^2 - \rho^2}}\, \mathrm{d}\rho\, \mathrm{d}\sigma. \tag{2.111}$$

We need to ensure that the solution has (3/2)-power behaviour as we approach the turnover curve. On $z = 0$, we have

$$\Upsilon_0(r, 0, t) = \int_0^{d_0(t)} \chi(\sigma, t) \int_0^{\infty} \mathrm{J}_0(\lambda r) \sin(\lambda\sigma) \mathrm{d}\lambda \mathrm{d}\sigma.$$

Using (2.106), we deduce that Υ_0 is only nonzero inside the disc $r = d(t)$. Thus, we look at the behaviour as we approach the turnover curve from inside the contact set. We write $r = d_0(t) - \delta$ where $0 < \delta \ll 1$. Then,

$$\Upsilon_0(d_0(t) - \delta, 0, t) = \int_{d_0(t)-\delta}^{d_0(t)} \frac{\chi(\sigma, t)}{\sqrt{\sigma^2 - (d_0(t) - \delta)^2}} \mathrm{d}\sigma. \tag{2.112}$$

Upon making the change of variables $\sigma = d_0(t) - \delta S$ we expand the integral to deduce that

$$\begin{aligned}\Upsilon_0(d(t) - \delta, 0, t) = \delta^{1/2} \int_0^1 \frac{\chi(d_0(t), t)}{\sqrt{2d_0(t)(1 - S)}} \mathrm{d}S + \\ \delta^{3/2} \int_0^1 \frac{\chi(d_0(t), t)(S + 1) - 4Sd_0(t)\chi'(d_0(t), t)}{4d_0(t)\sqrt{2d_0(t)(1 - S)}} \mathrm{d}S + O(\delta^{5/2})\end{aligned}$$

as $\delta \to 0$.

Due to the requirement that $\Upsilon_0 = O(\delta^{3/2})$ as $\delta \to 0$, we must force the coefficient of the $O(\delta^{1/2})$-term to vanish, giving the solvability condition for $d_0(t)$ that

$$\chi(d_0(t), t) = 0, \tag{2.113}$$

where $\chi(\sigma)$ is given by (2.110). Note that it follows that

$$\Upsilon_0 = -\frac{4\chi'(d_0(t), t)}{3\sqrt{2d_0(t)}} (d_0(t) - r)^{3/2} + O\left((d_0(t) - r)^{5/2}\right), \tag{2.114}$$

as $r \uparrow d_0(t)$. Therefore, by definition, the leading-order coefficient of the square-root in the expansion of the velocity potential at the turnover curve is given by

$$S(t) = \sqrt{\frac{2}{d_0(t)}} \dot{d}_0(t) \chi'(d_0(t), t), \tag{2.115}$$

where $\phi \sim S(t)\sqrt{d_0 - r}$ as $r \to d_0$.

This gives us all the tools we need to solve for Υ_0 and $d_0(t)$, which we can then use to solve for the free surface profile and the pressure using (2.98) and Bernoulli's equation respectively. In particular,

$$h_0(r, t) = -\int_0^{d_0(t)} \frac{\chi'(\sigma, t)}{\sqrt{r^2 - \sigma^2}} \mathrm{d}\sigma, \tag{2.116}$$

and

$$p_0 = \frac{\partial^2 \Upsilon_0}{\partial t^2} = \dot{d}(t)\chi_t(d(t),t)\int_0^\infty \mathrm{e}^{\lambda z}\mathrm{J}_0(\lambda r)\sin\sigma\lambda\,\mathrm{d}\lambda. \tag{2.117}$$

Hence, the pressure on the impactor is given by

$$p_0(r,0,t) = \frac{2\dot{d}(t)d(t)}{\pi\sqrt{d(t)^2 - r^2}} \quad \text{for} \quad r < d_0(t). \tag{2.118}$$

Since the inner and jet region pressure scales are the same order of magnitude as in two-dimensional Wagner theory, the vertical component of the leading-order hydrodynamic force on the impactor will be dominated by the outer pressure. Hence, F is of $O(1/\varepsilon^2)$ and the leading-order term is given by

$$F_0(t) = \int_0^{2\pi}\int_0^{d_0(t)} p_0(r,0,t) r\,\mathrm{d}r\,\mathrm{d}\theta = 4\dot{d}(t)d(t)^2. \tag{2.119}$$

2.3.5 Splash sheet

Before discussing specific examples, we will solve the leading-order splash sheet problem. The splash sheet is ejected from the turnover region and we assume it remains attached to the body. It has $O(\varepsilon)$-thickness and its thickness varies over distances of $O(1/\varepsilon)$. This is smaller than the radius of curvature of the impactor, and thus, by a similar argument to the two-dimensional case in §2.2.8, to leading order the zero-gravity shallow water equations hold in the splash sheet. These are given by

$$\frac{\partial \bar{h}_0}{\partial t} + \frac{\partial}{\partial \bar{x}}\left(\bar{u}_0\bar{h}_0\right) + \frac{\partial}{\partial \bar{y}}\left(\bar{v}_0\bar{h}_0\right) = 0, \tag{2.120}$$

$$\frac{\partial \bar{u}_0}{\partial t} + \bar{u}_0\frac{\partial \bar{u}_0}{\partial \bar{x}} + \bar{v}_0\frac{\partial \bar{u}_0}{\partial \bar{y}} = 0, \tag{2.121}$$

$$\frac{\partial \bar{v}_0}{\partial t} + \bar{u}_0\frac{\partial \bar{v}_0}{\partial \bar{x}} + \bar{v}_0\frac{\partial \bar{v}_0}{\partial \bar{y}} = 0, \tag{2.122}$$

where $\bar{x}, \bar{y}$ are orthogonal curvilinear coordinates based on the impactor (scaled with $1/\varepsilon$), $\bar{u}_0, \bar{v}_0$ are the leading-order components of the velocity in the $\bar{x}$ and $\bar{y}$ directions respectively (scaled with $1/\varepsilon$) and $\bar{h}_0$ is the leading-order normal thickness of the splash sheet (scaled with ε). As the extent of the splash sheet is much smaller than the radius of curvature of the body, we can without loss of generality, take $(\bar{x}, \bar{y})$ as Cartesian with the same origin and orientation as in the leading-order outer problem. Correspondingly, we shall drop the bar notation on $(\bar{x}, \bar{y})$.

Since the inner region is quasi-two-dimensional and moves with outward normal velocity v_n, the boundary condition for the leading-order splash sheet velocity is given by

$$\bar{\mathbf{u}}_0 = 2v_n\mathbf{n} \quad \text{at} \quad t = \omega_0(x,y), \tag{2.123}$$

where $\mathbf{u}_0 = (\bar{u}_0, \bar{v}_0)$ is the leading-order velocity and $\mathbf{n}$ is the outward-pointing normal to the projection of the turnover curve. The leading-order thickness of the splash sheet at $t = \omega_0(x, y)$ is given from (2.79) by

$$\varepsilon \frac{\pi S(x, y, t)^2}{16 v_n^2},$$

where $S(x, y, t)$ is the coefficient of the square root in the leading-order-outer velocity potential at the turnover curve, and hence given by (2.115) in the axisymmetric case. Therefore, the boundary condition on the leading-order splash sheet thickness is

$$\bar{h}_0 = \frac{\pi S(x, y, t)^2}{16 v_n^2} \quad \text{on} \quad t = \omega_0(x, y). \tag{2.124}$$

Oliver (2002) solves the splash sheet problem for general three-dimensional body profiles. Here, since we will be concentrating on axisymmetric body profiles, we simply present the solution for these impactors.

2.3.5.1 Axisymmetric problem

We parametrise the boundary data curve by θ and s, which represent polar angle around the turnover curve and time respectively. Thus,

$$(x, y) = d_0(s)(\cos\theta, \sin\theta), \quad (\bar{u}_0, \bar{v}_0) = 2\dot{d}_0(s)(\cos\theta, \sin\theta), \quad \bar{h}_0 = \frac{\pi \chi'(d_0(s), s)^2}{8 d_0(s)}, \tag{2.125}$$

where $s > 0, 0 \leq \theta < 2\pi$ and $\chi'(\sigma, t)$ is given by (2.109).

Thus, we seek to solve (2.120)-(2.122) subject to (2.125), which can be done using the method of characteristics. The characteristics correspond to particle paths:

$$\frac{\partial x}{\partial \tau} = \bar{u}_0, \quad \frac{\partial y}{\partial \tau} = \bar{v}_0, \quad \frac{\partial t}{\partial \tau} = 1,$$

where $\tau > 0$ parametrises time-of-travel along a characteristic.The characteristics are therefore given by

$$t = \tau + s, \quad x = \cos\theta \left(2\dot{d}_0(s)\tau + d_0(s)\right), \quad y = \sin\theta \left(2\dot{d}_0(s)\tau + d_0(s)\right), \tag{2.126}$$

while the velocities and thickness are given by

$$(\bar{u}_0, \bar{v}_0) = 2\dot{d}_0(s)(\cos\theta, \sin\theta), \quad \bar{h}_0 = \frac{\pi \chi'(d_0(s), s)^2}{8 d_0(s)} \frac{\mathrm{J}(0, \theta, s)}{\mathrm{J}(\tau, \theta, s)}, \tag{2.127}$$

where the Jacobian of the transformation, $\mathrm{J}(\tau, \theta, s)$, is defined as

$$\mathrm{J} = \frac{\partial(x, y, t)}{\partial(\tau, \theta, s)} = -4\ddot{d}_0(s)\dot{d}_0(s)\tau^2 - 2(\ddot{d}_0(s)d_0(s) - \dot{d}_0(s)^2)\tau + \dot{d}_0(s)d_0(s).$$

This is bounded for all $\tau, s > 0$ provided $\dot{d}_0(s), \ddot{d}_0(s)$ are bounded, and vanishes for

$$\tau = \frac{1}{2}\frac{\dot{d}_0(s)}{\ddot{d}_0(s)} \quad \text{and} \quad \tau = -\frac{1}{2}\frac{d_0(s)}{\dot{d}_0(s)}.$$

Thus, in reference to the similar constraints we saw in two dimensions in §2.2.8, if $\dot{d}_0(s) > 0, \ddot{d}_0(s) < 0$, then for $\tau > 0$, the Jacobian is bounded and nonzero. We note that this holds for any impactor of the form $z = r^n - t$ where $n \geq 1$. Thus provided that $\bar{h}_0 > 0$, the domain of definition is given by $t > 0$, $r = \sqrt{x^2 + y^2} > d_0(t)$. We shall see an example where $\bar{h}_0$ can vanish shortly.

2.3.6 Examples

We move on to some specific examples.

2.3.6.1 Impact of a cone

Consider the impact of a cone, which is defined in outer variables by $z = r - t$. Therefore, from (2.110), we have

$$\chi(\sigma, t) = \frac{2}{\pi}\int_0^\sigma \frac{\rho t - \rho^2}{\sqrt{\sigma^2 - \rho^2}}\mathrm{d}\rho.$$

Performing the integral by making the change of variable $\rho = \sigma \sin\vartheta$, we deduce that

$$\chi(\sigma, t) = \frac{2}{\pi}\left(\sigma t - \frac{\sigma^2\pi}{4}\right). \tag{2.128}$$

Thus, it follows from (2.102), (2.110)–(2.111), (2.128) that the solution for the displacement potential in the normal impact of a cone is given by

$$\Upsilon_0 = \int_0^{d_0(t)} \frac{2}{\pi}\left(\sigma t - \frac{\sigma^2\pi}{4}\right)\int_0^\infty e^{\lambda z}\sin\lambda\sigma \mathrm{J}_0(\lambda r)\,\mathrm{d}\lambda\,\mathrm{d}\sigma. \tag{2.129}$$

To find the turnover curve, we combine (2.113) with (2.128) to deduce

$$d_0(t) = \frac{4t}{\pi}. \tag{2.130}$$

The leading-order free surface displacement is given by

$$h_0(r, t) = r - \frac{2t}{\pi}\arcsin\left(\frac{4t}{\pi r}\right) - \sqrt{r^2 - \left(\frac{4t}{\pi}\right)^2} \quad \text{for} \quad r > d_0(t), \tag{2.131}$$

and the leading-order pressure on the impactor is

$$p_0(r, 0, t) = \frac{32t}{\pi^3}\frac{1}{\sqrt{(4t/\pi)^2 - r^2}} \quad \text{for} \quad r < d_0(t), \tag{2.132}$$

Two details that will be important in our splash sheet considerations are the normal speed of the turnover curve, which is given by

$$v_n = \frac{4}{\pi}, \tag{2.133}$$

and secondly, the coefficient

$$S(t) = \sqrt{\frac{2}{d_0(t)}}\chi'(d_0(t), t)\dot{d}_0(t) = -\frac{8\sqrt{t}}{\sqrt{2\pi^3}}, \tag{2.134}$$

where $\phi_0(r, 0, t) = S(t)\left(d_0(t) - r\right)^{1/2} + O\left(\left(d_0(t) - r\right)^{3/2}\right)$ as $r \uparrow d_0(t)$.

Using (2.133) and (2.134) with (2.126)-(2.127), we find that, in the splash sheet,

$$(x, y) = \frac{4}{\pi}\left(2\tau + s\right)\left(\cos\theta, \sin\theta\right), \quad \bar{h}_0 = \frac{1}{8}\frac{s^2}{2\tau + s}. \tag{2.135}$$

Recalling that $t = \tau + s$, we therefore find that the thickness of the sheet is given by

$$\bar{h}_0 = \frac{1}{2\pi r}\left(2t - \frac{\pi}{4}r\right)^2, \tag{2.136}$$

where $r = \sqrt{x^2 + y^2}$, so that $\bar{h}_0 = 0$ on the circle $r = 8t/\pi$. Thus, the splash sheet projection in the plane $z = 0$ is the annulus between the turnover curve $r = d_0(t)$ and the *touchdown curve*, $r = 2d_0(t)$. Hence, the splash sheet length along a ray, defined as the distance between the turnover and touchdown curves on a ray, is finite and exactly equal to $d_0(t)$.

2.3.6.2 Impact of a blunt body

We move on to consider a blunt body, that is $z = r^n - t$ where $n > 1$. Now, we have

$$\chi(\sigma, t) = \frac{2}{\pi}\int_0^\sigma \frac{\rho t - \rho^{n+1}}{\sqrt{\sigma^2 - \rho^2}}\mathrm{d}\rho.$$

The substitution $\rho = \sigma\sin\vartheta$ again facilitates the integration, which reveals that

$$\chi(\sigma, t) = \frac{2}{\pi}\left(\sigma t - 2^n\sigma^{n+1}\mathrm{B}\left(\frac{n+2}{2}, \frac{n+2}{2}\right)\right), \tag{2.137}$$

where $\mathrm{B}(\cdot, \cdot)$ is the beta function. Note that for $n = 1$, we simply have $B(3/2, 3/2) = \pi/8$, so that we recover the solution (2.128) for a cone.

To find the turnover curve location, we again use (2.113) with (2.137) to deduce that

$$d_0(t) = \left(\frac{t}{2^n\mathrm{B}((n+2)/2, (n+2)/2)}\right)^{1/n}. \tag{2.138}$$

Hence, the free surface displacement is given by

$$h_0(r,t) = -\frac{2t}{\pi}\arcsin\frac{d_0(t)}{r} + \frac{2d_0(t)}{\pi t r}\,{}_2\mathrm{F}_1\left(\frac{1}{2},\frac{n+1}{2},\frac{n+3}{2},\frac{d^2}{r^2}\right) \quad \text{for} \quad r > d_0(t), \tag{2.139}$$

where ${}_2\mathrm{F}_1(\cdot,\cdot,\cdot,\cdot)$ is the ordinary hypergeometric function. The pressure on the impactor is given by

$$p_0(r,0,t) = \frac{2t^{(2-n)/n}}{\pi Q}\frac{1}{\sqrt{t^{2/n}/Q - r^2}} \quad \text{for} \quad r < d_0(t), \tag{2.140}$$

where $Q = (2^n\mathrm{B}((n+2)/2,(n+2)/2))^{2/n}$.

The outward normal velocity of the turnover curve is given by

$$v_n = \frac{1}{n}\left(\frac{1}{2^n\mathrm{B}((n+2)/2,(n+2)/2)}\right)^{1/n} t^{1/n-1}, \tag{2.141}$$

while the coefficient of the square-root term in the velocity potential expansion at the turnover curve is given by

$$S(t) = -\frac{2\sqrt{2}}{\pi}\left(\frac{t}{2^n\mathrm{B}((n+2)/2,(n+2)/2)}\right)^{1/2n}. \tag{2.142}$$

Thus, using (2.141) and (2.142) we find that the leading-order splash sheet thickness (2.127) is

$$\bar{h}_0 = \frac{ns^{1+1/n}}{4\pi\mathrm{B}((n+2)/2,(n+2)/2)^{1/n}}\frac{1}{\mathrm{J}(\tau,\theta,s)}, \tag{2.143}$$

where $\tau > 0$, $s > 0$ and that the Jacobian is given by

$$\mathrm{J}(\tau,\theta,s) = \frac{4\tau^2 s^{2/n-2}(n-1) + 2\tau s^{2/n-1}n^2 + n^2 s^{2/n}}{4n^3 s\mathrm{B}((n+2)/2,(n+2)/2)^{2/n}}. \tag{2.144}$$

This is bounded and nonzero for all $s,\tau > 0$.

In the specific case where the impactor is a paraboloid, that is $n = 2$, we see that

$$\bar{h}_0 = \frac{2}{\pi}\sqrt{\frac{2}{3}}\frac{s^{7/2}}{(s+\tau)^2}, \tag{2.145}$$

which can be simplified by noting that $r = \sqrt{3/(2s)}t$, and hence

$$\bar{h}_0 = \frac{27}{4\pi}\frac{t^5}{r^7}. \tag{2.146}$$

In particular, $\bar{h}_0 > 0$ for all $r > 0$, $t > 0$, with $\bar{h}_0 \to 0$ as $t \downarrow 0$ for all $r > 0$. Thus, the splash sheet is thrown out to infinity at $t = 0^+$ and does not terminate on the impactor. This is analogous to the two-dimensional impact of a parabola, as described by Oliver (2002).

2.3.7 Summary

We have described the generalisation of Wagner theory to three-dimensional impacts, as performed in Wilson (1989), Howison et al. (1991), Oliver (2002) and Korobkin and Scolan (2006), in particular concentrating on axisymmetric body profiles of the form $z = r^n - t$. The asymptotic structure of the impact extends directly from that for two-dimensional impacts.

We explicitly showed that the inner problem is quasi-two-dimensional at leading order, and thus stated that the solution can be deduced from that in two-dimensional Wagner theory. The matching also follows analogously, so we were able to write down the Wagner condition and the leading-order thickness of the splash sheet.

The leading-order-outer problem was tackled by defining the displacement potential, Υ. We followed Korobkin and Scolan (2006) in showing that it is possible to solve the mixed boundary value problem by looking for separable solutions that satisfy the known behaviour of the displacement potential as we approach the projection of the turnover curve in any plane perpendicular to it. This produces a condition for the location of the turnover curve projection at leading-order.

Finally, we solved the zero-gravity shallow water equations in the splash sheet, assuming that it did not separate from the impactor. We solved the problem for a general axisymmetric impactor using the method of characteristics and outlined the solutions for the cases of a cone and of a paraboloid. The cone splash sheet has finite extent for all $t > 0$, whereas for a paraboloid it has infinite extent for all $t > 0$. Clearly this is not physical and this is a problem that has not been resolved in the literature. We do not seek to resolve it in this thesis and simply state that whether the splash sheet has finite or infinite extent for $t > 0$ has no influence on the leading-order theory provided that it does not separate from the impactor.

Chapter 3

Oblique water-entry

Inspired by examples such as an alighting seaplane or the skimming of a stone, we will now extend Wagner theory to oblique impacts. The problem configuration and modelling assumptions are exactly the same as those in Chapter 2, except that we now assume that our impactor has an additional component of impact velocity tangential to the undisturbed free surface. We aim to derive a solution to leading-order Wagner theory for a range of oblique impacts in two and three dimensions, to discuss how this solution differs from the normal-impact theory, and to consider the applicability and limitations of our results. This Chapter closely follows work that we published in Moore et al. (2012) and Moore et al. (2013a).

3.1 Two-dimensional Wagner theory

Firstly, we consider two-dimensional oblique impacts. We impose the same conditions on the impactor shape that were outlined in §2.2 and, since we shall use the same nondimensionalisation, we do not repeat that process here. In particular, throughout this section we shall assume for simplicity that the impactor is symmetric about its minimum point, although everything we deduce will follow for non-symmetric impactors as well. Suppose that we introduce an oblique component of impact velocity, $\dot{X}(t)/\varepsilon$, so that the dimensionless body profile is given by

$$z = f(\varepsilon x - X(t)) - t, \tag{3.1}$$

where $X(0) = 0$. The presence of an oblique impact velocity means that we can no longer assume symmetry of the flow about the minimum of the impactor. Aside from this, however, the problem formulation follows as in §2.2, with the appropriate change to the kinematic condition on the body. Therefore, in the fluid, the velocity potential

must satisfy

$$\frac{\partial^2\phi}{\partial x^2}+\frac{\partial^2\phi}{\partial z^2}=0. \tag{3.2}$$

On the body, the kinematic condition is given by

$$\frac{\partial\phi}{\partial z}=-1-\dot{X}(t)f'(\varepsilon x-X(t))+\varepsilon f'(\varepsilon x-X(t))\frac{\partial\phi}{\partial x} \tag{3.3}$$

on $z=f(\varepsilon x-X(t))-t$ for x in the contact set. On the free surface, the kinematic condition is

$$\frac{\partial\phi}{\partial z}=\frac{\partial h}{\partial t}+\frac{\partial\phi}{\partial x}\frac{\partial h}{\partial x}\quad\text{on}\quad z=h(x,t),\ x>d_+(t), x<d_-(t), \tag{3.4}$$

where we denote the x-coordinates of the leading $(+)$ and trailing $(-)$ turnover points by $d_\pm(t)$ respectively. The dynamic boundary condition is given by

$$p=0\quad\text{on}\quad z=h(x,t),\ x>d_+(t), x<d_-(t), \tag{3.5}$$

where the pressure is given by Bernoulli's equation

$$\frac{\partial\phi}{\partial t}+p+\frac{1}{2}|\nabla\phi|^2=0. \tag{3.6}$$

Initially, the fluid is quiescent and the free surface is undisturbed, while in the far-field we choose the appropriate behaviour for ϕ and h in order to guarantee that the spatially integrated kinetic energy is bounded. Hence,

$$\phi(x,z,0)=0 \qquad \text{for} \quad -\infty<x<\infty,\ z<0, \tag{3.7}$$

$$h(x,0)=0 \qquad \text{for} \quad -\infty<x<\infty, \tag{3.8}$$

$$\phi=O(1/r) \quad \text{as} \quad r=\sqrt{x^2+z^2}\to\infty, \tag{3.9}$$

$$h=O(1/x^2) \quad \text{as} \quad |x|\to\infty. \tag{3.10}$$

Finally, we require $d_\pm(0)=0$.

3.1.1 Asymptotic structure

The asymptotic structure for an oblique impact at small deadrise angles is the same as that described in §2.2.3 for the normal impact case. In particular, since the symmetry of the normal impacts described in §2.2 was not integral to the solution of the leading-order-inner problem in §2.2.5, by moving to a frame travelling with each turnover point, the resulting Helmholtz flow can be solved in exactly the same manner. That is to say, provided that the function $X(t)$ is at most of $O(1)$ for $t=O(1)$, then replacing $d(t)$ with $d_+(t)$ in Figure 2.4 gives the leading-order right-hand inner problem for

oblique impact. The left-hand problem follows similarly with $d(t)$ replaced by $d_-(t)$. Therefore, the Wagner condition at each turnover point follows as in (2.36) and the jet thicknesses also follow as in (2.79), with the appropriate definitions of S and v_n.

In the outer region, the problem can still be likened to the flow induced by an expanding flat plate on the free surface of a half-space. As we shall see shortly (cf. (3.12)), in the outer region the oblique component of impact velocity only enters (3.3) at leading order if $X(t) = O(1)$ for $t = O(1)$. If $X(t) = o(1)$, then the problem reduces to the normal impact case described in §2.2.4, with $d_+(t) = -d_-(t)$ at leading order. Hence, unless the oblique impact speed is large, the splash still looks symmetric to leading-order. This is a realisation of one of Trefethen and Panton (1990)'s paradoxes.

If $X(t)$ is much larger than $O(1)$, that is, if the oblique impact speed is much larger than $O(1/\varepsilon)$, then (3.3) implies that the forward motion will dominate the normal motion. Wagner theory does not hold in this regime, in which a new asymptotic solution is needed, though see, for example, Oliver (2002) and his discussion of planing. Here, we shall concentrate on the regime in which the oblique impact speed enters the leading-order problem and is not too large as to render Wagner theory inapplicable. Thus, we shall assume that $X(t) = O(1)$ for $t = O(1)$, so that the oblique speed is of $O(1/\varepsilon)$.

3.1.2 Leading-order-outer problem

As in §2.2.4, we rescale $x, z, d_\pm, \phi, p$ with $1/\varepsilon$ and expand the variables in asymptotic series in ε. The kinematic and dynamic boundary conditions linearise onto $z = 0$ at leading-order and the resulting leading-order problem for the outer velocity potential $\phi(x, z, t)$, free surface $h(x, t)$ and turnover points $d_\pm(t)$ is given by

$$\frac{\partial^2\phi}{\partial x^2} + \frac{\partial^2\phi}{\partial z^2} = 0 \qquad \text{in} \quad z < 0, \tag{3.11}$$

$$\frac{\partial\phi}{\partial z} = -1 - \dot{X}(t) f'\left(x - X(t)\right) \quad \text{on} \quad z = 0, d_-(t) < x < d_+(t), \tag{3.12}$$

$$\frac{\partial\phi}{\partial z} = \frac{\partial h}{\partial t} \qquad \text{on} \quad z = 0, x > d_+(t), x < d_-(t), \tag{3.13}$$

$$\phi = 0 \qquad \text{on} \quad z = 0, x > d_+(t), x < d_-(t), \tag{3.14}$$

subject to the initial and far-field conditions

$$h(x, 0) = 0 \qquad \text{for} \quad -\infty < x < \infty, \tag{3.15}$$

$$\phi = O(1/r) \quad \text{as} \quad r = \sqrt{x^2 + z^2} \to \infty, \tag{3.16}$$

$$h = O(1/x^2) \quad \text{as} \quad |x| \to \infty, \tag{3.17}$$

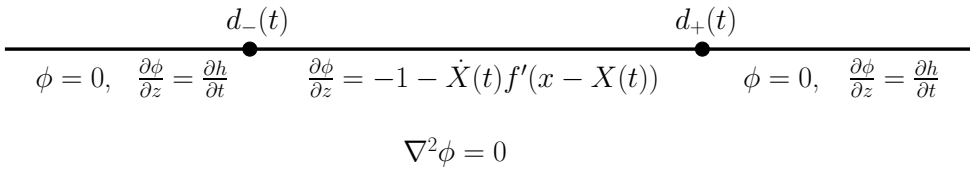

Figure 3.1: The linearised leading-order-outer problem for the velocity potential. The velocity potential has square-root behaviour at the turnover points. In the far-field, $\phi = O(1/r)$ as $r = \sqrt{x^2 + z^2} \to \infty$. Moreover, we have the initial conditions $h(x, 0) = 0$, $d_\pm(0) = 0$ and the Wagner conditions given in (3.18).

and $d_\pm(0) = 0$. Matching with the inner region requires, firstly, that the velocity potential has square-root behaviour at the two turnover points, $x = d_\pm(t)$, and secondly that the Wagner condition holds at each turnover point, viz.

$$h\left(x, t\right) = f\left(x - X(t)\right) - t \quad \text{at} \quad x = d_\pm(t). \tag{3.18}$$

The leading-order-outer problem is summarised in Figure 3.1.

3.1.2.1 Displacement potential formulation

In theory, the Riemann-Hilbert problem in Figure 3.1 is readily solved in the same manner as that for normal two-dimensional small deadrise impact as in Howison et al. (1991). However, as might be expected from the form of (2.39), this does not provide us with a simple way to find $d_\pm(t)$. We can skirt this problem by rewriting (3.11)–(3.18) in terms of the displacement potential, $\Upsilon(x, z, t)$, as defined in (2.54) in §2.2.11.1. The problem after this reformulation is depicted in Figure 3.2.

The important thing to note in Figure 3.2 is that there are no time derivatives on the time-dependent variables Υ, h and $d_\pm$.

3.1.2.2 Solution and breakdown

Let $\zeta = x + \mathrm{i}z$. Since we require $\Upsilon_x - \mathrm{i}\Upsilon_z$ to be bounded at both turnover points, the Riemann-Hilbert problem $\Upsilon_x - \mathrm{i}\Upsilon_z$ displayed in Figure 3.2 has index -1. The solution is given by

$$\Upsilon_x - \mathrm{i}\Upsilon_z = \frac{\mathrm{i}\sqrt{(\zeta - d_-(t))(\zeta - d_+(t))}}{\pi} \int_{d_-(t)}^{d_+(t)} \frac{t - f\left(\xi - X(t)\right)}{\sqrt{(\xi - d_-(t))(d_+(t) - \xi)}(\xi - \zeta)} \mathrm{d}\xi, \tag{3.19}$$

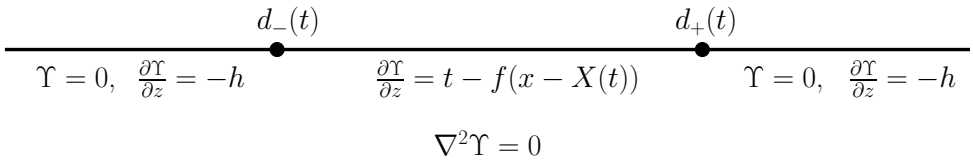

Figure 3.2: The linearised leading-order-outer problem for the displacement potential, Υ. The displacement potential has (3/2)-power behaviour at the turnover points and has far-field condition $\Upsilon = O(1/r)$ as $r = \sqrt{x^2 + z^2} \to \infty$.

where the square root $R(\zeta, t) = \sqrt{(\zeta - d_-(t))(\zeta - d_+(t))}$ is defined with a branch cut on $d_-(t) < x < d_+(t), z = 0$ and is positive for $x > d_+(t), z = 0$. A straightforward far-field expansion of (3.19) shows that we require the consistency conditions

$$\int_{d_-(t)}^{d_+(t)} \frac{[t - f(\xi - X(t))]\, \xi^k}{\sqrt{(\xi - d_-(t))(d_+(t) - \xi)}} \mathrm{d}\xi = 0 \quad \text{for} \quad k = 0, 1 \tag{3.20}$$

to hold in order to satisfy the required behaviour that $\Upsilon = O(1/r)$ as $r \to \infty$. As noted in Howison et al. (2004), these consistency conditions correspond to global conservation of mass for $k = 0$ and to global conservation of x-momentum for $k = 1$.

The solution of (3.20) requires the assumption that the moving minimum of the impactor lies between the two turnover points; that is we assume $d_-(t) < X(t) < d_+(t)$. This is to avoid the free surface intersecting the impactor, h having square-root singularities at the turnover points. We have also implicitly assumed that the turnover points are advancing, i.e. $\dot{d}_-(t) < 0 < \dot{d}_+(t)$, in order to avoid the linear instability described in §2.2.11.3.

We could solve (3.20) for $d_\pm(t)$, but as noted by Moore et al. (2013a), if we make the change of variables

$$d_\pm(t) = X(t) + \tilde{d}_\pm(t), \quad \zeta = X(t) + \tilde{\zeta}, \quad \xi = X(t) + \tilde{\xi} \tag{3.21}$$

then (3.19) reduces to

$$\Upsilon_{\tilde{x}} - i\Upsilon_z = \frac{R(\tilde{\zeta}, t)}{\pi} \int_{\tilde{d}_-(t)}^{\tilde{d}_+(t)} \frac{t - f(\tilde{\xi})}{R(\tilde{\xi} - \mathrm{i}0, t)(\tilde{\xi} - \tilde{\zeta})} \mathrm{d}\tilde{\xi} \tag{3.22}$$

with the consistency conditions

$$\int_{\tilde{d}_-(t)}^{\tilde{d}_+(t)} \frac{(t - f(\tilde{\xi}))\tilde{\xi}^k}{R(\tilde{\xi} - \mathrm{i}0, t)} \mathrm{d}\tilde{\xi} = 0 \tag{3.23}$$

for $k = 0, 1$.

Firstly, it is important to note that as the problem displayed in Figure 3.2 contains no time derivatives, the transformation (3.21) reduces the oblique outer problem for Υ in Figure 3.2 to the corresponding normal outer problem for Υ in Figure 2.5. We note this is clearly not true for the velocity potential problem as displayed in Figure 3.1. Secondly, (3.22) and (3.23) are exactly the solution for the equivalent displacement potential problem in the normal impact case: thus, if $\Upsilon(\tilde{x}, z, t)$ gives the displacement potential solution for normal impact, $\Upsilon(x - X(t), z, t)$ gives the oblique displacement potential. We can go further than this: if the normal impact problem has a solution, with turnover points $\pm a(t)$ and with free surface profile $z = h(\tilde{x}, t)$, then $d_{\pm}(t) = X(t) \pm a(t)$ are the turnover points for the corresponding oblique impact case with free surface profile given by $z = h(x - X(t), t)$ in the original stationary frame centred at the initial point of impact. We shall henceforth refer to this stationary frame as the laboratory 'lab' frame.

The above conclusions lead immediately to the interesting possibility of breakdown as described in §2.2.11.3, when the trailing turnover point is no longer advancing with respect to the lab frame. We will consider this possibility in detail presently.

We note that, although the free surface and turnover points are symmetric about the apex of the impactor, the velocity potential and pressure are asymmetric because they are defined by $\phi = -\Upsilon_t$ and $p = \Upsilon_{tt}$ respectively, where the time derivatives are with respect to the lab frame rather than the translating frame given by (3.21).

Finally, we reiterate that the displacement potential formulation and the change of variables (3.21) also apply for non-symmetric impactors.

3.1.2.3 Examples

We consider the impact of a symmetric wedge, $z = |x - X(t)| - t$. As we showed in §2.2.10.1, $a(t) = \pi t/2$. Therefore, when we introduce the oblique component of velocity, $\dot{X}(t)$, the leading and trailing turnover points are given by

$$d_{\pm}(t) = \pm\frac{\pi t}{2} + X(t), \tag{3.24}$$

to leading order. For a general oblique speed, we would expect to see breakdown at the smallest time t at which $\dot{X}(t) = \mp\pi/2$.

Consider the simplest example in which the wedge moves with a constant speed, with $X(t) = Ut$ for $U > 0$, where U is the ratio of the oblique to vertical speeds. It is clear that the leading turnover point is always advancing for all $t > 0$ for any $U > 0$. However, the trailing turnover point is advancing for all $t > 0$ only if $0 < U < \pi/2$, and it breaks down at $t = 0^+$ when $U = \pi/2$. Technically, there is a nonuniformity

in our asymptotic expansion when U is very close to $\pi/2$ for which the asymptotic structure is unknown. The theory does not hold for U larger than the critical value of $\pi/2$ so we can only speculate on how the impact evolves in this case. It is possible that there is immediate ventilation along the trailing side of the impactor, an idea discussed by Reinhard et al. (2012).

For a symmetric blunt impactor, $z = |x - X(t)|^n - t$, where $n > 1$, we found in §2.2.10.2 that

$$a(t) = \pm \left(\pi t / 2^n \mathrm{B}((n+1)/2, (n+1)/2)\right)^{1/n}.$$

Hence, we expect breakdown if $\dot{X}(t) = \mp(1/n)\left(\pi t / 2^n \mathrm{B}((n+1)/2, (n+1)/2)\right)^{(1-n)/n}$. In the case where $X(t) = Ut$ for $U > 0$, provided that $t \in (0, t_c)$ where

$$t_c = \left(\frac{1}{nU}\left(\frac{\pi}{2^n \mathrm{B}((n+1)/2, (n+1)/2)}\right)^{1/n}\right)^{n/(n-1)}, \tag{3.25}$$

both turnover points are advancing. However, when $t = t_c$, the trailing turnover point stops advancing. Therefore, Wagner theory will hold for a symmetric blunt impactor for all $U > 0$, for sufficiently small times. However, for any oblique impact speed, we expect there to be a time at which the theory breaks down and we conjecture that there will be a nonuniformity in our asymptotic expansion for times very close to the critical time, though we do not speculate any further here.

For large n, we can use Sterling's formula to approximate the beta function, giving

$$Ut_c = \frac{1}{n} - \frac{1}{2n^2}\log n + O\left(\frac{1}{n^2}\right) \quad \text{as} \quad n \to \infty. \tag{3.26}$$

Thus, as the body becomes flatter, the time period for which the impact is valid becomes very short.

3.1.3 Pressure at breakdown

Determining the velocity potential and pressure for an oblique impact is not as simple as finding the displacement potential or the free surface, and is typically best handled on a case-by-case basis. In general, we have

$$\phi(x, z, t) = -\frac{\mathrm{d}}{\mathrm{d}t}\Upsilon(x - X(t), z, t), \tag{3.27}$$

$$p(x, z, t) = \frac{\mathrm{d}^2}{\mathrm{d}t^2}\Upsilon(x - X(t), z, t), \tag{3.28}$$

where Υ is given by (3.19). However, it is straightforward to expand (3.19) near the trailing contact point to see how the pressure (and in the process, the velocity

potential) behaves as we approach breakdown. We shall restrict ourselves to cases where the breakdown occurs at the trailing turnover point: assuming the body is moving in the positive x-direction, this means we assume breakdown occurs at d_-.

For the moment, we remain in the frame moving with the minimum of the impactor and consider (3.22). Upon using the Plemelj formulae (and recalling the branch of the square root we defined), on the impactor, $\mathrm{d}\Upsilon/\mathrm{d}\tilde{\zeta}$ is given by

$$\begin{aligned}\Upsilon_{\tilde{x}} - \mathrm{i}\Upsilon_z &= \mathrm{i}\sqrt{(a-\tilde{x})(\tilde{x}+a)}\left[-\frac{t-f(\tilde{x})}{\sqrt{(a-\tilde{x})(\tilde{x}+a)}} + \frac{1}{\pi\mathrm{i}}I(\tilde{x})\right], \\ I(\tilde{x}) &= \fint_{-a}^{a}\frac{t-f(\tilde{\xi})}{\tilde{R}(\tilde{\xi},t)}\frac{\mathrm{d}\tilde{\xi}}{\tilde{\xi}-\tilde{x}},\end{aligned} \tag{3.29}$$

where the dash indicates a Cauchy principal value integral and

$$\tilde{R}(\tilde{\xi},t) = \sqrt{(a(t)-\tilde{\xi})(\tilde{\xi}+a(t))}.$$

If we then let $\tilde{x} = -a+\epsilon$ and define δ such that $0<\epsilon\ll\delta\ll 1$, we can write

$$I = I_1 + I_2 = \fint_{-a}^{-a+\delta} + \int_{-a+\delta}^{a}\frac{t-f(\bar{\xi})}{\tilde{R}(\tilde{\xi},t)}\frac{\mathrm{d}\tilde{\xi}}{\tilde{\xi}+a-\epsilon}. \tag{3.30}$$

In I_1, we make the change of variable $\tilde{\xi}+a=\epsilon S$, use the definition of the Cauchy principal value integral, expand and integrate to deduce that

$$\begin{aligned}I_1 &= \frac{1}{\sqrt{\epsilon}}\left(\frac{t-f(-a)}{\sqrt{2a}}\right)\log\left(\frac{\sqrt{\delta/\epsilon}-1}{\sqrt{\delta/\epsilon+1}}\right) + \sqrt{\epsilon}\left(\left(\frac{t-f(-a)}{2(2a)^{3/2}}\right) - \right. \\ &\left.\frac{f'(-a)}{\sqrt{2a}}\right)\left[2\sqrt{\frac{\delta}{\epsilon}} + \log\left(\frac{\sqrt{\delta/\epsilon}-1}{\sqrt{\delta/\epsilon+1}}\right)\right] + O(\epsilon^{3/2}).\end{aligned} \tag{3.31}$$

In I_2, we expand the integrand in powers of ϵ. After some algebra, we conclude that

$$\begin{aligned}I_1 &= \lim_{\gamma\to 0}\left[\int_{-a+\gamma}^{a}\frac{t-f(\tilde{\xi})}{\tilde{R}(\tilde{\xi},t)}\frac{\mathrm{d}\tilde{\xi}}{\tilde{\xi}-\tilde{x}} - \left(\frac{t-f(-a)}{\sqrt{2a}}\right)\frac{2}{\sqrt{\gamma}}\right] + \\ &\frac{2}{\sqrt{\delta}}\left(\frac{t-f(-a)}{\sqrt{2a}}\right) - 2\sqrt{\delta}\left(\frac{t-f(-a)}{2(2a)^{3/2}} - \frac{f'(-a)}{\sqrt{2a}}\right) + \\ &\epsilon\lim_{\gamma\to 0}\left[\int_{-a+\gamma}^{a}\frac{t-f(\tilde{\xi})}{\tilde{R}(\tilde{\xi},t)}\frac{\mathrm{d}\tilde{\xi}}{(\tilde{\xi}-\tilde{x})^2} - \left(\frac{t-f(-a)}{\sqrt{2a}}\right)\frac{2}{3\gamma^{3/2}} - \right. \\ &\left.\frac{2}{\sqrt{\gamma}}\left(\frac{t-f(-a)}{2(2a)^{3/2}} - \frac{f'(-a)}{\sqrt{2a}}\right)\right] + \frac{2\epsilon}{3\delta^{3/2}}\left(\frac{t-f(-a)}{\sqrt{2a}}\right) + \\ &\frac{2\epsilon}{\sqrt{\delta}}\left(\frac{t-f(-a)}{2(2a)^{3/2}} - \frac{f'(-a)}{\sqrt{2a}}\right) + O(\epsilon^2).\end{aligned} \tag{3.32}$$

Hence, upon expanding for large δ/ϵ in (3.31) and adding to (3.32), we deduce that as $\tilde{x} \downarrow -a$,

$$I = A(t) + O(\tilde{x} + a), \tag{3.33}$$

where

$$A(t) = \lim_{\gamma \to 0} \left[\int_{-a+\gamma}^{a} \frac{t - f(\tilde{\xi})}{\tilde{R}(\tilde{\xi}, t)} \frac{\mathrm{d}\tilde{\xi}}{\tilde{\xi} + a} - \left(\frac{t - f(-a)}{\sqrt{2a}} \right) \frac{2}{\sqrt{\gamma}} \right]. \tag{3.34}$$

Therefore, upon equating real parts in (3.29), we see that

$$\Upsilon_{\tilde{x}} \sim \frac{A(t)}{\pi} \sqrt{2a} \sqrt{\tilde{x} + a} \quad \text{as} \quad \bar{x} + a \downarrow 0. \tag{3.35}$$

Upon integrating (3.35) with respect to $\tilde{x}$ and returning to the original lab frame, we see that

$$\Upsilon \sim \frac{2A(t)}{3\pi} \sqrt{2a} \, (x - X(t) + a)^{3/2} \quad \text{as} \quad x - X(t) + a \downarrow 0. \tag{3.36}$$

From the definition of the displacement potential (2.54), we deduce that

$$\phi \sim \frac{A(t)}{\pi} (\dot{X}(t) - \dot{a}) \sqrt{2a} \, (x - X(t) + a)^{1/2} \quad \text{as} \quad x - X(t) + a \downarrow 0. \tag{3.37}$$

We note that this expression allows us to determine the coefficient of the square root in the leading order velocity potential as we approach the trailing turnover point, that is

$$S(t) = \frac{A(t)}{\pi} (\dot{X}(t) - \dot{a}) \sqrt{2a}, \tag{3.38}$$

which will be useful when we consider the trailing splash jet shortly.

Finally, the leading order form of Bernoulli's equation, $p = -\partial\phi/\partial t$, allows us to deduce that the pressure on the impactor as we approach the trailing turnover point is given by

$$p \sim \frac{A(t)}{2\pi} (\dot{X}(t) - \dot{a})^2 \sqrt{2a} \, (x - X(t) + a)^{-1/2} \quad \text{as} \quad x - X(t) + a \downarrow 0. \tag{3.39}$$

Thus, if we see breakdown at the trailing turnover point at $t = t_c$, so that $\dot{X}(t_c) - \dot{a}(t_c) = 0$, then clearly the coefficient of the inverse square-root singularity in the pressure expansion at $d_-(t)$ vanishes. Moreover, it is simple to show that the coefficient of the inverse square-root singularity as we approach the trailing turnover point in the complex velocity also vanishes. This behaviour is an indication of the asymptotic structure breaking down. We shall elaborate on this breakdown by considering two simple examples in §§3.1.3.1–3.1.3.2.

Note that since the impactor is symmetric, the displacement potential is even, and hence from (3.35) it is trivial to show that

$$\Upsilon_{\tilde{x}} \sim -\frac{A(t)}{\pi} \sqrt{2a} \sqrt{a - \tilde{x}} \quad \text{as} \quad \tilde{x} \to a. \tag{3.40}$$

Therefore, since it will be useful in our considerations of splash jets in §3.1.5, we state that the coefficient of the square-root term in the expansion of the velocity potential at $d_+ = X + a$ is given by

$$S(t) = -\frac{A(t)}{\pi}\sqrt{2a}(\dot{a} + \dot{X}). \tag{3.41}$$

3.1.3.1 Constant-speed symmetric wedge impact

Let us return to the symmetric wedge defined by $z = |x - Ut| - t$ in outer variables in the lab frame with $U > 0$. We recall that $d_\pm(t) = Ut \pm (\pi/2)t$. We can integrate (3.19) to find that the leading-order displacement potential is given by

$$\Upsilon(x, z, t) = zt + \mathrm{Re}\left(\frac{\mathrm{i}}{\pi}(\zeta - Ut)^2 \arcsin\left(\frac{\pi t}{2(\zeta - Ut)}\right) + \frac{\mathrm{i}t}{2}\left((\zeta - Ut)^2 - \left(\frac{\pi t}{2}\right)^2\right)^{1/2}\right)$$

where $\zeta = x + \mathrm{i}z$. The branch cuts for the square root and inverse sine functions are along the x-axis, from $x = Ut - \pi t/2$ to $x = Ut + \pi t/2$ and we take each of them to be real and positive for $x > Ut + \pi t/2$. It follows from the leading-order form of Bernoulli's equation that that the pressure on the impactor is given by $p = \partial^2\Upsilon/\partial t^2$, so that

$$p(x, 0, t) = \frac{((\pi/2)^2 - U^2)t + 2Ux}{\sqrt{(\pi t/2)^2 - (x - Ut)^2}} + \frac{2U^2}{\pi}\log\left|\frac{\pi t/2 - \sqrt{(\pi t/2)^2 - (x - Ut)^2}}{x - Ut}\right|, \tag{3.42}$$

for $x \in (Ut - \pi t/2, Ut + \pi t/2)$. We plot the pressure on the impactor against the similarity variable $\eta = x/t$ for various values of U in Figure 3.3 and note the following. Firstly, the pressure is clearly not symmetric about the wedge apex when $U > 0$. Secondly, the pressure is negative and infinite at the apex of the wedge, which is a product of the small-ε limit of the local corner flow there. Although we see this negative pressure for all $U > 0$, as we increase U, the region of negative pressure grows, particularly on the trailing edge of the wedge. At breakdown, we have $U = \pi/2$ and the point of zero pressure on the trailing edge coincides with the turnover point. In particular,

$$p(x, 0, t) = \frac{(U - \pi/2)^2 t}{\sqrt{\pi}\sqrt{x - (U - \pi/2)t}} + O\left(\sqrt{x - (U - \pi/2)t}\right) \quad \text{as} \quad x - (U - \pi/2)t \downarrow 0,$$

so that the coefficient of the inverse square-root singularity at the trailing turnover point tends to zero as $U \uparrow \pi/2$.

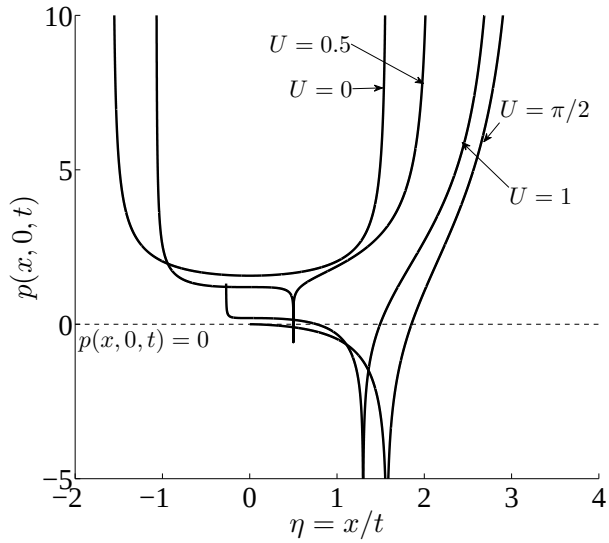

Figure 3.3: The pressure on an obliquely entering wedge as a function of $\eta = x/t$ for various values of U. This plot is based on one Moore et al. (2013a).

3.1.3.2 Constant-speed, symmetric parabola impact

We now consider the impact of the parabola $z = (x - Ut)^2 - t$ with $U > 0$. In this case, $d_\pm(t) = Ut \pm \sqrt{2t}$ ($n = 2$ in §2.2.10.2), and upon integrating (3.19) the displacement potential is given by

$$\Upsilon(x, z, t) = \mathrm{t}z + \mathrm{Re}\left[\frac{\mathrm{i}}{3}\left((\zeta - Ut)^3 - \left((\zeta - Ut)^2 - 2t\right)^{3/2}\right)\right], \tag{3.43}$$

where the branch cut for the final term on the right-hand side is along the x-axis, from $x = Ut - \sqrt{2t}$ to $x = Ut + \sqrt{2t}$, with the function real and positive for $x > Ut + \sqrt{2t}$. The leading-order-outer pressure on the impactor can be calculated from Bernoulli's equation to be

$$p(x, 0, t) = \frac{1 + 2U^2 t\,(U^2 t - 2) + 2Ux\,(1 - 2U^2 t + Ux)}{\sqrt{2t - (x - Ut)^2}}, \tag{3.44}$$

which we plot in Figure 3.4 for $U = 1$ at various times. This choice of U gives the critical time at which breakdown occurs to be $t_c = 1/2$. We see a region of negative pressure forming on the impactor *before* breakdown occurs. The point of zero pressure on the trailing edge of the parabola moves towards the turnover point as we approach the critical time, with the two coinciding when we reach breakdown. This is indicative of the coefficient of the inverse square-root singularity in the pressure vanishing at breakdown, as we saw in (3.39).

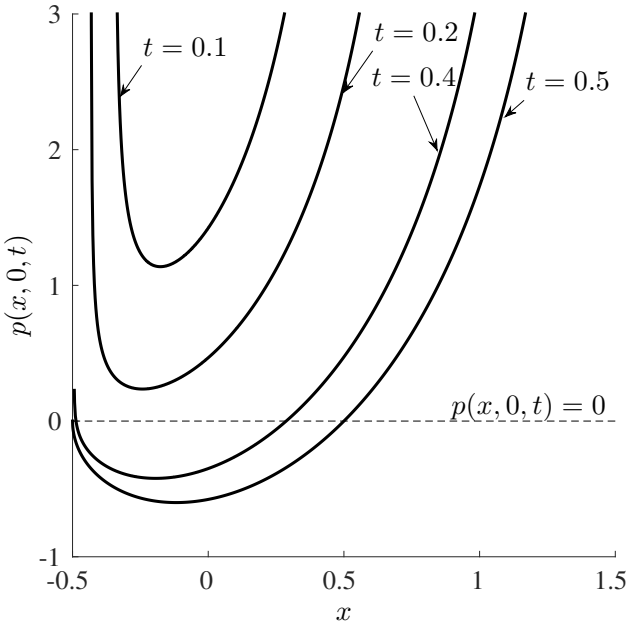

Figure 3.4: The pressure on a parabolic impactor for various times with $U = 1$. This plot is based on one Moore et al. (2013a).

3.1.4 Force on the impactor

How does the oblique component of velocity affect the upward hydrodynamic force on the impactor? At leading order, the vertical component of the force, $F(t)$, is still be dominated by the leading-order-outer pressure, which is given by

$$p(x,0,t) = \frac{\mathrm{d}^2}{\mathrm{d}t^2}\left(\Upsilon(x - X(t), 0, t\right), \tag{3.45}$$

for a general impactor. Recall that $d_{\pm}(t) = X(t) \pm a(t)$ at leading order. We can integrate (3.45) between $x = X(t) - a(t)$ and $x = X(t) + a(t)$ to obtain

$$\begin{aligned} F(t) \;=\; & \frac{\mathrm{d}}{\mathrm{d}t}\left(\int_{X-a}^{X+a} \frac{\mathrm{d}}{\mathrm{d}t}\Upsilon(x - X(t), 0, t)\,\mathrm{d}x\right) - \\ & \left(\dot{X}(t) - \dot{a}(t)\right)\left.\frac{\mathrm{d}\Upsilon}{\mathrm{d}t}\right|_{X-a} + \left(\dot{X}(t) + \dot{a}(t)\right)\left.\frac{\mathrm{d}\Upsilon}{\mathrm{d}t}\right|_{X+a}, \end{aligned} \tag{3.46}$$

using Leibniz's rule. Since the displacement potential has (3/2)-power behaviour in distance from the turnover points as we approach each turnover point, the final two terms on the right-hand side of (3.46) must vanish. Therefore, applying Leibniz's rule again

$$F(t) = \frac{\mathrm{d}^2}{\mathrm{d}t^2}\left(\int_{X-a}^{X+a} \Upsilon(x - X(t), 0, t)\,\mathrm{d}x\right), \tag{3.47}$$

where the boundary terms vanish for similar reasons. Making the change of variables $x - X(t) = s$ in the integrand, we find that the vertical component of the hydrodynamic force on the impactor is unchanged from that in the equivalent normal impact. Note that this result applies only if Wagner theory does not break down. Korobkin (1988) obtains this result for the oblique impact of a parabola for small penetration depth.

Note that under the assumption that the impactor cannot rotate, this result has the surprising effect that we can rule out any bouncing of the impactor due to the oblique motion. Hence, we would have to incorporate further effects, such as the rotation of the impactor, three-dimensional effects and separation of the viscous boundary layer to model, for example, the skipping of a stone.

3.1.5 Splash jets

As in the normal impact scenario as described in §2.2.8, the splash jets are modelled using the zero-gravity shallow-water equations:

$$\frac{\partial \bar{u}}{\partial t} + \bar{u}\frac{\partial \bar{u}}{\partial x} = 0, \tag{3.48}$$

$$\frac{\partial \bar{h}}{\partial t} + \frac{\partial}{\partial x}\left(\bar{h}\bar{u}\right) = 0, \tag{3.49}$$

where, $\bar{u}$ is the tangential component of the jet velocity, $\bar{h}$ is the jet thickness and to leading-order we take the body-fitted orthogonal coordinates to be the same as that in the outer region. We show in Appendix A that (3.48)–(3.49) are the leading-order equations governing the evolution of the splash jets even if the frame is accelerating, provided the components of acceleration are of order unity as $\varepsilon \to 0$. We must solve (3.48)–(3.49) subject to the boundary data

$$\bar{u} = 2(\dot{X}(t) + \dot{a}_{\pm}(t)), \quad \bar{h} = \frac{\pi S(t)^2}{8(\dot{X} + \dot{a}_{\pm})^2} \quad \text{at} \quad X = X(t) + a_{\pm}(t), \tag{3.50}$$

where the boundary condition on $\bar{h}$ comes from (2.79), with $S(t)$ given by (3.38) for the turnover point at $X(t) - a(t)$ and by (3.41) for the turnover point at $X(t) + a(t)$.

We can solve the jet problem using the method of characteristics. Let $\tau > 0$ parametrise time-of-travel along a characteristic and let $s > 0$ parametrise the boundary data. The characteristics are given by the particle paths, and we deduce

$$t = \tau + s, \quad x = 2(\dot{X}(s) + \dot{a}_{\pm}(s))\tau + X(s) + a_{\pm}(s), \tag{3.51}$$

where $\tau, s > 0$. Moreover, the tangential component of jet velocity and thickness are given by

$$\bar{u} = 2(\dot{X}(s) \pm \dot{a}(s)), \quad \bar{h} = \frac{\pi S(s)^2}{8(\dot{X} \pm \dot{a})^2}\frac{\mathrm{J}(0,s)}{\mathrm{J}(\tau,s)}, \tag{3.52}$$

where the Jacobian, $\mathrm{J}(\tau, s)$, is given by

$$\mathrm{J}(\tau, s) = \left(\dot{X}(s) \pm \dot{a}(s)\right) - 2\left(\ddot{X}(s) \pm \ddot{a}\right)\tau. \tag{3.53}$$

The jet solution holds provided the Jacobian is bounded and nonzero, and provided that Wagner theory holds. We shall now consider the particular cases of the constant-speed impacts of a wedge and a parabola.

3.1.5.1 Constant-speed, symmetric wedge impact

Firstly, we return to the case of constant-speed symmetric wedge impact, where the impactor is given by $z = |x - Ut| - t$ for $U > 0$. As stated previously, the leading-order locations of the turnover points in the constant-speed vertical impact of a symmetric wedge are given by $\pm a(t) = \pm\pi t/2$ and we can use this to deduce from (3.34) that the integral term of the coefficient of the inverse square-root singularity in the expansion of the leading-order-outer pressure on the impactor is given by $A(t) = 2$. Hence using (3.51)–(3.53) for the jet emanating from the leading turnover point, d_+, we have for $\tau, s > 0$,

$$t = \tau + s, \quad x = (2U + \pi)\tau + \left(U + \frac{\pi}{2}\right)s, \quad \bar{u} = 2U + \pi, \quad \bar{h} = \frac{s}{4}, \quad \mathrm{J}(\tau, s) = U + \frac{\pi}{2}. \tag{3.54}$$

Clearly, for all $\tau, s > 0$ the Jacobian is nonzero and bounded. Hence, provided that $U < \pi/2$ so that the leading-order theory has not broken down, the solution (3.54) is valid for all $\tau, s > 0$. We note that we can solve for (τ, s) in terms of (x, t) to obtain

$$\bar{h}(x, t) = \frac{(2U + \pi)t - x}{4U + 2\pi}, \tag{3.55}$$

for $(U + \pi/2)t < x < (2U + \pi)t$, the jet thickness vanishing at $x = (2U + \pi)t$. Hence, for a wedge, the leading jet terminates on the impactor and has length $(U + \pi/2)t$. As expected, we reproduce the behaviour seen in the vertical impact of a constant-speed wedge by setting $U = 0$.

The solution for the jet at the trailing turnover point is found similarly and we find that

$$x = (2U - \pi)\tau + \left(U - \frac{\pi}{2}\right)s, \quad \bar{u} = 2U - \pi, \quad \bar{h} = \frac{s}{4}, \quad \mathrm{J}(\tau, s) = U - \frac{\pi}{2}, \tag{3.56}$$

for $\tau, s > 0$. For $0 < U < \pi/2$, the Jacobian is bounded and nonzero for all $\tau, s > 0$. After solving for τ, s, we find that the jet thickness can be written as

$$\bar{h}(x, t) = \frac{x - (2U - \pi)t}{2\pi - 4U}. \tag{3.57}$$

Therefore, this jet also terminates on the impactor, and has length $(U - \pi/2)t$.

Once we reach the critical value of $U = \pi/2$, it is immediately apparent that the Jacobian is identically zero everywhere in the τ, s parameter space. Thus, our trailing jet solution breaks down immediately when the oblique speed reaches its critical value. Equivalently, as a consequence of the far-field behaviour of the velocity in the jet-root solution, the trailing jet problem breaks down at the critical speed as there is no longer any fluid entering the jet, which ceases to exist in the sense that it has zero length!

Moreover, the ratio of the maximum jet thickness (at the jet root) to the length of the jet is given by

$$\frac{1}{4\,(U - \pi/2)}.$$

Thus, as we approach breakdown with $U \uparrow \pi/2$, the aspect ratio of the jet becomes unbounded and the assumption we made in deriving the zero-gravity shallow water equations, that of a long, slender jet, no longer holds.

3.1.5.2 Constant-speed, symmetric parabola impact

We move on to consider the constant-speed impact of a symmetric parabola, where the body is given by $z = (x - Ut)^2 - t$ with $U > 0$ say. As stated previously, $\pm a(t) = \pm\sqrt{2t}$. Furthermore we can calculate $A(t) = \pi\sqrt{2t}$. Recall that for the constant-speed oblique impact of a parabola, the leading-order theory breaks down for all $U > 0$ at a critical time $t_c = 1/(2U^2)$. Thus, for the leading jet, (3.51)–(3.53) give

$$t = \tau + s, \quad x = \left(2U + \sqrt{\frac{2}{s}}\right)\tau + (Us + \sqrt{2s}), \quad \bar{u} = 2U + \sqrt{\frac{2}{s}}, \quad \bar{h} = \frac{\pi s^{3/2}}{2^{3/2}}\frac{\mathrm{J}(0,s)}{\mathrm{J}(\tau,s)}, \tag{3.58}$$

for $0 < \tau, s < t_c$, where the Jacobian is given by

$$\mathrm{J}(\tau, s) = \frac{1}{\sqrt{2}s^{3/2}}\left(\tau + s + \sqrt{2}Us^{3/2}\right). \tag{3.59}$$

Clearly, for $U > 0$, the Jacobian is bounded and nonzero for all $0 < \tau, s < t_c$, so the solution is valid for all τ, s in that range. Moreover, since $\mathrm{J}(\tau, s)$ is positive for all $0 < \tau, s < t_c$, the jet thickness is positive for all $0 < \tau, s < t_c$. However, the $\sqrt{2/s}$ term in x means that x takes all values up to infinity for $0 < \tau, s < t_c$. Hence, the jet does not terminate on the impactor for a parabola and has infinite extent at $t = 0^+$.

For the trailing jet, we find that

$$t = \tau + s, \quad x = \left(2U - \sqrt{\frac{2}{s}}\right)\tau + (Us - \sqrt{2s}), \quad \bar{u} = 2U - \sqrt{\frac{2}{s}}, \quad \bar{h} = \frac{\pi s^{3/2}}{2^{3/2}}\frac{\mathrm{J}(0,s)}{\mathrm{J}(\tau,s)}, \tag{3.60}$$

for $0 < \tau, s < t_c$, where the Jacobian is given by

$$\mathrm{J}(\tau, s) = -\frac{1}{\sqrt{2}s^{3/2}}\left(\tau + s - \sqrt{2}Us^{3/2}\right). \tag{3.61}$$

The Jacobian, $J(\tau, s)$, is bounded and nonzero for all $0 < \tau, s < t_c$, while $\bar{h} > 0$ for all $0 < \tau, s < t_c$, so the trailing jet does not terminate on the body either by a similar argument. Note that $J(0, t_c) = 0$, so that the solution (3.60) is no longer valid at breakdown.

Moreover, at breakdown, since the liquid velocity at the jet root $\bar{u}(d(t), t) \to 0$ as $t \to t_c$, the characteristics, or particle paths, are parallel to the boundary data curve at breakdown and hence the problem is no longer Cauchy. There is a finite amount of fluid mass in the jet at time $t = t_c$, which is effectively left behind by the jet-root. We do not speculate as to what happens to this mass.

Hence, in summary, for a given U, the trailing jet solution given parametrically by (3.60) and (3.61) is valid for all $0 < \tau, s < t_c$, but the solution breaks down at the turnover curve at time $t = t_c$ when there is no longer any fluid ejected into the trailing jet from the left-hand jet root. This solution and interpretation of breakdown will generalise to bodies of the form $f = |x - Ut|^n$ for integers $n > 1$.

3.1.6 Breakdown and cavitation

At breakdown the trailing turnover point is no longer advancing, so the local-in-space-and-time analysis discussed in §2.2.11.3 indicates that the leading-order solution is unstable to out-of-plane perturbations. Furthermore, at breakdown we see a loss of causality in the leading-order-outer problem, in which we cannot solve for the free surface once the trailing turnover point stops advancing.

In addition, we have shown that the asymptotic structure becomes invalid as breakdown is approached in the sense that the coefficients of the square-root singularities in the velocity and pressure vanish when the trailing turnover point stops advancing. Moreover, the zero-gravity shallow water equations can no longer be solved in the trailing splash jet; the characteristics becoming parallel to the boundary data curve in the (x, t)-plane at breakdown.

We noted that, although the pressure changes drastically once an oblique impact speed is introduced, the normal force on the impactor remains unchanged from the

normal impact scenario, even at the point of breakdown. This is a surprising result: the pressure increase on the leading side of the impactor must compensate exactly for the reduction in pressure on the trailing side. This is consistent with the numerical predictions in Figure 9 of Semenov and Yoon (2009).

On the trailing side of the impactor, there is the possibility of cavitation *prior* to breakdown. In the case of wedge impact, for any oblique impact speed, we see a large negative pressure at the apex due to the local flow round a corner. However, as we increase the oblique speed, the region of negative pressure grows, particularly on the trailing edge of the wedge. In general, a region of sufficiently large negative pressure leads to cavitation.

Semenov and Yoon (2009) argue that the dynamics of a growing cavity occur on the timescale taken for small bubbles to merge into a cavity, so that if the time taken for fluid particles to pass the region of negative pressure is shorter than the cavitation timescale then a cavity would not form. Moreover, they argue that in practical terms, as any impactor will be smooth about its line of symmetry at some, possibly microscopic, scale, we do not in actuality see a negative infinite pressure at the apex.

However, as we illustrated in particular with the parabola example in §3.1.3.2, a region of negative pressure also forms on the trailing edge of smooth impactors. For a fixed oblique speed, this region grows in size as we approach the critical time. The point of zero pressure closest to the trailing turnover point moves towards the trailing turnover point as time increases, with the two coinciding at breakdown. This is indicative of the coefficient of the inverse square-root singularity vanishing at breakdown.

Therefore, in each of these cases, there is the possibility of a patch cavity forming in the region of negative pressure. Models of such cavities are considered by Howison et al. (1994). Clearly, the introduction of a cavity in the leading-order-outer problem would make the analysis much more complex. We present a possible model for a three-dimensional patch cavity in Appendix B, and naturally there is an equivalent two-dimensional problem. However, we do not pursue this any further here; it is something that requires further consideration.

Alternatively as Semenov and Yoon (2009) postulate, one could suggest that the timescale for the formation of a cavity is much larger than the timescale for fluid particles to pass the region of negative pressure on the impactor. They argue that cavitation would then not occur, but that, at the moment of breakdown, the pressure vanishing at the trailing turnover point causes ventilation to occur on the trailing edge. Reinhard et al. (2012) propose several models of this ventilation using various criteria

to locate the point at which the free surface meets the impactor after ventilation (i.e. they propose several new Wagner conditions post separation).

We do not investigate cavitation or ventilation here, but it is important to note the various ways in which oblique Wagner theory may become invalid. The analysis so far in this thesis has been carried out under the assumption that neither cavitation nor ventilation occurs before breakdown.

3.1.7 Summary

In this section, we have extended two-dimensional small-deadrise Wagner theory to oblique impacts. The asymptotic structure of the impact is the same as that in normal water-entry at small deadrise angles. In order for the oblique component of impact velocity to enter the leading-order-outer problem, it is necessary to assume that the ratio of the horizontal to vertical impact speeds is on the order of the inverse of the deadrise angle. However, even with this large speed ratio, by introducing the displacement potential, we are able to show that the solution to the leading-order-outer problem retains a surprising link to the normal-impact theory. The turnover points and the leading-order-outer free surface are simply translations with respect to the oblique motion of the normal-impact turnover points and free surface. The leading-order-outer velocity potential and pressure do not have such simple relationships to their normal-impact counterparts. However, we were able to deduce that the z-component of the leading-order force on the impactor is independent of the oblique motion. This surprising result corroborates nicely with Korobkin (1988), who used a Lagrangian formulation to show that, at least in the early stages of the impact, the oblique motion does not alter the leading-order normal component of force on an impacting parabola for small penetration depths.

For a general oblique impact, it is possible for the trailing turnover point to stop advancing, leading to a breakdown of the theory as summarised in §3.1.6. We illustrated this possibility for some examples of symmetric impactors. In the constant-speed impact of a wedge, breakdown occurs instantly at a critical value of the oblique speed, whereas in a constant-speed, smooth-body impact, breakdown occurs for any (nonzero) oblique speed after a finite critical time. For smooth impactors there is, however, at least a short period of time where the Wagner solution is valid.

By expanding the displacement potential solution near the turnover point at which breakdown occurs, we showed that the coefficient of the square-root singularity in the leading-order-outer velocity and pressure on the impactor at this turnover point vanishes at the instant of breakdown. In the wedge example, breakdown renders invalid the small-aspect-ratio assumption in the splash jet, and in both the wedge

and blunt geometries, the speed of the fluid entering the jet vanishes at breakdown. At the critical speed for a wedge, or critical time for a blunt impactor, the Wagner asymptotic structure breaks down, there being a nonuniformity in the asymptotic expansions as we get sufficiently close to breakdown. We do not consider what models might apply close to breakdown in this thesis: this is an area that requires further investigation.

Finally, we discussed the possibility of cavitation and ventilation prior to breakdown driven by a region of negative pressure that forms on the impactor, but did not pursue any analysis of these possibilities.

3.2 Three-dimensional Wagner theory

Very few analytical studies of three-dimensional oblique impact problems have been performed. This is mainly due to the analytical difficulties encountered in studying them. One of the few works of note is that of Miloh (1991a), who considers the oblique impact of a sphere by generalising the two-dimensional oblique theory of Korobkin (1988), in which the impact time t is taken as a small parameter and the impactor is locally given by a paraboloid. Scolan and Korobkin (2012) use Galin's theorem to categorise a wide array of impacts of an elliptic paraboloid. They briefly consider oblique impacts and find some of the symmetries that we are going to highlight in this chapter.

By extending some of the ideas seen in §3.1, we will model a whole range of three-dimensional oblique impacts. Our results will rely on being able to determine solutions to three-dimensional normal impact problems. Many of our results are direct extensions of the two-dimensional theory.

3.2.1 Formulation of the dimensionless problem

We consider the same problem configuration as §2.3 but with the addition of oblique velocity components, $(\dot{X}(t)/\varepsilon, \dot{Y}(t)/\varepsilon)$ in the x- and y-directions respectively, so that the smooth, rigid, convex impactor is given by

$$z = f(\varepsilon x - X(t), \varepsilon y - Y(t)) - t \tag{3.62}$$

in dimensionless coordinates. We choose $X(0) = Y(0) = 0$ so that the impact begins at the origin at time $t = 0$.

In anticipation of the change of variables we will make, echoing §3.1, we define the projection of the turnover curve onto the (x, y)-plane for this oblique impact to

be given by

$$t = \omega(\varepsilon x - X(t), \varepsilon y - Y(t)), \tag{3.63}$$

Note that $t > \omega(\varepsilon x - X(t), \varepsilon y - Y(t))$ is the effective contact set in the outer region. As we saw in §2.3.6.2, leading-order Wagner theory predicts that the splash sheet for blunt impactors extends to infinity at time $t = 0^+$. The leading-order theory in the outer and inner regions holds whether or not the splash sheet is of infinite extent, provided that the splash sheet does not separate from the impactor. Thus, for convenience in stating the boundary conditions, we shall denote the projection onto the (x, y)-plane of the perimeter of the wetted region by

$$t = c(\varepsilon x - X(t), \varepsilon y - Y(t)). \tag{3.64}$$

The dimensionless model is as follows. The equation of motion for the velocity potential, $\phi(x, y, z, t)$, is

$$\nabla^2 \phi = 0 \tag{3.65}$$

in the fluid. In addition, we satisfy Bernoulli's equation in the fluid, which is given by

$$p + \frac{\partial \phi}{\partial t} + \frac{1}{2}|\nabla \phi|^2 = 0, \tag{3.66}$$

where $p(x, y, z, t)$ is the fluid pressure. Recall that $,i$ denotes differentiation with respect to i^{th} argument of a function. The kinematic condition on the body is given by

$$\varepsilon f_{,1} \frac{\partial \phi}{\partial x} + \varepsilon f_{,2} \frac{\partial \phi}{\partial y} - \frac{\partial \phi}{\partial z} = 1 + \dot{X} f_{,1} + \dot{Y} f_{,2}, \tag{3.67}$$

on $z = f(\varepsilon x - X(t), \varepsilon y - Y(t)) - t, t > c(\varepsilon x - X(t), \varepsilon y - Y(t))$. The kinematic condition on the free surface is

$$\frac{\partial \phi}{\partial z} = \frac{\partial h}{\partial t} + \frac{\partial \phi}{\partial x}\frac{\partial h}{\partial x} + \frac{\partial \phi}{\partial y}\frac{\partial h}{\partial y} \quad \text{on} \quad z = h(x, y, t), t < \omega(\varepsilon x - X(t), \varepsilon y - Y(t)), \tag{3.68}$$

while the dynamic boundary condition is given by

$$p = 0 \quad \text{on} \quad z = h(x, y, t), t < \omega(\varepsilon x - X(t), \varepsilon y - Y(t)). \tag{3.69}$$

Finally, the initial and far-field conditions are

$$\phi(x, y, z, 0) = 0 \qquad \text{for} \quad -\infty < x, y < \infty, z \leq 0, \tag{3.70}$$

$$h(x, y, 0) = 0 \qquad \text{for} \quad -\infty < x, y < \infty, \tag{3.71}$$

$$\phi = O\left(1/R^2\right) \quad \text{as} \quad R = \sqrt{x^2 + y^2 + z^2} \to \infty, \tag{3.72}$$

$$h = O\left(1/r^3\right) \quad \text{as} \quad r = \sqrt{x^2 + y^2} \to \infty. \tag{3.73}$$

We also demand that $\omega(0,0) = 0$.

The asymptotic structure for impactors of small deadrise angle, that is $0 < \varepsilon \ll 1$, described in §2.3.2 readily extends to oblique three-dimensional impacts. In particular, the analysis in §2.3.3 still holds and the inner region near the turnover curve is quasi-two-dimensional in each plane perpendicular to the turnover curve. Furthermore, as in §3.1, the oblique components of the velocity will only enter the leading-order-outer problem if $\dot{X}(t), \dot{Y}(t) = O(1)$ for $t = O(1)$, so that the oblique speed is $O(1/\varepsilon)$ larger than the normal speed; we shall assume that this holds henceforth.

3.2.2 Leading-order-outer problem

As in the case of normal impact, when $X = Y = 0$, we neglect the splash sheet on the body in the outer region. The scalings and expansions follow as in §2.3.4 and the leading-order-outer problem is given by:

$$\nabla^2 \phi_0 = 0 \qquad \text{in} \quad z \leq 0, \tag{3.74}$$

$$\frac{\partial \phi_0}{\partial z} = -1 - \dot{X} f_{,1} - \dot{Y} f_{,2} \quad \text{on} \quad z = 0, t > \omega_0(x - X(t), y - Y(t)), \tag{3.75}$$

$$\frac{\partial \phi_0}{\partial z} = \frac{\partial h_0}{\partial t} \qquad \text{on} \quad z = 0, t < \omega_0(x - X(t), y - Y(t)), \tag{3.76}$$

$$\phi_0 = 0 \qquad \text{on} \quad z = 0, t < \omega_0(x - X(t), y - Y(t)), \tag{3.77}$$

where (3.77) is derived from the leading-order version of Bernoulli's condition (3.66) and the initial condition that $\phi_0(x, y, z, 0) = 0$. The initial and far-field conditions are given by

$$h_0(x, y, 0) = 0 \qquad \text{for} \quad -\infty < x, y < \infty, \tag{3.78}$$

$$\phi_0 = O(1/R^2) \quad \text{as} \quad R \to \infty, \tag{3.79}$$

$$h_0 = O(1/r^3) \quad \text{as} \quad r \to \infty, \tag{3.80}$$

together with the condition that $\omega_0(0,0) = 0$.

In addition to this, matching to the inner jet-root regions is only possible if the velocity potential behaves as the square root of distance from the turnover curve as we approach the turnover curve in any plane perpendicular to it (cf. §2.3.4), and the Wagner condition,

$$h_0(x, y, t) = f(x - X(t), y - Y(t)) - t \quad \text{on} \quad t = \omega_0(x - X(t), y - Y(t)), \tag{3.81}$$

pertains.

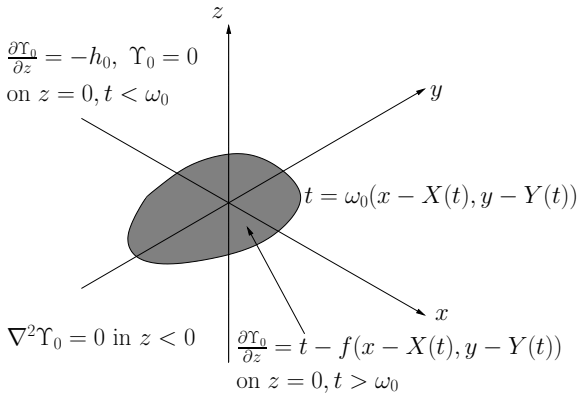

Figure 3.5: The leading-order-outer problem for the displacement potential, Υ_0. The smoothing effect of the integral transform means that the displacement potential has (3/2)-power behaviour in distance from the turnover curve as we approach in any plane perpendicular to it. Additionally, we require $\Upsilon_0 = O(1/R^2)$ as $R \to \infty$.

3.2.2.1 Displacement potential formulation

Adhering to the approach of §2.3.4.1, we simplify the problem by introducing the leading-order displacement potential, $\Upsilon_0(x, y, z, t)$ defined in (2.89). Since the Wagner condition (3.81) holds, we can simplify the boundary conditions in a similar manner to §2.3.4.1, which for the sake of brevity we do not repeat here. We display the displacement potential problem in Figure 3.5.

We note that as in the two-dimensional case, the displacement potential formulation of the problem in Figure 3.5 does not contain any time derivatives. Thus, when we move to a frame fixed with respect to the moving minimum of the impactor by making the change of variables

$$x = X(t) + \tilde{x}, \quad y = Y(t) + \tilde{y}, \tag{3.82}$$

the problem reduces to exactly that in §2.3.4.1. Hence, given a solution to the normal impact problem we are able to write down the solution to the corresponding oblique problem.

In particular, if $\Upsilon_0(\tilde{x}, \tilde{y}, z, t)$, $h_0(\tilde{x}, \tilde{y}, t)$ and $t = \omega_0(\tilde{x}, \tilde{y})$ are the leading-order-outer displacement potential, free surface and turnover curve for the normal impact of the body profile $z = f(\tilde{x}, \tilde{y}) - t$, then $\Upsilon_0(x - X(t), y - Y(t), z, t)$, $h_0(x - X(t), y - Y(t), t)$ and $t = \omega_0(x - X(t), y - Y(t))$ are the leading-order-outer displacement potential, free surface and turnover curve for the oblique impact of the body profile $z = f(x - X(t), y - Y(t)) - t$. This result is a direct analogue of the corresponding result for two-dimensional oblique impact problems, considered in §3.1. We note,

however, that as in two dimensions, the leading-order-outer velocity potential and pressure do not have such a simple relation with their normal-impact counterparts. We now exploit this analysis to investigate the oblique impact of axisymmetric bodies.

3.2.2.2 Axisymmetric oblique impact

Henceforth, we will drop the subscripts denoting the leading-order variables. We suppose the impactor is axisymmetric so that the body profile is given by $z = f(r) - t$, where the polar coordinates (r, θ) based on the minimum of the body profile are defined by

$$x - X(t) = r\cos\theta,\ y - Y(t) = r\sin\theta \tag{3.83}$$

for $r > 0$ and $0 \leq \theta < 2\pi$. We denote the location of the turnover curve projection by $r = d(t)$.

It follows from (2.102), (2.110) and (2.111) that the displacement potential is given by

$$\Upsilon(r, z, t) = \int_0^{d(t)} \chi(\sigma, t) \int_0^\infty e^{\lambda z} \sin\lambda\sigma \mathrm{J}_0(\lambda r)\mathrm{d}\lambda\mathrm{d}\sigma, \tag{3.84}$$

where

$$\chi(\sigma, t) = \frac{2}{\pi}\int_0^\sigma \frac{\rho(t - f(\rho))}{\sqrt{\sigma^2 - \rho^2}}\mathrm{d}\sigma. \tag{3.85}$$

As in §2.3.4.2, for Υ to have a (3/2)-power singularity as $z \uparrow 0, r \uparrow d(t)$ we must have

$$\chi(d(t), t) = 0, \tag{3.86}$$

which gives

$$\Upsilon = -\frac{4\chi'(d(t), t)}{3\sqrt{2d(t)}}\left(d(t) - r\right)^{3/2} + O\left(\left(d(t) - r\right)^{5/2}\right), \tag{3.87}$$

as $r \uparrow d(t)$, by (2.114). Note that, as previously, a prime indicates differentiation with respect to σ.

The definition of $\chi(\sigma, t)$ given in (3.85) and the condition (3.86) are identical to those given for normal axisymmetric impacts. However, given the definition of r, both the normal speed of the turnover curve and the coefficient of the square root in the local expansion of the velocity potential near the turnover curve are not the same as their normal impact counterparts.

In particular, if a curve is defined by $F(r, \theta, t) = 0$, then its outward normal velocity is given by

$$v_n = -\frac{1}{|\nabla F|}\frac{\mathrm{d}F}{\mathrm{d}t} = -\frac{1}{|\nabla F|}\left(\frac{\partial F}{\partial t} + \dot{r}\frac{\partial F}{\partial r} + \dot{\theta}\frac{\partial F}{\partial \theta}\right). \tag{3.88}$$

For the turnover curve, $F(r,\theta,t) = r - d(t)$, so that

$$v_n(\theta,t) = \dot{d}(t) + \dot{X}(t)\cos\theta + \dot{Y}(t)\sin\theta. \tag{3.89}$$

Hence, we might expect there to be values of $\dot{X}$, $\dot{Y}$, θ and t such that $v_n \leq 0$. Physically, this means the turnover curve is no longer advancing. Since the linear stability analysis of §2.2.11.3 is local in space and time, the conclusions generalise to three-dimensional impacts. Therefore, if the turnover curve is anywhere retreating, we expect to see linear instability and a breakdown of the solution as discussed for two-dimensional impacts in §3.1.2.2. Hence, we require $v_n > 0$ for the solution to hold.

The coefficient of the square root in the leading-order-outer velocity potential is easily derived from (3.87) by noting that $\phi = -\mathrm{d}/\mathrm{d}t(\Upsilon(r,\theta,z,t))$, giving

$$S(\theta,t) = \sqrt{\frac{2}{d(t)}}\chi'(d(t))v_n(\theta,t), \tag{3.90}$$

where $\phi(r,\theta,0,t) = S(\theta,t)\,(d(t)-r)^{1/2} + O((d(t)-r)^{3/2})$ as $r \uparrow d(t)$. In particular, we note that we can express the leading-order-outer pressure on the impactor as it approaches the turnover curve in terms of $S(\theta,t)$ and $v_n(\theta,t)$, namely

$$p(r,\theta,0,t) = -\frac{1}{2}S(\theta,t)v_n(\theta,t)\,(d(t)-r)^{-1/2} + O((d(t)-r)^{1/2}) \text{ as } r \uparrow d(t). \tag{3.91}$$

So, we conclude that at breakdown (i.e. $v_n = 0$), the coefficient of the inverse square-root singularities in the leading-order-outer velocity and pressure vanish, as in the case of breakdown in the two-dimensional theory (i.e. when $\dot{d}_{\pm}(t) = 0$) in §3.1.3.

Finally, we consider the leading-order vertical component of force on the impactor, $F(t)$, given for a general three-dimensional impactor in the lab frame by

$$F(t) = \iint_{t>\omega(x-X(t),y-Y(t))} \frac{\mathrm{d}^2}{\mathrm{d}t^2}\Upsilon(x-X(t),y-Y(t),0,t)\,\mathrm{d}x\mathrm{d}y. \tag{3.92}$$

Using Reynolds transport theorem it is straightforward to show that

$$\begin{aligned} F(t) &= \frac{\mathrm{d}^2}{\mathrm{d}t^2}\iint_{t>\omega(x-X(t),y-Y(t))} \Upsilon(x-X(t),y-Y(t),0,t)\,\mathrm{d}x\mathrm{d}y \\ &\quad - \int_{t=\omega(x-X(t),y-Y(t))} \left(\frac{\mathrm{d}\Upsilon}{\mathrm{d}t} + \Upsilon\right) v_n\,\mathrm{d}s, \end{aligned} \tag{3.93}$$

where s parametrises the boundary curve. However, we know that the displacement potential and its first derivative with respect to time vanish on the turnover curve,

and hence the line integral also vanishes. Therefore, making a change of variables $x - X(t) = \xi$, $y - Y(t) = \eta$ in the integrand in the double integral, we deduce that

$$F(t) = \frac{\mathrm{d}^2}{\mathrm{d}t^2} \iint_{t>\omega(x,y)} \Upsilon(\xi, \eta, t), \mathrm{d}\xi \mathrm{d}\eta. \tag{3.94}$$

Hence, as in two dimensions, the leading-order vertical component of force on the impactor remains unchanged from the normal impact case. This corroborates with the conclusions of Miloh (1991a) for the oblique impact of a sphere at small-times.

We move on to look at some specific examples of axisymmetric impact problems. We will seek to compare the results to the corresponding normal impact case, describing when our extended theory applies and when it breaks down.

3.2.2.3 Impact of a cone

We consider the oblique impact of a cone defined by $z = r - t$, where we recall that $r = \sqrt{(x - X(t))^2 + (y - Y(t))^2}$. Although our analysis will extend to any oblique impacts such that $\dot{X}$, $\dot{Y} = O(1)$, we shall restrict ourselves to the case that $X = Ut$ and $Y = 0$, with the constant $U > 0$ without loss of generality, to illustrate some of the applications of our theory.

As in the two-dimensional oblique entry of a wedge, locally to the apex of the cone, the sharp point causes the fluid to have an infinite negative pressure. For the sake of the following analysis we assume that the flow does not cavitate near to the apex. We discuss the possibility of cavitation in §3.2.5.

As in the normal impact case, we deduce from (3.85) that

$$\chi(\sigma, t) = \frac{2}{\pi}\left(\sigma t - \frac{\sigma^2 \pi}{4}\right), \tag{3.95}$$

and that

$$r = \sqrt{(x - Ut)^2 + y^2} = d(t) = \frac{4t}{\pi}, \tag{3.96}$$

defines the location of the turnover curve.

Thus, using (3.96), we deduce from (3.89) that the outward normal speed of the turnover curve is given by

$$v_n = \frac{4}{\pi} + U\cos\theta. \tag{3.97}$$

The normal impact speed is independent of t because the problem (3.74)-(3.81) for a cone admits a similarity solution in which distances scale with t.

The turnover curve is only advancing for

$$U < \min_{\theta \in (\pi/2, 3\pi/2)} -\frac{4}{\pi \cos\theta}, \tag{3.98}$$

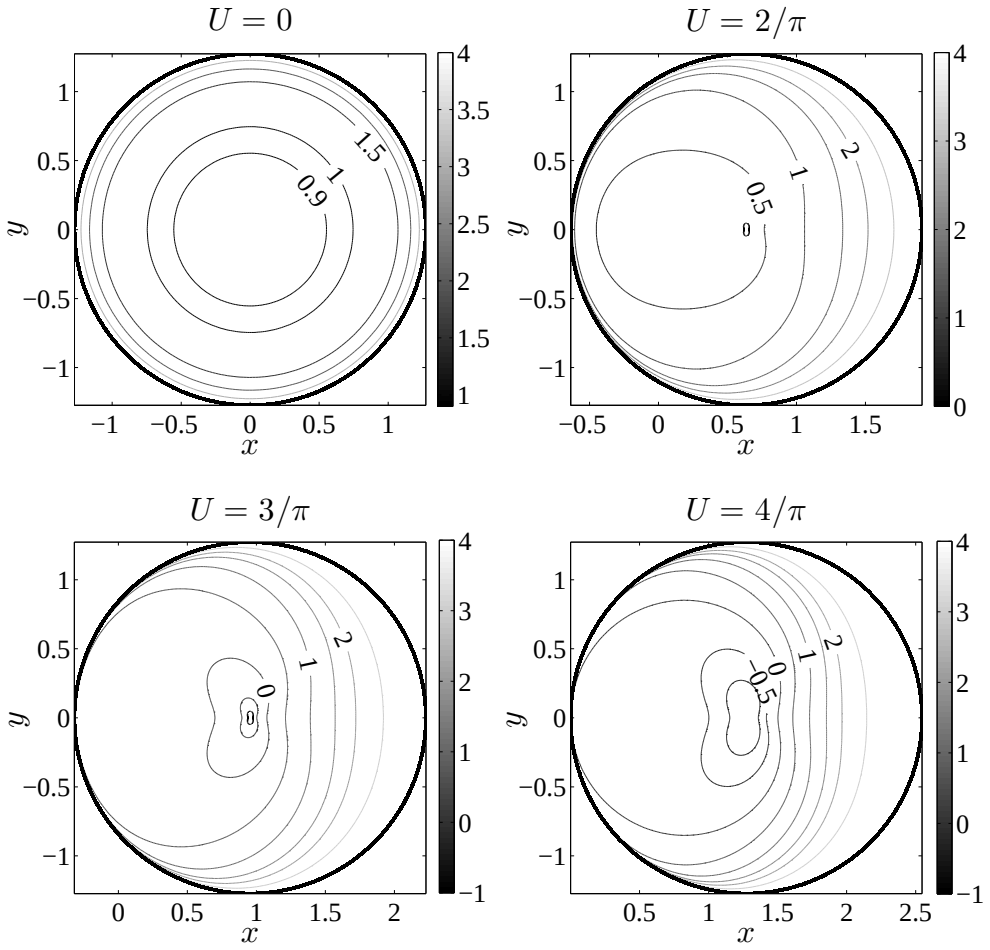

Figure 3.6: Contours of the leading-order-outer pressure on a cone at time $t = 1$ for $U = 0$ (top-left), $U = 2/\pi$ (top-right), $U = 3/\pi$ (bottom-left), and $U = 4/\pi$ (bottom-right). The circular turnover curve is depicted by a bold black line. As there is an inverse square-root singularity in the pressure as we approach this curve, we have truncated the contour domain for ease of viewing the behaviour on the interior of the turnover curve. At breakdown, the contour of zero pressure touches the turnover curve. This plot is based on one in Moore et al. (2012).

where the restriction on θ is present since we assumed $U > 0$ without loss of generality. Thus, we expect the turnover curve to stop advancing on the ray $\theta = \pi$ when $U = 4/\pi$. This is in the direction directly opposite that of the oblique motion. Therefore the theory applies for all $t > 0$ for $0 \leq U < 4/\pi$ but breaks down at $t = 0^+$ when $U \geq 4/\pi$.

In the lab frame, the leading-order-outer pressure on the impactor is given by $p(r,\theta,0,t) = \mathrm{d}^2/\mathrm{d}t^2\left(\Upsilon(r,\theta,0,t)\right)$. We can evaluate the displacement potential (3.84) on $z=0$ and thus recalling (2.106)–(2.107), find the pressure on the impactor in the contact set, giving

$$p(r,\theta,0,t) = -\frac{U^2}{2}\cosh^{-1}\frac{4t}{\pi r} + \frac{2t}{\pi\sqrt{(4t/\pi)^2 - r^2}}\left(\frac{16}{\pi^2} + \frac{2Ur}{t}\cos\theta + U^2\cos^2\theta\right), \tag{3.99}$$

for $r < 4t/\pi$. We plot contours of constant pressure on the impactor in Figure 3.6 (against x and y) for $U = 0,\ 2/\pi,\ 3/\pi,\ 4/\pi$. Since the cone admits a similarity solution in which distances scale with t, we only need to do this at one time instant, which we choose without loss of generality to be at $t=1$. When the cone has a forward velocity component, there is a region of negative pressure on the impactor inside the turnover curve. As U increases, the contour of zero pressure gradually spreads further from the apex until, at breakdown, it touches the turnover curve. This is an indication that at the critical value of U, the coefficient of the inverse square-root singularity in the expansion of the leading-order-outer pressure near the turnover curve vanishes at this point of intersection.

Finally, the coefficient of the square-root term in the expansion of the velocity potential as we approach the turnover curve can be calculated directly from (3.90) and (3.97), giving

$$S(\theta,t) = \sqrt{\frac{2}{d(t)}}\chi'(d(t))\left(\dot{d}(t) + U\cos\theta\right) = -\sqrt{\frac{2t}{\pi}}\left(\frac{4}{\pi} + U\cos\theta\right). \tag{3.100}$$

This will be useful in our analysis of the splash sheet in §3.2.4.

3.2.2.4 Impact of a blunt body

Our second example is that of a smooth axisymmetric body, with profile of the form $z = r^n - t$, where $n > 1$. Again, we let $X = Ut$ and $Y = 0$, and take $U > 0$.

Integrating (3.85) for $\chi(\sigma,t)$, we deduce that

$$\chi(\sigma,t) = \frac{2}{\pi}\left(\sigma t - 2^n\sigma^{n+1}\mathrm{B}\left(\frac{n+2}{2},\frac{n+2}{2}\right)\right), \tag{3.101}$$

where $\mathrm{B}(\cdot,\cdot)$ is the beta function. Therefore, by (3.86), the turnover curve is given by

$$r = \sqrt{(x-Ut)^2 + y^2} = d(t) = \left(\frac{t}{2^n\mathrm{B}((n+2)/2,(n+2)/2)}\right)^{1/n}, \tag{3.102}$$

so that the outward normal speed of the turnover curve is given by

$$v_n = \frac{1}{n}\left(\frac{1}{2^n\mathrm{B}((n+2)/2,(n+2)/2)}\right)^{1/n} t^{1/n-1} + U\cos\theta. \tag{3.103}$$

It follows from (3.103) that for $U > 0$, the outward normal velocity $v_n > 0$ for $0 < t < t_c$, but that $v_n = 0$ on $\theta = \pi$ when

$$t_c = \left(nU \left(2^n \mathrm{B}((n+2)/2, (n+2)/2) \right)^{1/n} \right)^{n/(1-n)}. \tag{3.104}$$

As in the impact of a cone, the breakdown of the Wagner theory first occurs at the point on the turnover curve in the direction opposite the horizontal motion. However, unlike in §3.2.2.3, assuming there to be no cavitation on the impactor prior to breakdown, Wagner theory will hold for all $U > 0$, if only for a small time period $t \in (0, t_c)$.

To consider the solution and breakdown in more detail, we consider the particular case where $n = 2$, i.e. the impactor is a paraboloid. In this case, the leading-order pressure on the impactor is given by

$$p(r, \theta, 0, t) = -\frac{8U^2}{3\pi} \sqrt{\frac{3t}{2} - r^2} + \frac{1}{\sqrt{(3t/2)^2 - r^2}} \left(\frac{3}{2\pi} + \frac{4Ur\cos\theta}{\pi} + \frac{8U^2 r^2 \cos^2\theta}{3\pi} \right), \tag{3.105}$$

where $r < \sqrt{3t/2}$. We plot contours of constant pressure in Figure 3.7. We consider the case in which U is chosen so that the critical time is given by $t_c = 1$. The plots represent snapshots of the impact at various times. Prior to breakdown, a region of negative pressure forms on the trailing side of the paraboloid. As we hit breakdown, the contour of zero pressure touches the turnover curve: at this intersection point the coefficient of the inverse square-root singularity in the pressure expansion near the turnover curve vanishes. We discuss the possibility of cavitation occurring prior to breakdown in §3.2.5.

Finally, since it will be needed in §3.2.4, we note that the coefficient of the square-root term in the expansion of the velocity potential as we approach the turnover curve, (3.90), is given by

$$S(\theta, t) = -\frac{2\sqrt{2}}{\pi} \left(\frac{t}{2^n \mathrm{B}((n+2)/2, (n+2)/2)} \right)^{1/2n} v_n(\theta, t). \tag{3.106}$$

3.2.3 A non-axisymmetric example: elliptic paraboloid

Scolan and Korobkin (2001) present a novel inverse method of constructing solutions to the Wagner problem for normal impact. The method relies on specifying a turnover curve, say $t = \omega_0(x, y)$, and using the Wagner condition

$$f(x, y) = \omega_0(x, y) + h_0(x, y, \omega_0(x, y)) \tag{3.107}$$

to construct a body profile that would have generated this turnover curve in the forward problem. We shall not go into further details here, but we shall use an

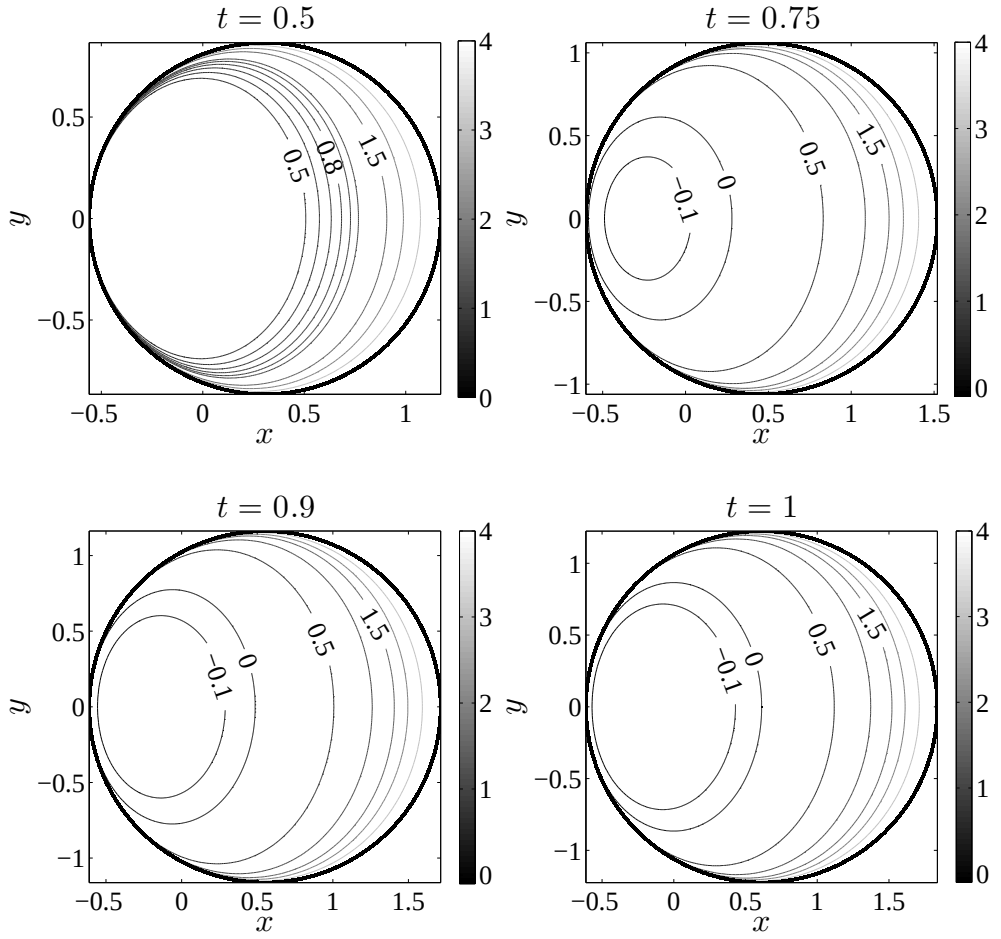

Figure 3.7: Contours of the leading-order-outer pressure on a paraboloid for different times: $t = 0.5$ (top-left), $t = 0.75$ (top-right), $t = 0.9$ (bottom-left), and $t = 1$ (bottom-right). The circular turnover curve is depicted by a bold black line. As there is an inverse square-root singularity in the pressure as we approach this curve, we have again truncated the contour domain for ease of viewing the behaviour on the interior of the turnover curve. At breakdown, the contour of zero pressure touches the turnover curve. This plot is based on one in Moore et al. (2012).

example from Scolan and Korobkin (2001) to consider how breakdown occurs for a non-axisymmetric body profile. In a vertical impact, the elliptic paraboloid

$$z = \left(\frac{x}{a}\right)^2 + \left(\frac{y}{b}\right)^2 - t,$$

where, without loss of generality, we assume $a > b$, admits the elliptic turnover curve

$$\left(\frac{x}{A(t)}\right)^2 + \left(\frac{y}{B(t)}\right)^2 = 1, \tag{3.108}$$

where $A(t) = \alpha\sqrt{t}$, $B(t) = \beta\sqrt{t}$ and

$$\begin{aligned} \alpha &= a\sqrt{1 + (1-e^2)D(e)/E(e)}, & (3.109)\\ \beta &= b\sqrt{2 - (1-e^2)D(e)/E(e)}, & (3.110)\\ e &= \sqrt{1 - \frac{\beta^2}{\alpha^2}}, & (3.111)\\ D(e) &= \frac{1}{e^2}\left(K(e) - E(e)\right); & (3.112) \end{aligned}$$

in these expressions the elliptic integrals of the first kind, $K(e)$ and $E(e)$ are given by

$$K(e) = \int_0^{\pi/2} \frac{1}{\sqrt{1 - e^2\sin^2\theta}}\,\mathrm{d}\theta, \quad E(e) = \int_0^{\pi/2} \sqrt{1 - e^2\sin^2\theta}\,\mathrm{d}\theta. \tag{3.113}$$

If we introduce the oblique components of velocity $(X(t), Y(t))$ to the impactor, the theory in §3.2.2.1 can be applied to deduce that the turnover curve is given by

$$\left(\frac{x - X(t)}{A(t)}\right)^2 + \left(\frac{y - Y(t)}{B(t)}\right)^2 = 1, \tag{3.114}$$

where (3.109)–(3.112) still apply. We shall consider the specific example in which

$$(X(t), Y(t)) = Ut(\cos\theta_0, \sin\theta_0),$$

where $U > 0$ and, without loss of generality, we restrict the angle the oblique velocity makes to the major semi-axis of the ellipse defined by (3.114), so that $0 \le \theta_0 \le \pi/2$. The outward normal speed of the elliptic turnover curve, calculated from (3.88) vanishes provided $\mathrm{d}F/\mathrm{d}t$ vanishes, with F given by

$$F(x, y, t) = \left(\frac{x - X(t)}{A(t)}\right)^2 + \left(\frac{y - Y(t)}{B(t)}\right)^2 - 1.$$

After some algebraic manipulation, we conclude that the outward normal speed vanishes if and only if

$$A(t)B(t)^2\cos\gamma\left(U\cos\theta_0 - \dot{A}(t)\cos\gamma\right) + B(t)A(t)^2\sin\gamma\left(U\sin\theta_0 + \dot{B}(t)\sin\gamma\right) = 0, \tag{3.115}$$

where $x - X(t) = A(t)\cos\gamma$, $y - Y(t) = B(t)\sin\gamma$ for $-\pi < \gamma \leq \pi$ parametrises (3.114). Hence for a given U, θ_0, α, β, the critical time, t_c at which breakdown first occurs on the turnover curve is

$$t_c = \min_{\gamma} \frac{\alpha\beta}{4U^2} \frac{1}{\left(\beta\cos\gamma\cos\theta_0 + \alpha\sin\gamma\sin\theta_0\right)^2}. \tag{3.116}$$

In order to find the time of breakdown, we must minimise the right-hand side of (3.116) with respect to γ. At a critical point of the right-hand side of (3.116), we require

$$\tan\gamma = \frac{\alpha}{\beta}\tan\theta_0, \tag{3.117}$$

which uniquely determines the value of γ at which the function takes its minimum value, this value of γ being in the range $-\pi \leq \gamma \leq \pi/2$ due to the restriction we made on θ_0. If we now relate γ to the polar angle θ, we note that

$$\tan\theta = \frac{B(t)}{A(t)}\tan\gamma = \frac{\beta}{\alpha}\tan\gamma.$$

Hence, even though the impactor is axisymmetric, breakdown occurs at $\theta = \theta_0 - \pi$, the direction opposite the motion. This is a correction to the conclusion in Moore et al. (2012), since they compare θ_0 to γ, as opposed to the true polar angle, θ.

3.2.4 Splash sheet

The three-dimensional oblique splash sheet problem is a generalisation of the normal-impact solution that we described in §2.3.5. In the notation of §2.3.5, the jet thickness, $\bar{h}(x, y, t)$ and x-, y-components of jet velocity $\bar{u}(\bar{x}, \bar{y}, t)$, $\bar{v}(x, y, t)$ satisfy in the lab frame, at leading order, the zero-gravity shallow water equations:

$$\frac{\partial\bar{h}}{\partial t} + \frac{\partial}{\partial x}\left(\bar{u}\bar{h}\right) + \frac{\partial}{\partial y}\left(\bar{v}\bar{h}\right) = 0, \tag{3.118}$$

$$\frac{\partial\bar{u}}{\partial t} + \bar{u}\frac{\partial\bar{u}}{\partial x} + \bar{v}\frac{\partial\bar{u}}{\partial y} = 0, \tag{3.119}$$

$$\frac{\partial\bar{v}}{\partial t} + \bar{u}\frac{\partial\bar{v}}{\partial x} + \bar{v}\frac{\partial\bar{v}}{\partial y} = 0. \tag{3.120}$$

We show in Appendix A that (3.118)–(3.120) are the leading-order equations governing the evolution of the splash sheet even if the frame is accelerating, that is $\ddot{X}(t) \neq 0$ or $\ddot{Y}(t) \neq 0$), provided the components of acceleration are of order unity as $\varepsilon \to 0$.

The boundary data for (3.118)–(3.120) on the turnover curve are given by

$$(\bar{u}, \bar{v}) \cdot \mathbf{n} = 2v_n, \quad \bar{h} = \frac{\pi S^2}{16 v_n^2} \quad \text{at} \quad t = \omega(x - X(t), y - Y(t)), \tag{3.121}$$

where $\mathbf{n}$ is the outward-pointing unit normal to the turnover curve and S is the coefficient of the square-root term in the expansion of the leading-order-outer velocity potential as we approach the turnover curve, as defined in (3.90).

3.2.4.1 Axisymmetric solution

For axisymmetric impactors, we solve (3.118)–(3.120) using the method of characteristics subject to the boundary data (3.121). Using (3.90), the boundary data are given by

$$\bar{u} = 2v_n \cos\theta, \quad \bar{v} = 2v_n \sin\theta, \quad \bar{h} = \frac{\pi\chi'(d(s),s)^2}{8d(s)}, \tag{3.122}$$

on the boundary curve

$$x = X(s) + d(s)\cos\theta, \quad y = Y(s) + d(s)\sin\theta, \tag{3.123}$$

in which $s > 0$ parametrises time, $0 \leq \theta < 2\pi$ parametrises the angle around the turnover curve, $\chi(\sigma, t)$ is given by (3.85) and v_n is given by (3.89).

Let $\tau \geq 0$ parametrise time-of-travel along a characteristic. The characteristics are given by particle paths, and we deduce that $\bar{u}, \bar{v}$ and subsequently $\bar{h}$ are given by

$$\bar{u} = 2v_n\cos\theta,\ \bar{v} = 2v_n\sin\theta,\ \bar{h} = \frac{\pi\chi'(d(s),s)^2}{8d(s)}\frac{J(0,\theta,s)}{J(\tau,\theta,s)}, \tag{3.124}$$

where

$$t = \tau + s, \quad x = X(s) + (2v_n\tau + d(s))\cos\theta, \quad y = Y(s) + (2v_n\tau + d(s))\sin\theta \tag{3.125}$$

and the Jacobian, $J(\tau, \theta, s)$, is given by

$$\begin{aligned} J(\tau,\theta,s) \;=\; & -4v_n\frac{\partial v_n}{\partial s}\tau^2 + 2\left(2v_n^2 - \dot{d}(s)v_n - d(s)\frac{\partial v_n}{\partial s}\right. \\ & \left. -\dot{X}\left(v_n\cos\theta + \frac{\partial v_n}{\partial\theta}\sin\theta\right) + \dot{Y}\left(\cos\theta\frac{\partial v_n}{\partial\theta} - v_n\sin\theta\right)\right)\tau + v_n d(s). \end{aligned}$$

For the solution to be valid, we require the Jacobian to be bounded and nonzero for all $\tau,\ s > 0$ and $0 \leq \theta < 2\pi$, and $\bar{h} > 0$. On the turnover curve, that is at $\tau = 0$, we see that $J(0,\theta,s) = v_n d(s)$. Hence, if the outward normal speed of the turnover curve vanishes, the Jacobian at that point also vanishes. Moreover, $(\bar{u}, \bar{v}) = 0$ at the point of breakdown on the turnover curve if v_n vanishes. Therefore, as in two-dimensions, at breakdown there is no fluid entering the splash sheet from the inner region and hence the solution in the splash sheet is no longer valid for reasons discussed in §3.1.5. We shall illustrate this breakdown with two examples.

3.2.4.2 Splash sheet generated by an obliquely impacting cone

Firstly, we return to the impact of the cone, which is given by $z = r - t$, where we recall that

$$r = \sqrt{(x - X(t))^2 + (y - Y(t))^2}.$$

We consider the specific example in which the oblique components of impact velocity are given by $X(t) = Ut$ and $Y(t) = 0$ respectively, where $U > 0$. The turnover curve is defined by $r = 4t/\pi$. The solution for the thickness of the splash sheet is given by

$$\bar{h} = \frac{s}{8} \frac{\mathrm{J}(0, \theta, s)}{\mathrm{J}(\tau, \theta, s)}, \tag{3.126}$$

where

$$\mathrm{J}(\tau, \theta, s) = \left(\frac{32}{\pi^2} + \frac{16U}{\pi} \cos\theta + 2U^2 \right) \tau + \frac{4s}{\pi} \left(\frac{4}{\pi} + U \cos\theta \right). \tag{3.127}$$

Now, given that $\tau, s, U \geq 0$, it is evident that

$$\min_{\theta} \mathrm{J}(\tau, \theta, s) = \mathrm{J}(\tau, \pi, s) = 2 \left(\frac{4}{\pi} - U \right)^2 \tau + \left(\frac{4}{\pi} - U \right).$$

Therefore, we must have that $\mathrm{J}(\tau, \theta, s) > 0$ for all $\tau, s > 0, 0 \leq \theta < 2\pi$ when $0 \leq U < 4/\pi$. When $U = 4/\pi$, $\mathrm{J}(\tau, \pi, s) = 0$ and the solution breaks down.

To determine the manner of the breakdown, we consider the touchdown curve, that is the tip of the splash sheet, which is thrown out at time $t = 0$. In the above solution, this corresponds to the curve of points for which $\bar{h} = 0$. We find that

$$x = 2t \cos\theta \left(U \cos\theta + \frac{4}{\pi} \right), \; y = 2t \sin\theta \left(U \cos\theta + \frac{4}{\pi} \right) \tag{3.128}$$

gives the equation of the touchdown curve parametrically. In particular, when $U = 0$, we recover from (3.128) the circular touchdown curve

$$x^2 + y^2 = 4d(t)^2,$$

consistent with the analysis in §2.3.6.1. For $U = 4/\pi$, (3.128) represents the cardioid

$$x = \frac{4t}{\pi} \left(\cos 2\theta + 2\cos\theta + 1 \right), \; y = \frac{4t}{\pi} \left(\sin 2\theta + 2\sin\theta \right),$$

with a cusp at $\theta = \pi$. For all intermediate values of U, the touchdown curve is a limaçon.

To help visualise the breakdown, we plot the splash sheet for different values of U in Figure 3.8. Since the cone admits a similarity solution in which distance scales

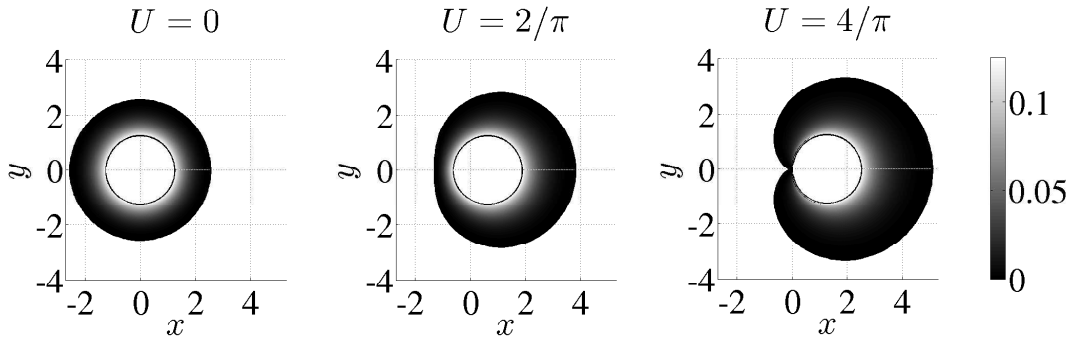

Figure 3.8: Cone splash sheet at $t = 1$ for $U = 0, 2/\pi, 4/\pi$ (from left to right). The plots represent a top-down view of the splash sheet between the touchdown curve and turnover curve. In each plot, the shading represents the thickness of the splash sheet. This plot is based on one in Moore et al. (2012).

linearly with time, t, it is sufficient to plot at one instant only. In Figure 3.8 we therefore plot the solution with $t = 1$.

In Figure 3.8 we see the formation of the limaçon. As we reach the critical value of U, a cusp forms on the touchdown curve, touching the turnover curve on the ray $\theta = \pi$. Thus, when the splash sheet stops advancing on this ray, the small-aspect-ratio assumption that we made when deriving the splash sheet equations breaks down. We can check this result as follows: from (3.128), the extent of the splash sheet along the ray $\theta = \pi$ is given by

$$|-2t\,(-U + 4/\pi) - (Ut - 4t/\pi)| = t\,|U - 4/\pi|\,.$$

The maximum thickness of the splash sheet along that ray is on the turnover curve (cf. Figure 3.8) and is equal to $t/8$. Hence, as $U \uparrow 4/\pi$, the aspect ratio blows up. This breakdown is analogous to that found in the oblique entry of a two-dimensional wedge with small deadrise angle.

3.2.4.3 Splash sheet generated by an obliquely impacting blunt profile

We consider a general smooth axisymmetric profile $z = r^n - t$, where $n > 1$, with $X(t) = Ut$ and $Y(t) = 0$, where $U > 0$. The turnover curve is given by (3.102). Moreover, we note that the outward normal speed of the turnover curve, (3.103), can

be written as

$$v_n = \frac{d(s)}{ns} + U\cos\theta.$$

In particular, requiring $v_n > 0$ on $\theta = \pi$, the condition that the turnover curve is advancing on this ray, gives

$$\frac{d(s)}{ns} > U.$$

At breakdown, equality holds in the above statement.

Using (3.124)–(3.125), the splash sheet solution for an obliquely impacting blunt profile is given by

$$x = (2v_n\tau + d(s))\cos\theta + Us, \tag{3.129}$$

$$y = (2v_n\tau + d(s))\sin\theta, \tag{3.130}$$

$$\bar{h} = \frac{1}{\pi}n^2 s^{2-1/n}\left(\mathrm{B}\left(\frac{n+2}{2},\frac{n+2}{2}\right)\right)^{1/n}\frac{\mathrm{J}(0,\theta,s)}{\mathrm{J}(\tau,\theta,s)}, \tag{3.131}$$

where $0 < s < t_c$, $0 \le \tau < t_c$, $0 \le \theta < 2\pi$, t_c is given in (3.104) and the Jacobian may be written in the form

$$\begin{aligned}\mathrm{J}(\tau,\theta,s) =& \frac{4(n-1)}{n^2s^2}d(s)\left(\frac{d(s)}{ns} + U\cos\theta\right)\tau^2 + \\ & 2\left(\left(\frac{d(s)}{ns} + U\cos\theta\right)^2 + \frac{(n-1)d(s)^2}{n^2s^2}\right)\tau + d(s)\left(\frac{d(s)}{ns} + U\cos\theta\right).\end{aligned} \tag{3.132}$$

It is straightforward to show that the Jacobian is bounded for all $0 < s < t_c$, $0 \le \tau < t_c$, $0 \le \theta < 2\pi$, and while $v_n > 0$, it is clear that the coefficient of each of the τ^2-, τ-, τ^0-terms in (3.132) is positive for $n > 1$. Therefore, the Jacobian is nonzero for all $0 < s < t_c$, $0 \le \tau < t_c$, $0 \le \theta < 2\pi$ and the solution is valid.

At breakdown, $\theta = \pi, s = t_c$, leaving

$$\mathrm{J}(\tau,\pi,t_c) = 2U^2(n-1)\tau.$$

So we see that the Jacobian vanishes on the turnover curve at $\theta = \pi$. Moreover, the characteristics are given by particle paths, viz.

$$\frac{\partial x}{\partial\tau} = \bar{u},\ \frac{\partial y}{\partial\tau} = \bar{v},\ \frac{\partial t}{\partial\tau} = 1.$$

At breakdown, we have $\bar{u} = \bar{v} = 0$ on the turnover curve at $\theta = \pi$. Hence, the characteristics are parallel to the turnover curve at $\theta = \pi$. There is no longer any fluid entering the splash sheet at this point, the same as for the breakdown of the oblique entry of a two-dimensional symmetric parabola, as discussed in §3.1.5.2.

3.2.5 Breakdown and cavitation

The conclusions drawn in §3.1.6 extend to three-dimensional oblique impacts as the linear stability analysis described in §2.2.11.3 is local in space and time. Hence, when the turnover curve is no longer advancing, the problem becomes unstable. Moreover, there is a lack of causality in the leading-order-outer problem and we cannot solve for the free surface.

We showed that the coefficients of the square-root singularities in the leading-order-outer velocity and pressure, (3.90)–(3.91), vanish at breakdown. Hence, the Wagner asymptotic structure breaks down when the turnover curve stops advancing. Moreover, we can no longer solve the splash sheet problem, since the characteristics are parallel to the turnover curve at breakdown. This is because there is no longer fluid entering the splash sheet from the inner region. In the particular example of a constant-speed cone impact, we showed that the small-aspect-ratio assumption made in the derivation of the splash sheet problem becomes invalid at breakdown.

As in two-dimensional oblique impacts, we saw regions of negative pressure forming on the impactor before breakdown (see Figures 3.6 and 3.7). Breakdown coincided with the contour of zero pressure touching the turnover curve. However, it is possible that cavitation occurs before the turnover curve stops advancing. In particular, we could see a patch cavity forming in the region of negative pressure. This would make the problem somewhat more complex. The model presented in Appendix B is a possible way to incorporate cavitation before breakdown in the Wagner asymptotic regime. We do not consider ideas of cavitation any further here, but we state that the above analysis is carried out under the assumption that there is no cavitation on the impactor prior to breakdown. This is an area that requires further investigation.

3.2.6 Summary

In this section, we generalised Wagner theory for three-dimensional normal impacts to oblique impacts in which the oblique component of the impact velocity has magnitude on the order of the inverse of the deadrise angle. As in two dimensions, transforming the leading-order-outer potential problem using the displacement potential made the problem much more tractable. By making a change of variables in the displacement potential formulation, we could reduce the problem to the corresponding normal impact problem. Hence, given a solution for the leading-order location of turnover curve projection, leading-order-outer free surface and leading-order displacement potential in the normal impact of a body $z = f(x, y) - t$, we are able to write down the leading-order turnover curve projection, leading-order-outer free surface and leading-order

displacement potential for the oblique entry of the same body profile.

We looked at the case of axisymmetric oblique impact in more detail. In particular, we highlighted the possibility of breakdown occurring when the outward normal speed of the turnover curve vanishes. If this occurs, an instability would arise in a neighbourhood of the retreating turnover curve and our theory would break down. More importantly we are no longer able to solve for the leading-order-outer free surface if the turnover curve is retreating. These properties of breakdown are analogous to those seen due to a retreating turnover point in two-dimensional oblique impact problems. Moreover, the coefficients of the inverse square-root singularities in the leading-order-outer velocity and pressure vanish at the point of breakdown on the turnover curve. This indicates a breakdown of the asymptotic structure.

We looked at two specific examples of axisymmetric impacts with a constant oblique speed in the x-direction. For an obliquely impacting cone, which has a similarity solution, we find that provided the oblique speed is less than a critical value the solution remains valid for all time. However, at this critical value, the theory breaks down at $t = 0^+$. For a general smooth axisymmetric body, there exists a finite time at which the outward normal speed of the turnover curve vanishes for any nonzero oblique speed.

In both the case of a cone and a paraboloid, we studied the leading-order-outer pressure on the body and noted that regions of negative pressure form prior to breakdown. These regions grow in size as we approach breakdown and the contour of zero pressure on the impactor touches the turnover curve at breakdown. There is the possibility that cavitation occurs prior to breakdown, but we did not consider this further here. We saw similar behaviour in the two-dimensional impact of a wedge and parabola.

Assuming that cavitation does not occur, we investigated the splash sheet problem. For the case of the cone, the splash sheet has finite extent, terminating on the impactor at the touchdown curve. Whilst the turnover curve is always a circle in the moving frame, for nonzero oblique impact speeds, the touchdown curve is a limaçon with minimum distance from the turnover curve on the ray pointing in the direction opposite the tangential motion. At the critical oblique speed, the touchdown curve becomes a cardioid with the cusp touching the turnover curve, so the small-aspect-ratio assumption in the spray sheet is invalid. The failure of the small-aspect-ratio assumption means there is a nonuniformity in our asymptotic expansion. The nature of the breakdown of the asymptotic structure may benefit from a more careful inspection of the inner and splash sheet regions close to breakdown. This is an open problem that we do not pursue here. In the case of a smooth impactor, the splash

sheet is thrown out to infinity at the moment of impact, so the idea of a touchdown curve does not apply. As we approach the critical time, the fluid entering the jet at the turnover curve has vanishing speed at the point of break down and the theory is no longer valid.

Chapter 4

Air-cushioning in Wagner theory

4.1 Introduction

4.1.1 The role of air before impact

In this chapter we consider the influence of the surrounding gas on Wagner theory. Howison et al. (1991) compare the leading-order pressure profiles predicted by Wagner theory for an impacting parabola with experimental readings of the pressure at various points on the parabola extracted from Nethercote et al. (1986). There is good agreement away from the nose (minimum) of the parabola, but Wagner theory over-predicts the pressure close to the nose, and at the nose itself, the theory predicts an infinite pressure at the instant of impact. The experimental data shows oscillations in the pressure at the minimum point and Howison et al. (1991) posit that the discrepancy between the theory and experiments is due to non-negligible air pressure in the gap or *cushion* between the impactor and the liquid prior to impact.

The idea that the surrounding gas plays in important role before impact is supported by data from drop tests of flat-bottomed bodies and wedges of small deadrise angle presented in Chuang (1967) and Hagiwara and Yuhara (1974). Chuang (1967) only finds significant air entrapment for flat-bottomed bodies and wedges with deadrise angle smaller than about one degree. The empirical data is used to correct the maximum pressure felt on the impactor predicted by Wagner (1932). Hagiwara and Yuhara (1974) also only find significant air entrapment for wedges of deadrise angle smaller than approximately three degrees. Driscoll and Lloyd (1982) present a series of drop tests for flat-bottomed wedges and find that first contact between the body and liquid tends to be at the edge of the flat-bottomed section, with an air pocket trapped between these contact points. They also record a pressure pulse caused by the collapse of the resulting entrapped air pocket.

Verhagen (1967) models the impact of a finite-width flat plate onto a liquid half-space and introduces a one-dimensional compressible air-cushioning layer between the plate and liquid. He solves the resulting problem numerically and finds that the free surface is deformed by the air motion, with a depression under the centre of the plate and bumps towards the tips of the plate (cf. Figure 4.1 replacing the flat-bottomed impactor with a flat plate). Verhagen makes the assumption that, when the air velocity reaches the local sound speed in the gap between these bumps and the plate, the flow chokes: the air velocity no longer increases and is thereafter fixed at the speed of sound. After impact, Verhagen models the trapped air as a cavity whose pressure depends on time only. The pressure on the impactor is then evaluated from this model. Despite several approximations, he finds that the modelling predictions are in reasonable agreement with his own experimental results. Lewison and Maclean (1968) and Lewison (1970) also present experiments on flat-plate impacts and compare their results to numerical solutions of a one-dimensional model of the air flow. Their model is based on empirical assumptions about the air pressure, and as such they can only achieve qualitative agreement with the experimental data and their model is sensitive to the initial conditions they feed into it.

Astley (1974) also considers the impact of a finite-width flat plate and models the air flow as ideal and compressible. Astley makes the assumption that the free surface beneath the plate moves down with a uniform velocity, which is determined as part of the solution. Results are presented for cases in which the compressibility of the water is negligible and non-negligible. Astley finds that the water compressibility is important, as it reduces the maximum pressure on the impactor, giving values closer to the recorded experimental values in Chuang (1967) and Lewison and Maclean (1968). However, the lack of a model for the free surface deformation means that results only qualitatively match the experimental data. Asryan (1979) presents two models for the flow in the air gap before the impact of a flat plate based on the assumption that deflections to the free surface are smaller than the thickness of the gap. His first model assumes the air is ideal and incompressible, and his second assumes the air is viscous and compressible. He solves both of these models numerically and provides an estimate on the time at which the flat plate touches down on the fluid.

It is not until Wilson (1991) that a model for pre-impact air cushioning is systematically derived. Looking at the impact of flat-bottomed body profiles, Wilson assumes that the air layer is ideal and incompressible, and reduces the model to two equations for the horizontal component of the air velocity and the liquid free surface. His model is based on two small parameters: the aspect ratio of the air layer and the density ratio between the air and the liquid. Since one of his equations involves the

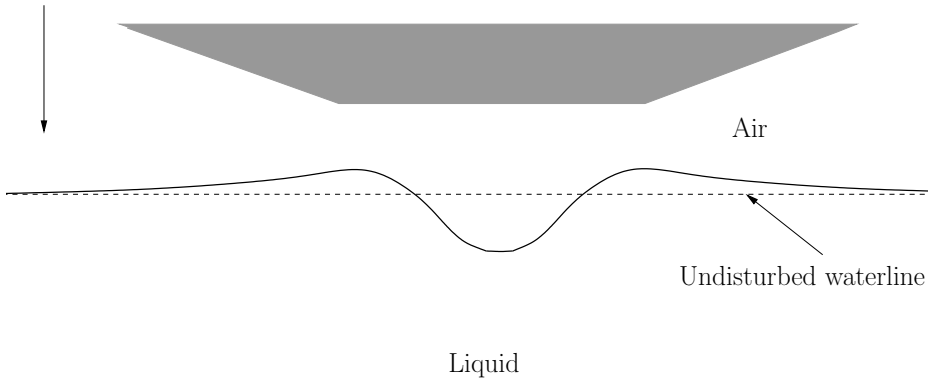

Figure 4.1: Schematic depicting the free surface displacement due to air-cushioning prior to an impact based on work in Wilson (1991).

Hilbert transform of the second time derivative of the free surface location, it is analytically intractable, but Wilson presents asymptotic solutions for small time and for weak coupling through the density ratio, as well as numerical solutions. The model predicts the characteristic rise of the free surface at the edge of the flat-bottomed section of the impactor, with a depression underneath the flat section due to the air carried along with the stagnation point on the body. We give a schematic of the pre-impact picture in Figure 4.1. He states that this behaviour is seen much more starkly with blunter bodies and that, for sharper bodies, such as an impacting wedge, the air can escape more readily from underneath the falling impactor. This corroborates the findings of Chuang (1967) and Hagiwara and Yuhara (1974), who find that air-cushioning is only significant for wedges of deadrise angle smaller than 1-3 degrees. Wilson points out that an inviscid model is only applicable during the initial stages of the motion, with compressibility becoming more important as the air gap thins.

Smith et al. (2003) derive an inviscid liquid-viscous air balance for their model of two-dimensional droplet impact onto a solid surface in the presence of an air-cushioning layer. They derive a critical droplet Reynolds number based on the droplet diameter and impact speed at which the viscous forces in the air become important. The resulting model couples the lubrication equation in the air to a Hilbert integral that describes the inviscid flow in the droplet. Smith et al. (2003) solve this system numerically, and they find similar behaviour to Wilson (1991), with the free surface of the droplet being depressed by the air layer about the line of symmetry and touchdown occurring away from this line. The calculations indicate that the air pressure and speed continue to rise in the narrowing air gap close to touchdown, and the authors note that these rapid increases will lead to compressibility becoming important close

to touchdown.

Korobkin et al. (2008) use a similar model to investigate air-cushioning in shallow-water impact, in which the Hilbert integral is replaced by the inviscid thin-film equations in the liquid. They solve the resulting system numerically and find similar behaviour to the deep-water analysis of Smith et al. (2003); however, due to the simplification of the equation of motion in the liquid in the thin-film regime, Korobkin et al. (2008) are able to make more analytic progress in modelling the touchdown of the free surface at the edges of the trapped air pocket and they find good qualitative agreement with the numerical solution.

Purvis and Smith (2004) introduce surface tension effects to the model of Smith et al. (2003). Initially, the influence of surface tension on the evolution of the liquid free surface is small, but as the free surface of the droplet approaches touchdown with the solid free surface as described in Smith et al. (2003), surface tension slows the free surface down and prevents touchdown entirely. As Purvis and Smith (2004) point out, this inhibition happens at very small length and time scales relative to the droplet diameter and the impact timescale, at which other physical effects may come into play. Vanden-Broeck and Smith (2009) consider surface tension effects in the inviscid air-inviscid liquid regime of Wilson (1991). They seek travelling-wave solutions of the problem, in which the constant scaled speed of the travelling-wave coordinate must be solved for as part of the problem. They present both a weakly nonlinear and nonlinear analysis, and their computations indicate that surface tension inhibits the touchdown of the droplet free surface onto the solid substrate.

4.1.2 Bubble entrapment

The trapped air pocket is of interest in several industrial fields. An entrapped bubble can introduce contaminants to the bulk fluid in a chemical process, or may have an undesirable side effect in printing processes, such as printing polymetric circuits, as discussed in Sirringhaus et al. (2000). On the other hand, small bubbles may be important in boiling as they can act as nucleation sites, speeding up the boiling process. Thus, the role of air-cushioning in impact theory and the size of the resulting entrapped bubble has been of interest to a number of experimentalists.

Leng (2001) illustrates that air-cushioning can lead to free surface deformation in droplet impact experiments. The use of ultra-high-speed cameras allow Thoroddsen et al. (2003) to capture this deformation in detail for droplet impacts onto a pool of the same fluid. They find that the larger the Reynolds number in the air based on the droplet impact speed and diameter, the thinner the initial pocket of trapped air. Moreover, increasing the radius of the drop increases the diameter of the disk

of trapped air, which is consistent with the modelling predictions of Chuang (1967), Hagiwara and Yuhara (1974) and Wilson (1991), who all found that air-cushioning is more appreciable for flatter bodies.

A similar behaviour is found for droplets of very small radius on the order of tens of micrometres in van Dam and Le Clerc (2004). They find that the volume of the entrapped bubble decreases with the impact speed. The experimental data for the entrapped bubble volume matches well with a scaling law derived by balancing the liquid inertia with the lubrication forces in the gas. Thoroddsen et al. (2005) perform further experiments and conclude that there is no link between the Reynolds number of the drop and the initial size of the trapped air layer; the radius of the drop is found to be much more crucial than the impact speed.

Josserand and Zaleski (2003) and Mehdi-Nejad et al. (2003) both find air entrapment in their numerical simulations of drop impact, but are unable to discern much about the behaviour due to the very small lengthscales and timescales involved. Mehdi-Nejad et al. (2003) compare experiments and numerics for the impacts of droplets of water, n-heptane and molten nickel, finding entrapment in all three cases. Hicks and Purvis (2010) and Hicks and Purvis (2011) perform an in-depth theoretical and numerical analysis attempting to derive scaling laws for the size of entrapped air bubbles in both normal and oblique droplet impacts. Hicks and Purvis (2010) extends the inviscid-lubrication model of Smith et al. (2003) to three-dimensional bodies. Numerical simulations for an impacting spherical droplet are used to estimate the volume of the bubble. Their resulting scaling law underpredicts the results in van Dam and Le Clerc (2004) and Thoroddsen et al. (2005), which they attribute to their neglect of air compressibility. The regime in which air compressibility effects are important is discussed in Hicks and Purvis (2011).

4.1.3 The role of air in splashing and spreading

The papers discussed so far in this section have been inspired by the need to understand the influence of air on the force on an impacting body or on the entrainment of a bubble during an impact. However, recent work has indicated that the surrounding gas is also pivotal in the splash mechanism itself. Xu et al. (2005) show that reducing the pressure of the surrounding gas can completely repress splashing in droplet impact on a substrate. For high-velocity impacts, the threshold pressure, at which the droplet spreads as opposed to splashes, is much lower. They suggest that the spreading/splashing regimes are linked to the dominance of one of two stresses on the droplet: stress caused by the air and stress caused by surface tension. The air promotes splashing, whereas surface tension promotes spreading.

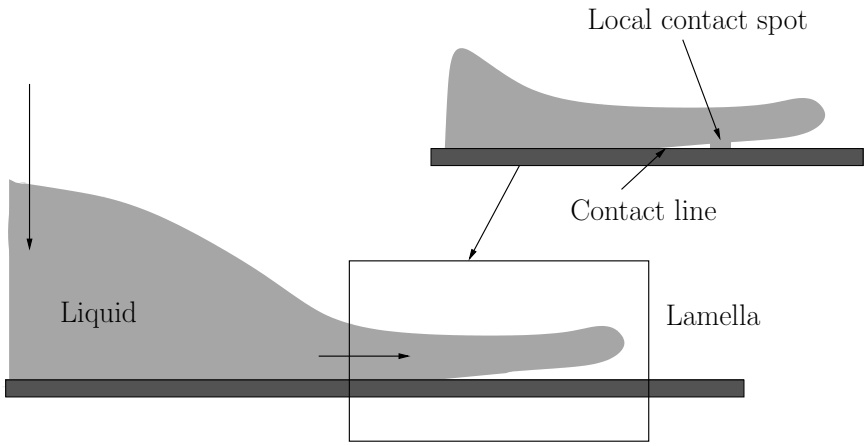

Figure 4.2: Touchdown of the lower free surface of a lamella. The contact line catches up with the wetted patch and entraps an air bubble. This schematic is based on one in Thoroddsen et al. (2010).

Supporting the importance of air in splashing, Rein and Delplanque (2008) link air entrainment under the lamella (a rim of expanding liquid) of a spreading droplet to so-called 'corona splashes' where the lamella lifts off the substrate and can splash. To investigate air entrainment under a lamella, Thoroddsen et al. (2010) use viscous drops of a water/glycerin mixture, so that the Reynolds numbers are on the order of 100-1000. Their experiments show a large number of air bubbles get entrained under the drops as they spread on the solid substrate. Thoroddsen et al. (2010) suggest that the advancing rim of the droplet becomes separated from the substrate and, as a result, the lamella rides on a thin film of air. They then show that air entrainment under the lamella is caused by the liquid surface touching down on the substrate so that a bubble is trapped as the advancing contact line between the lamella and the substrate catches up to this point of touchdown. We depict this mechanism for air entrainment in the schematic in Figure 4.2. Palacios et al. (2012) find similar entrainment of bubbles in water/glycerin droplet impact for Reynolds numbers ranging from 100-2500.

Driscoll et al. (2010) consider higher viscosity droplet experiments. They find that if splashing occurs, an ejecta (or splash sheet) is emitted from the spreading lamella and that this sheet can break up into smaller droplets. The ambient gas is shown to be crucial in the formation of this ejecta sheet, since at low ambient air pressure, no ejecta is emitted from the front of the lamella, cf. Figure 4.3. Moreover, in the splashing regime, air entrainment under the advancing lamella is found to occur, but otherwise they do not see evidence of air bubbles under the lamella. However, they do show that the central air bubble discussed by Thoroddsen et al. (2003) etc.

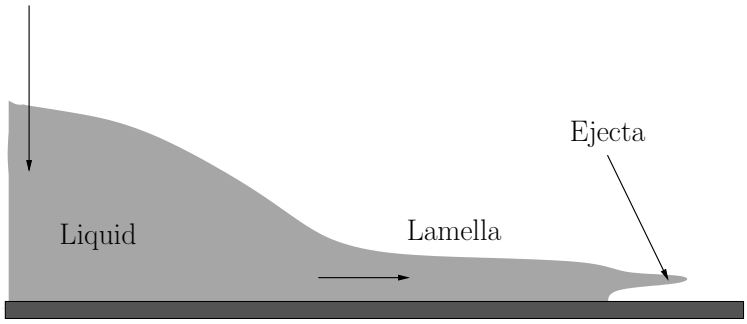

Figure 4.3: Ejection of a thin sheet from the front of a spreading droplet. This schematic is based on the experiments in Driscoll et al. (2010).

(that is, the bubble trapped due to air-cushioning before impact) can be entrapped under the droplet even if the ambient gas pressure is not high enough for splashing to be triggered. Even in cases where bubble entrainment occurs, Driscoll and Nagel (2011) state that the entrainment ceases at a critical lamella speed before the ejecta is emitted. This speed is shown to be independent of impact velocity and the pressure in the surrounding gas. Moreover, Driscoll and Nagel (2011) confirm that no significant air layer underneath the lamella persists until the time at which the ejecta sheet is formed and suggest instead that the air in front of the advancing lamella causes a splash. This conclusion is supported by the results in de Ruiter et al. (2012).

Mandre et al. (2009), Mani et al. (2010) and Mandre and Brenner (2012) argue that a droplet impacting on a solid surface starts to spread on the air-cushioning layer *before* it touches down. The viscous air layer trapped between the impinging droplet and the solid surface transitions from incompressible to compressible as the drop nears touchdown. They argue that the large pressure in this air gap slows the droplet down and that the droplet starts to spread before the layer ruptures. In Mandre and Brenner (2012), they claim that the layer thins to thicknesses on the order of the nanometres and that the continuum model breaks down. They argue that touchdown then occurs and that the boundary layer in the liquid that subsequently forms on the substrate can cause the lamella to lift off and splash. Experimental evidence of the 'skating' stage where the droplet spreads on a very thin layer of air before touching down is given in Kolinski et al. (2012). However, the suggestion that the splash is caused by viscosity in the liquid after touchdown remains unproven.

4.1.4 The role of air post-impact

It is clear that air-cushioning has a role to play post-impact as well as pre-impact, but the theoretical understanding of its post-impact influence is poor. Purvis and Smith

(2004) attempt to extend the inviscid liquid/viscous air model of Smith et al. (2003) to post-impact. Purvis and Smith (2004) assume that, in the absence of surface tension, the model proposed by Smith et al. (2003) before impact eventually touches down. Purvis and Smith (2004) neglect any entrapped air and assume that the liquid is directly in contact with the solid substrate over a finite-width contact set and that, outside of this contact set, the theory of Smith et al. (2003) can be applied in the air sandwiched between the droplet and the solid substrate. The size of the contact set is unknown in advance and must be solved for as a part of the solution. They solve the resulting mixed boundary value problem using the Wiener-Hopf method, which necessitates the introduction of an eigenfunction to get the required behaviour at the contact points, where the free surface is assumed to have a square-root shape. They solve the resulting system numerically and conclude that for weak air motion, the role of the air becomes negligible and the Wagner solution prevails, but for smaller time there is a slight increase in the spread of the droplet.

There are a couple of modelling assumptions in the model of Purvis and Smith (2004) that might play an important role in improving their model. The first is that they do not consider the inner region close to the contact points in detail, although they state that to leading-order the region is likely to be dominated by inertial forces in both the air and liquid. Moreover, they neglect the presence of any jet on the substrate, which will be present according to Wagner theory, and of appreciable length in the outer region. This introduces a continuity of tangential velocity condition on the air flow, as opposed to the no-slip condition applied on the substrate. We will consider both of these points in detail in this chapter, in which we will consider the effect of introducing an air region in leading-order Wagner theory. Like Purvis and Smith (2004), we shall consider the slightly artificial situation in which the role of the air before impact is neglected, and we assume that contact between the impactor and the liquid initiates at a point. Our theory will enable us to investigate the correction to the classical theory due to the surrounding gas. As always in impact theory, given the complexity of the fluid structure and flow changes over small lengthscales and timescales, asymptotic theory is key in providing a basis for numerical solutions of the problem. Our air-cushioning model is a first step in this regard.

4.2 Two-dimensional, small-deadrise impacts

Much of the analysis in this section is based on the work we presented in Moore et al. (2013b). We consider the effects of a cushioning air layer when a rigid impactor enters a liquid half-space that lies in $z^* < 0$; where, as usual, (x^*, z^*) are Cartesian

coordinates centred at the initial point of contact and an asterisk indicates a dimensional variable. At time $t^* = 0$, the impactor is assumed to be touching the liquid half-space, with air filling the region not occupied by the body or the liquid. Both the air and the liquid are assumed to be at rest. We impulsively move the body so that at times $t^* > 0$ its position is given by

$$\frac{z^*}{L} = f\left(\frac{\varepsilon x^*}{L}\right) - \frac{t^*}{T},$$

where L is a characteristic penetration depth and T is the impact timescale The function f, which will be taken to be even for simplicity, is such that $f(0) = 0$ and f increases as $|x^*|$ increases. As in Wagner theory, we will consider profiles for which the deadrise angle is small, corresponding to the dimensionless parameter ε being small. Note that since f is even, the flow will be symmetric about $x^* = 0$.

As in Wagner theory, we assume that the liquid is incompressible, inviscid and initially quiescent, with density ρ_l. For $t^* > 0$, the impactor penetrates the liquid, the free surface is violently disturbed and two splash jets form along the sides of the body. We assume that these splash jets do not separate from the impactor so that the liquid occupies the region depicted in Figure 4.4. We denote the multivalued free surface by $z^* = h^*(x^*, t^*)$. We denote the two turnover points where $\partial h^*/\partial x^*$ is unbounded by $x^* = \pm d^*(t^*)$. For the sake of the analysis in the air region, it is important to consider separately the components of the free surface *above* the turnover point (i.e. the jet), denoted by $z^* = Lf(\varepsilon x^*/L) - (L/T)t^* - h^*_+$, and the free surface *below* the turnover point (i.e. bounding the bulk of the liquid), denoted by $z^* = h^*_-$.

We neglect surface tension and gravity, and our comments in §2.2.1 on whether these assumptions (along with those in the liquid) are reasonable still apply here. We will also assume that the air is ideal and incompressible throughout this chapter, assumptions we shall comment on further in §4.2.2. The air has density ρ_a.

As we saw in §§2.2.10.1–2.2.10.2, Wagner theory predicts that, at leading order in ε, the splash jets are of infinite extent for smooth symmetric two-dimensional impactors for all $t^* > 0$, but touch down in finite distance for a wedge for all $t^* > 0$. That the splash jets extend an infinite distance in zero time for smooth symmetric impactors is clearly unphysical, but this problem has not been resolved in the literature and we do not attempt to do so here. We emphasise that, regardless of whether the splash jets are finite or infinite, the analysis in this chapter pertains only if the jets do not separate from the impactor. However, subject to the aforementioned caveats, for convenience when we write our boundary conditions, we shall define the wetted region to be the part of the impactor in contact with the liquid and the non-wetted region to be the part of the impactor in contact with the air. The problem configurations

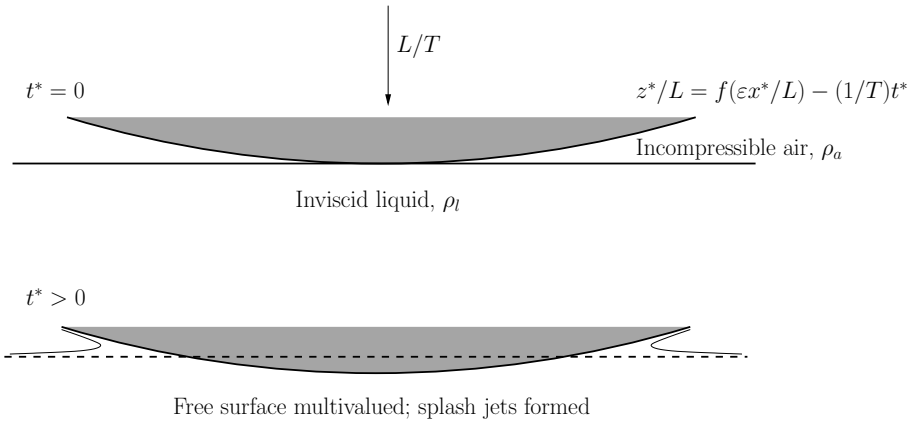

Figure 4.4: The problem configuration before and after impact. This figure is based on one published in Moore et al. (2013b).

for $t^* = 0$ and $t^* > 0$ are illustrated in Figure 4.4.

4.2.1 Dimensionless model

For brevity we shall just state the dimensionless model in this chapter, in which we have nondimensionalised distances with L, time with T, velocities with (L/T), velocity potential with L^2/T and pressure with $\rho_i(L/T)^2$, where $i = a, l$ in the air and liquid respectively. Dimensionless variables are indicated with a prime. The dimensionless body profile is given by

$$z' = f(\varepsilon x') - t'.$$

Hereafter, variables in the air will be represented by an uppercase letter and variables in the liquid will be represented by a lowercase letter. Since the flow in both fluids is initially irrotational, there are velocity potentials in the liquid and air such that $\mathbf{u}' = \nabla\phi'$ and $\mathbf{U}' = \nabla\Phi'$, where $\mathbf{u}'$, $\mathbf{U}$' are the liquid and air velocities respectively. Therefore, the equation of motion in the liquid is given by

$$\nabla^2\phi' = 0. \tag{4.1}$$

Naturally Φ' must satisfy Laplace's equation in the air as well. However, in the majority of this section, it is more useful to use Euler's equations in the air, which

are

$$\frac{\partial U'}{\partial t'} + U'\frac{\partial U'}{\partial x'} + W'\frac{\partial U'}{\partial z'} = -\frac{\partial P'}{\partial x'}, \tag{4.2}$$

$$\frac{\partial W'}{\partial t'} + U'\frac{\partial W'}{\partial x'} + W'\frac{\partial V'}{\partial z'} = -\frac{\partial P'}{\partial z'}, \tag{4.3}$$

$$\frac{\partial U'}{\partial x'} + \frac{\partial W'}{\partial z'} = 0, \tag{4.4}$$

where $\mathbf{U}' = (U', W')$ and P' is the air pressure. The condition of irrotationality in the air is then given by

$$\frac{\partial U'}{\partial z'} - \frac{\partial W'}{\partial x'} = 0. \tag{4.5}$$

On the body, the kinematic conditions on $z' = f(\varepsilon x') - t'$ are given by

$$\frac{\partial \phi'}{\partial z'} = -1 + \varepsilon f'(\varepsilon x')\frac{\partial \phi'}{\partial x'} \quad \text{on the wetted region,} \tag{4.6}$$

$$W' = -1 + \varepsilon f'(\varepsilon x')U' \quad \text{on the non-wetted region,} \tag{4.7}$$

where f' indicates the derivative of f with respect to its argument (not to be confused with the primes on dimensionless variables). The kinematic conditions on the free surface are given by

$$\frac{\partial \phi'}{\partial n'} = \mathbf{U}' \cdot \mathbf{n} = v_{fs} \quad \text{on} \quad z' = h'(x', t'),\ |x'| > d'(t'), \tag{4.8}$$

where v_{fs} is the outward normal speed of, and $\mathbf{n}$ is the outward-pointing normal to, the free surface, and $\partial/\partial n'$ is the outward normal derivative. In the absence of surface tension, the dynamic boundary condition on the free surface is given by

$$p' = \rho P' \quad \text{on} \quad z' = h'(x', t'),\ |x'| > d'(t'), \tag{4.9}$$

where $\rho = \rho_a/\rho_l$ is the density ratio. The fluid pressures p', P' are given by Bernoulli's equation in each fluid:

$$\frac{\partial \phi'}{\partial t'} + p' + \frac{1}{2}\left|\nabla \phi'\right|^2 = 0 \text{ in the liquid,} \quad \frac{\partial \Phi'}{\partial t'} + P' + \frac{1}{2}\left|\mathbf{U}'\right|^2 = 0 \text{ in the air.} \tag{4.10}$$

Initially, we assume that there is no motion in the air or liquid and that the free surface is undisturbed. Therefore,

$$\phi'(x', z', 0) = 0, \quad \mathbf{U}'(x', z', 0) = 0, \quad h'(x', 0) = 0, \quad d'(0) = 0. \tag{4.11}$$

Finally, we require some far-field conditions on the liquid and air velocities. In classical Wagner theory, Mackie (1969) argues that the dynamic boundary condition $p' = 0$ and Bernoulli's equation mean that the flow cannot support a logarithmic singularity

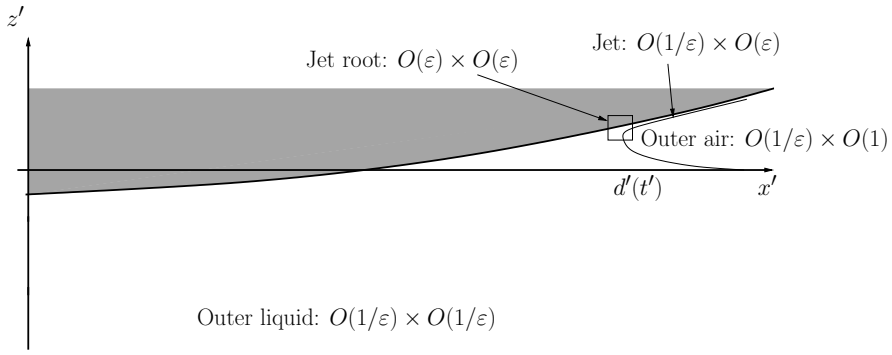

Figure 4.5: Proposed asymptotic structure in the Wagner limit with the inclusion of a cushioning air layer. This figure is based on one in Moore et al. (2013b).

in the velocity potential in the far-field (under the assumption that h' is integrable). However, introducing the air layer, we no longer have this restriction, so we make the apparently conservative assumption that the liquid and air flows are no stronger than sources with unknown strengths Q_1, Q_2 respectively, so that

$$\phi' = \frac{Q_1(t')}{\pi} \log r' + o(1) \quad \text{as} \quad r' = (x'^2 + y'^2)^{1/2} \to \infty, \tag{4.12}$$

$$\Phi' = \frac{Q_2(t')}{\pi} \log r' + o(1) \quad \text{as} \quad r' = (x'^2 + y'^2)^{1/2} \to \infty, \tag{4.13}$$

with the $o(1)$ terms representing dipoles.

4.2.2 Asymptotic structure

We now propose the asymptotic structure illustrated in Figure 4.5 for the small deadrise angle regime in which $0 < \varepsilon \ll 1$. We assume in our analysis that the density ratio, ρ, is also small. We base this structure on that for classical Wagner theory discussed in §2.2.3. Thus, we expect the free surface to turn over in two small jet-root regions (the turnover regions) of size of $O(\varepsilon) \times O(\varepsilon)$ on the body, as in classical Wagner impacts. The liquid is ejected from this region into a long, thin jet on the body of thickness of $O(\varepsilon)$ and whose thickness varies over distances of $O(1/\varepsilon)$. At leading order, the main bulk of the liquid does not see the jet and acts as if it were being loaded by an expanding plate whose size is the same as the distance between the turnover points, which is of $O(1/\varepsilon)$.

On a horizontal lengthscale of $O(1/\varepsilon)$ and vertical lengthscale of $O(1)$, the air layer is situated between the free surface of the outer liquid region and the jet/body, as well as filling the cavity in the inner region. Other configurations are certainly possible, but we do not propose any here.

4.2.2.1 Modelling assumptions in the air

We will now return to our assumptions in the air layer. The assumption that the air is incompressible reduces to the requirement that the Mach number in the air is small. Since the velocity scale is comparable to the turnover point speed, $L/(\varepsilon T)$, this means that we require

$$\mathrm{Ma} = \frac{L}{c_a T} \ll \varepsilon,$$

where $c_a = 3 \times 10^2$ ms^{-1} is the speed of sound in air. In general, this condition is readily satisfied. Returning to the example in §2.2.1 taken from the droplet impact experiments in Thoraval et al. (2012), the first snapshots in their experiments are captured at time 10^{-5} s, where the penetration depth is on the order of 10^{-4} m. Hence Ma $\approx 10^{-3}$, so that our assumption of air incompressibility seems reasonable provided that ε is not too small.

Recall that we also assumed that the air is inviscid. In the outer air region, the above asymptotic structure dictates that free surface deflections will be of $O(1)$, so that the vertical component of velocity in the air will also be of $O(1)$. Hence by the continuity equation, the tangential component of velocity is of $O(1/\varepsilon)$. Suppose we were to consider the full Navier-Stokes equations in the air, with Reynolds number given by

$$\mathrm{Re}_a = \frac{L^2}{T\nu_a},$$

where $\nu_a \approx 10^{-5}$ m^{2}s^{-1}. Then, using the above argument about the size of the velocity components, the largest viscous terms in the air are of $O(1/(\varepsilon \mathrm{Re}_a))$ where as the inertial terms in the air are of $O(1/\varepsilon)$. Hence, we can neglect the viscous terms provided that the Reynolds number in the air is large. Using the same values for L and T as in the example from Thoraval et al. (2012), we find that

$$\mathrm{Re}_a \approx 10^2,$$

so our assumption is reasonable. We can make a similar argument in the inner air region.

4.2.3 Leading-order-outer scalings

In the liquid region, we apply the Wagner scalings of §2.2.4 by writing

$$(x', z') = \frac{1}{\varepsilon}(x, z), \quad d' = \frac{1}{\varepsilon} d, \quad \phi' = \frac{1}{\varepsilon}\phi, \quad p' = \frac{1}{\varepsilon} p, \quad h'_- = h, \quad t' = t.$$

In the air region, the near flatness of the impactor means that there is an order of magnitude difference between horizontal and vertical lengthscales. Hence, we scale

$$x' = \frac{1}{\varepsilon}x, \quad z' = \hat{z}, \quad U' = \frac{1}{\varepsilon}U, \quad W' = W, \quad P' = \frac{1}{\varepsilon^2}P, \quad h'_+ = \varepsilon h_+.$$

Under these scalings, the dynamic boundary condition on the lower free surface becomes

$$p = \lambda P, \tag{4.14}$$

where $\lambda = \rho/\varepsilon$. This key parameter is a measure of the relative importance of the density difference between the air and liquid, and the flatness of the body profile characterised by the deadrise angle. In the current analysis, we shall assume that $\lambda = O(1)$.

4.2.4 Leading-order-outer air region

By symmetry, we need only consider the air layer for $x > d(t)$. We assume that the jet does not separate from the impactor. Since the jet is thin, to leading-order the outer air region simply sees the outward-normal velocity of the body. After using the scalings given in §4.2.3 and expanding (4.2)–(4.5), (4.7)–(4.8) in powers of ε, the leading-order problem is given by

$$\left(\frac{\partial U_0}{\partial t} + U_0\frac{\partial U_0}{\partial x}\right) + W_0\frac{\partial U_0}{\partial \hat{z}} = -\frac{\partial P_0}{\partial x}, \tag{4.15}$$

$$0 = -\frac{\partial P_0}{\partial \hat{z}}, \tag{4.16}$$

$$\frac{\partial U_0}{\partial x} + \frac{\partial W_0}{\partial \hat{z}} = 0, \tag{4.17}$$

$$\frac{\partial U_0}{\partial \hat{z}} = 0, \tag{4.18}$$

for $x > d_0(t)$, $h_0(x,t) < \hat{z} < f(x) - t$. Here a subscript zero denotes a leading-order variable. On the body the kinematic condition is given by

$$W_0 = -1 + f'(x)U_0 \quad \text{on} \quad \hat{z} = f(x) - t, \ x > d_0(t), \tag{4.19}$$

while on the free surface the kinematic condition is given by

$$W_0 = \frac{\partial h_0}{\partial t} + U_0\frac{\partial h_0}{\partial x} \quad \text{on} \quad \hat{z} = h_0(x,t), \ x > d_0(t). \tag{4.20}$$

The dynamic boundary condition on $\hat{z} = h_0(x,t)$ is given by (4.14).

It is straightforward to deduce that (4.18) forces $U_0(x,\hat{z},t) = U_0(x,t)$. Similarly, (4.16) forces $P_0(x,\hat{z},t) = P_0(x,t)$. Thus, from (4.15), it follows that

$$\frac{\partial U_0}{\partial t} + U_0\frac{\partial U_0}{\partial x} = -\frac{\partial P_0}{\partial x} \quad \text{for} \quad x > d_0(t). \tag{4.21}$$

Moreover, we can integrate the leading-order form of (4.17) across the air layer and apply (4.19)–(4.20) to deduce the usual squeeze-film conservation equation

$$\frac{\partial}{\partial t}\left(f(x)-t-h_0\right)+\frac{\partial}{\partial x}\left(\left(f(x)-t-h_0\right)U_0\right)=0 \quad \text{for} \quad x>d_0(t). \tag{4.22}$$

We require boundary and initial conditions on both h_0 and U_0 to solve (4.21)–(4.22). We assume that the initial conditions are given by

$$h_0(x,0)=0, \quad U_0(x,0)=0. \tag{4.23}$$

It will transpire from matching with the inner region that the appropriate boundary condition on the free surface is simply given by the Wagner condition

$$h_0(d_0(t),t)=f(d_0(t))-t \tag{4.24}$$

The second matching condition is that there is no flux of air into the turnover point, so that we require

$$U_0(d_0(t),t)=\dot{d}_0(t). \tag{4.25}$$

To show that these are indeed the correct conditions, we shall delay considering the leading-order-outer liquid region until we have described both the inner and jet regions in detail.

4.2.5 Inner & jet region scalings

The behaviour of the liquid jets, as well as that of the air and liquid in the turnover region will be important in the leading-order-outer theory in a sense that will be made more precise shortly. Therefore, we shall consider the scalings in these regions briefly before turning to the outer problem. By symmetry, we shall only consider the right-hand jet root and jet.

4.2.5.1 Turnover region

In the liquid, we apply the Wagner scalings as given in §2.2.5. Thus, we move to a travelling-wave frame based on the turnover point, writing:

$$x'=\frac{d(t)}{\varepsilon}+\varepsilon\bar{x} \quad z'=(f(d(t))-t)+\varepsilon\bar{z}, \quad \phi'=\dot{d}(t)\bar{x}+\bar{\phi}, \quad p'=\frac{1}{\varepsilon^2}\bar{p}, \tag{4.26}$$

where the velocity potential scale accounts for the moving frame. As usual, a dot indicates differentiation with respect to time. In the inner region, the multivalued free surface is given by $\bar{z}=\bar{h}(\bar{x},t)$, where

$$h'=(f(d(t))-t)+\varepsilon\bar{h}. \tag{4.27}$$

The kinematic condition (4.8) implies that the pertinent scaling for the velocity potential in the air is given by

$$\Phi' = \dot{d}(t)\bar{x} + \bar{\Phi}. \tag{4.28}$$

Thus, from Bernoulli's equation, (4.10), the pressure scale in the air is given by

$$P' = \frac{1}{\varepsilon^2}\bar{P}. \tag{4.29}$$

Therefore, from (4.9), (4.26) and (4.29), we deduce that the dynamic boundary condition in the inner region is given by

$$\bar{p} = \rho\bar{P}. \tag{4.30}$$

Hence, as we are assuming that the density ratio is small in our analysis (as we saw in §4.2.3, we are in particular considering the distinguished limit in which $\rho = O(\varepsilon)$) we deduce that to leading order in ε, the dynamic boundary condition in the turnover region is given by $\bar{p} = 0$. Using this condition, it is straightforward to show that, to leading order, the flow in the liquid collapses directly to the standard Helmholtz flow as presented for Wagner theory in §2.2.5. Furthermore, the upper branch of the free surface, denoted by $\bar{h}_0$ to leading order, asymptotes to $\bar{h}_0 \sim -J(t)$ as $\bar{x} \to \infty$ for some thickness $J(t)$, which in theory can be determined by matching the inner region solution to the outer region in the liquid. The lower branch of the free surface asymptotes to $\bar{h}_0 \sim -4\sqrt{J(t)/\pi}\sqrt{\bar{x}}$ as $\bar{x} \to \infty$. In particular, this means that the outer velocity potential and outer free surface must have square-root behaviour at leading order as we approach the turnover points in the outer problem. Moreover, we were correct to state the Wagner condition (4.24) must hold.

Hence, to leading order the liquid flow decouples from that of the air. Therefore, the leading-order-inner air problem is given by

$$\nabla^2\bar{\Phi} = 0, \tag{4.31}$$

solved in the cavity, which has $\bar{h}_0$ as its boundary. On this boundary, we require

$$\frac{\partial\bar{\Phi}_0}{\partial\bar{z}} = \frac{\partial\bar{h}_0}{\partial\bar{x}}\frac{\partial\bar{\Phi}_0}{\partial\bar{x}} \quad \text{or} \quad \frac{\partial\bar{\Phi}_0}{\partial\bar{n}} = 0 \quad \text{on} \quad \bar{z} = \bar{h}_0. \tag{4.32}$$

Since we subtracted the velocity due to the moving frame from Φ_0, the appropriate far-field condition is given by

$$\frac{\partial\bar{\Phi}_0}{\partial\bar{x}} \to 0 \quad \text{as} \quad \bar{x} \to \infty. \tag{4.33}$$

Therefore, up to an arbitrary constant, the unique solution to the inner region problem is given by

$$\bar{\Phi}_0 = 0. \tag{4.34}$$

Hence, the flow in the inner region is entirely due to the moving frame, so that the matching condition for the tangential component of air velocity in the outer region is exactly as given in (4.25).

4.2.5.2 Jet

Assuming that the jet does not separate from the impactor, we can make the standard Wagner scalings in the jet, as given in §2.2.8, so that the liquid pressure is scaled by

$$\frac{\rho_l L^2}{\varepsilon^2 T^2}.$$

The relevant scale for the air pressure is given in §4.2.3, namely $\rho_a L^2/(\varepsilon^2 T^2)$. In that section, we assumed that $\lambda = O(1)$ on the free surface, which is equivalent to saying

$$\frac{\rho_a L^2}{\varepsilon^2 T^2} \sim \frac{\rho_l L^2}{\varepsilon T^2}.$$

Since the pressure scale is an order of magnitude larger in the jet, the air flow does not affect the jet to leading order, which is therefore governed by the zero-gravity shallow water equations, as described in §2.2.8. However, corrections to the leading-order jet flow are now dominated by the suction pressure exerted by the air and this may promote jet separation. The physics governing the onset of separation remains an open question that we do not pursue any further here. Under the assumption that the jet does not separate, the jet does not affect the leading-order-outer flow in the air described in §4.2.4. We now return to our considerations of the outer region.

4.2.6 Leading-order-outer liquid problem

As in the case of oblique water entry, it is easiest to consider the liquid problem by introducing the leading-order displacement potential,

$$\Upsilon_0(x, z, t) = -\int_0^t \phi_0(x, z, \tau)\, \mathrm{d}\tau. \tag{4.35}$$

Under the scalings given in §4.2.3 and using the Wagner conditions

$$h_0(\pm d_0(t), t) = f(\pm d_0(t)) - t, \tag{4.36}$$

the leading-order form of (4.1), (4.6)–(4.12) is that depicted in Figure 4.6, in which we have set $\zeta = x + \mathrm{i}z$. The function $\mathcal{F}_0(x, t)$ represents the leading-order influence

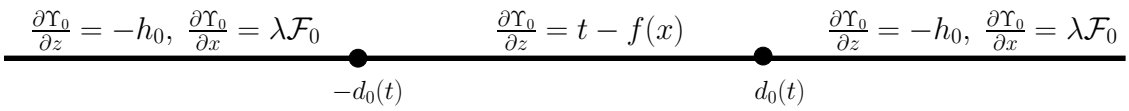

Figure 4.6: Leading-order problem for the displacement potential, Υ_0. In addition, in the far field we require $\Upsilon_0 = O(\log r)$ as $r \to \infty$ and we also require the free surface to be integrable. The smoothing effect of the integral in (4.35) means that we require $\Upsilon_0 = O\left(|\zeta \mp d_0(t)|^{3/2}\right)$ as $\zeta \to \pm d_0(t)$.

of the air layer on the liquid flow, and is defined by

$$\frac{\partial^2 \mathcal{F}_0}{\partial t^2} = \frac{\partial P_0}{\partial x}. \tag{4.37}$$

We can integrate this expression twice with respect to time, which introduces two functions of integration, $A(x)$, $B(x)$. Since $\partial \Upsilon_0 / \partial x = \lambda \mathcal{F}_0$ on the free surface, we know that

$$\frac{\partial \Upsilon_0}{\partial x} = \lambda \left[A(x)t + B(x) + \int_0^t \int_0^s \frac{\partial P_0}{\partial x} \, \mathrm{d}\tau \mathrm{d}s \right]. \tag{4.38}$$

At $t = 0$, Υ_0 and hence its derivative with respect to x vanish, so that $B(x) = 0$. Furthermore, since $\phi_0 = 0$ initially, $\partial \Upsilon_0 / \partial t = 0$ at $t = 0$, and hence $A(x) = 0$. Thus,

$$\mathcal{F}_0 = \int_0^t \int_0^s \frac{\partial P_0}{\partial x}(x, \tau) \, \mathrm{d}\tau \mathrm{d}s. \tag{4.39}$$

The function $\mathcal{F}_0$ is odd in x by the symmetry of the problem. Henceforth, we shall drop the subscripts denoting the leading-order variables.

The problem for the complex derivative of the displacement potential displayed in Figure 4.6 is of Riemann-Hilbert type, with index -1, since we require boundedness at the two turnover points. The solution is

$$\begin{aligned} \frac{\partial \Upsilon}{\partial x} - \mathrm{i} \frac{\partial \Upsilon}{\partial z} \quad = \quad & -\frac{\mathrm{i}\sqrt{\zeta^2 - d^2}}{\pi} \left[\int_{-\infty}^{-d} \frac{\lambda \mathcal{F}(\xi, t)}{\sqrt{\xi^2 - d^2}(\xi - \zeta)} \, \mathrm{d}\xi \right. \\ & \left. - \int_{-d}^{d} \frac{t - f(\xi)}{\sqrt{d^2 - \xi^2}(\xi - \zeta)} \, \mathrm{d}\xi - \int_{d}^{\infty} \frac{\lambda \mathcal{F}(\xi, t)}{\sqrt{\xi^2 - d^2}(\xi - \zeta)} \, \mathrm{d}\xi \right]. \end{aligned} \tag{4.40}$$

This solution automatically satisfies the Wagner condition (4.36), while the consistency condition

$$\frac{1}{\pi} \int_{-d}^{d} \frac{t - f(\xi)}{\sqrt{d^2 - \xi^2}} \, \mathrm{d}\xi + \frac{2\lambda}{\pi} \int_{d}^{\infty} \frac{\mathcal{F}(\xi, t)}{\sqrt{\xi^2 - d^2}} \, \mathrm{d}\xi = 0 \tag{4.41}$$

guarantees that $\mathrm{d}\Upsilon/\mathrm{d}\zeta = O(1/\zeta)$ as $|\zeta| \to \infty$.

We can evaluate (4.40) on $\zeta = x - \mathrm{i}0,\ x > d(t)$ to deduce that

$$h(x,t) = \frac{\sqrt{x^2-d^2}}{\pi}\left[\int_{-d}^{d} \frac{t - f(\xi)}{\sqrt{d^2-\xi^2}(\xi - x)}\,\mathrm{d}\xi + 2\lambda x \dashint_{d}^{\infty} \frac{\mathcal{F}(\xi,t)}{\sqrt{\xi^2-d^2}(\xi^2-x^2)}\,\mathrm{d}\xi\right], \tag{4.42}$$

where the dash indicates a Cauchy principal value integral. Note that (4.41) ensures that $h \to 0$ as $x \to \infty$ and the symmetry of the problem guarantees that h is integrable. Furthermore, if $\lambda = 0$, (4.42) is simply the Wagner solution for the leading-order-outer free surface, as given in §2.2.4.2.

We can relate the leading-order location of the turnover point, $d(t)$, to the air pressure gradient using (4.41). If we make the change of variables $\xi = d\sin\theta$ in the first integral and $\xi = d\cosh\psi$ in the second integral in (4.41), we obtain

$$\frac{\pi t}{2} = \int_0^{\pi/2} f(d\sin\theta)\,\mathrm{d}\theta - \lambda\int_0^{\infty} \mathcal{F}(d\cosh\psi, t)\,\mathrm{d}\psi, \tag{4.43}$$

where we have used the assumption that the body profile is symmetric. The condition (4.43) generalises the Wagner solution to take account of air cushioning.

4.2.7 Summary of the problem

Hence the leading-order problem for $x > d(t)$ is given by (4.21), (4.22), (4.25), (4.39), (4.42) and (4.43). In summary and after dropping the subscripts denoting leading-order variables, the leading-order system for the free surface displacement, $h(x,t)$, the tangential component of air velocity, $U(x,t)$, the function $\mathcal{F}(x,t)$ is given by

$$h = \frac{\sqrt{x^2-d^2}}{\pi}\left[\int_{-\pi/2}^{\pi/2} \frac{t - f(d\sin\theta)}{d\sin\theta - x}\,\mathrm{d}\theta + \frac{2\lambda x}{d^2}\dashint_{0}^{\infty} \frac{\mathcal{F}(d\cosh\psi,t)}{\cosh^2\psi - x^2}\,\mathrm{d}\psi\right], \tag{4.44}$$

$$0 = \frac{\partial}{\partial t}\left(f(x) - t - h\right) + \frac{\partial}{\partial x}\left(\left(f(x) - t - h\right)U\right), \tag{4.45}$$

$$\mathcal{F} = -\int_0^t\int_0^s \frac{\partial U}{\partial t}(x,\tau) + U(x,\tau)\frac{\partial U}{\partial x}(x,\tau)\,\mathrm{d}\tau\mathrm{d}s, \tag{4.46}$$

where the turnover point location, $d(t)$, is given by

$$\frac{\pi t}{2} = \int_0^{\pi/2} f(d\sin\theta)\,\mathrm{d}\theta - \lambda\int_0^{\infty} \mathcal{F}(d\cosh\psi, t)\,\mathrm{d}\psi, \tag{4.47}$$

and we must impose the boundary conditions

$$U(d(t),t) = \dot{d}(t), \quad h(d(t),t) = f(d(t)) - t \tag{4.48}$$

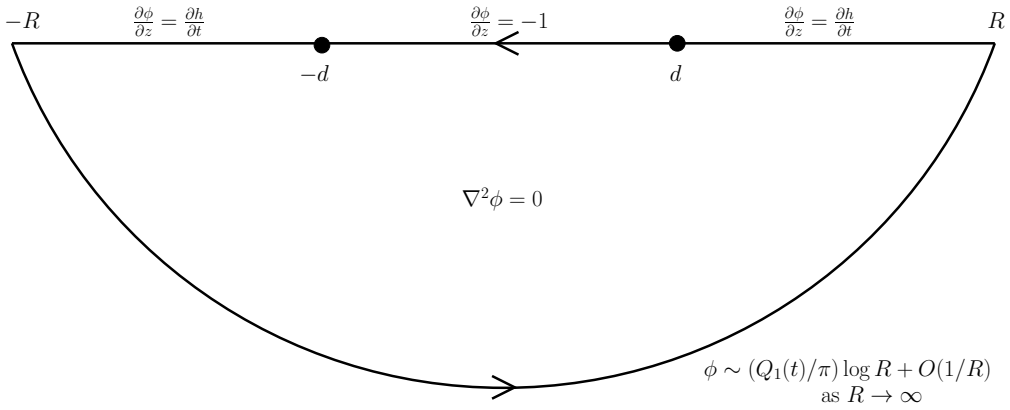

Figure 4.7: Contour considered for conservation of mass.

along with the initial conditions

$$h(x,0) = 0, \quad U(x,0) = 0. \tag{4.49}$$

Note that (4.44) comes from making the substitutions $\xi = d\sin\theta$ and $\xi = d\cosh\psi$ in the first and second integrals of (4.42) respectively.

4.2.7.1 Conservation of mass

In stating the far-field expansion (4.12), we argued that the presence of an air layer could support a source/sink in the far-field of the velocity potential of the liquid. We define the coefficient of this source/sink to be $Q_1(t)$. In order to relate this coefficient to $h(x,t)$ and $d(t)$, it is possible to use Green's theorem in a conservation-of-mass argument on the leading-order-outer velocity potential problem. Define the contour ∂D as depicted in Figure 4.7, where $R \gg 1$ and let its interior be D. By Green's theorem, it is apparent that

$$0 = \iint_D \nabla^2\phi \,\mathrm{d}S = \oint_{\partial D} \nabla\phi \cdot \mathbf{n} \,\mathrm{d}s,$$

where $\mathbf{n}$ is an outward-pointing normal to ∂D. Therefore, since $\mathrm{d}s$ is given by $R\mathrm{d}\theta$ on the semi-circular arc and $-\mathrm{d}x$ on the x-axis, we deduce that

$$0 = \int_d^\infty \frac{\partial h}{\partial t}\,\mathrm{d}x - 2d + \int_{-\infty}^{-d} \frac{\partial h}{\partial t}\,\mathrm{d}x + Q_1(t),$$

after letting $R \to \infty$. Using the symmetry of the problem and (4.36), we conclude that

$$0 = \frac{\partial}{\partial t}\left[\int_{d(t)}^\infty h(x,t)\,\mathrm{d}x + \frac{\bar{Q}_1(t)}{2} - td(t)\right] + \dot{d(t)}f(d(t)), \tag{4.50}$$

where

$$\bar{Q}_1(t) = \int_0^t Q_1(\tau)\,\mathrm{d}\tau. \tag{4.51}$$

We note here that this is not an additional equation to be solved as part of the leading-order system in §4.2.7, since that is closed for $h(x,t)$, $U(x,t)$, $\mathcal{F}(x,t)$ and $d(t)$; we could expand the displacement potential solution (4.40) for large ζ to find $Q_1(t)$, but (4.50) will generally be easier to compute.

4.2.8 Small-λ solution

It is possible to make analytic progress in (4.44)–(4.49) if we assume that the effect of the air-cushioning layer is small, that is $\lambda \ll 1$. Physically, this means that the density ratio is much smaller than the deadrise angle. Typically, the air-water density ratio is $\rho \approx 10^{-3}$, so this assumption does not greatly restrict our choice of impactors. We can proceed to terms of $O(\lambda)$ in an asymptotic expansion of (4.44)–(4.49) under the assumption that $\varepsilon \ll \lambda \ll 1$; if $\lambda = O(\varepsilon)$ as $\varepsilon \to 0$, the air cushioning enters the second-order problem described in Oliver (2007), a distinguished limit we do not pursue here.

Therefore, we seek a small-λ perturbation of the system (4.44)–(4.49) of the form

$$h = h_0+\lambda h_1+O(\lambda^2),\ U = U_0+\lambda U_1+O(\lambda^2),\ \mathcal{F} = \mathcal{F}_0+\lambda\mathcal{F}_1+O(\lambda^2),\ d = d_0+\lambda d_1+O(\lambda^2)$$

as $\lambda \to 0$.

As stated previously, at leading-order (4.44) reduces to the Wagner solution

$$h_0(x,t) = \frac{\sqrt{x^2 - d_0(t)^2}}{\pi} \int_{-d_0}^{d_0} \frac{t - f(d_0\sin\theta)}{d_0\sin\theta - x}\,\mathrm{d}\zeta \tag{4.52}$$

for $x > d_0(t)$, where, from (4.47), $d_0(t)$ is given by the classical Wagner formula (cf. (2.39)),

$$\frac{\pi t}{2} = \int_0^{\pi/2} f(d_0(t)\sin\theta)\,\mathrm{d}\theta. \tag{4.53}$$

Moreover, since the contribution to the leading-order force on the impactor due to the air pressure is $O(\lambda)$, we see no deviation from the leading-order vertical component force described in Wagner theory.

Integrating the conservation of mass equation (4.45) and applying the boundary condition (4.48), we find that the leading-order tangential air velocity in the cavity is

$$U_0(x,t) = \frac{1}{f(x) - t - h_0(x,t)} \left[x - d_0(t) + \int_{d_0}^{x} \frac{\partial h_0}{\partial t}(\zeta,t)\,\mathrm{d}\zeta\right] \tag{4.54}$$

for $x > d_0(t)$. In theory, the function $\mathcal{F}_0(x,t)$ for $x > d_0(t)$ can then be determined from the leading-order form of (4.46); however, we have only been able to obtain explicit expressions on a case-by-case basis, as we shall describe shortly. Once we have found $\mathcal{F}_0(x,t)$, the $O(\lambda)$ correction to position of the turnover point may be calculated from (4.47) to be given by

$$d_1(t) = \frac{\int_0^\infty \mathcal{F}_0(d_0(t)\cosh\psi, t)\,\mathrm{d}\psi}{\int_0^{\pi/2} f'(d_0\sin\theta)\sin\theta\,\mathrm{d}\theta}, \tag{4.55}$$

where f' indicates the derivative of f with respect to its argument. Note that the denominator on the right-hand side of (4.55) can be simplified using (4.53), viz.

$$\int_0^{\pi/2} f'(d_0\sin\theta)\sin\theta\,\mathrm{d}\theta = \frac{\pi}{2\dot{d}_0(t)}. \tag{4.56}$$

Hence, if $\dot{d}_0(t) > 0$, the displacement, $\lambda d_1(t)$, of the turnover point due to the presence of an air-cushioning layer depends upon the sign of the function $\mathcal{F}_0(x,t)$.

Finally, we note that the $O(\lambda)$-correction to the force on the impactor is given by

$$F_1(t) = \int_{-d_0(t)}^{d_0(t)} \frac{d_1(t)}{d_0(t)}\frac{\partial}{\partial x}\left(xp_0(x,0,t)\right) + p_1(x,0,t)\,\mathrm{d}x + 2\int_{d_0(t)}^{\infty} P_0(x,t)\,\mathrm{d}x, \tag{4.57}$$

where the leading-order liquid pressure on the impactor is given by the Wagner solution (2.20), and the $O(\lambda)$-correction, p_1, must be calculated from (4.40) evaluated on the impactor between $x = -d_0(t)$ and $x = d_0(t)$.

We shall elucidate these findings by considering two examples. Firstly will shall look at parabolic impactors and we will match this Wagner solution to an 'outer-outer' problem of air flow around a cylinder. The second example will consider wedge impacts and we shall indicate where the theory discussed above breaks down.

4.2.8.1 Parabolic impactors

Analytic progress is possible when the dimensionless body profile is parabolic, that is

$$f(x) = \frac{x^2}{2}. \tag{4.58}$$

Then, (4.52) and (4.53) can be trivially integrated to find the well-known Wagner solution for parabolic impact, given by

$$h_0(x,t) = \frac{x^2}{2} - t - \frac{|x|}{2}\sqrt{x^2 - d_0(t)^2}, \quad \text{for} \quad x > d_0(t) = 2\sqrt{t}. \tag{4.59}$$

It follows that the horizontal component of air velocity can be found from (4.54) to be given by

$$U_0(x,t) = \frac{2}{x} \quad \text{for} \quad x > 2\sqrt{t} \tag{4.60}$$

so that there is a sink in the far-field in the air, and in particular the first term in the small-λ expansion of $Q_2(t)$ in (4.13) is given by $Q_{20} = 2\pi$. Thus, as we let $x \to \infty$, the velocity potential in the air must have a logarithmic singularity. In contrast, the air pressure does not have this logarithmic behaviour at infinity; we can use (4.60) and (4.21) to show that

$$P_0 = -\frac{2}{x^2} \quad \text{for} \quad x > 2\sqrt{t}. \tag{4.61}$$

Note that the leading-order air pressure is negative everywhere; this is caused by the deceleration of the air as the gap thickness between the body and the liquid increases as $x \to \infty$.

Upon integrating (4.60) we deduce that

$$\mathcal{F}_0(x,t) = \frac{2t^2}{x^3} \quad \text{for} \quad x > 2\sqrt{t}, \tag{4.62}$$

which is strictly positive. We can now calculate the correction to the turnover point location by utilising (4.55), which gives

$$d_1(t) = \frac{1}{8}. \tag{4.63}$$

Therefore, even though the correction to the turnover point location places it further from the initial point of impact, the turnover point speed remains the same as that for uncushioned impact. This displacement is due to the strictly positive pressure gradient in the air. If we compare this to the results in Figure 3b of Purvis and Smith (2004), we can see some similarity with the equivalent viscous air-inviscid liquid solution for parabola impact. In that figure, for earlier times the value of their turnover point location, $\ell(T)$, is slightly increased from its large-time limit, given by the Wagner solution. However, Purvis and Smith (2004) point out that they see a slight decrease in the turnover point speed, $\dot{\ell}(T)$ for a short time period, which we do not see here. We also note that (4.63) implies that there is a temporal nonuniformity in our expansion when $t = O(\lambda^2)$, which we will discuss shortly.

Using (4.44), the $O(\lambda)$-correction to the free surface location is given by

$$h_1(x,t) = \frac{x\sqrt{t}}{8\sqrt{x^2-4t}} + \frac{4xt^2}{\pi}\sqrt{x^2-4t}\int_{2\sqrt{t}}^{\infty} \frac{1}{s^3(s^2-x^2)\sqrt{s^2-4t}}\,\mathrm{d}s,$$

for $x > 2\sqrt{t}$. The principal value integral can be simplified to

$$\int_1^{\infty} \frac{1}{S^3(S^2-X^2)\sqrt{S^2-1}}\,\mathrm{d}S = -\frac{\pi(2+X^2)}{4X^4},$$

so that

$$h_1(x,t) = \frac{x\sqrt{t}}{8\sqrt{x^2-4t}} - \frac{(x^2+8t)\sqrt{t}\sqrt{x^2-4t}}{8x^3} \quad \text{for} \quad x > 2\sqrt{t}. \tag{4.64}$$

We note that as $x \to \infty$,

$$h_1 \sim -\frac{t^{3/2}}{2x^2} \tag{4.65}$$

so that the free surface is displaced downwards from the Wagner free surface in the far-field.

The analysis of §4.2.7.1 allows us to see whether there is a source/sink in the far-field expansion of the displacement potential solution in the liquid. By writing $\bar{Q}_1 = \lambda \bar{Q}_{10} + O(\lambda^2)$ and proceeding to terms of $O(\lambda)$ in (4.50), a straightforward asymptotic analysis of the integral terms means that

$$0 = \frac{\bar{Q}_{10}(t)}{2} + \frac{t}{8} + \int_{2\sqrt{t}}^{\infty} h_1(x,t)\,\mathrm{d}x + \frac{1}{16\sqrt{t}} \int_{2\sqrt{t}}^{\infty} \frac{\partial}{\partial x}\left(x h_0(x,t)\right)\,\mathrm{d}x. \tag{4.66}$$

Upon evaluating the integrals, we deduce that

$$Q_{10}(t) = 0; \tag{4.67}$$

that is, there is no source/sink term at leading order in the far-field of the velocity potential in the liquid. We note that this is a correction of Moore et al. (2013b), since they made a typographical error in their equation (3.12), which should read exactly as in (4.66).

That $\bar{Q}_{10}(t) = 0$ allows us to propose a physical interpretation to the displacement of the turnover point from the Wagner solution, (4.63). From (4.65), we see that the correction to the free surface location, $\lambda h_1(x,t)$ shifts the Wagner free surface down for the majority of x, and in particular in the far-field. Thus the displaced fluid must be compensated by increasing d_1 and/or introducing an effective source/sink in the liquid flow. Since we have shown the latter cannot occur, that d_1 is positive is simply a result of global conservation of mass in the liquid at $O(\lambda)$.

In order to calculate the correction to the leading-order vertical component of force on the impactor due to the presence of an air layer, we first need to calculate the correction to the hydrodynamic pressure in the liquid. From (4.40), we deduce that, for $|x| < d(t)$ on the impactor,

$$\frac{\partial \Upsilon}{\partial x} = -\frac{x}{2}\sqrt{d^2 - x^2} + \frac{2\lambda x}{\pi}\sqrt{d^2 - x^2} \int_d^{\infty} \frac{\mathcal{F}(\xi,t)}{\sqrt{\xi^2 - d^2}} \frac{\mathrm{d}\xi}{\xi^2 - x^2}, \tag{4.68}$$

where we emphasise that here Υ, $\mathcal{F}$ and d are the unexpanded forms of the variables (i.e. they should not be interpreted as the leading-order terms in a small-λ expansion). We will refer to the non-integral term as the Wagner term and the second as the non-Wagner term. To calculate the force on the impactor from (4.68), we must integrate with respect to x and differentiate twice with respect to t to find the pressure on the

impactor and then integrate this pressure between $-d$ and d. For the Wagner term, this is simple, and we deduce that

$$F_w = \frac{d^2\dot{d}^2\pi}{2} + \frac{d^2\pi}{4}\left(\dot{d}^2 + d\ddot{d}\right) \sim 2\pi + \frac{3\pi}{16\sqrt{t}}\lambda \quad \text{as} \quad \lambda \to 0. \tag{4.69}$$

Since there is a factor of λ in the non-Wagner term, it suffices to use the leading-order forms of d and $\mathcal{F}$. Upon substituting (4.62) into (4.68) and evaluating, we find that

$$F_{nw} \sim \left(2 - \frac{9\pi}{16}\right)\frac{\lambda}{\sqrt{t}} + \ldots \quad \text{as} \quad \lambda \to 0 \tag{4.70}$$

Hence, the upward force on the impactor due to the liquid is

$$F_l \sim 2\pi + \left(2 - \frac{3\pi}{8}\right)\frac{\lambda}{\sqrt{t}} + \ldots \quad \text{as} \quad \lambda \to 0 \tag{4.71}$$

It is straightforward to integrate (4.61) to find that contribution to the upward force on the impactor due to the air is given by

$$F_a \sim -\frac{2\lambda}{\sqrt{t}} \quad \text{as} \quad \lambda \to 0. \tag{4.72}$$

It follows that the overall force on the impactor is given to $O(\lambda)$ by

$$F \sim 2\pi - \frac{3\lambda\pi}{8\sqrt{t}} \quad \text{as} \quad \lambda \to 0. \tag{4.73}$$

Hence, the force on the impactor is reduced by the introduction of an air layer, as we might expect since the air is cushioning the impact. The hydrodynamic force is increased by the presence of the air, due to the displacement of the turnover point so that the effective contact set is increased. However, the air being forced out of the narrow layer between the impactor and the liquid in effect gives the body some lift, which is significant enough in magnitude to overcome this increased hydrodynamic force from the liquid. As time increases, the $O(\lambda)$-correction to the upward force tends to zero. However, for time sufficiently small, there is a nonuniformity in the expansions for the location of the turnover point and for the upward force on the impactor, namely when $t = O(\lambda^2)$ as $\lambda \to 0$, so that our small-λ solution breaks down. When we rescale the variables into this small-time region by writing

$$(x, z, \xi) = \lambda\left(\tilde{x}, \tilde{z}, \tilde{\xi}\right), \quad (s, \tau, t) = \lambda^2(\tilde{s}, \tilde{\tau}, \tilde{t}), \quad h = \lambda^2\tilde{h}, \quad U = \frac{\tilde{U}}{\lambda}, \quad \mathcal{F} = \lambda\tilde{\mathcal{F}},$$

in (4.44)–(4.49), we recover the original system with $\lambda = 1$. Typically, we have to tackle this system numerically, and we do not pursue this further here. We do note,

however, that it is in this small-time region that the initial condition on U will become important. Up until this point we have not used an initial condition on U. In fact, our leading-order small-λ solution for U is independent of time, t. In a small-time temporal boundary layer, we would expect to impose the initial condition on the air flow. This temporal boundary layer is a subtle issue, particularly as other physical effects may also enter the problem, for example, air compressibility.

4.2.8.2 Cylindrical impactors

We noted previously that, for an impacting parabola, the velocity potential in the air has a logarithmic singularity in the far-field. In order to complete the picture for parabolic impacts, we seek to match the 'outer' Wagner solution to an 'outer-outer' solution that resolves this singularity.

The body profile (4.58) is the local form of a circle. Therefore, we consider the two-dimensional impact of a circular cylinder, neglecting variations to the resulting flow along the cylinder. Consider the dimensional cross-section of a circular cylinder of the form

$$(z^* - R_0 + (L/T)t^*))^2 + x^{*2} = R_0^2, \tag{4.74}$$

where R_0 is the radius of the circle, which we assume is large compared to the penetration depth, L, and (L/T) is the impact speed. We wish to consider the air flow caused due to the penetration of the circle into the liquid on the penetration timescale of T, where $L/R_0 \ll 1$. We nondimensionalise as in §4.2.1 by writing

$$x^* = Lx', \quad z^* = Lz', \quad t^* = Tt',$$

and consider perturbations to the air and liquid motion on the scale of the penetration depth,

$$\phi^* = \frac{L^2}{T}\phi', \quad p^* = \rho_l \frac{L^2}{T^2}p', \quad h^* = Lh', \quad \Phi^* = \frac{L^2}{T}\Phi', \quad P^* = \rho_a \frac{L^2}{T^2}P'.$$

Under these scalings, the cylinder is given by

$$z' = \frac{1}{2}\left(\sqrt{\frac{L}{R_0}}x'\right)^2 - t' + \frac{L}{2R_0}(z' + t')^2. \tag{4.75}$$

Therefore, close to the initial point of impact, the impactor is approximated by the parabola $\varepsilon^2 x'^2/2 - t'$ provided that

$$\varepsilon = \sqrt{\frac{L}{R_0}}. \tag{4.76}$$

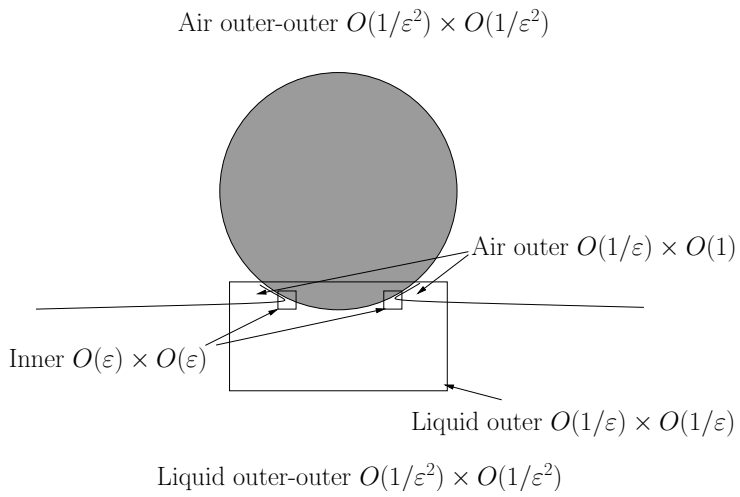

Figure 4.8: Asymptotic structure for the two-dimensional impact of a circular cylinder.

We can use the asymptotic structure described in §4.2.2 to describe the flow close to the initial point of impact as previously. However, when x', $z' = O(1/\varepsilon^2)$, we are in a region in which the impactor is a cylinder touching the liquid free surface at the origin in the Euclidean plane. This is an 'outer-outer' region in which the deadrise angle of the impactor is no longer small everywhere and we need to look at the solution of the problem in more depth. We depict the asymptotic structure in Figure 4.8.

In the outer-outer region, we make the scalings

$$(x', z') = \frac{1}{\varepsilon^2}(\check{x}, \check{z}). \tag{4.77}$$

In the far-field of the outer region discussed in §4.2.8.1, in terms of the 'outer-outer' variables, the velocity potential in the liquid, the velocity in the air and the free surface displacement are of $O(1)$, $O(1/\varepsilon)$ and $O(\varepsilon^2)$ respectively, so that we scale

$$\phi' = \check{\phi}, \quad p = \check{p}, \quad \Phi' = \frac{1}{\varepsilon^2}\check{\Phi}, \quad P = \check{P}, \quad h' = \varepsilon^2\check{h}. \tag{4.78}$$

We substitute these scalings into (4.1)–(4.11) and note that the dynamic boundary condition on the free surface is

$$\check{p} = \rho\check{P} \quad \text{on} \quad \check{z} = \check{h}(\check{x}, t), \tag{4.79}$$

so that, under the assumption that $0 < \rho \ll 1$, the liquid and air problems decouple at leading-order.

After expanding the variables in powers of ε, the leading-order governing equation in the liquid is then given by

$$\nabla^2\check{\phi}_0 = 0 \quad \text{for} \quad \check{z} < 0. \tag{4.80}$$

In the liquid, the leading-order kinematic condition on the free surface is given by

$$\frac{\partial \check{\phi}_0}{\partial \check{z}} = \frac{\partial \check{h}_0}{\partial t} \quad \text{on} \quad \check{z} = 0., \tag{4.81}$$

and the dynamic boundary condition is

$$\check{p}_0 = 0 \quad \text{on} \quad \check{z} = 0, \tag{4.82}$$

where the liquid pressure is related to the velocity potential through Bernoulli's equation, which is given to leading-order by

$$\check{p}_0 = -\frac{\partial \check{\phi}_0}{\partial t}. \tag{4.83}$$

Hence, since the initial condition $\check{\phi}_0(\check{x}, \check{z}, 0) = 0$ must hold, (4.82) is equivalent to

$$\check{\phi}_0 = 0 \quad \text{on} \quad \check{z} = 0. \tag{4.84}$$

Thus, the leading-order solution for $\check{\phi}_0$ is simply the harmonic function satisfying the Dirichlet boundary condition (4.84) that matches to the far-field expansion of the Wagner solution in the outer region. Expanding (2.16) in §2.2.4.2 in the far-field, we find that the solution $\check{\phi}_0$ of the outer-outer problem must satisfy

$$\check{\phi}_0 \sim \frac{4t\check{z}}{\check{x}^2 + \check{z}^2} \quad \text{as} \quad \check{x}^2 + \check{z}^2 \to 0. \tag{4.85}$$

Clearly therefore, the solution of (4.80), (4.84) subject to (4.85) is

$$\check{\phi}_0 = \frac{4t\check{z}}{\check{x}^2 + \check{z}^2}, \tag{4.86}$$

whereby (4.81) can be integrated to find that

$$\check{h}_0(\check{x}, t) = \frac{2t}{\check{x}^2}, \tag{4.87}$$

where we have used the initial condition $\check{h}_0(\check{x}, 0) = 0$. Moreover, using the leading-order Bernoulli equation, (4.83), we find that

$$\check{p}_0(\check{x}, \check{z}, t) = -\frac{4\check{z}}{\check{x}^2 + \check{z}^2}. \tag{4.88}$$

Note that the flow in the liquid is thus the dipole flow that is the far-field of the solution of the problem in Figure 4.6.

In the air, the leading-order governing equation is

$$\nabla^2 \check{\Phi}_0 = 0 \quad \text{for} \quad \check{z} > 0,\ \check{x}^2 + (\check{z} - 1)^2 > 1. \tag{4.89}$$

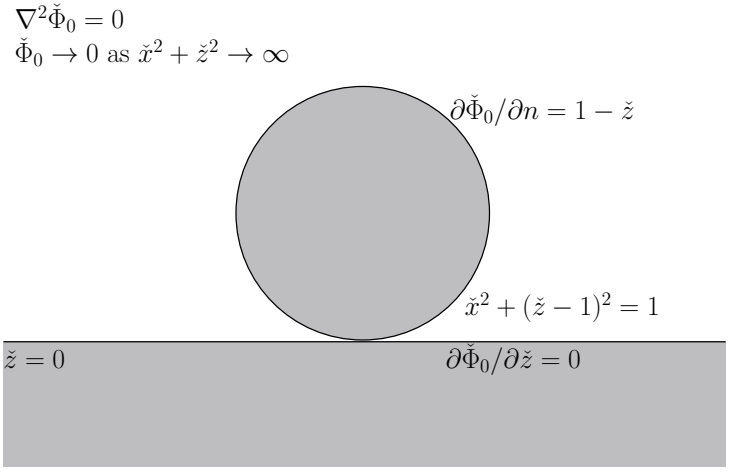

Figure 4.9: A cylinder with a large radius of curvature impacting a liquid half-space. The outer-outer region is essentially flow around a cylinder with a singularity where the cylinder touches the liquid half-space, which behaves like a solid boundary on this scale. The outward normal derivative is denoted by $\partial/\partial n$.

On the cylinder in the air region, the leading-order kinematic condition is given by

$$\frac{\partial\check{\Phi}_0}{\partial\check{z}} = -1 + \check{x}\frac{\partial\check{\Phi}_0}{\partial\check{x}} + \left(1 + \frac{\partial\check{\Phi}_0}{\partial\check{z}}\right)\check{z} \quad \text{on} \quad (\check{z}-1)^2 + \check{x}^2 = 1, \tag{4.90}$$

while the kinematic condition on the leading-order free surface is

$$\frac{\partial\check{\Phi}_0}{\partial\check{z}} = 0 \quad \text{on} \quad \check{z} = 0. \tag{4.91}$$

We depict the problem in Figure 4.9. The solution needs to match to the far-field of the leading-order velocity in the outer region, as given by (4.60) in §4.2.8.1.

As in the classical theory of cushioning between rigid impactors as described in, for example, Jeffery (1912) and Czaykowski (1970), we can define

$$\xi + \mathrm{i}\eta = \frac{2\mathrm{i}}{\check{x} + \mathrm{i}\check{z}} \tag{4.92}$$

to transform the problem (4.89)–(4.91) into the following one for $\check{\Phi}(\xi, \eta)$:

$$\frac{\partial^2\check{\Phi}_0}{\partial\xi^2} + \frac{\partial^2\check{\Phi}_0}{\partial\eta^2} = 0 \quad \text{for} \quad 0 < \xi < 1, \ -\infty < \eta < \infty; \tag{4.93}$$

here $\xi = 0$ is $z = 0$ and $\xi = 1$ is the impactor. Note that the point of contact between the cylinder and the free surface of the liquid is in the far-field in the (ξ, η)-plane.

The boundary conditions are given by

$$\frac{\partial \check{\Phi}_0}{\partial \xi} = 0 \quad \text{on} \quad \xi = 0, \tag{4.94}$$

$$\frac{\partial \check{\Phi}_0}{\partial \xi} = \frac{2(1-\eta^2)}{(1+\eta^2)^2} = g(\eta) \quad \text{on} \quad \xi = 1. \tag{4.95}$$

We can solve the problem (4.93)–(4.95) in the strip $0 < \xi < 1$ by using a Fourier transform in η. We define the Fourier transform of $\check{\Phi}_0$ with respect to η to be given by

$$\bar{\Phi}(\xi, k) = \int_{-\infty}^{\infty} \check{\Phi}_0(\xi, \eta) \mathrm{e}^{\mathrm{i}k\eta} \, \mathrm{d}\eta, \tag{4.96}$$

and define the Fourier transform of $g(\eta)$ with respect to η to be $\bar{g}(k)$. Therefore, by (4.93),

$$\frac{\partial^2 \bar{\Phi}}{\partial \xi^2} - k^2 \bar{\Phi} = 0,$$

so that applying the boundary conditions on $\xi = 0$ and $\xi = 1$, we have

$$\frac{\partial \bar{\Phi}}{\partial \xi} = \frac{\bar{g}(k) \sinh k\xi}{\sinh k}. \tag{4.97}$$

Hence, using the convolution theorem, we find that

$$\frac{\partial \check{\Phi}_0}{\partial \xi}(\xi, \eta) = \frac{1}{2\pi} \int_{-\infty}^{\infty} \frac{2(1-s^2)}{(1+s^2)^2} \int_{-\infty}^{\infty} \mathrm{e}^{-\mathrm{i}k(s-\eta)} \frac{\sinh k\xi}{\sinh k} \, \mathrm{d}k \, \mathrm{d}s. \tag{4.98}$$

We can deduce the far-field flow from the fact that as $\eta \to \infty$,

$$\frac{\partial \check{\Phi}_0}{\partial \xi} = 0 \quad \text{on} \quad \xi = 0, \quad \frac{\partial \Phi_0}{\partial \xi} \sim -\frac{2}{\eta^2} \quad \text{on} \quad \xi = 1,$$

giving,

$$\frac{\partial \check{\Phi}_0}{\partial \xi} \sim -\frac{2\xi}{\eta^2} \quad \text{as} \quad \eta \to \infty, \tag{4.99}$$

so that

$$\check{\Phi}_0 \sim -\frac{\xi^2}{\eta^2} + C(\eta) \quad \text{as} \quad \eta \to \infty, \tag{4.100}$$

where we can determine $C(\eta)$ by applying conservation of mass on the strip. Green's theorem gives that

$$0 = \int_0^1 \frac{2\xi^2}{\eta^3} + \frac{\mathrm{d}C}{\mathrm{d}\eta} \, \mathrm{d}\xi + \frac{2\eta}{1+\eta^2} \quad \text{as} \quad \eta \to \infty,$$

so that after integrating and expanding, we must have

$$C(\eta) \sim -2 \log \eta + A + o(1) \quad \text{as} \quad \eta \to \infty,$$

where A is an arbitrary constant. Returning to $(\check{x},\check{z})$-coordinates,

$$\check{\Phi}_0(\check{x},\check{z}) \sim -\frac{\check{z}^2}{\check{x}^2} - 2\log\frac{2\check{x}}{\check{x}^2+\check{z}^2} + A \quad \text{as} \quad \check{x}^2+\check{z}^2 \to 0. \tag{4.101}$$

In the outer region recall that

$$\Phi_0 = 2\log x \quad \text{as} \quad x \to \infty. \tag{4.102}$$

To match between (4.101) and (4.102), recall that

$$\check{x} = \varepsilon x, \quad \check{z} = \varepsilon^2 \bar{z}.$$

Defining the intermediate coordinates X and Z by

$$\check{x} = \varepsilon^\alpha X, \quad \check{z} = \varepsilon^{2\alpha} Z$$

where $0 < \alpha < 1$, we expand to find that

$$\begin{aligned} \Phi_{\text{outer}} &= 2\log X + 2(\alpha-1)\log\varepsilon, \\ \Phi_{\text{outer-outer}} &= -\frac{\varepsilon^{2\alpha}Z^2}{X^2} - 2\log 2 + 2\log X - 2\alpha\log\varepsilon + A + \ldots, \end{aligned}$$

so that choosing $\alpha = 1/2$ and $A = 2\log 2$ completes the matching between the outer and outer-outer solutions.

4.2.8.3 Wedge impactors

We move on to consider the wedge given in dimensionless coordinates by

$$z = \varepsilon|x| - t,$$

Since there is no natural lengthscale in the wedge impact problem, we can find a similarity solution to (4.44)–(4.47) of the form

$$\eta = \frac{x}{\alpha t}, \quad \chi = \frac{\xi}{\alpha t}, \quad d = \alpha t, \quad h = t h^\dagger(\eta), \quad U = U^\dagger(\eta), \quad \mathcal{F} = t\mathcal{F}^\dagger(\eta),$$

where the speed of the turnover point, α, has been introduced for convenience. Under this transformation and omitting the algebraic manipulation in (4.46), the problem (4.44)–(4.47) for $\eta > 1$ becomes

$$h^\dagger = -1 + \frac{2\alpha\eta}{\pi}\arcsin\left(\frac{1}{\eta}\right) + \frac{2\lambda\eta}{\pi}\sqrt{\eta^2-1}\int_1^\infty \frac{\mathcal{F}^\dagger(\chi)}{\sqrt{\chi^2-1}(\chi^2-\eta^2)}\,\mathrm{d}\chi, \tag{4.103}$$

$$U^\dagger = \frac{\alpha}{\alpha\eta - 1 - h^\dagger(\eta)}\left[(1-h^\dagger(\eta))\eta + \alpha - 2 + 2\int_1^\eta h^\dagger(\chi)\,\mathrm{d}\chi\right], \tag{4.104}$$

$$\mathcal{F}^\dagger = 1 - \eta\int_\eta^\infty \frac{U^\dagger(\chi)}{\chi^2}\,\mathrm{d}\chi - \frac{1}{\alpha}\int_\eta^\infty \frac{\chi-2\eta}{2\chi^3}U^\dagger(\chi)^2\,\mathrm{d}\chi, \tag{4.105}$$

$$0 = \frac{\pi}{2} - \alpha + \lambda\int_0^\infty \mathcal{F}^\dagger(\cosh\psi)\,\mathrm{d}\psi. \tag{4.106}$$

Henceforth, we drop the cumbersome dagger notation indicating the similarity variables. In the regime in which $\lambda \ll 1$, we can use (4.103) and (4.106) to deduce that, at leading order in λ, the free surface profile and turnover point location are given by the classical wedge-entry results

$$h_0(\eta) = -1 + \eta \arcsin \frac{1}{\eta} \quad \text{for} \quad \eta > 1 \quad \text{and} \quad \alpha_0 = \frac{\pi}{2}. \tag{4.107}$$

In the far-field, the leading-order elevation of the free surface has the characteristic Wagner behaviour

$$h_0 \sim \frac{1}{6\eta^2} \quad \text{as} \quad \eta \to \infty. \tag{4.108}$$

The tangential component of velocity in the air is found by using (4.104) to deduce that

$$U_0(\eta) = \frac{\sqrt{\eta^2 - 1}}{\eta - (2/\pi)\eta \arcsin(1/\eta)} \quad \text{for} \quad \eta > 1, \tag{4.109}$$

so that

$$U_0(\eta) \sim 1 + \frac{2}{\pi\eta} \quad \text{as} \quad \eta \to \infty \tag{4.110}$$

in the far-field. Thus, in a wedge impact, there is a rigid-body motion of the air in the far-field, and hence we were not conservative enough in our far-field expansion in the air in (4.13), where we assumed that the air had at worst a source/sink in the far-field. Note that there is still a sink term, and its leading-order coefficient is $Q_{20} = \pi$. In theory, we can use (4.21) to find an expression for the leading-order air pressure, but there is not a simple closed form expression for it. A numerical integration has been performed and is displayed in Figure 4.10. It is clear that the pressure becomes unbounded as $\eta \to \infty$. A straightforward far-field analysis of (4.21) using (4.110) allows us to deduce that

$$P_0(\eta) \sim -\log \eta + \left(\frac{2}{\pi} - \frac{\pi}{2}\right)\frac{1}{\eta} \quad \text{as} \quad \eta \to \infty. \tag{4.111}$$

The logarithmic singularity in the pressure suggests that when $\log \eta = O(1/\lambda)$, there is a non-uniformity in the small-λ asymptotics as $\lambda P = O(1)$ on the free surface, so that the air pressure enters the leading-order dynamic boundary condition in the liquid.

We can use (4.105) and (4.109) to determine $\mathcal{F}_0$. Again, however, there is no simple closed expression for $\mathcal{F}_0$, so we use quadrature and display the results in Figure 4.10. In contrast to the parabola example, $\mathcal{F}_0$ is strictly negative. This is due to a reversal in the sign of the pressure gradient. In the far-field, we can use (4.105) and (4.110) to deduce that

$$\mathcal{F}_0 \sim -\frac{1}{\pi\eta} + \left(\frac{1}{6} - \frac{2}{3\pi^2}\right)\frac{1}{\eta^2} + \quad \text{as} \quad \eta \to \infty. \tag{4.112}$$

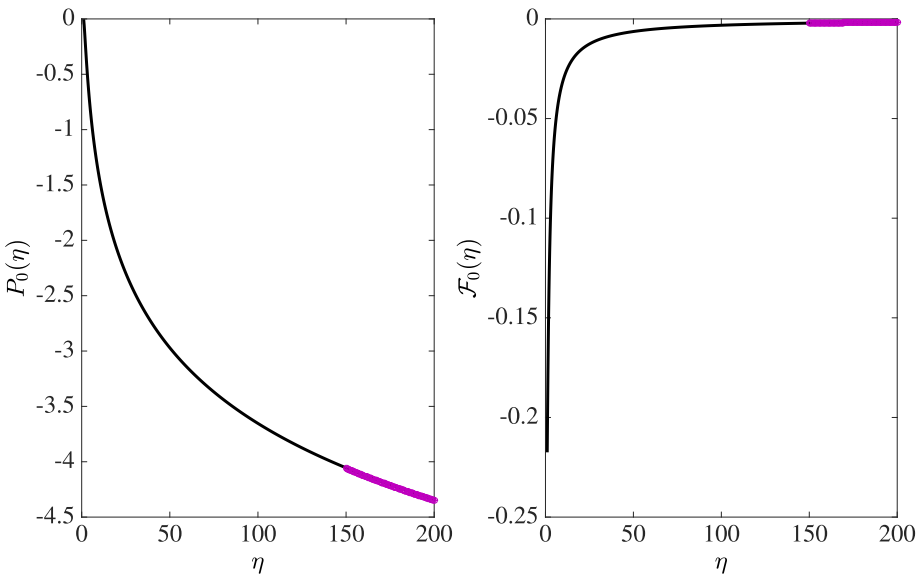

Figure 4.10: The leading-order air pressure (left) and the function $\mathcal{F}_0(\eta)$ (right). There is a logarithmic singularity in the air pressure in the far-field. Moreover, since the pressure gradient is always negative, $\mathcal{F}_0(\eta)$ is a strictly negative function. The far-field asymptotes given in (4.111) and (4.112) are represented by the magenta circles. This plot is based on one in Moore et al. (2013b).

Since $\mathcal{F}_0$ is strictly negative, (4.106) implies that the correction to the turnover point location, λd_1 is negative, so that to $O(\lambda)$, the turnover point is closer to the minimum point of the wedge than in Wagner theory. Indeed, using quadrature on (4.106), we find that

$$\alpha_1 = -0.400 \quad \text{to three significant figures.}$$

Since α represents the speed of the turnover point, the $O(\lambda)$-correction reduces the turnover point speed from the Wagner solution- this is in contrast to the parabola example.

The $O(\lambda)$-correction to the elevation of the free surface is given by

$$h_1(\eta) = \frac{2\alpha_1\eta}{\pi}\arcsin\left(\frac{1}{\eta}\right) + \frac{2\eta}{\pi}\sqrt{\eta^2-1}\fint_1^\infty \frac{\mathcal{F}_0(\chi)}{\sqrt{\chi^2-1}(\chi^2-\eta^2)}\,\mathrm{d}\chi, \tag{4.113}$$

an expression that follows from (4.103). A local and far-field analysis imply that

$$h_1(\eta) \sim \alpha_1 + \frac{2\sqrt{2}}{\pi}\left(\int_1^\infty \frac{\mathcal{F}(\chi)}{(\chi^2-1)^{3/2}} - \frac{\mathcal{F}(1)}{2\sqrt{2}(\chi-1)^{3/2}}\,\mathrm{d}\chi - \alpha_1\right)\sqrt{\eta-1} \tag{4.114}$$

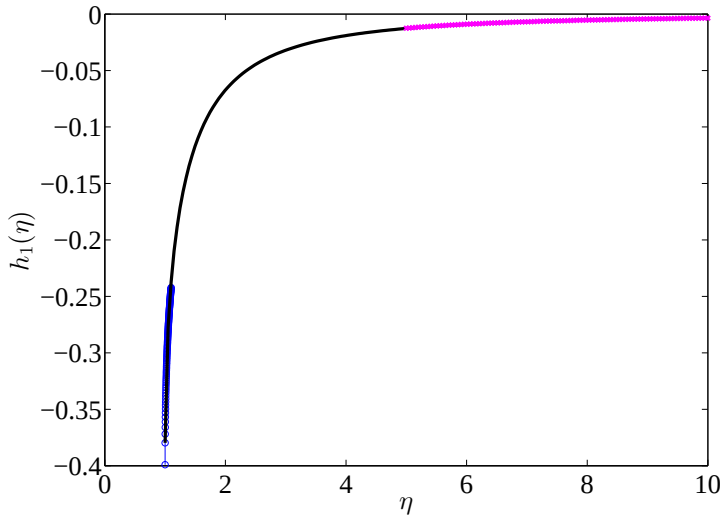

Figure 4.11: The first-order correction to the liquid free surface, depicted by the black line. Its asymptotic behaviour near the turnover point given by (4.114) is denoted by blue circles, and its far-field behaviour given by (4.115)–(4.117) is depicted by the magenta crosses.

as $\eta \downarrow 1$, and

$$h_1(\eta) \sim \frac{b}{\eta^2}\log\eta + \frac{c}{\eta^2} \quad \text{as} \quad \eta \to \infty, \tag{4.115}$$

where

$$b = -\frac{2}{\pi}\left(\frac{1}{6} - \frac{2}{3\pi^2}\right), \tag{4.116}$$

$$c = \frac{\alpha_1}{3\pi} - \frac{2}{\pi^2} + \frac{1}{\pi}\int_1^\infty \frac{\mathcal{F}_0(\chi)}{\sqrt{\chi^2-1}}\,\mathrm{d}\chi - \frac{2}{\pi}\int_1^\infty \frac{\chi^2\mathcal{F}_0(\chi)}{\sqrt{\chi^2-1}} + \frac{1}{\pi} - \left(\frac{1}{6} - \frac{2}{3\pi^2}\right)\frac{1}{\chi}\,\mathrm{d}\chi. \tag{4.117}$$

In Figure 4.9 we plot h_1 using quadrature, together with the asymptotes given by (4.114) and (4.115).

At this point we recall the analysis in §4.2.7.1, which tells us that if a source/sink exists in the far-field of the displacement potential, its coefficient must satisfy (4.50). In similarity form, this condition is given by

$$0 = \alpha\int_1^\infty h^\dagger(\eta)\,\mathrm{d}\eta + \frac{\lambda\bar{Q}_1^\dagger}{2} - \alpha + \frac{\alpha^2}{2}, \tag{4.118}$$

Since the $O(\lambda)$-correction to the turnover point is negative (i.e. $\alpha_1 < 1$) and $h_1 < 0$ for all $\eta > 1$, global conservation of mass at $O(\lambda)$ implies that $\bar{Q}_{10}$ in (4.118) is

positive, corresponding to a source, with (4.118) at $O(\lambda)$ giving

$$\bar{Q}_{10} = -\pi \left(\frac{\alpha_1}{2} + \int_1^\infty h_1(\chi)\, \mathrm{d}\chi \right) \approx 0.326 \tag{4.119}$$

to 3 significant figures.

Comparing (4.108) to (4.115)–(4.117), it is clear that, consistent with the nonuniformity in the pressure for large η, there is a nonuniformity in the asymptotic expansion of h as $\lambda \to 0$ as we move far away from the point of impact. The far-field expansion of h_1 suggests that the asymptotic analysis of (4.103)–(4.106) needs to be reconsidered when $\log \eta = O(1/\lambda)$ and that in such a region the free surface will contain terms involving η^λ as $\lambda \to 0$. As the nonuniformity occurs when $\log \eta = O(1/\lambda)$, this is a nonuniformity both for large x when $t = O(1)$ and for small t when $x = O(1)$. The resolution of this nonuniformity is an open problem, which we do not pursue further here.

4.2.9 Summary

We have used Wagner theory to derive a model for air-cushioning in constant-velocity, two-dimensional impacts onto a half-space of ideal, incompressible fluid. Under the assumption that the air is also ideal and incompressible, we have used the displacement potential to write down the local impact model. The flow in the liquid in the inner regions local to the turnover points is the same as that for Wagner theory provided that the air-to-liquid density ratio, ρ, is small. This assumption allows us to trivially solve the inner problem in the air and write down the Wagner condition for the free surface in the leading-order-outer potential problem.

Our model reduced to an integro-differential system, given succinctly in §4.2.7, for the leading-order free surface profile, the leading-order turnover curve location, leading-order tangential component of velocity in the air and a function, $\mathcal{F}$, which describes the effect of the air pressure. Throughout, we assumed that the parameter $\lambda = \rho/\varepsilon$ is at most order unity and that the free surface is integrable in the far-field.

We considered the physically-relevant liquid-air regime in which λ is small. As expected, at leading-order, the solution is simply that given by Wagner theory as discussed in §2.2. However, we were able to deduce a general expression for the correction to the turnover point location due to the influence of the air layer. We also stated that the presence of an air layer allows the possibility of a source/sink in the far-field of the liquid flow. We proceeded to consider two specific examples of impact to highlight the novelties of the solution.

Firstly, we discussed the impact of a parabola. We derived the leading-order tangential component of the air velocity and the function $\mathcal{F}$ from the Wagner solution,

which allowed us to state the first-order correction to the free surface profile and the turnover point location. The turnover point is displaced slightly further from the axis of symmetry of the parabola, but its speed remained unchanged from its value in Wagner theory. We deduced that there can be no source/sink in the far-field of the liquid for the impact of a parabola, but it was trivial to see that the leading-order velocity potential in the air has a logarithmic singularity in the far-field. We justified this behaviour by considering the parabola as a local approximation to an impacting circular cylinder and modelling an 'outer-outer' flow using potential theory. The logarithmic behaviour was shown to be inevitable at the point of impact.

The second example we considered was that of a symmetric wedge. We derived the similarity form of our integro-differential system and solved for the leading-order forms of the air velocity and the function $\mathcal{F}$ from the Wagner solution. We noted that for the wedge, the function $\mathcal{F}$ was strictly negative, as opposed to being strictly positive, as in the case of the parabola. This was found to be caused by a logarithmic singularity in the far-field air pressure, which we did not see in the parabolic example. This form of the function $\mathcal{F}$ caused the turnover point to have a speed that is slower than the Wagner turnover speed. The logarithmic singularity in the air pressure and a nonuniformity in the far-field expansion for the free surface indicated that there is an 'outer-outer' region in which the liquid and air pressures balance on the free surface and terms of the form $(t^3/x^2)\log(x/t)$ appear in the free surface profile. The resolution of this nonuniformity remains an open problem.

4.2.9.1 Extensions

Naturally, everything we discussed in this section can be extended to non-symmetric impactors, with the caveat that the air flow in the left and right cavities and outer regions must be considered separately. Of particular relevance would be the extension of this air-cushioning theory to oblique impacts.

We also noted that the model has a nonuniformity for small time (equivalent to $\lambda = O(1)$), which means it would be of merit to consider whether we need further physical effects in our model to incorporate the small-time behaviour. In particular, given our somewhat artificial set-up, what does the impulsive start to the impact mean for the air motion as $t \downarrow 0^+$?

It would be of interest to derive a similar set of equations for situations where the air can be modelled as a lubricating viscous layer. This could be particularly valuable in validating the post-impact theory of Purvis and Smith (2004) and we certainly believe that the displacement potential is a much more malleable tool for numerical simulations of flow behaviour both before and after impact.

4.3 Three-dimensional impacts

Due to the convenience of the displacement potential formulation of the leading-order-outer problem, much of our two-dimensional analysis extends to three-dimensional impacts. We shall present the three-dimensional analysis in detail here, in particular concentrating on axisymmetric body profiles, since analytic progress is possible in a manner similar to that in §2.3.4. Most of the theory presented here is based on that published in Moore and Oliver (2014).

As in §4.2.1, for brevity, we shall simply state the dimensionless model here. At $t' = 0$, the minimum point of a rigid three-dimensional impactor is assumed to be touching a liquid half-space, with air filling the region not occupied by the body or the liquid. We impulsively move the body so that for $t' > 0$ its position is given by

$$z' = f(\varepsilon x', \varepsilon y') - t'. \tag{4.120}$$

where, as usual, ε is assumed to be small. The function f is assumed to be smooth, except possibly at the origin, and to be increasing with distance from the origin. Both the liquid and air are assumed to be ideal, incompressible and initially irrotational. We neglect both surface tension and gravity in the following analysis.

Proceeding as in Wagner theory, for times $t' > 0$, the impactor penetrates the liquid and some of the fluid is displaced into a splash sheet. We denote the multivalued free surface by $z' = h'(x', y', t')$. The projection into the (x', y')-plane of the curve along which $\nabla h'$ is unbounded is defined by $t' = \omega'(\varepsilon x', \varepsilon y')$. In the outer region, the interior of this curve in the (x', y')-plane shall be referred to as the contact set. As in two dimensions, we consider separately the components of the free surface above (i.e. the splash sheet) and below (i.e. bounding the bulk of the liquid) the turnover curve, and denote them by $z' = f(\varepsilon x', \varepsilon y') - t' - h'_+$ and $z' = h'_-$ respectively. With the same caveats and limitations on the splash sheet that we have discussed previously in §2.3 and §3.2, for convenience we define the wetted region to be the part of the impactor in contact with the liquid and the non-wetted region to be the part of the impactor in contact with the air.

As previously, we shall represent variables in the liquid with lower-case letters and variables in the air with upper-case letters. The velocities in the liquid and air are denoted by $\mathbf{u}'$ and $\mathbf{U}'$ respectively and, due to our assumptions on the two fluids, there exist velocity potentials $\phi'(x', y', z', t')$, $\Phi'(x', y', z', t')$ such that $\mathbf{u}' = \nabla\phi'$, $\mathbf{U}' = \nabla\Phi'$. In the liquid, the governing equation of motion is

$$\nabla^2\phi' = 0. \tag{4.121}$$

As in two-dimensions, it is easier to use the Euler equations in the air region, which are given by

$$\begin{aligned}
\frac{\partial U'}{\partial t'} + U'\frac{\partial U'}{\partial x'} + V'\frac{\partial U'}{\partial y'} + W'\frac{\partial U'}{\partial z'} &= -\frac{\partial P'}{\partial x'}, && (4.122)\\
\frac{\partial V'}{\partial t'} + U'\frac{\partial V'}{\partial x'} + V'\frac{\partial V'}{\partial y'} + W'\frac{\partial V'}{\partial z'} &= -\frac{\partial P'}{\partial y'}, && (4.123)\\
\frac{\partial W'}{\partial t'} + U'\frac{\partial W'}{\partial x'} + V'\frac{\partial W'}{\partial y'} + W'\frac{\partial W'}{\partial z'} &= -\frac{\partial P'}{\partial z'}, && (4.124)\\
\frac{\partial U'}{\partial x'} + \frac{\partial V'}{\partial y'} + \frac{\partial W'}{\partial z'} &= 0, && (4.125)
\end{aligned}$$

where $\mathbf{U}' = (U', V', W')$ and P' is the air pressure. The condition of irrotationality in the air is then given by

$$\nabla \wedge \mathbf{U}' = \mathbf{0}. \tag{4.126}$$

The no-flux conditions on the impactor $z' = f(\varepsilon x', \varepsilon y') - t'$ are given by

$$\begin{aligned}
\frac{\partial \phi'}{\partial z'} &= -1 + \varepsilon f_{,1}\frac{\partial \phi'}{\partial x'} + \varepsilon f_{,2}\frac{\partial \phi'}{\partial y'} \quad \text{on the wetted region,} && (4.127)\\
W' &= -1 + \varepsilon f_{,1}U' + \varepsilon f_{,2}V' \qquad \text{on the non-wetted region,} && (4.128)
\end{aligned}$$

where the subscript $,i$ indicates differentiation with respect to argument i. The kinematic conditions on the free surface are given by

$$\frac{\partial \phi'}{\partial n'} = \mathbf{U}' \cdot \mathbf{n} = v_{fs} \quad \text{on} \quad z' = h'(x', y', t'),\ t' < \omega'(\varepsilon x', \varepsilon y'), \tag{4.129}$$

where $\mathbf{n}$ is the outward-pointing normal of, $\partial/\partial n'$ is the outward normal derivative to, and v_{fs} is the outward normal speed of, the free surface. In the absence of viscosity and surface tension, the dynamic boundary condition on the free surface is given by

$$p' = \rho P' \quad \text{on} \quad z' = h'(x', y', t'),\ t' < \omega'(\varepsilon x', \varepsilon y'), \tag{4.130}$$

where the liquid and air pressures $p'(x', y', z', t'),\ P'(x', y', z', t')$ satisfy the Bernoulli equations

$$\begin{aligned}
\frac{\partial \phi'}{\partial t'} + p' + \frac{1}{2}\left|\nabla \phi'\right|^2 &= 0, && (4.131)\\
\frac{\partial \Phi'}{\partial t'} + P' + \frac{1}{2}\left|\mathbf{U}'\right|^2 &= 0, && (4.132)
\end{aligned}$$

in the liquid and air regions respectively.

Initially, the liquid and air are quiescent, and the free surface is undisturbed, so that

$$\phi'(x', y', z', 0) = 0,\ \mathbf{U}'(x', y', z', 0) = 0,\ h'(x', y', 0) = 0. \tag{4.133}$$

Moreover, we require $\omega'(0,0) = 0$.

In this thesis, we will only consider solutions for which the free surface elevation is integrable in the far-field. Hence, we require

$$h' = O\left(\frac{\log(r)^j}{r'^{2+k}}\right) \quad \text{as} \quad r' = \sqrt{x'^2 + y'^2} \to \infty, \tag{4.134}$$

for some $j, k > 0$. Furthermore, motivated by §4.2, we shall make the conservative assumptions that the velocity potential in the liquid decays no more strongly than a source/sink in the far-field and that the air velocity is bounded, so that

$$\phi' = O\left(\frac{1}{\sqrt{r'^2 + z'^2}}\right) \quad \text{as} \quad \sqrt{r'^2 + z'^2} \to \infty, \tag{4.135}$$

$$\mathbf{U}' = O(1) \quad \text{as} \quad \sqrt{r'^2 + z'^2} \to \infty. \tag{4.136}$$

4.3.1 Asymptotic structure

The asymptotic structure for the small deadrise angle regime in which $0 < \varepsilon \ll 1$ generalises directly from the two-dimensional theory. We shall assume that the density ratio, ρ, is small, but assume that $\varepsilon \ll \lambda = \rho/\varepsilon = O(1)$, so that the leading-order-outer air and liquid regions couple through the dynamic boundary condition on the free surface, as we shall see presently.

Under the assumptions above, we expect the free surface to turn over in a small inner region on the impactor in the neighbourhood of the turnover curve. As we showed in §2.3.3, this inner region is of size of $O(\varepsilon)$ in each plane perpendicular to the turnover curve and is quasi-two-dimensional. This quasi-two-dimensionality means that the results regarding the air flow in the cavity in the turnover region from §§4.2.4–4.2.5 can be applied directly in our three-dimensional analysis. In particular, since we assume that the density ratio is small, the liquid and air problems will decouple in the inner region at leading order. The liquid problem is therefore the same as in three-dimensional Wagner theory, as described by §2.3.3. In the inner region, the air moves at the same velocity as the quasi-two-dimensional free surface in each plane perpendicular to the turnover curve, so that it is stationary in the relevant moving frame.

The liquid is ejected from the turnover region into a slender splash sheet of thickness of $O(\varepsilon)$ and whose thickness varies over distances of $O(1/\varepsilon)$. The sheet is assumed to not separate from the impactor. At leading order, the main bulk of the liquid, in a region of size of $O(1/\varepsilon)$, does not see the splash sheet and the body and kinematic boundary conditions are applied inside and outside the effective contact set respectively.

In the outer air region, which is trapped between the body/splash sheet and the main liquid bulk, the horizontal lengthscales are an order of magnitude larger than the vertical lengthscale. Therefore, the air layer is of extent of $O(1/\varepsilon)$ and thickness of $O(1)$.

4.3.2 Leading-order-outer analysis

In the liquid region, we neglect the splash sheet and apply the familiar Wagner scalings

$$(x', y', z') = \frac{1}{\varepsilon}(x, y, z), \quad \phi' = \frac{1}{\varepsilon}\phi, \quad p' = \frac{1}{\varepsilon}p, \quad h'_- = h, \quad t' = t, \quad \omega' = \omega.$$

In the air region, the order of magnitude difference between the horizontal and vertical lengthscales means we must scale

$$(x', y') = \frac{1}{\varepsilon}(x, y), \quad z' = \hat{z}, \quad \Phi = \frac{1}{\varepsilon^2}\Phi \quad P' = \frac{1}{\varepsilon^2}P, \quad h'_+ = \varepsilon h_+.$$

Hence, as expected, the dynamic boundary condition on the lower free surface is given by

$$p = \lambda P,$$

where $\lambda = \rho/\varepsilon$.

4.3.2.1 Air region

In the outer air region, we can follow the same steps as in §4.2.4, to deduce that the leading-order x- and y-components of the air velocity, $U(x, y, t)$ and $V(x, y, t)$, leading-order air pressure, $P(x, y, t)$, and leading-order air layer thickness, $\eta(x, y, t) = f(x, y) - t - h(x, y, t)$, must satisfy the equations

$$\frac{\partial U}{\partial t} + U\frac{\partial U}{\partial x} + V\frac{\partial U}{\partial y} = -\frac{\partial P}{\partial x}, \tag{4.137}$$

$$\frac{\partial V}{\partial t} + U\frac{\partial V}{\partial x} + V\frac{\partial V}{\partial y} = -\frac{\partial P}{\partial y}, \tag{4.138}$$

$$\frac{\partial \eta}{\partial t} + \frac{\partial}{\partial x}(\eta U) + \frac{\partial}{\partial y}(\eta V) = 0 \tag{4.139}$$

for $t < \omega(x, y)$, subject to the boundary conditions

$$(U, V) \cdot \mathbf{n} = v_n, \ \eta(x, y, t) = 0 \quad \text{on} \quad t = \omega(x, y), \tag{4.140}$$

where v_n is the outward normal speed of, and $\mathbf{n}$ is the outward-pointing unit normal to the projection of the turnover curve in the (x, y)-plane. The first condition in (4.140) is the matching condition to the inner air flow and the second is simply the

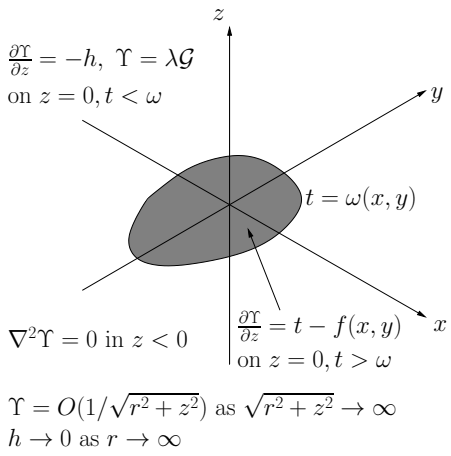

Figure 4.12: Leading-order displacement potential problem for air-cushioning in three-dimensional impacts. Additionally, matching to the inner region, we expect Υ to have (3/2)-power behaviour as we approach the turnover curve. This figure is based on one in Moore and Oliver (2014).

Wagner condition. In general, we would expect to require initial conditions on h, U and V, which we take to be

$$h(x, y, 0) = 0, \quad U(x, y, 0) = 0, \quad V(x, y, 0) = 0. \tag{4.141}$$

We will be particularly interested in axisymmetric impactors, for which (4.137)–(4.139) reduce to

$$\frac{\partial U_r}{\partial t} + U_r \frac{\partial U_r}{\partial r} = -\frac{\partial P_r}{\partial r}, \tag{4.142}$$

$$\frac{\partial \eta_r}{\partial t} + \frac{1}{r} \frac{\partial}{\partial r} (r \eta_r U_r) = 0, \tag{4.143}$$

where $\eta_r(r, t) = f(r) - t - h_r(r, t)$ is the axisymmetric air layer thickness, $h_r(r, t)$ is the axisymmetric free surface elevation, $U_r(r, t)$ is the radial component of air velocity, $P_r(r, t)$ is the axisymmetric air pressure and $r = d(t)$ is the turnover curve location (where the subscripts denote axisymmetric variables, not partial differentiation with respect to r). Furthermore, the boundary conditions (4.140) become

$$U_r(r, t) = \dot{d}(t),\ \eta_r(r, t) = 0 \quad \text{on} \quad r = d(t), \tag{4.144}$$

where $r = d(t)$ is the axisymmetric turnover curve. The initial conditions follow directly from (4.141).

4.3.2.2 Liquid region

In the outer liquid region, as in the two-dimensional case, the analysis is simpler if we formulate the leading-order-outer liquid problem using the displacement potential,

$$\Upsilon = -\int_0^t \phi(x, y, z, \tau)\,\mathrm{d}\tau. \tag{4.145}$$

The leading-order problem is that shown in Figure 4.12, where $\mathcal{G}(x, y, t)$ is defined by

$$\frac{\partial^2 \mathcal{G}}{\partial t^2} = P \tag{4.146}$$

giving

$$\mathcal{G}(x, y, t) = \int_0^t \int_0^s P(x, y, \tau)\,\mathrm{d}\tau\mathrm{d}s, \tag{4.147}$$

and we have used the fact that Υ and $\partial\Upsilon/\partial t$ must vanish at $t = 0$. Note that in our three-dimensional analysis, the function $\mathcal{G}$ depends on the air pressure, as opposed to $\mathcal{F}$ depending on the air pressure gradient in §4.2.6. This is purely for convenience: in two-dimensions we solved a Riemann-Hilbert problem for $\Upsilon_x - \mathrm{i}\Upsilon_z$, so we required a boundary condition on Υ_x as opposed to Υ. In three dimensions we are able to solve the problem using the condition on Υ directly.

We can make significant analytical progress when the impactor is axisymmetric. Let $\Upsilon_r(r, z, t)$ be the axisymmetric displacement potential and $\mathcal{G}_r(r, t)$ be the axisymmetric version of $\mathcal{G}$. Following §2.3.4, we seek a separable solution for the displacement potential. It is straightforward to deduce that

$$\Upsilon_r(r, z, t) = \int_0^\infty \alpha(s, t)\mathrm{J}_0(sr)\mathrm{e}^{sz}\,\mathrm{d}s, \tag{4.148}$$

where J_0 is the Bessel function of the first kind of order zero. The coefficient $\alpha(s, t)$ is found by applying the kinematic condition on the contact set, $r < d(t)$, and the dynamic boundary condition on the non-contact set, $r > d(t)$. Hence, $\alpha(s, t)$ must satisfy the dual integral equations

$$t - f(r) = \int_0^\infty s\alpha(s, t)\mathrm{J}_0(sr)\,\mathrm{d}s \quad \text{for} \quad r < d(t), \tag{4.149}$$

$$\lambda\mathcal{G}_r(r, t) = \int_0^\infty \alpha(s, t)\mathrm{J}_0(sr)\,\mathrm{d}s \quad \text{for} \quad r > d(t). \tag{4.150}$$

We can reduce these dual integral equations to Titchmarsh form by scaling

$$(r, z) = d(R, Z),\ s = \frac{S}{d},\ \alpha(s, t) = \beta(S, t),\ g(R, t) = t - f(dR),\ \mathcal{G}_r(r, t) = \hat{\mathcal{G}}_r(R, t),$$

so that the turnover curve is fixed at $R = 1$ and the dual integral equations become

$$d(t)^2 g(R,t) = \int_0^\infty S\beta(S,t)\mathrm{J}_0(SR)\,\mathrm{d}S \quad \text{for} \quad R < 1, \tag{4.151}$$

$$\lambda d(t)\hat{\mathcal{G}}_r(R,t) = \int_0^\infty \beta(S,t)\mathrm{J}_0(SR)\,\mathrm{d}S \quad \text{for} \quad R > 1. \tag{4.152}$$

This system has the solution (see Sneddon (1966) pp. 86-87):

$$\beta(S,t) = \frac{\sqrt{2S}}{\Gamma(1/2)}\left[\int_0^1 \sqrt{\sigma}k_1(\sigma,t)\mathrm{J}_{1/2}(\sigma S)\,\mathrm{d}\sigma + \int_1^\infty \sqrt{\sigma}k_2(\sigma,t)\mathrm{J}_{1/2}(\sigma S)\,\mathrm{d}\sigma\right], \tag{4.153}$$

where $\mathrm{J}_{1/2}$ is the Bessel function of the first kind of order $1/2$, and

$$k_1(\sigma,t) = d(t)^2\int_0^\sigma \frac{\tau g(\tau,t)}{\sqrt{\sigma^2-\tau^2}}\,\mathrm{d}\tau, \tag{4.154}$$

$$k_2(\sigma,t) = -2\lambda d(t)\frac{\partial}{\partial\sigma}\left(\sigma\int_\sigma^\infty \frac{\tau\hat{\mathcal{G}}_r(\tau,t)}{\sqrt{\tau^2-\sigma^2}}\,\mathrm{d}\tau\right). \tag{4.155}$$

Note that in order for the integral in (4.155) to exist, we require there to be $l, m > 0$ such that

$$\hat{\mathcal{G}}_r = O\left(\frac{\log(R)^l}{R^{1+m}}\right) \quad \text{as} \quad R \to \infty. \tag{4.156}$$

We shall discuss this requirement in more detail when we look at the far-field behaviour of the solution.

We recall the identities

$$\mathrm{J}_{1/2}(\sigma S) = \sqrt{\frac{2}{\pi\sigma S}}\sin(\sigma S), \quad \Gamma\left(\frac{1}{2}\right) = \sqrt{\pi}.$$

Therefore, defining $\Upsilon_r(r,z,t) = \hat{\Upsilon}_r(R,Z,t)$, the leading-order-outer solution is given by

$$\hat{\Upsilon}_r(R,Z,t) = \frac{1}{d(t)}\int_0^\infty \beta(S,t)\mathrm{J}_0(SR)\mathrm{e}^{SZ}\,\mathrm{d}S, \tag{4.157}$$

$$\beta(S,t) = \frac{2}{\pi}\left[\int_0^1 k_1(\sigma,t)\sin(\sigma S)\,\mathrm{d}\sigma + \int_1^\infty k_2(\sigma,t)\sin(\sigma S)\,\mathrm{d}\sigma\right], \tag{4.158}$$

along with (4.154)–(4.155).

As in three-dimensional Wagner theory, we can find a condition for $d(t)$, by enforcing the correct behaviour of the displacement potential at the turnover curve. Since the velocity must have an inverse square-root singularity, we require $\hat{\Upsilon}_r$ to have

3/2-power behaviour as $(R,Z)\to(1,0)$. Hence, we evaluate (4.157) on $Z=0$ and write $R=1-\delta$, where $0<\delta\ll 1$, to find that

$$\hat{\Upsilon}_r(1-\delta,0,t)=\frac{2}{\pi d(t)}\left[\int_{1-\delta}^{1}\frac{k_1(\sigma,t)}{\sqrt{\sigma^2-(1-\delta)^2}}\,\mathrm{d}\sigma+\int_{1}^{\infty}\frac{k_2(\sigma,t)}{\sqrt{\sigma^2-(1-\delta)^2}}\,\mathrm{d}\sigma\right]. \quad (4.159)$$

Using (4.154)–(4.155) and integrating by parts, we find

$$\hat{\Upsilon}_r(1-\delta,0,t)=\frac{2}{\pi}\left[I_1(1-\delta,t)+I_2(1-\delta,t)+I_3(1-\delta,t)\right], \quad (4.160)$$

where

$$I_1(1-\delta,t) = d(t)\int_{1-\delta}^{1}\frac{1}{\sqrt{\sigma^2-(1-\delta)^2}}\int_0^{\sigma}\frac{\tau g(\tau,t)}{\sqrt{\sigma^2-\tau^2}}\,\mathrm{d}\tau\mathrm{d}\sigma, \quad (4.161)$$

$$I_2(1-\delta,t) = -2\lambda\int_{1}^{\infty}\frac{\sigma^2}{(\sigma^2-(1-\delta)^2)^{3/2}}\int_{\sigma}^{\infty}\frac{\tau\hat{\mathcal{G}}_r(\tau,t)}{\sqrt{\tau^2-\sigma^2}}\,\mathrm{d}\tau\mathrm{d}\sigma, \quad (4.162)$$

$$I_3(1-\delta,t) = \frac{2\lambda}{\sqrt{1-(1-\delta)^2}}\int_{1}^{\infty}\frac{\tau\hat{\mathcal{G}}_r(\tau,t)}{\sqrt{\tau^2-1}}\,\mathrm{d}\tau. \quad (4.163)$$

As $\delta\to 0$, we find that the singular terms in (4.161)–(4.163) are given by

$$\begin{aligned}
I_1 &= \left(\sqrt{2}d(t)\int_0^1\frac{\tau g(\tau,t)}{\sqrt{1-\tau^2}}\,\mathrm{d}\tau\right)\delta^{1/2}+O\left(\delta^{3/2}\right),\\
I_2 &= \left(-\sqrt{2}\lambda\int_1^{\infty}\frac{\tau\hat{\mathcal{G}}_r(\tau,t)}{\sqrt{\tau^2-1}}\,\mathrm{d}\tau\right)\delta^{-1/2}+2\lambda\left[\frac{7}{4\sqrt{2}}\int_1^{\infty}\frac{\tau\hat{\mathcal{G}}_r(\tau,t)}{\sqrt{\tau^2-1}}\,\mathrm{d}\tau\right.\\
&\qquad\left.+\sqrt{2}\left(\frac{\partial}{\partial\sigma}\int_{\sigma}^{\infty}\frac{\tau\hat{\mathcal{G}}_r(\tau,t)}{\sqrt{\tau^2-\sigma}}\,\mathrm{d}\tau\right)\Bigg|_{\sigma=1}\right]\delta^{1/2}+O\left(\delta^{3/2}\right),\\
I_3 &= \left(\sqrt{2}\lambda\int_1^{\infty}\frac{\tau\hat{\mathcal{G}}_r(\tau,t)}{\sqrt{\tau^2-1}}\,\mathrm{d}\tau\right)\delta^{-1/2}+\left(\frac{\lambda}{2\sqrt{2}}\int_1^{\infty}\frac{\tau\hat{\mathcal{G}}_r(\tau,t)}{\sqrt{\tau^2-1}}\,\mathrm{d}\tau\right)\delta^{1/2}+O\left(\delta^{3/2}\right).
\end{aligned}$$

In order for Υ to have 3/2-power behaviour as $(R,Z)\to(1,0)$, the coefficient of the $O(\delta^{1/2})$ term in (4.160) must vanish, giving

$$d(t)\int_0^1\frac{\tau g(\tau,t)}{\sqrt{1-\tau^2}}\,\mathrm{d}\tau+2\lambda\int_1^{\infty}\frac{\tau\hat{\mathcal{G}}_r(\tau,t)}{\sqrt{1-\tau^2}}\,\mathrm{d}\tau+2\lambda\left(\frac{\partial}{\partial\sigma}\int_{\sigma}^{\infty}\frac{\tau\hat{\mathcal{G}}_r(\tau,t)}{\sqrt{\tau^2-\sigma^2}}\,\mathrm{d}\tau\right)\Bigg|_{\sigma=1}=0, \quad (4.164)$$

provided (4.156) holds so that the second and third integrals exist. In theory, this allows us to determine the correction to the turnover curve location due to the cushioning air layer. Note that if $\lambda=0$, (4.164) is simply the Wagner condition for the turnover curve, as expected.

By definition, recall that $g(R,t) = t - f(dR)$. In the first integral of (4.164) we write $\tau = \sin\theta$, while in the second integral we put $\tau = \cosh\xi$, and in the third integral we set $\tau = \sigma\cosh\xi$. After some algebraic manipulation, we deduce from (4.164) that

$$\begin{aligned} 0 &= td(t) - d(t)\int_0^{\pi/2} f(d(t)\sin\theta)\sin\theta\,\mathrm{d}\theta \\ &\quad +4\lambda\int_0^{\infty}\hat{\mathcal{G}}_r(\cosh\xi,t)\cosh\xi\,\mathrm{d}\xi + 2\lambda\int_0^{\infty}\hat{\mathcal{G}}_r'(\cosh\xi,t)\cosh^2\xi\,\mathrm{d}\xi. \end{aligned} \tag{4.165}$$

Here, $\hat{\mathcal{G}}_r'(\cdot,\cdot)$ indicates differentiation with respect to the first argument.

Finally, we can utilise the kinematic boundary condition on the body and integration by parts to deduce that $\hat{h}_r = h_r(dR,t)$ is given by

$$\hat{h}_r(R,t) = \frac{2}{\pi d(t)^2}\left[\frac{k_1(1,t)-k_2(1,t)}{\sqrt{R^2-1}} - \int_0^1 \frac{k_1'(\sigma,t)}{\sqrt{R^2-\sigma^2}}\,\mathrm{d}\sigma - \int_1^R \frac{k_2'(\sigma,t)}{\sqrt{R^2-\sigma^2}}\,\mathrm{d}\sigma\right], \tag{4.166}$$

for $R > 1$, again under the assumption (4.156).

4.3.3 Summary of the problem

If we write $U_r(r,t) = \hat{U}_r(R,t)$, $P_r(r,t) = \hat{P}_r(R,t)$, then we find that the impact is governed by the following equations: for $R > 1$, $\hat{h}_r(R,t)$, $\hat{U}_r(R,t)$, $\hat{P}_r(R,t)$ and $\hat{\mathcal{G}}_r(R,t)$ must satisfy

$$\hat{h}_r = \frac{2}{\pi d^2}\left[\frac{k_1(1,t)-k_2(1,t)}{\sqrt{R^2-1}} - \int_0^1 \frac{k_1'(\sigma,t)}{\sqrt{R^2-\sigma^2}}\,\mathrm{d}\sigma - \int_1^R \frac{k_2'(\sigma,t)}{\sqrt{R^2-\sigma^2}}\,\mathrm{d}\sigma\right], \tag{4.167}$$

$$0 = \left(\frac{\partial}{\partial t} - \frac{\dot{d}R}{d}\frac{\partial}{\partial R}\right)\left(f(dR) - t - \hat{h}_r\right) + \frac{1}{dR}\frac{\partial}{\partial R}\left(R\hat{U}_r\left(f(dR) - t - \hat{h}_r\right)\right), \tag{4.168}$$

$$-\frac{1}{d}\frac{\partial\hat{P}_r}{\partial R} = \left(\frac{\partial}{\partial t} - \frac{\dot{d}R}{d}\frac{\partial}{\partial R}\right)\hat{U}_r + \frac{\hat{U}_r}{d}\frac{\partial\hat{U}_r}{\partial R}, \tag{4.169}$$

$$\hat{P}_r = \left(\frac{\partial^2}{\partial t^2} - \frac{2\dot{d}R}{d}\frac{\partial^2}{\partial R\partial t} + \frac{\dot{d}^2R^2}{d^2}\frac{\partial^2}{\partial R^2} + \frac{\left(2\dot{d}^2 - d\ddot{d}\right)R}{d^2}\frac{\partial}{\partial R}\right)\hat{\mathcal{G}}_r, \tag{4.170}$$

where for $0 \le \sigma \le 1$,

$$k_1(\sigma,t) = d^2\left(\sigma t - \sigma\int_0^{\pi/2} f(d(t)\sigma\sin\theta)\sin\theta\,\mathrm{d}\theta\right), \tag{4.171}$$

and for $\sigma > 1$,

$$k_2(\sigma, t) = -2\lambda d \frac{\partial}{\partial \sigma}\left[\sigma^2 \int_0^\infty \hat{\mathcal{G}}_r(\sigma \cosh\xi, t)\cosh\xi \,\mathrm{d}\xi\right]; \tag{4.172}$$

moreover, $d(t)$ is governed by

$$\begin{aligned} 0 = td(t) - d(t)\int_0^{\pi/2} f(d(t)\sin\theta)\sin\theta \,\mathrm{d}\theta \\ + 4\lambda \int_0^\infty \hat{\mathcal{G}}_r(\cosh\xi, t)\cosh\xi \,\mathrm{d}\xi + 2\lambda \int_0^\infty \hat{\mathcal{G}}_r'(\cosh\xi, t)\cosh^2\xi \,\mathrm{d}\xi, \end{aligned} \tag{4.173}$$

and we must impose the boundary conditions

$$\hat{U}_r = \dot{d}(t), \quad \hat{h}_r = f(d(t)) - t \quad \text{at} \quad R = 1 \tag{4.174}$$

and the far-field conditions that $\hat{h}_r$ is integrable and $\hat{P}_r$ vanishes. In particular, we note that the integrals in (4.172) and (4.173) exist only if the condition (4.156) pertains. Finally, we require the initial conditions

$$h_r(r, 0) = 0, \quad U_r(r, 0) = 0. \tag{4.175}$$

4.3.4 Far-field expansion

While performing a systematic far-field expansion is best approached on a case-by-case basis – as will become apparent in our small-λ solution for a paraboloid – we can deduce the leading-order terms in the expansion for the air velocity from (4.168). Suppose the axisymmetric body profile is given by $f(r) = r^n$, where $n \geq 1$. Since we require $\hat{h}_r$ to be integrable in the far-field, it is clear that

$$\left(\frac{\partial}{\partial t} - \frac{\dot{d}R}{d}\frac{\partial}{\partial R}\right)\left(f(dR) - t - \hat{h}_r\right) \sim -1 \tag{4.176}$$

as $R \to \infty$. Hence, in order to maintain a balance in (4.168), we can conclude that for $1 \leq n < 2$,

$$\hat{U}_r \sim \frac{1}{2d^{n-1}R^{n-1}} + \frac{t}{2d^{2n-1}R^{2n-1}} \quad \text{as} \quad R \to \infty \tag{4.177}$$

and for $n \geq 2$,

$$\hat{U}_r \sim \frac{1}{2d^{n-1}R^{n-1}} + \frac{A(t)}{R^{2n-1}} \quad \text{as} \quad R \to \infty \tag{4.178}$$

where $A(t)$ is a degree of freedom.

Now, for $n = 1$, after substituting the expansion for $\hat{U}_r$ into (4.169), we deduce that

$$\hat{P}_r \sim -\frac{1}{2}\log R \quad \text{as} \quad R \to \infty, \tag{4.179}$$

and hence that the air pressure has a singularity even stronger than a source at infinity. It follows from (4.170) that $\hat{\mathcal{G}}_r = O(\log R)$ as $R \to \infty$, which violates (4.156). Hence, the method as described does not work for a cone.

For $1 < n < 2$, we can substitute (4.177) into (4.169) to deduce that

$$\hat{P}_r \sim \frac{3-n}{8(n-1)d^{2(n-1)}} \frac{1}{R^{2(n-1)}} + \dots \quad \text{as} \quad R \to \infty. \tag{4.180}$$

It then follows from (4.170) that $\hat{\mathcal{G}}_r = O(1/R^{2(n-1)})$ as $R \to \infty$. Therefore, (4.156) holds if and only if $n > 3/2$.

When $n \geq 2$, we do not have an explicit expression for the $O(1/R^{2n-1})$ term in (4.178), so we cannot give an explicit expansion for $\hat{P}_r$ as $R \to \infty$. However, it is straightforward to show that $\hat{P}_r$, and hence $\hat{\mathcal{G}}_r$, are of $O(1/R^{2(n-1)})$ as $R \to \infty$, so that (4.156) is satisfied and therefore the method holds.

Since the method breaks down when $1 \leq n \leq 3/2$, before applying our method we would need to subtract from the displacement potential a harmonic function that accounts for the non-integrable singularity in $\hat{\mathcal{G}}_r$ in the far-field. We do not pursue this analysis any further here and leave this for later work. Henceforth, we focus only on impactors for which $n > 3/2$.

4.3.5 Small-λ solution

With $f(r) = r^n$, note that we can integrate (4.171) explicitly to find that

$$k_1(\sigma, t) = d(t)^2 \left(\sigma t - 2^n d(t)^n \sigma^{n+1} \mathrm{B}\left(\frac{n+2}{2}, \frac{n+2}{2} \right) \right), \tag{4.181}$$

where $\mathrm{B}(\cdot, \cdot)$ is the beta function. Similarly, (4.173) becomes

$$\begin{aligned} 0 \;=\; & t d(t) - 2^n d(t)^{n+1} \mathrm{B}\left(\frac{n+2}{2}, \frac{n+2}{2} \right) \\ & + 4\lambda \int_0^\infty \hat{\mathcal{G}}_r(\cosh\xi, t) \cosh\xi \, \mathrm{d}\xi + 2\lambda \int_0^\infty \hat{\mathcal{G}}_r'(\cosh\xi, t) \cosh^2\xi \, \mathrm{d}\xi, \end{aligned} \tag{4.182}$$

As we did in two dimensions, we shall now move on to the regime in which the air-to-liquid density ratio is small so that $\lambda \ll 1$.

We begin by expanding $\hat{h}_r$, $\hat{U}_r$, $\hat{P}_r$, $\hat{\mathcal{G}}_r$, $d(t)$, k_1 and k_2 in (4.167)–(4.170), (4.172), (4.181) and (4.182) in powers of λ and denote leading-order variables with a superscript (0). At leading order, (4.182) reduces to

$$d^{(0)}(t) = \frac{t^{1/n}}{2} \left(\mathrm{B}\left(\frac{n+2}{2}, \frac{n+2}{2} \right) \right)^{-1/n}, \tag{4.183}$$

which is the Wagner solution, as given by (2.138) in §2.3.6.2. Furthermore, (4.172) implies that $k_2 = O(\lambda)$ and from (4.181) we see that

$$k_1^{(0)}(\sigma, t) = \frac{\sigma t^{(n+2)/n}}{4} \left(\mathrm{B}\left(\frac{n+2}{2}, \frac{n+2}{2} \right) \right)^{-2/n} (1 - \sigma^n) \,. \tag{4.184}$$

Hence, the leading-order-outer free surface is found from (4.167) to be given by

$$\hat{h}_r^{(0)}(R, t) = \frac{2t}{\pi R} \left[{}_2\mathrm{F}_1 \left(\frac{1}{2}, \frac{n+1}{2}, \frac{n+3}{2}, \frac{1}{R^2} \right) - R \arcsin \frac{1}{R} \right] \tag{4.185}$$

for $R > 1$, where ${}_2\mathrm{F}_1(\cdot, \cdot, \cdot, \cdot)$ is the ordinary hypergeometric function, cf (2.139).

Since $\hat{h}_r^{(0)}$ is linear in t and $d^{(0)}$ is proportional to $t^{1/n}$, we seek a similarity solution to the leading-order forms of (4.168)–(4.170) by writing

$$\begin{gathered} \hat{h}_r^{(0)} = t\tilde{h}_r(R), \quad d^{(0)} = \alpha t^{1/n}, \quad \hat{U}_r^{(0)} = t^{(1-n)/n} \tilde{U}_r(R), \\ \hat{P}_r^{(0)} = t^{2(1-n)/n} \tilde{P}_r(R), \, \hat{\mathcal{G}}_r^{(0)} = t^{2/n} \tilde{\mathcal{G}}_r(R), \end{gathered} \tag{4.186}$$

where $\alpha = (1/2)\mathrm{B}((n+2)/2, (n+2)/2)^{-1/n}$. Under this transformation (4.168)–(4.170) become

$$1 + \tilde{h}_r - \frac{R}{n} \frac{\mathrm{d}\tilde{h}_r}{\mathrm{d}R} = \frac{1}{\alpha R} \frac{\mathrm{d}}{\mathrm{d}R} \left(R\tilde{U}_r (\alpha^n R^n - 1 - \tilde{h}_r) \right). \tag{4.187}$$

$$\frac{\mathrm{d}\tilde{P}_r}{\mathrm{d}R} = \alpha \left(\frac{n-1}{n} \right) \tilde{U}_r + \frac{\alpha R}{n} \frac{\mathrm{d}\tilde{U}_r}{\mathrm{d}R} - \tilde{U}_r \frac{\mathrm{d}\tilde{U}_r}{\mathrm{d}R}, \tag{4.188}$$

$$\tilde{P}_r = \frac{R^2}{n^2} \frac{\mathrm{d}^2\tilde{\mathcal{G}}_r}{\mathrm{d}R^2} + \frac{R\,(n-3)}{n^2} \frac{\mathrm{d}\tilde{\mathcal{G}}_r}{\mathrm{d}R} + \frac{2\,(2-n)}{n^2} \tilde{\mathcal{G}}_r \tag{4.189}$$

for $R > 1$. Upon integrating (4.187) with respect to R and applying the boundary condition (4.174), we find that the leading-order radial air velocity is given by

$$\tilde{U}_r(R) = \frac{1}{R\left(\alpha^n R^n - 1 - \tilde{h}_r \right)} \int_1^R \alpha s \left(1 + \tilde{h}_r(s) - \frac{s}{n} \tilde{h}_r'(s) \right) \mathrm{d}s \tag{4.190}$$

for $R > 1$

On a case-by-case basis, it is then in principle straightforward to integrate (4.188) with respect to R subject to the far-field condition that $\tilde{P}_r \to 0$ as $R \to \infty$. Once we know $\tilde{P}_r$, (4.189) is simply a second-order ordinary differential equation for the function $\tilde{\mathcal{G}}_r$, which we can solve using the method of variation of parameters to obtain the solution

$$\tilde{\mathcal{G}}_r(R) = R^{2-n} \int_R^\infty \frac{n\tilde{P}_r(s)}{s^{3-n}} \, \mathrm{d}s - R^2 \int_R^\infty \frac{n\tilde{P}_r(s)}{s^3} \, \mathrm{d}s, \tag{4.191}$$

valid for $R > 1$.

Having found the leading-order versions of $\tilde{H}_r$, $\tilde{U}_r$, $\tilde{P}_r$ and $\tilde{\mathcal{G}}_r$, we can use (4.182) to deduce that the location of the turnover curve is given by $d \sim d^{(0)}(t)+\lambda d^{(1)}(t)+\ldots$ as $\lambda \to 0$, where $d^{(1)}(t)$ is given by

$$d^{(1)}(t) = \frac{2}{n}\left[2\int_0^\infty \tilde{\mathcal{G}}_r(\cosh\xi)\cosh\xi\,\mathrm{d}\xi + \int_0^\infty \tilde{\mathcal{G}}_r'(\cosh\xi)\cosh^2\xi\,\mathrm{d}\xi\right] t^{(2-n)/n}. \quad (4.192)$$

There is a temporal nonuniformity in our small-λ asymptotic expansion as we approach the moment of impact. When $t = O(\lambda^{n/(n-1)})$, comparing (4.183) with (4.192), we note that $\lambda d_1 = O(d_0)$ and hence we scale into the small-time regime by writing

$$\begin{gathered} d = \lambda^{1/(n-1)}\bar{d}, \quad t = \lambda^{n/(n-1)}\bar{t}, \quad (k_1,k_2) = \lambda^{(n+2)/(n-1)}\left(\bar{k}_1,\bar{k}_2\right), \\ h = \lambda^{n/(n-1)}\bar{h}, \qquad U = \frac{\bar{U}}{\lambda}, \qquad P = \frac{\bar{P}}{\lambda^2}, \quad \hat{\mathcal{G}}_r = \lambda^{2/(n-1)}\bar{G}_r, \end{gathered} \quad (4.193)$$

which returns (4.167)–(4.173) with $\lambda = 1$, a version of the full problem that can only be tackled numerically.

4.3.6 Impact of a paraboloid

We now consider the example of an impacting paraboloid, so that $n = 2$. By (4.183) and (4.185), the leading-order turnover curve location is given by

$$d^{(0)}(t) = \sqrt{\frac{3t}{2}}, \quad (4.194)$$

while the leading-order free surface elevation is given by

$$\hat{h}_r^{(0)}(R,t) = \frac{2t}{\pi}\left[\left(\frac{3}{2}R^2 - 1\right)\arcsin\left(\frac{1}{R}\right) - \frac{3}{2}\sqrt{R^2-1}\right] \quad (4.195)$$

for $R > 1$. It is trivial to note that (4.195) satisfies the leading-order Wagner condition

$$\hat{h}_r^{(0)}(1,t) = d^{(0)}(t)^2 - t,$$

and that in the far-field

$$\hat{h}_r^{(0)}(R,t) = \frac{4t}{15\pi R^3} + O\left(\frac{1}{R^5}\right) \quad \text{as} \quad R \to \infty. \quad (4.196)$$

Upon integrating (4.190) and applying the boundary condition (4.174), we deduce that

$$\hat{U}_r^{(0)}(R,t) = \sqrt{\frac{6}{t}}\frac{1}{2R}\left[\frac{2\sqrt{R^2-1} - 2R^2\arcsin(1/R) + \pi R^2}{3\pi R^2 - 2\pi - 6R^2\arcsin(1/R) + 4\arcsin(1/R) + 6\sqrt{R^2-1}}\right] \quad (4.197)$$

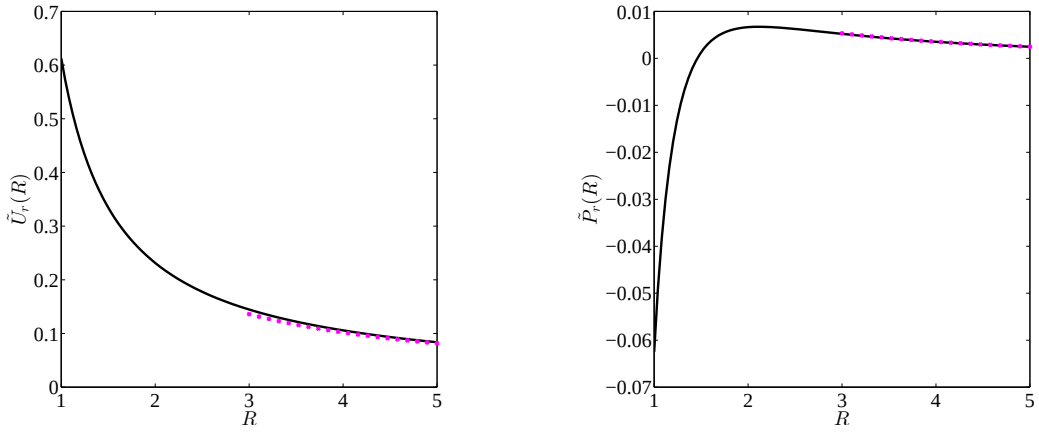

Figure 4.13: Leading-order tangential air velocity, given by (4.190), and air pressure, given by (4.199) as well as their asymptotic behaviour for large R, as denoted by the magenta circles. This figure is based on one in Moore and Oliver (2014).

for $R > 1$. Note that we can clearly see the small-time singularity in this expression: $\hat{U}_r \to \infty$ as $t \to 0$. In the far-field,

$$\hat{U}_r^{(0)} = \frac{1}{\sqrt{t}}\left(\frac{1}{\sqrt{6}}\frac{1}{R} + O\left(\frac{1}{R^3}\right)\right) \quad \text{as} \quad R \to \infty, \tag{4.198}$$

so that the air velocity potential has a logarithmic singularity at infinity. This compares favourably with Czaykowski (1970), who finds logarithmic behaviour for the velocity potential at the point of contact in his solution for the touchdown of a rigid sphere onto a rigid flat surface.

Recalling the similarity formulation in §4.3.5, when $n = 2$ we can exactly integrate (4.188) with respect to R and apply the far-field condition that $\hat{P}_r^{(0)} \to 0$ as $R \to \infty$ to obtain the leading-order air pressure

$$\hat{P}_r^{(0)}(R) = -\frac{\tilde{U}_r^{(0)2}}{2t} + \frac{1}{2t}\sqrt{\frac{3}{2}}\left(R\tilde{U}_r^{(0)} - \frac{1}{\sqrt{6}}\right), \tag{4.199}$$

for $R > 1$. In the far-field,

$$\hat{P}_r^{(0)} = \frac{1}{12t}\frac{1}{R^2} - \frac{1}{3\pi t}\frac{1}{R^3} + O\left(\frac{1}{R^4}\right) \quad \text{as} \quad R \to \infty, \tag{4.200}$$

We plot the similarity form of the air pressure and radial component of velocity in Figure 4.13. Note that the air pressure is not monotonically increasing in R, unlike in the parabola example we studied in two-dimensions. There is in fact a maximum pressure at $R \approx 2.117$.

Unfortunately, we must solve for $\hat{\mathcal{G}}_r^{(0)}$ numerically using (4.191). We do this by splitting the range of integration into $[R, N]$ and $[N, \infty)$ say, where $N \gg 1$. The

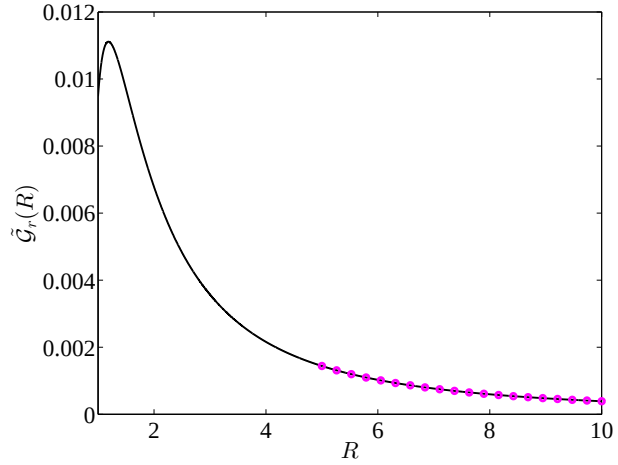

Figure 4.14: The function $\tilde{\mathcal{G}}_r(R)$ as defined by (4.191) and its associated far-field asymptotic behaviour as denoted by the magenta circles. Again, this plot is based on one in Moore and Oliver (2014).

integrand over the latter interval is approximated using the far-field expansion of the air pressure as given by (4.200). The resulting plot of the similarity function $\tilde{\mathcal{G}}_r(R)$ is given in Figure 4.14. We note that, in particular,

$$\hat{\mathcal{G}}_r^{(0)}(R) = \frac{t}{24R^2} - \frac{4t}{45\pi R^3} + O\left(\frac{1}{R^4}\right) \quad \text{as} \quad R \to \infty, \tag{4.201}$$

so that $\hat{\mathcal{G}}_r^{(0)}$ meets the far-field criterion given in (4.156).

Finally, to find the $O(\lambda)$-correction to the turnover curve, we substitute $\hat{\mathcal{G}}_r^{(0)}$ into (4.192). After some algebraic manipulation, we find that

$$d^{(1)}(t) = 4\int_0^\infty \cosh\xi \left(\int_{\cosh\xi}^\infty \frac{(s^2 - 2\cosh^2\xi)}{s^3}\tilde{P}_r(s)\,\mathrm{d}s\right)\,\mathrm{d}\xi, \tag{4.202}$$

an expression we can only evaluate numerically. We find that $d^{(1)} = 0.036654$ to five significant figures. Hence, for small values of λ, the presence of a cushioning air layer increases the distance of the Wagner turnover curve from the minimum point of the paraboloid, although the speed of the turnover curve remains unchanged.

In order to interpret this result for $d^{(1)}$, we proceed as we did in §4.2.8.1 and discern whether there can be a far-field source/sink in the liquid. Consider the far-

field behaviour of $\hat{h}_r^{(1)}(R,t)$. At $O(\lambda)$, (4.167) gives

$$\begin{aligned}\hat{h}_r^{(1)}(R,t) &= \frac{2d^{(1)}\sqrt{6t}}{\pi}\left(R^2\arcsin\frac{1}{R}-\sqrt{R^2-1}-\frac{2}{3\sqrt{R^2-1}}\right)- \\ &\quad \frac{4}{3t\pi}\left[\frac{k_2^{(0)}(1,t)}{\sqrt{R^2-1}}+\int_1^R\frac{\partial}{\partial\sigma}\left(k_2^{(0)}(\sigma,t)\right)\frac{1}{\sqrt{R^2-\sigma^2}}\,\mathrm{d}\sigma\right] \qquad (4.203)\end{aligned}$$

for $R>1$, where we note that $k_2^{(0)}(1,t)=-2d^{(0)}d^{(1)}t$. Using our numerical solutions for $\hat{\mathcal{G}}_r^{(0)}$ and $d^{(1)}$, we can approximate $\partial k_2^{(0)}/\partial\sigma$ at leading order. Therefore, we solve for $\hat{h}_r^{(1)}$ numerically and plot the result in Figure 4.15. Expanding (4.203) close to the turnover point, we deduce that

$$\hat{h}_r^{(1)}\sim\sqrt{6t}d_1-\frac{8}{\pi}\left(\sqrt{3t}d_1+\frac{k_2^{(0)\prime}(1,t)}{3\sqrt{2}\pi t}\right)\sqrt{R-1}+2\sqrt{6t}d_1(R-1) \qquad (4.204)$$

as $R\to1^+$. Moreover, as $R\to\infty$, the dominant behaviour is determined by the integral term and we find that

$$\hat{h}_r^{(1)}\sim-\frac{16t^{1/2}}{45\pi^2}\sqrt{\frac{2}{3}}\frac{\log R}{R^3}\quad\text{as}\quad R\to\infty. \qquad (4.205)$$

We plot both of these asymptotes in Figure 4.15. Using (4.205) and the plot in Figure 4.15, we see that $\hat{h}_r^{(1)}<0$ for $R>R^*\approx1.356$, so that the $O(\lambda)$-correction to the free surface is negative in this range. By conservation of mass, we expect the displacement of fluid due to the free surface correction to be balanced by an increase in the turnover curve location and/or by an effective source/sink in the far-field. However, as $\hat{\Upsilon}_r=\hat{\mathcal{G}}_r$ on the free surface, $\hat{\Upsilon}_r$ is of $O(1/R^2)$ as $R\to\infty$ on the free surface, so there cannot be a source or sink in the far field. Thus, the mass of liquid displaced by the $O(\lambda)$-correction to the free surface is compensated entirely by shifting the turnover curve away from minimum of the paraboloid.

As is evident from (4.205), there is a nonuniformity in the far-field expansion of $\hat{h}_r$ when $\log R=O(1/\lambda)$. This is reminiscent of the far-field nonuniformity for the wedge example we saw in §4.2.8.3 and we do not consider further here the resolution of this nonuniformity.

In theory, it is possible to calculate the force on the impactor by finding the correction to the liquid pressure due to the air from (4.148). However, this is nontrivial as we do not have an analytic expression for the function $\hat{\mathcal{G}}_r^{(0)}$, and so we do not pursue it here. As in the two-dimensional impact of a parabola, we would expect the air cushion to reduce the force on the impactor.

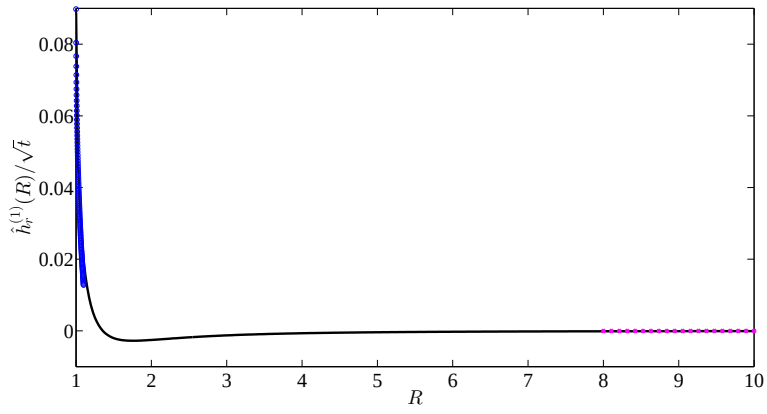

Figure 4.15: Numerical solution for the $O(\lambda)$-correction to the free surface location, as given by (4.203). The behaviour as $R \to 1$ given by (4.204) and the far-field behaviour given in (4.205) are represented by the circles. This plot is based on one in Moore and Oliver (2014).

4.3.7 Summary

In this section we extended our model for inviscid, incompressible air-cushioning effects in impact problems to three-dimensions, in particular for axisymmetric body profiles. To leading-order in the deadrise angle, we were able to determine a coupled system of integro-differential equations for the liquid free surface, air pressure, location of the turnover curve and the radial component of air velocity.

A far-field analysis showed that our method holds for any body profile of the form $f(r) = r^n$ where $n > 3/2$ and we proceeded to find the solution in the asymptotic limit in which the air/liquid density ratio is much smaller than the deadrise angle. This enabled us to find an expression for the correction to the turnover curve location due to the air layer. We considered the particular example of an impacting paraboloid and found that the turnover curve is displaced slightly further from the minimum point of the paraboloid due to the air pressure, but that its speed is unchanged at $O(\lambda)$.

4.3.7.1 Extensions and open questions

As mentioned above, the method described in this section breaks down for the impact of a cone as there is a singularity in the air pressure which is too strong, making the function $\hat{\mathcal{G}}_r$ non-integrable, as it breaks the condition (4.156). The resolution of this breakdown is an open question in post-impact air-cushioning.

We can also consider extensions similar to those outlined after our two-dimensional analysis in §4.2.9.1. The nonuniformity as $t \to 0$ in the small-λ asymptotics needs to be addressed. Typically this will involve numerical methods, but considerations of other physical effects might be necessary.

Chapter 5

Air-cushioning of splash jets and sheets

5.1 Introduction

Wagner theory tells us that, in an impact, a splash jet or sheet is produced in the turnover region as the free surface is violently displaced. The Wagner jet is almost universally assumed to not separate from the impactor and in Chapter 4 we showed that this implies that its influence on the outer air flow was small. Moreover, we noted in Chapter 2 that for smooth impactors, the splash jet or sheet is predicted to have infinite extent in Wagner theory, which is physically unrealistic. In this chapter, motivated by experimental works, we aim to derive a more systematic model of splash jet (and sheet) evolution, incorporating a range of physical effects into our model. Before moving on to the modelling proper, we will begin by outlining the experimental motivation to the chapter and then briefly discussing the existing literature on jets.

5.1.1 Droplet impacts

Two specific sets of experiments motivate the work in this chapter, which seeks to gain a better model describing the evolution of a jet or sheet. The first set of experiments depict the wonderful deflection and bending of ejecta sheets seen in droplet impacts. Thoroddsen (2002) consider the ejecta sheets produced by drops of high Weber numbers and of various viscosities. Their experiments distinguish various regimes. For higher viscosity droplets, the ejecta sheet[1] is shot out at a speed of approximately twice the impact speed and is shown to persist (i.e. to not break up

[1]We shall use 'ejecta sheet' and 'splash jet' interchangeably.

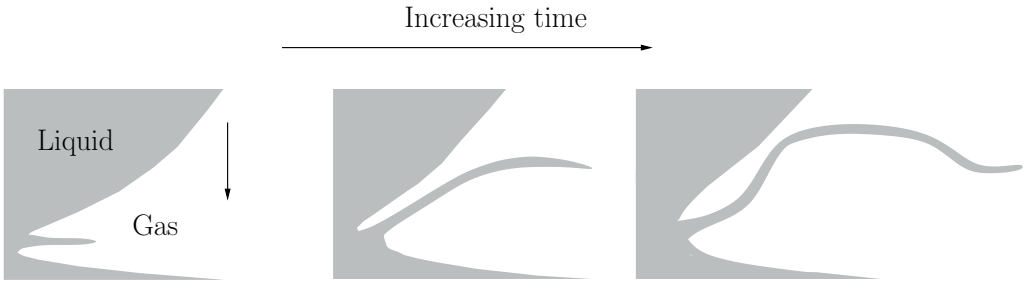

Figure 5.1: Side-on view of the bending of a splash sheet due to the surrounding gas layer. This schematic is based on the experimental pictures in Thoroddsen et al. (2011) and Thoraval et al. (2012). Note that the thin gas layer can either be that trapped between the impinging droplet and the sheet or that between the sheet and the bulk fluid.

into smaller droplets) for a significant time. In this period, the sheet is shown to bend and touch the deep liquid pool into which the drop is impacting. This touchdown occurs away from the tip of the sheet and results in microdroplets being slung away from the pool/impacting droplet. For lower viscosities, the sheets have much higher speeds, up to $10-20$ times faster than the impact speed. These sheets break up into spray very quickly, although given the limitations in the photographic equipment it is possible there is earlier bending and touchdown of the sheet.

Thoroddsen et al. (2011) discuss the influence of air in the bending and touchdown of ejecta sheets. They perform the same experiments under atmospheric pressure and under a partial vacuum, and see suppression of the touchdown-slingshot behaviour described above in the partial vacuum. They then derive a simple ballistic model to describe the motion of an inviscid sheet produced when a solid sphere impacts a liquid half-space. Introducing an air drag on the sheet causes it to bend and display qualitatively similar behaviour to the experiments. We have drawn a schematic of how the splash sheet evolves in these impacts in Figure 5.1.

More complex bending and knuckling of sheets is displayed in the experiments of Zhang et al. (2012a,b). When a droplet impacts a deep pool of the same liquid they show that there are two distinct jets: the thin, fast ejecta sheet of Thoroddsen (2002), and a later-emerging and somewhat thicker 'lamella'. They consider distinct regimes based on the Reynolds number. For high Reynolds numbers, the lamella and ejecta remain separate and both are seen to curve and bend as described by Thoroddsen (2002). At lower Reynolds numbers, the lamella can bend so substantially as to merge with the ejecta sheet, forming a single sheet.

Thoraval et al. (2012) give a characterisation of different ejecta evolutions from

experimental images of water-glycerin droplets impacting a deep pool of the same liquid. They also use numerical simulations to show how the touchdown of an evolving ejecta can cause the entrapment of air bubbles and the shedding of vorticity into the main droplet.

These experimental works, together with the numerical and experimental evidence in Duchemin and Josserand (2011) and Kolinski et al. (2012) that an air layer persists underneath a spreading droplet just before impact suggests that the surrounding gas has a crucial effect on the evolution of lamellae and ejecta sheets.

5.1.2 Droplet spreading

The second set of experiments motivating this chapter concern the, not unrelated, field of the spreading of viscous droplets when they impact on a substrate. Although ejecta sheets can be produced at the front of the spreading drop (which gives rise to possible undulations and bending as we have just discussed) there is also the possibility of air[2] being entrapped underneath the advancing droplet front. As we discussed in the introduction to the previous chapter, Thoroddsen et al. (2010) show that the 'lamella' (here this is the droplet front) of a spreading drop may levitate on a thin cushion of air, recall Figure 4.2. Their droplets have a range of Reynolds numbers, from $100 - 2000$, and Weber numbers, from $80 - 2400$; these numbers are based on the droplet diameter and impact speed. As depicted in Figure 4.2, the lower free surface of the lamella may touch down on the substrate below and, as the contact line catches up with this patch of touchdown, a bubble of air becomes entrapped. Palacios et al. (2012) find similar behaviour in their impact experiments, showing that there appears to be a limiting ring, that is a maximum radius for which bubble entrapment is observed, to these entrapped bubbles, suggesting that the lamella stops skating on a layer of air a certain time after impact.

Both of the phenomena illustrated in Figures 4.2 and 5.1 involve thin liquid sheets and their interaction with the surrounding gas. In the former, the lamellae tend to be thicker than the layer of air they skate upon, whereas in the latter, the ejecta sheets tend to be thinner than (later stages of the impact) or comparable to (earlier stages of the impact) the gas layers trapped between the sheets and the bulk liquid. It is unclear in both cases whether the main interaction between the liquid and the gas is at the tip of the liquid sheet or due to the pressure difference between the gas above and below the sheet.

[2]A word on notation: we shall use 'air' and 'gas' fairly interchangeably in this chapter. Naturally the ambient fluid can be any liquid or gas, but since it is air in the most common applications we will sometimes lapse into referring to it as such.

5.1.3 Literature review

In this chapter, we seek to investigate what can induce a liquid jet or sheet to undulate, bend and even touch down. Our model will incorporate both the pressure-jump and tip mechanisms. Although there is certainly much existing research on jets, there has been no study of the configurations we have just described: that is jet motion induced by thin layers of gas trapped between the jet and a surface or bulk fluid. We shall therefore attempt to derive some simple canonical models to gain some understanding of the mechanisms governing the interaction between a splash jet (or sheet) and a thin air-cushioning layer. There will be several open questions and possibilities for further research, but we shall indicate that the surrounding gas certainly provides a potential mechanism for the phenomena seen in these experiments.

Nonetheless, it is still of interest to consider the variety of jet studies in the literature. The following papers are concerned with the instability of the liquid jets themselves and their resulting break up. Although this is an important topic in its own right, their analyses are not directly applicable to the bending described above, as we are not concerned with the break up of the jet or sheet, rather the gas layer beneath the jet or sheet. Indeed, in the numerical simulations of Thoraval et al. (2012), it is a reasonable approximation to assume that the splash sheet is of constant speed and thickness along its length during the period of deformation caused by the surrounding gas. However, the results and techniques of the following studies are relevant to any work on jets, particularly in light of the stability analysis we will perform.

A comprehensive review of the following analyses and further studies of jet break-up that are not relevant here (for example, charged jets or jets breaking up under gravity) is given in Eggers and Villermaux (2008). We shall discuss some of the most relevant presently.

Rayleigh (1878) studied the instability of an infinite static cylinder of ideal fluid due to capillary forces. For axially-symmetric disturbances, Rayleigh finds the steady state is unstable to small perturbations. Rayleigh's instability is a temporal instability in which the amplitude of the oscillations grows uniformly along the jet. Keller et al. (1973) argue that in a real jet, which is produced from a nozzle (or a jet-root) oscillations will be negligible close to the nozzle and are more appreciable in amplitude further along the jet. They use a complex wavenumber and real frequency to find so-called spatial instabilities to the steady-state cylinder of ideal fluid due to capillary forces, which do not grow in time, but rather in distance from the nozzle. They find infinitely many unstable modes and show that Rayleigh's mode is not the most unstable.

Squire (1953) looks for long-wavelength instabilities of two-dimensional jets of

ideal fluid between two static, unbounded air layers. The perturbations to the base state are driven by surface tension and the air-liquid density ratio, while gravity is neglected throughout the analysis. The jet thickness is assumed to be thin compared to the wavelength of the disturbances. Squire describes two different types of modes that characterise the stability analysis. Symmetric modes are ones in which the oscillations of the upper and lower free surfaces of the jet are out-of-phase in such a manner that the jet centreline is undisturbed. These disturbances are unstable for long wavelengths provided that surface tension is sufficiently small, but Squire states that antisymmetric modes, in which the oscillations of the free surfaces are in-phase, grow more quickly than the symmetric modes. Squire finds the maximum wavenumber at which instability can occur and compares the theory to experimental results. Hagerty and Shea (1955) consider the symmetric modes in more detail, but they too find that the unstable antisymmetric modes grow more rapidly. The analysis in Hagerty and Shea (1955) is restricted to cases where the undisturbed jet thickness is assumed to remain constant. It should be noted that this assumption is reasonable provided the wavelength of the disturbance is shorter than the lengthscale over which changes in jet thickness are appreciable.

Dombrowski and Hooper (1962) compare the results of Squire (1953) and Hagerty and Shea (1955) to experiments in which a laminar sheet is formed from a single nozzle. They vary the ambient air pressure and show that as the air-liquid density ratio is reduced, the instabilities described in the theory are inhibited, with droplets only forming at the tip of the sheet. However, as the ambient pressure is increased, the sheet is more unstable to small perturbations. They conclude by estimating the size of the drops formed in the break up of the sheet due to this instability. Tharakan et al. (2002) argue that the linear theory is no longer valid when the amplitude of the disturbances gets sufficiently large. As a result they consider the nonlinear breakup of fluid sheets. They find that as the size of the amplitude of the initial disturbance is increased, the size of the resulting break-up length is reduced. Unsurprisingly, they show that this break-up length can also be reduced by increasing the Weber number (i.e. reducing the influence of surface tension).

Although he completely neglects the air, Taylor (1959) uses the antisymmetric/symmetric wave idea in his analysis of ideal, incompressible fluid sheets, performing both a stability analysis and experiments to depict the antisymmetric waves produced by a disturbance. Taylor finds that stationary antisymmetric waves can form on a fluid sheet, taking the form of cardioids centred around the point of disturbance. He then observes these waves experimentally.

Keller and Kolodner (1954) consider a base state in which a spatially-uniform

sheet of ideal fluid moves normally to its bounding surfaces with a constant acceleration caused by a pressure jump across the boundaries of the sheet, simulating an explosion. Their analysis adapts the approach of Taylor (1950), who considers the acceleration of a semi-infinite fluid normally to its bounding surface. The base state is then subjected to out-of-plane perturbations, and Keller and Kolodner (1954) find a dispersion relation between the frequency and wavenumber of the perturbations. The relation depends on both surface tension and the sheet acceleration. Keller and Kolodner (1954) show that a range of unstable modes exist, and when the surface tension is dominated by the acceleration of the sheet, are able to estimate the size of the most unstable mode. They use this value of the most unstable mode to estimate the size of the resulting drops in the break-up of the sheet.

Sterling and Sleicher (1975) consider a cylindrical column of Newtonian fluid moving with uniform velocity in a stationary, inviscid, incompressible medium. The viscosity of the liquid is retained in the model. The base state is given an arbitrary small axisymmetric disturbance and Sterling and Sleicher (1975) derive a dispersion relation between the wavenumber and frequency of this disturbance. The dispersion relation depends on the viscosity and surface tension of the liquid, the speed of the base state, and the density ratio between the liquid and the surrounding medium. Sterling and Sleicher (1975) show that in the appropriate limit it matches with that found by Rayleigh (1878). They deduce that the aerodynamic forces have a destabilising effect on the jet, although in their comparisons to experimental data they are forced to modify their dispersion relation using an empirical parameter that represents the viscosity of the surrounding medium in order to achieve good agreement. Gordillo and Perez-Saborid (2005) provide a theoretical basis for this empirical factor by including the gas viscosity in their model. Their asymptotic theory yields a similar value to the empirical factor in Sterling and Sleicher (1975).

Inspired by applications to explosive charges, Frankel and Weihs (1985) look at the stability of an ideal, incompressible cylindrical jet whose base state has an axial velocity that increases linearly along the length of the jet; that is, the jet is undergoing a purely extensional flow and the cylinder radius is a function of time in the base state. Frankel and Weihs (1985) perturb this base state by small-amplitude standing waves. As a consequence of the extensional flow in the base state, the wavelength of each initial perturbation increases with time. They find that the dominant wavelength changes with time, so that the later in time the motion is considered, the shorter the initial wavelength of the most unstable mode. They neglect several physical effects, such as the surrounding fluid and the viscosity of the jet, the latter of which is introduced in Frankel and Weihs (1987). Viscosity is shown to be destabilising early

in the perturbation, increasing the range of wavelengths whose amplitudes diverge, but it damps the rapidly growing perturbations at later times.

Perhaps the closest analysis to what we do in §5.4 is Tammisola et al. (2011), who consider the stabilising and destabilising effect of a gas flow around a thin jet. The base-state gas flow is derived through Stokes boundary layer theory and they perform a stability analysis for various base states of the jet. They are particularly interested in the initial velocity difference between the jet and the air; when this is small, the air acts to stabilise small perturbations to the jet. Given the breadth of their various flow regimes, the main way in which our analysis will differ from Tammisola et al. (2011) is in the presence of the substrate and the assumption that the lower gas layer is also thin.

As well as these investigations into liquid jets, we will see shortly that in regimes where the reduced Reynolds number in the splash jet (or lamella) is small, the jet flow can behave as though it is extensional, and the resulting models bear similarities to those for the stretching of viscous fibres. The classical work in this field is Trouton (1906), who considers the extension of a viscous fluid purely under gravity; the resulting model bears his name. Of most relevance here are the broad array of extensions to the Trouton model discussed by Dewynne et al. (1992), Dewynne et al. (1994), Howell (1994) and van de Fliert et al. (1995). In particular, van de Fliert et al. (1995) consider the evolution of a viscous thread under an external pressure gradient and their calculations on the role of inertia in the appendix to that paper are a generalised version of the two-dimensional jet equation given in §5.3.1. Furthermore, our pressure-jump equation given (in one form) by (5.56) is an extension of the centreline equation in Howell (1994) for a two-dimensional extensional flow with inertia, gravity and surface tension included.

The coupled nature of these extensional and, in several regimes, inviscid flow models to the surrounding gas flow is what makes the work in this chapter novel, and what makes it challenging. For this reason, we concentrate on two-dimensional jets for the majority of this chapter, although we shall describe the corresponding three-dimensional equations. We hope to give at least some evidence that the resulting theory can describe some mechanisms for splash-jet bending and lamella touchdown, as discussed at the start of this chapter.

5.2 Formulation of the problem

In order to provide a basic model that hopes to provide some insight into the many splash jet and splash sheet phenomena described in §5.1, we consider a canonical

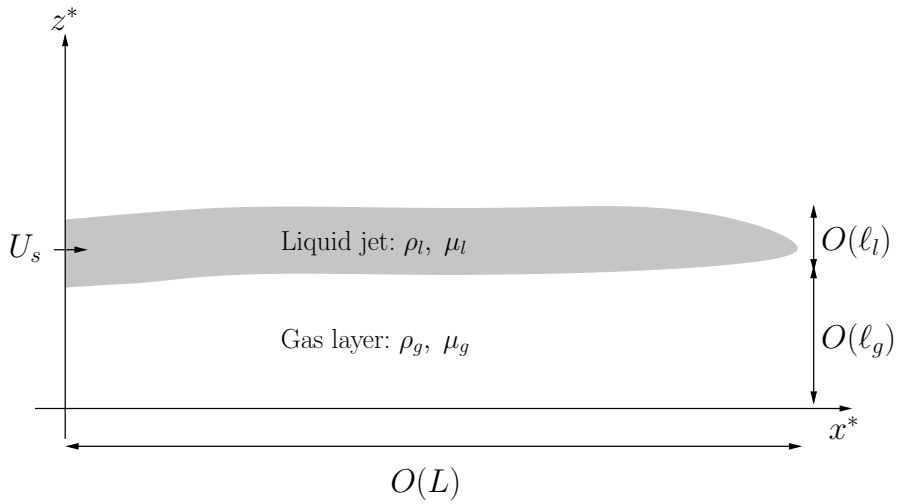

Figure 5.2: A gas cushioning layer is trapped between a liquid jet and a solid surface.

two-dimensional problem in which a liquid jet is shot from an orifice over a rigid, solid substrate. A cushioning gas layer is sandwiched between the jet and the solid surface. At early times, the jet has an order one aspect ratio. The orifice is at $x^* = 0$ in the (x^*, z^*)-plane, with the axes chosen so that the substrate lies along $z^* = 0$. Here and hereafter, an asterisk indicates a dimensional variable. Both the liquid and gas are assumed to be Newtonian and incompressible. The liquid has density ρ_l and viscosity μ_l, and the gas has density ρ_g and viscosity μ_g. Throughout our analysis, we shall neglect the flow in the gas above the jet, assuming that its effect on the jet motion is small compared to the gas layer below. We will check this assumption *a posteriori*.

We suppose that the jet is shot out at a typical speed U_s, that it has a thickness ℓ_l, and that the gas layer has a typical thickness ℓ_g. We are interested in the deflection of the jet caused by the pressure jump between the cushioning gas layer and the quiescent gas above the jet. To this end, we neglect initially the flow near the orifice and the flow near the tip of the jet and consider, in the small-aspect ratio limit, the deflection of the bulk of the jet. Let L be the lengthscale over which deflections to the jet due to this pressure jump are caused. The aspect ratios of the jet and gas layer are assumed to be small; so that $\varepsilon_g = \ell_g/L$ and $\varepsilon_l = \ell_l/L$ are such that $0 < \varepsilon_g,\ \varepsilon_l \ll 1$. The lengthscale L will be determined in terms of the other parameters in order to bring in the pressure jump at leading-order. The configuration is depicted in Figure 5.2.

Note that as well as neglecting the flow near the nozzle, the flow near the jet tip and the early-time evolution when the jet has an order-unity aspect ratio, a further caveat here is that several of the experimental papers we discussed in §5.1 were concerned

with droplet impact into a liquid pool. Our model is readily adapted to consider a large bulk of fluid instead of a solid substrate, but we do not consider that in this thesis.

For the rest of our analysis, variables in the jet are denoted by a lower-case letter and variables in the gas by an upper-case letter. The velocities in the jet and gas are denoted by $\mathbf{u}^* = (u^*, w^*)$ and $\mathbf{U}^* = (U^*, W^*)$ respectively. Moreover, the liquid and gas pressures are denoted by p^* and P^*. The lower free surface of the jet is denoted by $z^* = H^*$ and the upper free surface by $z^* = H^* + h^*$.

In the gas layer, the incompressible Navier-Stokes equations must hold, so that

$$\begin{aligned} \rho_g \left(\mathbf{U}^*_{t^*} + \left(\mathbf{U}^* \cdot \nabla\right) \mathbf{U}^*\right) &= -\nabla P^* + \mu_g \nabla^2 \mathbf{U}^* - \rho_g \mathbf{g}, & (5.1) \\ \nabla \cdot \mathbf{U}^* &= 0, & (5.2) \end{aligned}$$

where ∇ is the gradient operator and $\mathbf{g} = (0, g)^T$ is the acceleration due to gravity. A subscript independent variable indicates differentiation with respect to that variable. In the jet, the corresponding Navier-Stokes equations are given by

$$\begin{aligned} \rho_l \left(\mathbf{u}^*_{t^*} + \left(\mathbf{u}^* \cdot \nabla\right) \mathbf{u}^*\right) &= -\nabla p^* + \mu_l \nabla^2 \mathbf{u}^* - \rho_l \mathbf{g}, & (5.3) \\ \nabla \cdot \mathbf{u}^* &= 0. & (5.4) \end{aligned}$$

On the substrate, the no-flux, no-slip boundary conditions are

$$\mathbf{U}^* = \mathbf{0} \quad \text{on} \quad z^* = 0. \tag{5.5}$$

On the upper and lower free surfaces of the jet, the kinematic boundary conditions are given by

$$\begin{aligned} W^* &= H^*_{t^*} + U^* H^*_{x^*} && \text{on} \quad z^* = H^*, & (5.6) \\ w^* &= H^*_{t^*} + u^* H^*_{x^*} && \text{on} \quad z^* = H^*, & (5.7) \\ w^* &= (H^* + h^*)_{t^*} + u^* (H^* + h^*)_{x^*} && \text{on} \quad z^* = H^* + h^*, & (5.8) \end{aligned}$$

The normal stress condition on $z^* = H^*(x^*, t^*)$ is given by

$$\begin{aligned} p^* - P^* - \frac{\sigma}{\left(1 + H^{*2}_{x^*}\right)^{3/2}} H^*_{x^* x^*} = \frac{2}{\left(1 + H^{*2}_{x^*}\right)} \left[H^{*2}_{x^*} \left(\mu_l u^*_{x^*} - \mu_g U^*_{x^*}\right) + \right. \\ \left. \mu_l w^*_{z^*} - \mu_g W^*_{z^*} - H^*_{x^*} \left(\mu_l \left(u^*_{z^*} + w^*_{x^*}\right) - \mu_g \left(U^*_{z^*} + W^*_{x^*}\right)\right)\right], \end{aligned} \tag{5.9}$$

while on $z^* = H^*(x^*, t^*) + h^*(x^*, t^*)$ it is given by

$$\begin{aligned} p^* + \frac{\sigma}{\left(1 + \left(H^*_{x^*} + h^*_{x^*}\right)^2\right)^{3/2}} \left(H^* + h^*\right)_{x^* x^*} = \\ \frac{2\mu_l}{\left(1 + \left(H^*_{x^*} + h^*_{x^*}\right)^2\right)} \left[\left(H^*_{x^*} + h^*_{x^*}\right)^2 u^*_{x^*} + w^*_{z^*} - \left(H^*_{x^*} + h^*_{x^*}\right) \left(u^*_{z^*} + w^*_{x^*}\right)\right], \end{aligned} \tag{5.10}$$

where σ is the constant coefficient of surface tension between the liquid and the air. The tangential stress condition on $z^* = H^*(x^*, t^*)$ is given by

$$\mu_l \left[2H^*_{x^*}\left(u^*_{x^*} - w^*_{z^*}\right) + \left(H^{*2}_{x^*} - 1\right)\left(u^*_{z^*} + w^*_{x^*}\right)\right] = \mu_g \left[2H^*_{x^*}\left(U^*_{x^*} - W^*_{z^*}\right) + \left(H^{*2}_{x^*} - 1\right)\left(U^*_{z^*} + W^*_{x^*}\right)\right], \quad (5.11)$$

while on $z^* = H^*(x^*, t^*) + h^*(x^*, t^*)$ it is given by

$$\mu_l \left[2\left(H^*_{x^*} + h^*_{x^*}\right)\left(u^*_{x^*} - w^*_{z^*}\right) + \left(\left(H^*_{x^*} + h^*_{x^*}\right)^2 - 1\right)\left(u^*_{z^*} + w^*_{x^*}\right)\right] = 0. \quad (5.12)$$

Finally, the continuity of velocity condition on the lower free surface gives

$$\mathbf{u}^* = \mathbf{U}^* \quad \text{on} \quad z^* = H^*. \quad (5.13)$$

In general, we must also prescribe boundary conditions at the orifice and at the tip of the jet. While we shall move on to consider the problem of a 'growing jet', at first we will simplify the model and consider the bulk of the jet. This is for two reasons. Firstly, we wish to consider whether the jet is inherently unstable to small perturbations due to the presence of this thin gas layer. We expect this analysis to elucidate the mechanism whereby we see the advancing lamella described in Thoroddsen et al. (2010) touching down on the substrate, trapping air bubbles. Secondly, in a growing jet model, we expect there to be three regions of interest: a 'main body' region in which the jet has a small aspect ratio and is governed by the equations we will derive presently, along with inner 'tip' and 'nozzle' regions which have an order unity aspect ratio. Therefore, we shall ignore the tip and nozzle for now and concentrate on reducing the above equations by performing an asymptotic analysis in the small-aspect-ratio limit.

In the gas, we nondimensionalise by scaling

$$(x^*, z^*, H^*) = L(x, \varepsilon_g \hat{z}, \varepsilon_g H),\ (U^*, W^*) = U_s(U, \varepsilon_g W),\ P^* = \frac{\mu_g U_s}{\varepsilon_g^2 L} P,\ t^* = \frac{L}{U_s} t,$$

and in the jet by scaling

$$(x^*, z^*, H^*, h^*) = L(x, \varepsilon_l \bar{z}, \varepsilon_g H, \varepsilon_l h),\ (u^*, w^*) = U_s(u, \varepsilon_l w),\ p^* = \rho_l U_s^2 p,\ t^* = \frac{L}{U_s} t.$$

The different pressure scales may be surprising, but the reasoning will become evident in §5.3.

The incompressible Navier-Stokes equations in the gas (5.1)–(5.2) become

$$\varepsilon_g^2 \mathrm{Re}_g \left(U_t + UU_x + WU_{\hat{z}}\right) = -P_x + \varepsilon_g^2 U_{xx} + U_{\hat{z}\hat{z}}, \quad (5.14)$$

$$\varepsilon_g^4 \mathrm{Re}_g \left(W_t + UW_x + WW_{\hat{z}}\right) = -P_{\hat{z}} + \varepsilon_g^4 W_{xx} + \varepsilon_g^2 W_{\hat{z}\hat{z}} - \frac{\varepsilon_g^3 \mathrm{Re}_g}{\mathrm{Fr}^2}, \quad (5.15)$$

$$U_x + W_{\hat{z}} = 0, \quad (5.16)$$

while in the jet (5.3)–(5.4) become

$$\begin{aligned}
\varepsilon_l^2 \mathrm{Re}_l \left(u_t + uu_x + wu_{\bar{z}}\right) &= -\varepsilon_l^2 \mathrm{Re}_l p_x + \varepsilon_l^2 u_{xx} + u_{\bar{z}\bar{z}}, && (5.17)\\
\varepsilon_l^2 \mathrm{Re}_l \left(w_t + uw_x + ww_{\bar{z}}\right) &= -\mathrm{Re}_l p_{\bar{z}} + \varepsilon_l^2 w_{xx} + w_{\bar{z}\bar{z}} - \frac{\varepsilon_l \mathrm{Re}_l}{\mathrm{Fr}^2}, && (5.18)\\
u_x + w_{\bar{z}} &= 0, && (5.19)
\end{aligned}$$

where the Froude number and the Reynolds numbers in the liquid and gas are defined by

$$\mathrm{Fr} = \frac{U_s}{\sqrt{gL}}, \quad \mathrm{Re}_l = \frac{\rho_l L U_s}{\mu_l}, \quad \mathrm{Re}_g = \frac{\rho_g L U_s}{\mu_g}.$$

On the solid surface, (5.5) becomes

$$U = W = 0 \quad \text{on} \quad \hat{z} = 0. \tag{5.20}$$

The kinematic boundary conditions on the free surfaces (5.6)–(5.8) become

$$\begin{aligned}
W &= H_t + uH_x && \text{on} \quad \hat{z} = H, && (5.21)\\
w &= \eta \left(H_t + uH_x\right) && \text{on} \quad \bar{z} = \eta H, && (5.22)\\
w &= \eta \left(H_t + uH_x\right) + h_t + uh_x && \text{on} \quad \bar{z} = \eta H + h, && (5.23)
\end{aligned}$$

where the ratio of the aspect ratios is given by $\eta = \varepsilon_g/\varepsilon_l = \ell_g/\ell_l$. Moreover, the continuity of velocity condition on the lower free surface (5.13) becomes

$$U(x, H, t) = u(x, \eta H, t), \ \eta W(x, H, t) = w(x, \eta H, t). \tag{5.24}$$

By (5.9), the normal stress condition on $\bar{z} = \eta H$ is given by

$$\begin{aligned}
p - \lambda \varepsilon_l^2 P|_{\hat{z}=H} = {} & \frac{\varepsilon_l \eta H_{xx}}{\mathrm{We}\left(1 + \varepsilon_l^2 \eta^2 H_x^2\right)^{3/2}} + \frac{2}{\mathrm{Re}_l \left(1 + \varepsilon_l^2 \eta^2 H_x^2\right)} \left[\varepsilon_l^2 \eta^2 H_x^2 \left(u_x - \mu U_x|_{\hat{z}=H}\right)\right.\\
& \left. + w_{\bar{z}} - \mu W_{\hat{z}}|_{\hat{z}=H} - H_x \left(\eta \left(u_{\bar{z}} + \varepsilon_l^2 w_x\right) - \mu \left(U_{\hat{z}} + \varepsilon_l^2 \eta^2 W_x\right)|_{\hat{z}=H}\right)\right], \quad (5.25)
\end{aligned}$$

while on $\bar{z} = \eta H + h$, (5.10)

$$\begin{aligned}
p = {} & -\frac{\varepsilon_l \left(\eta H_{xx} + h_{xx}\right)}{\mathrm{We}\left(1 + \varepsilon_l^2 \left(\eta H_x + h_x\right)^2\right)^{3/2}} + \frac{2}{\mathrm{Re}_l \left(1 + \varepsilon_l^2 \left(\eta H_x + h_x\right)^2\right)}\\
& \times \left[\varepsilon_l^2 \left(\eta H_x + h_x\right)^2 u_x + w_{\bar{z}} - \left(\eta H_x + h_x\right)\left(u_{\bar{z}} + \varepsilon_l^2 w_x\right)\right], \quad (5.26)
\end{aligned}$$

where the Weber number is defined by

$$\mathrm{We} = \frac{\rho_l L U_s^2}{\sigma}.$$

The parameter λ, which represents the relative size of the lubrication pressure in the gas layer to the jet pressure, is given by

$$\lambda = \frac{\rho}{\varepsilon_l^2 \varepsilon_g^2 \mathrm{Re}_g} = \frac{\mu}{\eta^2 \varepsilon_l^4 \mathrm{Re}_l}, \tag{5.27}$$

where $\rho = \rho_g/\rho_l$ is the density ratio and μ_g/μ_l is the viscosity ratio. Finally, the tangential stress condition (5.11) on $\bar{z} = \eta H$ becomes

$$\begin{aligned} &2\varepsilon_l^2 \eta^2 H_x \left(u_x - w_{\bar{z}}\right) + \eta \left(\varepsilon_l^2 \eta^2 H_x^2 - 1\right) \left(u_{\bar{z}} + \varepsilon_l^2 w_x\right) \\ &\quad = \mu \left[2\varepsilon_l^2 \eta^2 H_x \left(U_x - W_{\hat{z}}\right) + \left(\varepsilon_l^2 \eta^2 H_x^2 - 1\right) \left(U_{\hat{z}} + \varepsilon_l^2 \eta^2 W_x\right)\right]_{\hat{z}=H}. \end{aligned} \tag{5.28}$$

and on $\bar{z} = \eta H + h$, (5.12) becomes

$$2\varepsilon_l^2 \left(\eta H_x + h_x\right) \left(u_x - w_{\bar{z}}\right) + \left(\varepsilon_l^2 \left(\eta H_x + h_x\right)^2 - 1\right) \left(u_{\bar{z}} + \varepsilon_l^2 w_x\right) = 0, \tag{5.29}$$

5.2.1 Summary of the dimensionless parameters

In terms of the characteristic jet length, L, jet speed U_s, jet thickness ℓ_l, air-layer thickness, ℓ_g, jet and gas densities, ρ_l and ρ_g, jet and gas viscosities, μ_l and μ_g, surface tension coefficient σ and acceleration due to gravity, g, the dimensionless parameters in the full model are

$$\begin{gathered} \varepsilon_l = \frac{\ell_l}{L}, \quad \varepsilon_g = \frac{\ell_g}{L}, \quad \eta = \frac{\varepsilon_g}{\varepsilon_l}, \quad \rho = \frac{\rho_g}{\rho_l}, \quad \mu = \frac{\mu_g}{\mu_l}, \quad \mathrm{Fr} = \frac{U_s}{\sqrt{gL}}, \\ \mathrm{Re}_l = \frac{\rho_l L U_s}{\mu_l}, \quad \mathrm{Re}_g = \frac{\rho_g L U_s}{\mu_g}, \quad \mathrm{We} = \frac{\rho_l L U_s^2}{\sigma}, \quad \lambda = \frac{\rho}{\varepsilon_l^2 \varepsilon_g^2 \mathrm{Re}_g}. \end{gathered} \tag{5.30}$$

5.3 Asymptotics in the thin-layer limit

As we have already mentioned, throughout our analysis, we shall assume the aspect ratios of both the jet and the gas layer are small. Furthermore, we shall assume that $\eta = O(1)$. We can consider scenarios in which the gas layer is much thinner than the jet or vice versa by taking subsequently the sub-limits as $\eta \to 0$ and $\eta \to \infty$ respectively. There are clearly a variety of different asymptotic regimes based on the size of the reduced Reynolds numbers in the jet and the gas, the Weber number, the Froude number, μ and λ. We shall at first consider four particular regimes based on the reduced Reynolds numbers in each of the two fluids.

5.3.1 Viscous jet/viscous gas limit

We start with the limit in which viscosity dominates over inertia in both the jet and the gas as it is perhaps the most challenging asymptotically. Thus, we assume that

Re_l, Re_g are order unity, but the reduced Reynolds number in each fluid are small, viz.

$$\varepsilon_l^2 \mathrm{Re}_l \ll 1, \varepsilon_g^2 \mathrm{Re}_g \ll 1. \tag{5.31}$$

We shall retain both gravity and surface tension in the model by assuming that

$$\mathrm{St}^* = \frac{\mathrm{Re}_l}{\varepsilon_l \mathrm{Fr}^2} = O(1), \quad \gamma = \frac{1}{\varepsilon_l \mathrm{We}} = O(1). \tag{5.32}$$

Here St^* is the reduced Stokes number. Our model aims to describe the motion of a splash jet due to a gas pressure jump across it. To this end, we assume that the parameter λ as defined in (5.27) is of order unity. In addition to these assumptions, we shall also assume that both the viscosity and density ratios are small, namely $0 < \rho, \mu \ll 1$. We note that under the assumption that λ is of order unity, $\mu/\mathrm{Re}_l = O(\eta^2 \varepsilon_l^4)$, so that the viscous stresses on the right-hand side of (5.25) are an order of magnitude smaller than the gas pressure. Moreover, the largest contribution from the gas layer in the tangential stress condition (5.28) is $-\mu U_{\hat{z}}$, which is of $O(\varepsilon_l^4 \mathrm{Re}_l)$.

Note that had we included the gas region above the jet, its leading-order contribution on the jet motion would be through the tangential stress boundary condition. The jet motion would induce a boundary layer at the free surface of the jet, and this boundary layer would produce a shear of $O(1/\sqrt{\mathrm{Re}_g})$ on the jet. Provided that $\varepsilon_l^2 \gg \mu/\sqrt{\mathrm{Re}_g}$, we can neglect this shear stress at leading and first order in the analysis that follows. This does not seem unreasonable given the restrictions we already have on the viscosity ratio.

Hence, based on the assumptions above, we can find the lengthscale L over which we see pressure-driven deflections of the jet by choosing it to satisfy $\lambda = 1$, giving

$$L = \left(\frac{\rho_l U_s \ell_l^2 \ell_g^2}{\mu_g} \right)^{1/3}. \tag{5.33}$$

We shall discuss whether this is a reasonable lengthscale in §5.3.5.

Much of the following analysis follows that for viscous fibres, as described by Howell (1994) and van de Fliert et al. (1995). We expand all of the independent variables in powers of ε_l^2 – this is without loss of generality, since we have assumed that $\eta = O(1)$ – and denote leading-order variables by a subscript zero. In the jet, the leading-order forms of (5.17) and of the tangential stress conditions (5.29)–(5.28) give

$$u_{0\bar{z}\bar{z}} = 0 \quad \text{with} \quad u_{0\bar{z}} = 0 \quad \text{on} \quad \bar{z} = \eta H_0, \ \eta H_0 + h_0,$$

which allows us to deduce that, to leading-order, $u_0 = u_0(x,t)$. Therefore, (5.19) gives, at leading order,

$$w_0 = -u_{0x} z + \eta \left(H_{0t} + (u_0 H_0)_x \right), \tag{5.34}$$

where we have applied the leading-order version of (5.23). Therefore, on applying (5.22), we derive the conservation of mass equation

$$h_{0t} + (u_0 h_0)_x = 0. \tag{5.35}$$

The leading-order jet pressure is found from the leading-order versions of (5.18), (5.25), (5.26) to be given by

$$p_0(x,t) = -\frac{2}{\mathrm{Re}_l} u_{0x}. \tag{5.36}$$

In the gas layer, the leading-order version of (5.15) tells us that the pressure does not vary across the layer, that is $P_0 = P_0(x,t)$. We integrate the leading-order version of (5.14) twice with respect to $\hat{z}$ and apply the leading-order versions of the no-slip condition (5.20) and the continuity of velocity condition (5.24) to find that

$$U_0(x,\hat{z},t) = \frac{P_{0x}\hat{z}}{2}\left(\hat{z} - H_0\right) + \frac{u_0 z}{H_0}. \tag{5.37}$$

We can therefore integrate the leading-order version of (5.16) across the gas layer and use the leading-order version of (5.21) to find that the leading-order gas flow is governed by the lubrication equation,

$$H_{0t} + \left(\frac{u_0 H_0}{2} - \frac{H_0^3 P_{0x}}{12}\right)_x = 0. \tag{5.38}$$

Since the leading-order streamfunction in the gas, $\Psi_0(x,\hat{z},t)$, will be of use in §5.5.3.2, we note that as $U_0 = \partial\Psi_0/\partial\hat{z}$,

$$\Psi_0 = \frac{P_{0x}\hat{z}^3}{6} - \frac{P_{0x}H_0\hat{z}^2}{4} + \frac{\hat{z}^2}{2H_0}. \tag{5.39}$$

At $O(\varepsilon_l^2)$, we can integrate (5.17) across the jet to find that

$$h_0\left(u_{0t} + u_0 u_{0x}\right) = \frac{3}{\mathrm{Re}_l} h_0 u_{0xx} + \frac{1}{\mathrm{Re}_l}\left[u_{1\bar{z}}\right]_{\bar{z}=\eta H_0}^{\eta H_0 + h_0} \tag{5.40}$$

where a subscript 1 indicates a first-order variable (corresponding to terms of $O(\varepsilon_l^2)$ in our asymptotic expansions). At $O(\varepsilon_l^2)$, the tangential stress conditions (5.28)–(5.29) reduce to

$$u_{1\bar{z}} = 4\eta H_{0x} u_{0x} + \eta H_0 u_{0xx} - \eta\left(H_{0tx} + (u_0 H_0)_{xx}\right) \quad \text{on} \quad \bar{z} = \eta H_0, \tag{5.41}$$

$$u_{1\bar{z}} = 4(\eta H_{0x} + h_{0x}) u_{0x} + (\eta H_0 + h_0) u_{0xx} - \eta\left(H_{0tx} + (u_0 H_0)_{xx}\right) \quad \text{on} \quad \bar{z} = \eta H_0 + h_0, \tag{5.42}$$

so that (5.40) implies

$$h_0\left(u_{0t}+u_0u_{0x}\right)=\frac{4}{\mathrm{Re}_l}\left(h_0u_{0x}\right)_x. \tag{5.43}$$

The term on the right-hand side of (5.43) is the Trouton term seen in extensional flow models for viscous fibres. Note that, as argued by Howell (1994), (5.43) can also be deduced via an application of the Fredholm alternative to the $O(\varepsilon_l^2)$-version of (5.17).

To close the system, we integrate $O(\varepsilon_l^2)$-version of (5.18) across the jet and apply the $O(\varepsilon_l^2)$-versions of (5.25)–(5.26). The algebra is quite involved. Utilising (5.43), the correction to the tangential jet velocity, u_1, must satisfy

$$u_{1\bar{z}\bar{z}}=\frac{4}{h_0}\left(h_0u_{0x}\right)_x-3u_{0xx}, \tag{5.44}$$

subject to first-order versions of the tangential stress conditions (5.41)–(5.42). This differential equation can be solved, and in particular, we deduce that

$$\left[u_{1\bar{z}}\right]_{\bar{z}=\eta H_0}^{\eta H_0+h_0}=4h_{0x}u_{0x}+h_0u_{0xx} \tag{5.45}$$

and

$$\begin{aligned}\left[u_{1x}\right]_{\bar{z}=\eta H_0}^{\eta H_0+h_0} &= \left(\frac{4h_{0x}u_{0x}}{h_0}+u_{0xx}\right)_x\frac{h_0^2}{2}-\eta H_{0x}h_0\left(\frac{4h_{0x}u_{0x}}{h_0}+u_{0xx}\right)\\ &\quad +h\left(4\eta H_xu_x+\eta Hu_{xx}-\eta\left(H_{tx}+\left(uH\right)_{xx}\right)\right)_x.\end{aligned} \tag{5.46}$$

At $O(\varepsilon_l^2)$, the normal stress conditions (5.25)–(5.26) give

$$p_1=-\gamma\left(\eta H_{0xx}+h_{0xx}\right)+\frac{2}{\mathrm{Re}_l}\left[2\left(\eta H_{0x}+h_{0x}\right)^2u_{0x}-u_{1x}-\left(\eta H_{0x}+h_{0x}\right)\left(u_{1\bar{z}}+w_{0x}\right)\right] \tag{5.47}$$

on $\bar{z}=\eta H_0+h_0$, and

$$p_1=\lambda P_0+\gamma\eta H_{0xx}+\frac{2}{\mathrm{Re}_l}\left[2\eta^2H_{0x}^2u_{0x}-u_{1x}-\eta H_{0x}\left(u_{1\bar{z}}+w_{0x}\right)\right] \tag{5.48}$$

on $\bar{z}=\eta H_0$.

Now, at $O(\varepsilon_l^2)$, (5.18) is given by

$$\mathrm{Re}_l\left(w_{0t}+u_0w_{0x}+w_0w_{0\bar{z}}\right)=-\mathrm{Re}_lp_{1\bar{z}}+w_{0xx}+w_{1\bar{z}\bar{z}}-\mathrm{St}^*. \tag{5.49}$$

Upon integrating this expression across the layer, the left-hand side becomes

$$\mathrm{Re}_l\left[\bar{w}_t+u_0\bar{w}_x-\bar{w}u_{0x}-\left(\eta(H_{0t}+u_0H_{0x})+h_{0t}+u_0h_{0x}\right)^2+\eta^2(H_{0t}+u_0H_{0x})^2\right]$$

where

$$\bar{w}=\int_{\eta H_0}^{\eta H_0+h_0}v_0\,\mathrm{d}\bar{y}=h_0\left(-\frac{h_0u_{0x}}{2}+\eta(H_{0t}+u_0H_{0x})\right).$$

Thus,

$$\begin{aligned}\text{LHS} &= \text{Re}_l\left[h_0^2u_{0x}^2+\eta h_0\left(u_0^2H_{0xx}+2u_0H_{0xt}+H_{0tt}\right)-\right.\\ &\quad\left.\frac{h_0^2}{2}\left(\frac{4(h_0u_{0x})_{0x}}{h_0}\right)_x+4\eta H_{0x}(h_0u_{0x})_{0x}\right].\end{aligned}\tag{5.50}$$

Similarly, utilising (5.45)–(5.48), the right-hand side is

$$\lambda\text{Re}_lP_0+\gamma\text{Re}_l\left(2\eta H_{0xx}+h_{0xx}\right)-\text{St}^*h_0+2\left(h_0h_{0x}u_{0x}\right)_x+4\eta\left(h_0H_{0x}u_{0x}\right)_x.\tag{5.51}$$

Therefore,

$$\begin{aligned}h_0^2u_{0x}^2 &+ \eta h_0\left[\left(u_0^2-\frac{4u_{0x}}{\text{Re}_l}-\frac{2\gamma}{h_0}\right)H_{0xx}+2u_0H_{0xt}+H_{0tt}\right]\\ &= \lambda P_0-\frac{h_0}{\varepsilon_l\text{Fr}^2}+\gamma h_{0xx}+\frac{2}{\text{Re}_l}\left(2h_0\left(h_{0x}u_{0x}\right)_x+h_0^2u_{0xxx}\right).\end{aligned}\tag{5.52}$$

5.3.1.1 Summary

After dropping the subscript zero denoting a leading-order variable, the governing equations for the horizontal jet speed, $u(x,t)$ and jet thickness, $h(x,t)$ are given by

$$h_t+(uh)_x = 0,\tag{5.53}$$

$$h\left(u_t+uu_x\right) = \frac{4}{\text{Re}_l}(hu_x)_x,\tag{5.54}$$

which decouple from the equations governing the gas pressure, $P(x,t)$ and gas layer thickness, $H(x,t)$, namely

$$H_t+\frac{1}{2}(uH)_x-\frac{1}{12}\left(H^3P_x\right)_x=0\tag{5.55}$$

and

$$\begin{aligned}h^2u_x^2 &+ \eta h\left[\left(u^2-\frac{4u_x}{\text{Re}_l}-\frac{2\gamma}{h}\right)H_{xx}+2uH_{xt}+H_{tt}\right]\\ &= \lambda P-\frac{h}{\varepsilon_l\text{Fr}^2}+\gamma h_{xx}+\frac{2}{\text{Re}_l}\left(2h\left(h_xu_x\right)_x+h^2u_{xxx}\right).\end{aligned}\tag{5.56}$$

We will investigate the stability properties of this model shortly, after considering other asymptotic limits based on the reduced Reynolds numbers in each fluid.

5.3.2 Inviscid jet/viscous gas limit

In the limit in which the reduced Reynolds number is large in the jet, the jet is approximately inviscid. If we assume that the gas is predominantly viscous, the

derivation as described in §5.3.1 yields a similar model. In the jet, we make the additional assumption that the flow is approximately irrotational, with

$$\frac{\partial u}{\partial \bar{z}} - \varepsilon_l^2 \frac{\partial w}{\partial x} = 0, \tag{5.57}$$

in the fluid. At leading order, this condition tells us that u_0 does not vary across the jet. Moreover, (5.18) with $\mathrm{Re}_l = \infty$ tells us that to leading-order p_0 does not vary across the jet, and thus is zero due to the leading-order dynamic boundary condition on the upper free surface. The governing equations are found by integrating the leading-order forms of (5.17) and (5.19) across the jet, and we find that

$$h_t + (uh)_x = 0, \tag{5.58}$$

$$u_t + uu_x = 0, \tag{5.59}$$

where we have again dropped the subscript zero indicating a leading-order variable. As in the viscous-viscous case, these equations decouple from the gas motion. Note, we could also have naïvely set $\mathrm{Re}_l = \infty$ into (5.54) to reduce (5.53)–(5.54) to (5.58)-(5.59).

Clearly, at leading-order, (5.55) must still hold in the gas layer. Moreover, integrating (5.18) across the jet, we derive the pressure-jump equation

$$h^2 u_x^2 + \eta h \left[\left(u^2 - \frac{2\gamma}{h} \right) H_{xx} + 2uH_{xt} + H_{tt} \right] = \lambda P - \frac{1}{\varepsilon_l \mathrm{Fr}^2} + \gamma h_{xx}. \tag{5.60}$$

Note that, since λ is still as defined in (5.27), the lengthscale L must be given by (5.33).

5.3.3 Inviscid jet/inviscid gas limit

If we further assume that the reduced Reynolds number in the gas is large so that both fluids are approximately inviscid, the gas pressure scale must be chosen as $\rho_g U_s^2$ as opposed to $\mu_g U_s/(\varepsilon_g^2 L)$. Thus, the dimensionless dynamic boundary condition on the lower free surface reduces to

$$p - \rho' \varepsilon_l^2 P|_{\hat{z}=H} = \frac{\eta\gamma\varepsilon_l^2 H_{xx}}{(1+\eta^2\varepsilon_l^2 H_x^2)^{3/2}}, \tag{5.61}$$

where $\rho'\varepsilon_l^2 = \rho$. Setting $\rho' = 1$ gives us a different characteristic lengthscale over which jet deflections are appreciable to that given in (5.33). We find that

$$L = \frac{\rho_l^{1/2}}{\rho_g^{1/2}} \ell_l. \tag{5.62}$$

The analysis is the same as in §5.3.2, but now the shallow-water equations replace the lubrication equation (5.55) in the gas layer, so that, at leading order,

$$U_t + UU_x = -P_x, \tag{5.63}$$

$$H_t + (UH)_x = 0. \tag{5.64}$$

where $U(x,t)$ is the leading-order x-component of velocity in the gas. Note that to derive these equations from first principles, we would require the condition of irrotational flow in the air, namely

$$\frac{\partial U}{\partial \hat{z}} - \varepsilon_g^2 \frac{\partial W}{\partial x} = 0. \tag{5.65}$$

The pressure-jump equation is the same as (5.60), with λ replaced by ρ'.

5.3.4 Viscous jet/inviscid gas limit

In the final limit that we shall consider, we assume that the reduced Reynolds number in the liquid is small while the reduced Reynolds number in the gas is large. This is simply an amalgam of §5.3.1 and §5.3.3: in the gas, (5.63)–(5.64) hold to leading-order, along with (5.53)–(5.54) in the liquid jet. The pressure-jump equation is the same as in (5.56), but with λ replaced by ρ' as defined in §5.3.3. Note that in this limit, L is given by (5.62).

5.3.5 Applicability of the model

Is our model appropriate for splash jet evolution or the spreading of a lamella on a layer of air? Certainly, in many situations, for example in the droplet impact experiments in Thoraval et al. (2012), there is no solid surface, and the thin air layer is bounded by the splash jet and a large region of bulk fluid. Therefore, our model can only give qualitative predictions to the evolution of such jets; for a more thorough analysis, we would need to replace the no-slip, no-flux conditions with continuity of stress and velocity conditions. This is something we do not consider in this thesis, but it is something to bear in mind in this section, as we will use Thoraval et al. (2012) as an example. Notwithstanding this concern, to answer the questions we posed above, we must estimate the key parameters in our model. The four regimes discussed in this section fall into two broader cases:

- the gas layer can be modelled as inviscid;
- the gas layer can be modelled as viscous.

In the inviscid gas case, the reduced Reynolds number in the gas must be large, viz:

$$\varepsilon_g^2 \mathrm{Re}_g = \frac{\rho_g \ell_g^2 U_s}{\mu_g L} \gg 1, \tag{5.66}$$

where L, given by (5.62) must be comparable to the length of the jet, else the pressure jump across the layer cannot be responsible for any deviations to the jet evolution. In the viscous gas case, the reduced Reynolds number in the gas must be small. For our model to be applicable, the length of the jet must be comparable to (5.33). In each scenario, we can then estimate the size of $\varepsilon_l^2 \mathrm{Re}_l$ and work out which sub-regime we are in. Naturally, there are several further possibilities, in particular cases where $\varepsilon_g^2 \mathrm{Re}_g = O(1)$ or $\varepsilon_l^2 \mathrm{Re}_l = O(1)$, but we do not consider these here, and we expect that the models derived in §§5.3.1–5.3.4 apply to a range of splash jet/lamella phenomenon. Note that even in cases where our model does apply, if the gas layer gets sufficiently thin, that is, if the jet approaches touchdown, compressibility of the gas may become important and a new model will be required. This is something we do not consider in this thesis.

We summarise the experimental parameters we use in this section in Table 5.1. For our first example, we consider one of the numerical simulations in Thoraval et al. (2012). In Figure S3b, $\ell_l \sim 3.4 \times 10^{-5}$ m, $\ell_g \sim 1.7 \times 10^{-4}$ m and the length of the jet is $L_{jet} \sim 10^{-3}$ m. The physical parameters are given by $\mu_g = 1.81 \times 10^{-5}$ Pas, $\mu_l = 3 \times 10^{-3}$ Pas, $\rho_l = 1.1 \times 10^3$ kgm^{-3} and $\rho_g = 1.21$ kgm^{-3}. The authors estimate the velocity of the jet at its root to be $U_s \sim 20$ ms^{-1}. Using these figures, we find that the splash jet would be best modelled using the inviscid-inviscid model described in

	Thoraval et al. (2012)	Driscoll & Nagel (2011)	Thoroddsen et al. (2010)
ρ_l	1.1×10^3 kgm^{-3}	1.2×10^3 kgm^{-3}	10^3 kgm^{-3}
ρ_g	1.21 kgm^{-3}	1.21 kgm^{-3}	1.21 kgm^{-3}
μ_l	3×10^{-3} Pas	1.3×10^{-2} Pas	4.8×10^{-2} Pas
μ_g	1.81×10^{-5} Pas	1.81×10^{-5} Pas	1.81×10^{-5} Pas
σ	6.74×10^{-2} Nm^{-1}	6.3×10^{-2} Nm^{-1}	7.2×10^{-2} Nm^{-1}
U_s	20 ms^{-1}	3 ms^{-1}	1.2 ms^{-1}
ℓ_l	3.4×10^{-5} m	10^{-5} m	–
ℓ_g	1.7×10^{-4} m	–	–
L_{jet}	10^{-3} m	6×10^{-4} m	4×10^{-4} m

Table 5.1: Parameters from the three experiments.

§5.3.3 because

$$L = \rho^{-1/2}\ell_l \sim 1.03 \times 10^{-3}\,\mathrm{m}, \quad \varepsilon_g^2 \mathrm{Re}_g \sim 49.68, \quad \varepsilon_l^2 \mathrm{Re}_l \sim 11.1, \tag{5.67}$$

where we have calculated L from (5.62). We also note that $\eta \sim 5$.

In Driscoll and Nagel (2011), the thin sheet emitted from the front of the expanding lamella of an impacting droplet is shown to shoot over a layer of air. They estimate $\ell_l \sim 10^{-5}$ m and $L_{jet} \sim 6 \times 10^{-4}$ m. The gas parameters are as in the previous example, while $\rho_l = 1.2 \times 10^3$ kgm^{-3} and $\mu_l = 1.3 \times 10^{-2}$ Pas (so that the liquid is more viscous). While it is not measured, Driscoll et al. (2010) estimate the speed of the lamella at ejection to be $U_s \sim 3$ ms^{-1}. Although the authors state that the gas layer is thicker than the ejecta sheet, they do not give a value for the thickness, indeed, due to its difficulty to capture and measure, there is a unfortunate lack of data for the thickness of the gas layer under the lamella/thin sheet at ejection in the literature in general. However, we note that if the gas is dominated by inviscid forces, then L, as calculated from (5.62), is

$$L = \rho^{-1/2}\ell_l \sim 3 \times 10^{-4}\,\mathrm{m}, \tag{5.68}$$

which is comparable to L_{jet}. If this supposition is true, we require the reduced Reynolds number in the gas to be large, so we require $\ell_g \gg 10^{-4}$ m. This does not seem unreasonable. Moreover, based on the value of L calculated above,

$$\varepsilon_l^2 \mathrm{Re}_l \sim 2.6 \times 10^{-2}, \tag{5.69}$$

so that the liquid jet can be modelled as viscous. This is evidence that the inviscid gas, viscous jet model in §5.3.4 may be the most appropriate here.

It is reasonable to suggest that the viscous gas regime is more likely to apply to the air layer under the spreading lamella in Thoroddsen et al. (2010), cf. Figure 4.2. Unfortunately, we are again without the data to thoroughly check this hypothesis. The physical parameters in the gas are as in the previous examples, and $\mu_l = 4.8 \times 10^{-2}$ Pas, $\rho_l \sim 10^3$ kgm^{-3}. The spreading velocity of the lamella is estimated by the authors to be $U_s \sim 1.2$ ms^{-1}. The length of the lamella can be estimated from Figure 2d in that paper as $L_{jet} \sim 4 \times 10^{-4}$ m. Therefore, if the gas were viscous, we would require

$$L_{jet} > L \sim (4.05 \times 10^2)(\ell_l \ell_g)^{2/3}\,\mathrm{m}, \tag{5.70}$$

and

$$1 \gg \varepsilon_g^2 \mathrm{Re}_g = (7.55 \times 10^3)\frac{\ell_g^{4/3}}{\ell_l^{2/3}}. \tag{5.71}$$

Thus, if the lamella has thickness $\ell_l \sim 10^{-5}$ m, a gas layer thickness of $\ell_g \sim 10^{-6}$ m would satisfy these conditions. In such an example, $\varepsilon_l^2 \mathrm{Re}_l \sim 1/10$, so the lamella could be modelled as viscous as well.

Although it clearly would be desirable to have more data to compare to, there is good evidence that our models may be applicable to splash jet/ejecta/lamella phenomena. We now move on to investigate the stability of our model under further assumptions on the jet thickness and velocity.

5.4 Linear stability analysis

Whether the liquid jet is dominated by viscous forces so that (5.53)–(5.54) hold, or by inviscid forces, so that (5.58)–(5.59) hold, $h = u = \text{const}$ is a spatially-uniform steady-state solution on an unbounded domain. Remarkably, this agrees with numerical simulations of Thoraval (reported privately and summarised in Thoraval et al. (2012)) even for a finite jet, aside for a region near the tip where surface tension dominates, rounding the rim. Therefore, as a reasonable first approximation, we assume that u, h are constant, which is unity by our nondimensionalisation.

5.4.1 Viscous gas layer

The leading-order thickness of the gas layer, H, and the leading-order pressure in the gas layer, P, are governed by (5.55)–(5.56), which with $u = 1$, $h = 1$, become

$$\begin{aligned} H_t + \frac{1}{2}H_x - \left(\frac{H^3}{12}P_x\right)_x &= 0, \\ \eta\left[(1-2\gamma)\,H_{xx} + 2H_{xt} + H_{tt}\right] &= \lambda P - \frac{1}{\varepsilon_l \mathrm{Fr}^2}, \end{aligned}$$

giving

$$H_t + \frac{1}{2}H_x - \Gamma\left[H^3\left((1-2\gamma)H_{xx} + 2uH_{xt} + H_{tt}\right)_x\right]_x = 0, \tag{5.72}$$

where

$$\Gamma = \frac{\eta}{12\lambda}.$$

We note that the effect of gravity has dropped out of the model (5.72) because it is accounted for in the steady-state solution of the pressure, P.

Clearly, the constant solution $H = 1$ is a spatially-uniform steady-state solution to (5.72). We now analyse the stability of this solution to perturbations of the form

$$H(x,t) = 1 + \delta H_1 \mathrm{e}^{\mathrm{i}(kx - \omega t)}, \tag{5.73}$$

where $0 < \delta \ll 1$ and the wavenumber k is assumed to be real and positive. We seek a dispersion relation between the frequency, ω, and k. We will neglect terms of $O(\delta^2)$ and smaller in our linear stability analysis. Upon substituting into (5.72), we find in the usual way from the terms of $O(\delta)$ that

$$-\mathrm{i}\omega + \frac{\mathrm{i}k}{2} - \Gamma\left((1-2\gamma)k^4 - 2k^3\omega + \omega^2 k^2\right) = 0.$$

Writing $\sigma = -i\Gamma k^2(\omega - k)$, we find that

$$\sigma^2 + \sigma + a - b\mathrm{i} = 0, \tag{5.74}$$

where

$$a = 2\Gamma^2\gamma k^6, \quad b = \frac{\Gamma k^3}{2}. \tag{5.75}$$

It is trivial to note that $a,\ b > 0$ for all $k > 0$.

Thus, we find the two roots are given by

$$\sigma_\pm = \frac{1}{2}\left(-1 \pm \sqrt{1 - 4\,(a - b\mathrm{i})}\right), \tag{5.76}$$

where the principal branch of the square-root is taken. For instability, we are interested in the values of k for which $\mathrm{Im}(\omega_\pm) > 0$, or equivalently, $\mathrm{Re}(\sigma_\pm) > 0$. In §5.5, we shall devote much attention to the regime in which the role of surface tension is assumed to be negligible, that is $\gamma = 0$, and in many experimental situations this estimate is reasonable. Therefore, in investigating (5.74), we shall consider cases where $\gamma = 0$ and $\gamma > 0$ separately.

5.4.1.1 Case 1: $\gamma = 0$

We begin with the case in which the effects of surface tension are negligible, so that $\gamma = 0$ and $a = 0$ in (5.74), from which it follows that

$$\mathrm{Re}(\sigma_\pm) = \frac{1}{2}\left(-1 \pm \frac{1}{\sqrt{2}}\left(1 + \sqrt{1 + 16b^2}\right)^{1/2}\right),$$

and hence that

$$\mathrm{Im}(\omega_\pm) = \frac{1}{2\Gamma k^2}\left(-1 \pm \left(\frac{1 + \sqrt{1 + 4\Gamma^2 k^6}}{2}\right)^{1/2}\right). \tag{5.77}$$

Since Γ is positive for all $k > 0$, it is trivial to note that

$$\frac{1}{2}\left(1 + \sqrt{1 + 4\Gamma^2 k^6}\right) > 1,$$

and thus

$$\mathrm{Im}(\omega_+) > 0,\ \mathrm{Im}(\omega_-) < 0 \quad \text{for all} \quad k > 0.$$

Hence, in the absence of surface tension, ω_- is always a stable branch of the dispersion relation, in the sense that perturbations will decay, whereas ω_+ is always unstable since perturbations will grow exponentially. However, as

$$\mathrm{Im}(\omega_+) \sim \frac{1}{2\sqrt{\Gamma}}\frac{1}{\sqrt{k}} \quad \text{as} \quad k \to \infty,$$

the problem is *well-posed* in the sense of Hadamard, the growth rate being bounded above for sufficiently small wavelengths.

We plot $\mathrm{Im}(\omega_\pm(k))$ for various values of Γ in Figure 5.3. It is clear that increasing Γ decreases the value of the wavenumber, k_m, at which $\mathrm{Im}(\omega_+)$ achieves its maximum. This is equivalent to an increase in the most unstable wavelength with increasing Γ.

We recall that

$$\Gamma = \frac{\eta}{12\lambda} = \frac{\ell_g}{12\ell_l\lambda}. \tag{5.78}$$

Therefore, if we recall that $\lambda = 1$ with our choice of L, increasing Γ is equivalent to increasing the thickness of the gas layer or decreasing the thickness of the jet.

We seek the maximum wavenumber, k_m. Elementary calculus reveals that k_m is given by

$$k_m = \left(\frac{74 + 6\sqrt{153}}{\Gamma^2}\right)^{1/6} = \frac{(74 + 6\sqrt{153})^{1/6} 12^{1/3} \ell_l^{1/3}}{\ell_g^{1/3}}. \tag{5.79}$$

We plot the maximum wavenumber as a function of Γ in Figure 5.4. This confirms that, as we increase Γ, the maximum wavenumber decreases and hence the wavelength of the most unstable mode increases. It would be beneficial to compare this wavenumber to the wavenumbers seen in bubble entrapment in, for example, Thoroddsen et al. (2010) and Palacios et al. (2012) to see if this instability is the mechanism for lamella touchdown during droplet spreading. Unfortunately, due to the lack of estimates for ℓ_g and ℓ_l this is not currently possible (indeed, we do not even know that the viscous gas regime is the most appropriate); however this estimate of the dimensionless wavenumber would be a useful comparison for future experimental (or numerical) work.

The phase speed of the unstable modes is given by

$$c(k) = 1 - \frac{1}{2^{3/2}\Gamma k^3}\left(\sqrt{1 + 4\Gamma^2 k^6} - 1\right)^{1/2}. \tag{5.80}$$

Independently of Γ, the phase speed is strictly increasing for $k > 0$, with

$$c(k) = \begin{cases} \dfrac{1}{2} + \dfrac{\Gamma^2}{4}k^6 + O\left(k^8\right) & \text{as} \quad k \to 0, \\ 1 - \dfrac{1}{2\sqrt{\Gamma}}k^{-3/2} + O\left(k^{-9/2}\right) & \text{as} \quad k \to \infty. \end{cases} \tag{5.81}$$

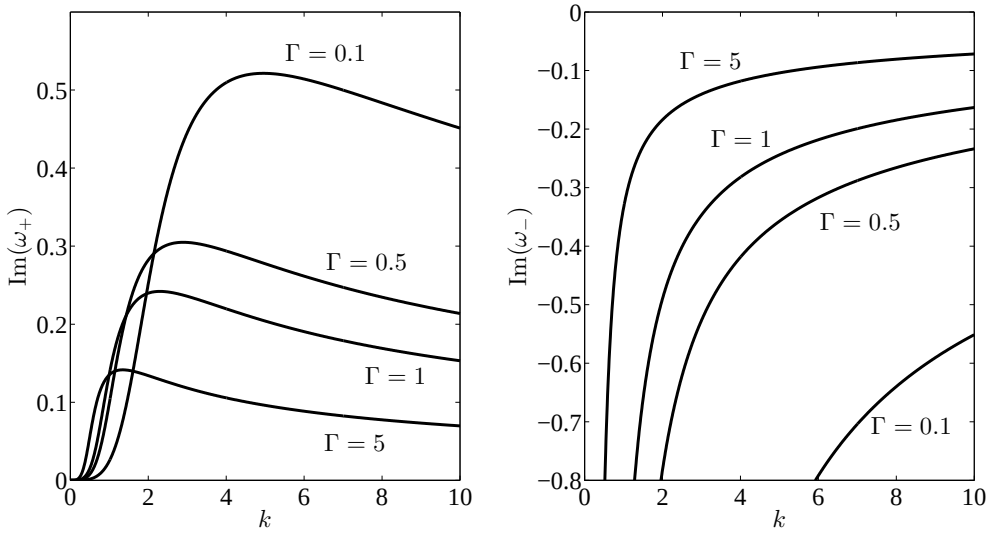

Figure 5.3: Dispersion relation branches for various values of the parameter Γ. Clearly, ω_+ is an unstable branch of the dispersion relation for all $k > 0$, but ω_- is a stable branch for all $k > 0$. The size of the most unstable wavenumber decreases as we increase Γ, although the magnitude of $\mathrm{Im}(\omega_+)$ decreases as we increase Γ. Note that for all Γ, $\mathrm{Im}(\omega_+)$ decays as $k \to \infty$.

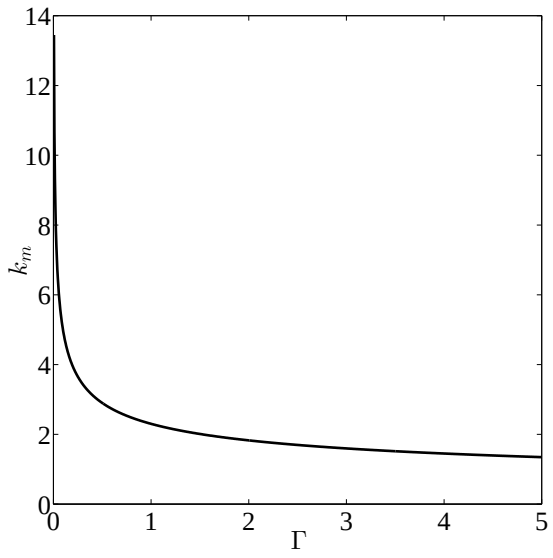

Figure 5.4: The maximum wavenumber, k_m, as a function of Γ. Clearly, as we increase Γ, the wavelength of the most unstable mode increases.

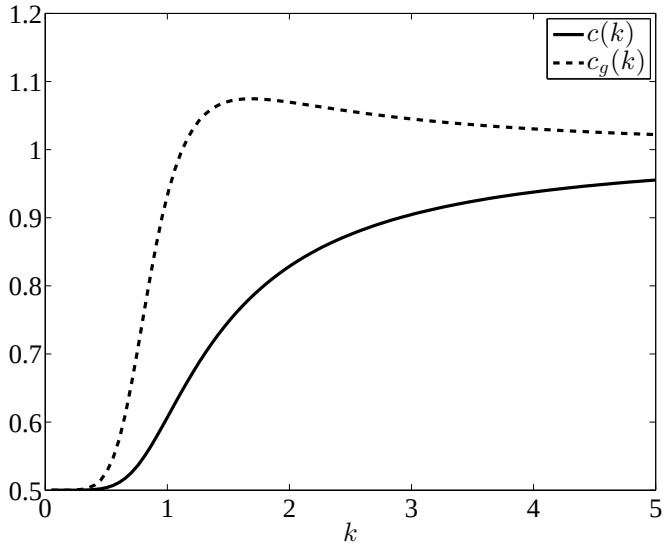

Figure 5.5: Phase speed (block) and group velocity (dash) of the unstable modes as a function of the dimensionless wavenumber, k, with $\Gamma = 1$. The waves propagate along the jet in the positive x-direction at all wavelengths.

Thus, the modes travel upstream along the jet. We plot the phase speed as a function of the wavenumber in Figure 5.5.

Clearly these waves will be dispersive because $\mathrm{Re}(\omega_+)$ is nonlinear in the wavenumber. The group velocity is given by

$$c_g(k) = 1 - \frac{3\Gamma k^3}{\sqrt{2}\sqrt{1+4\Gamma^2 k^6}\sqrt{-1+\sqrt{1+4\Gamma^2 k^6}}} + \frac{\sqrt{-1+\sqrt{1+4\Gamma^2 k^6}}}{\sqrt{2}\Gamma k^3}. \tag{5.82}$$

Unlike $c(k)$, the group velocity is not monotonic in k. Its small and large wavelength limits are given by

$$c_g(k) = \begin{cases} \dfrac{1}{2} + \dfrac{7\Gamma^{3/2}}{4} k^6 + O\left(k^8\right) & \text{as} \quad k \to 0, \\ 1 + \dfrac{1}{4\sqrt{\Gamma}} k^{-3/2} + O\left(k^{-9/2}\right) & \text{as} \quad k \to \infty. \end{cases} \tag{5.83}$$

We plot the group velocity in Figure 5.5.

5.4.1.2 Case 2: $\gamma > 0$

We now consider the linear stability analysis of a jet with surface tension included, that is $a > 0$ in (5.76). It is straightforward to show that, for $a > 0$,

$$\mathrm{Im}\,(\omega_{\pm}) = \frac{1}{2\Gamma k^2}\left(-1 \pm \left(\frac{(1-4a)+\sqrt{(1-4a)^2+16b^2}}{2}\right)^{1/2}\right). \tag{5.84}$$

Now, for an instability in either branch, we require

$$1 - 4a + \sqrt{(1-4a)^2 + 16b^2} > 2,$$

so that upon rearranging, we deduce that instability can only occur when $b^2 > a$, i.e.

$$\gamma < \frac{1}{8}. \tag{5.85}$$

It is interesting to note that this requirement is *independent of* k. Hence, if γ satisfies (5.85), then the positive branch of the dispersion relation is unstable for *all* wavenumbers $k > 0$, as we saw when we neglected surface tension. We plot $\mathrm{Im}(\omega_{\pm})$ with fixed $\Gamma = 1$ for various values of γ in Figure 5.6.

It is clear that as we increase the importance of surface tension through the parameter γ, we see three starkly different behaviours in $\mathrm{Im}(\omega_+)$, while there is no qualitative change in the behaviour of $\mathrm{Im}(\omega_-)$. From (5.85), we know that the critical value at which we see a change in stability is given by $\gamma = 1/8$. For γ smaller than this value, that is when surface tension is sufficiently small, ω_+ is an unstable branch of the dispersion relation for all wavenumbers $k > 0$, with far-field behaviour

$$\mathrm{Im}(\omega_+) \sim \frac{1}{2\Gamma}\left(-1 + \sqrt{\frac{b^2}{a}}\right)\frac{1}{k^2} \quad \text{as} \quad k \to \infty,$$

so that we have well-posedness for $\gamma < 1/8$. When $\gamma = 1/8$, $\mathrm{Im}(\omega_+)$ is identically zero for all $k > 0$, and hence the steady-state is neutrally stable. For $\gamma > 1/8$, we note that $\mathrm{Im}(\omega_+) < 0$ for all $k > 0$, so that we have stability for all wavenumbers.

Note that if we fix $0 < \gamma < 1/8$, and vary Γ to discern the maximum wave number, phase speed and group velocity of the unstable modes, we would draw the same conclusions as in the case in which surface tension is negligible, so we do not report that analysis here. If we fix $\Gamma = 1$, we can investigate the effect of γ on the wavenumber of the most unstable mode. Unfortunately the algebra is not as tractable as in the case in which $\gamma = 0$, so we are forced to do this numerically. We plot k_m as a function of γ in Figure 5.7. As we increase the importance of surface tension, we increase the wavelength of the most unstable mode from its value in (5.79).

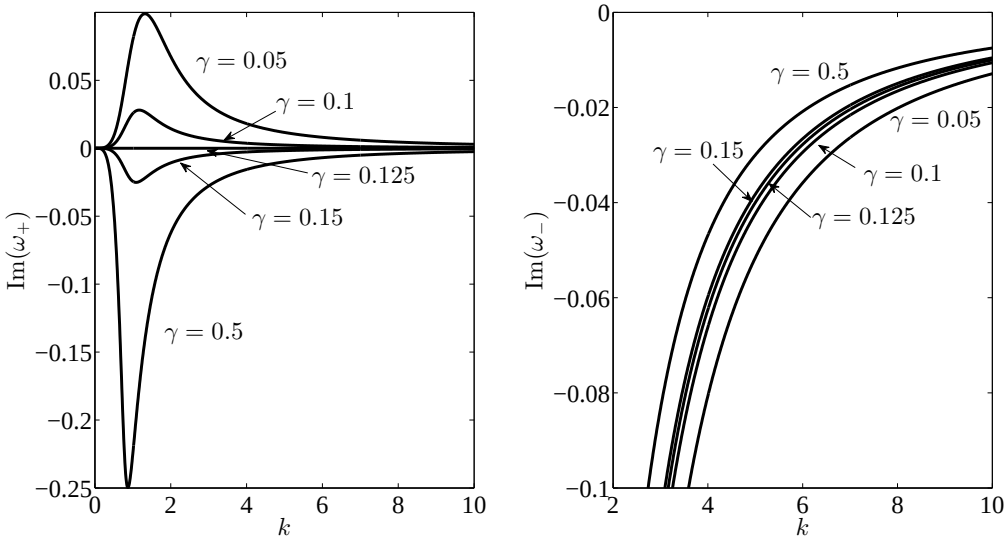

Figure 5.6: Dispersion relation branches for fixed $\Gamma = 1$ for various values of the surface tension parameter, γ. Clearly, ω_+ is an unstable branch for all $k > 0$, provided that $\gamma < 1/8$, but vanishes for all $k > 0$ (i.e. neutral stability) when $\gamma = 1/8$, while being stable for all $k > 0$ when $\gamma > 1/8$. Note that the other branch of the dispersion relation, ω_-, is stable for all $k > 0$ for any $\gamma > 0$.

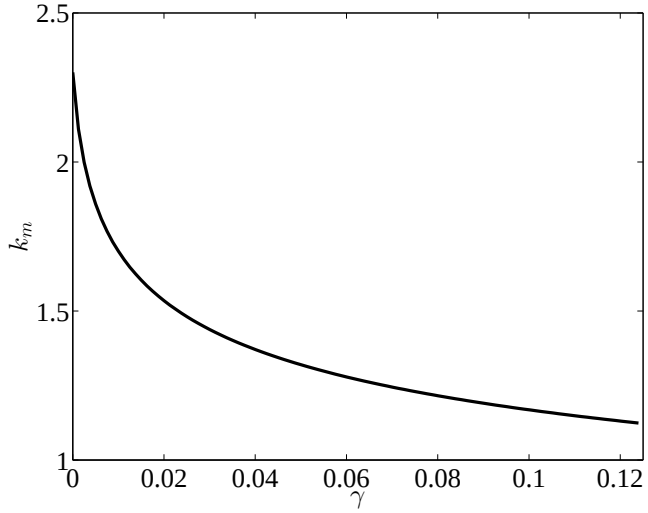

Figure 5.7: The wavenumber of the most unstable mode, k_m, as a function of γ with $\Gamma = 1$. Clearly, as we increase γ, the wavelength of the most unstable mode increases.

5.4.2 Inviscid gas

In the inviscid gas regime, we expect there to be a Kelvin-Helmholtz-type instability provided that surface tension is small enough. We now perform a similar stability analysis to that in §5.4.1 of (5.60), (5.63)–(5.64), under the assumption that the jet has constant speed and thickness, and the gas has a constant tangential speed in the base state, which we denote by U_0. We find the dispersion relation is given by

$$0 = (\eta k^2 + \rho')\omega^2 - 2k\left(\eta k^2 + \rho' U_0\right)\omega + \eta(1-2\gamma)k^4 + \rho' U_0^2 k^2, \tag{5.86}$$

giving

$$\omega_\pm = \frac{k}{\rho' + \eta k^2}\left(\rho' U_0 + \eta k^2 \pm k\sqrt{2\gamma\eta(\rho' + \eta k^2) - \rho'\eta(U_0-1)^2}\right). \tag{5.87}$$

Again, we require $\mathrm{Im}(\omega_\pm) > 0$ for instability. As before, we shall consider the case where surface tension is negligible before the case where $\gamma > 0$, both for simplicity and to tie in with the latter parts of this chapter.

5.4.2.1 Case 1: $\gamma = 0$

When surface tension is negligible,

$$\omega_\pm = \frac{k}{\rho' + \eta k^2}\left(\rho' U_0 + \eta k^2 \pm k\sqrt{\rho'\eta}\mathrm{i}(U_0 - 1)\right), \tag{5.88}$$

so that unless the unperturbed speed in the gas layer is the same as the constant jet speed, there is always a range of unstable modes. If $U_0 < 1$, ω_- is unstable for all $k > 0$ and ω_+ is stable for all $k > 0$. If $U_0 > 1$, this is reversed. When $U_0 = 1$, the modes are neutrally stable.

Fixing $\rho' = 1$, $\eta = 1$, we plot $\mathrm{Im}(\omega_\pm)$ in Figure 5.8 for a range of unperturbed gas speeds. Clearly, as $k \to \infty$, the unstable branch of the dispersion relation tends to a constant value. Without loss of generality, let us assume that $U_0 > 1$. Then,

$$\mathrm{Im}(\omega_+) \sim \sqrt{\frac{\rho'}{\eta}}(U_0 - 1) - \left(\frac{\rho'}{\eta}\right)^{3/2}\frac{U_0 - 1}{k^2} + \ldots \quad \text{as} \quad k \to \infty. \tag{5.89}$$

Since this is bounded above as we increase the wavenumber, we do not have arbitrarily large growth for arbitrarily small wavelengths and the problem is well-posed.

Still assuming that $U_0 > 1$, the phase speed of the unstable modes is given by

$$c(k) = \frac{\rho' U_0 + \eta k^2}{\rho' + \eta k^2}. \tag{5.90}$$

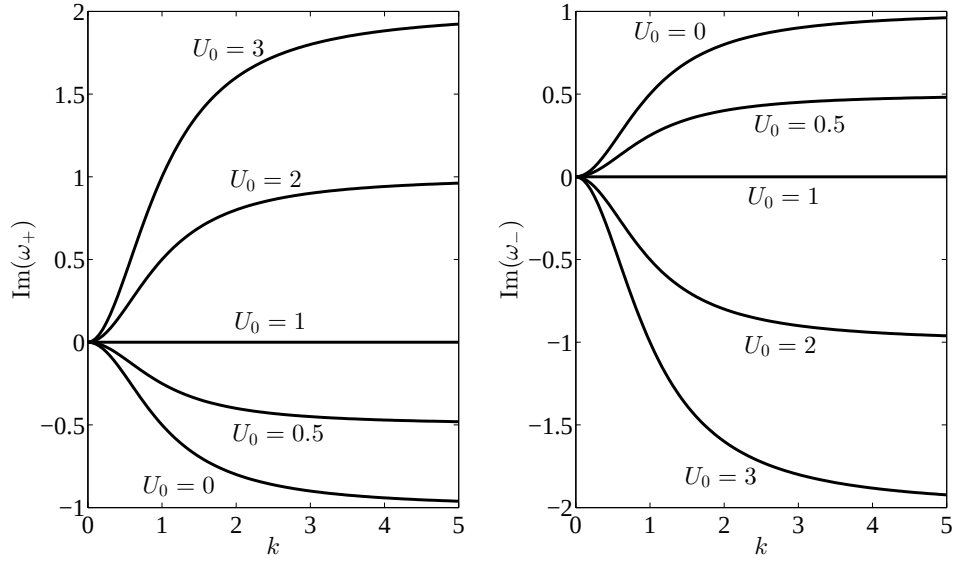

Figure 5.8: Dispersion relation branches for fixed $\rho' = 1$, $\eta = 1$ for various values of the unperturbed gas speed, U_0. When the gas speed is not the same as the constant jet speed, corresponding to $U_0 \neq 1$, one of the branches of the dispersion relation is unstable for all $k > 0$. The unstable branch switches from ω_- to ω_+ at $U_0 = 1$.

Note that for small wavelengths, $c(k) \approx 1$. The waves are again dispersive since the group velocity is given by

$$c_g(k) = c(k) + \frac{2k^2\eta\rho'(1 - U_0)}{(\rho' + \eta k^2)^2}. \tag{5.91}$$

However, $c_g \to c$ as $k \to \infty$. Note that when $U_0 = 1$, the group and phase velocities are the same since $\omega_\pm = k$, so the waves are non-dispersive.

5.4.2.2 Case 2: $\gamma > 0$

As in §5.4.1, we expect surface tension, if sufficiently large, to stabilise the jet. Recalling (5.87), if $0 < \gamma < (U_0 - 1)^2/2$, there is a range of unstable wavenumbers

$$0 < k < \sqrt{\frac{\rho'}{2\eta\gamma}\left((U_0 - 1)^2 - 2\gamma\right)}. \tag{5.92}$$

If $\gamma > (U_0 - 1)^2/2$, the constant solution is neutrally stable. We plot $\mathrm{Im}(\omega_\pm)$ for fixed $\rho' = 1$, $\eta = 1$ and $U_0 = 1/2$ over a range of γ in Figure 5.9.

We notice that, in contrast to the zero surface tension case, there is a most unstable wavenumber, k_m, when $\gamma > 0$. Finding k_m is an exercise in differentiation and we

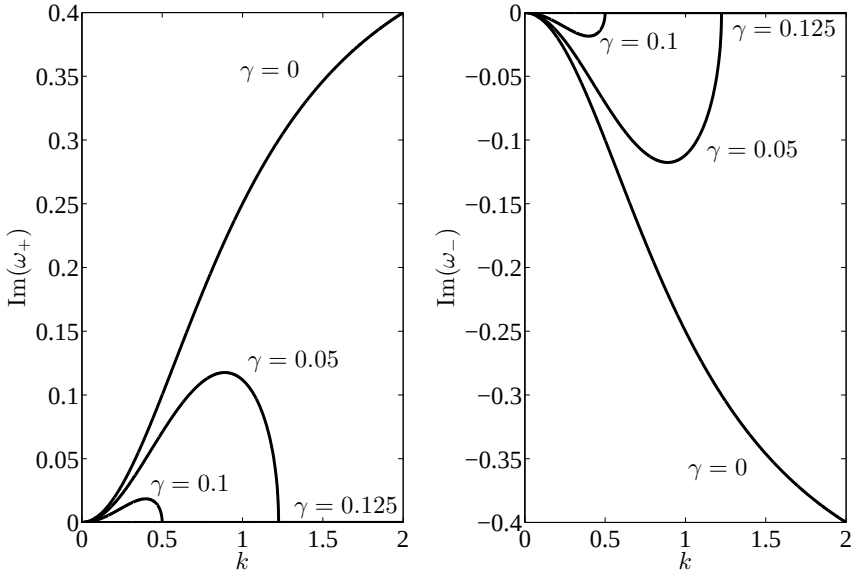

Figure 5.9: Dispersion relation branches for fixed $\rho' = 1$, $\eta = 1$ and $U_0 = 1/2$ for various values of the coefficient of surface tension, γ. While γ is less than the critical value of $1/8$, there is a range of wavenumbers for which $\mathrm{Im}(\omega_+) > 0$ and we have instability. For $\gamma \geq 1/8$, the jet is neutrally stable to perturbations. Note that surface tension also stabilises small wavelength perturbations, that is to say, there is a finite $k > 0$ for which $\mathrm{Im}(\omega_\pm(k)) = 0$ for all $k > 0$.

conclude that

$$k_m = \left(\frac{\rho'}{2\eta} \left(-3 + \sqrt{1 + (4/\gamma)(U_0 - 1)^2} \right) \right)^{1/2}. \tag{5.93}$$

The outer square-root is only real while $0 < \gamma < (U_0 - 1)^2/2$, that is while there remain unstable modes. Given the definitions of γ, η and ρ' along with a suitable estimate of the unperturbed gas speed, U_0, this maximum wavenumber could be compared to experimental data for the spacing between entrapped bubble rings under lamellae or the undulations of a splash jet, provided we are in the correct gas-flow regime.

5.4.3 Summary

For both viscous and inviscid gas layers, our jet model is unstable to small perturbations provided that the coefficient of surface tension, γ, is sufficiently small. We recall that

$$\gamma = \frac{1}{\varepsilon_l \mathrm{We}} = \frac{\sigma}{\rho_l \ell_l U_s^2}.$$

This parameter is typically very small in droplet impacts. Suppose, for example, the impacting fluid is water, so that $\sigma = 7.2 \times 10^{-4}$ Nm^{-1} and $\rho_l = 10^{-3}$ kgm^{-3}, and let us assume that $U_s = O(1)$. Then

$$\gamma \sim 7.2 \times 10^{-7} \ell_l^{-1}. \tag{5.94}$$

Therefore, even for jets whose thickness is on the order of micrometres, the surface tension coefficient is much smaller than unity.

Hence, in a typical impact scenario, we would expect a lamella or splash jet over a gas layer to be unstable to small perturbations. This is a possible mechanism for the touchdown of lamellae in droplet spreading, as described by Thoroddsen et al. (2010). Reliable estimates of the gas layer thickness, jet thickness and jet speed are required to compare the maximum wavenumber given by (5.79) (in the viscous gas regime) or by (5.93) (in the inviscid gas regime) to these experiments.

However, the splash jet buckling and touchdown phenomena seen in, for example Thoroddsen et al. (2011) or Thoraval et al. (2012), appear to be due to more dynamic behaviour as the jet grows. Therefore, we will now move on to the modelling of a finite, but growing jet, in which the nozzle and tip effects may be important.

5.5 Growing jet

At the outset, we state that there are a lot of open questions and that there is much scope for further research in our model of a growing jet. We will make several simplifying assumptions in the derivation of our model, and the importance of each assumption needs to be studied in detail. Nevertheless, we hope that our model provides some useful insight into the growth of a splash jet.

Consider the jet configuration depicted in Figure 5.10. A jet is shot out of a nozzle at $x^* = 0$ at a typical speed U_s over a solid substrate. The jet is assumed to have a typical thickness of ℓ and typical length L. A layer of air of typical thickness ℓ is trapped between the jet and the substrate, and the region above the jet is assumed to be an unbounded region of air. We have indicated four specific regions in Figure 5.10. Region I is an order unity aspect ratio region near the nozzle at $x^* = 0$. In region II, the length of the jet is assumed to be much larger than the thickness of the jet. Region III is situated about the tip of the jet, where the aspect ratio is again of order unity. Region IV represents the unbounded air region above the jet.

The model has the potential to be very complicated and we shall make a series of simplifying assumptions at the outset. Firstly, we shall assume that the jet has already formed, so that $\ell \ll L$. Naturally there is a short timescale over which the

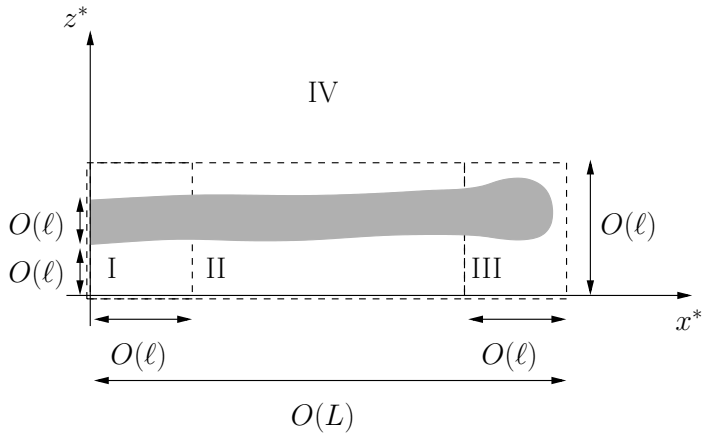

Figure 5.10: Configuration for the growing jet problem. We assume that the jet length is of $O(L)$ compared to the jet/gas layer thickness of $O(\ell)$. The bulk of the jet is in region II, while the tip is in region III, located about $x^* = s^*(t^*)$, $z^* = H^*(s^*(t^*), t^*)$. See text for further details.

length and thickness of the splash jet are comparable. In this thesis, we will make the assumption that the long-time effect of this initiation stage is small, and that jet evolution for later times is well-described by our model. This, naturally, is something that needs to be addressed in more detail. Secondly, we shall neglect the flow in region I near the nozzle and assume that its influence on the main body of the jet is well described by the boundary conditions we shall prescribe at $x^* = 0$ shortly. Thirdly, although a matching condition to the flow in region IV is of importance in region III, we shall neglect it completely in region II, so that the analysis of §§5.2–5.3 can be used. Hence, for simplicity, we assume that the flow in region IV is well-approximated by the far-field condition we apply in region III.

Under these assumptions, we suppose that the length of the jet is much larger than ℓ, so that the tip is a distance of $O(L)$ away from the nozzle. In the region II, the horizontal lengthscale is of $O(L)$ compared to the vertical lengthscales of $O(\ell)$ in the jet and gas, so we expect the analysis of §5.3 to hold subject to inlet conditions at $x^* = 0$ and matching conditions towards the tip. In the tip region, labelled by III, the aspect ratio is $O(1)$, that is $x^* - s^*(t^*) = z^* = O(\ell)$, where the horizontal coordinate of the jet tip is defined to be $x^* = s^*(t^*)$.

Naturally, we could derive a model in any of the four regimes we discussed in detail in §§5.2–5.3. In this thesis, we shall investigate the regime in §5.3.2 in detail. Hence, we assume that the reduced Reynolds number in the gas is small and that the Reynolds number in the jet is large. As described in §5.3.2, the governing equations

in region II are

$$h_t + (uh)_x = 0, \tag{5.95}$$

$$u_t + uu_x = 0, \tag{5.96}$$

$$H_t + \frac{1}{2}(uH)_x = \frac{1}{12}\left(H^3 P_x\right)_x, \tag{5.97}$$

$$h^2 u_x^2 + h\left[\left(u^2 - \frac{2\gamma}{h}\right)H_{xx} + 2uH_{xt} + H_{tt}\right] = \lambda P - \frac{h}{\varepsilon_l \mathrm{Fr}^2} + \gamma h_{xx}. \tag{5.98}$$

We shall discuss the appropriate boundary conditions for this problem in detail after considering the tip region, but we assume that the jet velocity and thickness are prescribed at the nozzle, viz.

$$u(0,t) = u_s(t), \quad h(0,t) = h_s(t), \tag{5.99}$$

where the functions $h_s(t)$, $u_s(t)$ are given.

We can in principle solve (5.95)–(5.96) subject to (5.99) using the method of characteristics. If τ parametrises distance along the characteristic and υ parametrises the initial data, we conclude that

$$t = \tau + \upsilon, \quad x = u_s(\upsilon)\tau, \quad u(\tau,\upsilon) = u_s(\upsilon), \quad h(\tau,\upsilon) = \frac{h_s(\upsilon)u_s(\upsilon)}{(u_s(\upsilon) - u_s'(\upsilon)\tau)}, \tag{5.100}$$

for τ, $\upsilon > 0$, which is valid provided that the Jacobian $J(\tau,\upsilon) = u_s(\upsilon) - u_s'(\upsilon)\tau$ is nonzero and bounded.

For the rest of this chapter, we will consider the simplest example, in which $u_s(t) = 1$, $h_s(t) = 1$ are both constant for $t > 0$. Thus, $u = 1$, $h = 1$ so that the jet has constant speed and thickness. Therefore, the model in region II predicts that the jet tip is at $x = t$ and that the jet has a finite thickness there. Clearly, we need to consider the model in region III in more detail.

5.5.1 Tip region

Close to the tip, there is a different asymptotic regime in which the large-aspect-ratio assumption is no longer valid. In this thesis, we will assume that the tip region is of size of $O(\ell) \times O(\ell)$, centred about the tip, $x^* = s^*(t^*)$. Now, the bulk region believes the jet tip is at $x^* = U_s t^*$, but we may lose mass and momentum from the bulk region into the tip region due to action of surface tension or air resistance, which may alter the location of the tip. However, under the assumptions we have made on the sizes of the bulk and inner region, the correction to the location of the tip must be small. Since the amount of fluid that has been injected into the jet at time t^* is of $O(\rho_l \ell L)$,

the amount of fluid in the bulk region is of $O(\rho_l \ell L)$ and the amount of fluid in the jet tip is of $O(\rho_l \ell^2)$, any correction to the location of the tip due to the flow in the tip region must be of $O(\varepsilon_l)$, so that $s(t^*) = U_s t^* + \varepsilon_l s_1(t^*)$.

Clearly there are other possible structures for the growing jet with a larger tip region, in which the tip region accounts for a comparable amount of mass to the bulk region, and the bulk region is therefore shorter, but we do not speculate on what such jets might look like here.

Bearing the above in mind, we scale into the tip region by writing

$$x^* - U_s t^* = \ell\tilde{x}, \quad s_1^* = \ell\tilde{s}_1 \quad z^* = \ell\tilde{z}, \quad H^* = \ell\tilde{H}, \quad h^* = \ell\tilde{h}, \quad t^* = \frac{L}{U_s}t,$$

where the liquid and gas velocities and pressures are scaled by

$$(u^*, U^*) - U_s = U_s(\tilde{u}, \tilde{U}), \quad (w^*, W^*) = U_s(\tilde{w}, \tilde{W}), \quad p^* = \rho_l U_s^2, \quad P^* = \frac{\mu_g U_s}{\ell}\tilde{P}.$$

Therefore, defining $\varepsilon_l = \ell/L$,

$$\begin{aligned}
\varepsilon_l\tilde{u}_t + \tilde{u}\tilde{u}_{\tilde{x}} + \tilde{w}\tilde{u}_{\tilde{z}} &= -\tilde{p}_{\tilde{x}} + \frac{1}{\varepsilon_l \mathrm{Re}_l}\left(\tilde{u}_{\tilde{x}\tilde{x}} + \tilde{u}_{\tilde{z}\tilde{z}}\right), && (5.101)\\
\varepsilon_l\tilde{w}_t + \tilde{u}\tilde{w}_{\tilde{x}} + \tilde{w}\tilde{w}_{\tilde{z}} &= -\tilde{p}_{\tilde{z}} + \frac{1}{\varepsilon_l \mathrm{Re}_l}\left(\tilde{w}_{\tilde{x}\tilde{x}} + \tilde{w}_{\tilde{z}\tilde{z}}\right) - \frac{\varepsilon_l}{\mathrm{Fr}^2}, && (5.102)\\
\tilde{u}_{\tilde{x}} + \tilde{w}_{\tilde{z}} &= 0 && (5.103)
\end{aligned}$$

in the jet for $\tilde{H}(\tilde{x}, t) < \tilde{z} < \tilde{H}(\tilde{x}, t) + \tilde{h}(\tilde{x}, t)$ and $\tilde{x} < \tilde{s}_1(t)$, and

$$\begin{aligned}
\varepsilon_l \mathrm{Re}_g\left(\varepsilon_l\tilde{U}_t + \tilde{U}\tilde{U}_{\tilde{x}} + \tilde{W}\tilde{U}_{\tilde{z}}\right) &= -\tilde{P}_{\tilde{x}} + \tilde{U}_{\tilde{x}\tilde{x}} + \tilde{U}_{\tilde{z}\tilde{z}}, && (5.104)\\
\varepsilon_l \mathrm{Re}_g\left(\varepsilon_l\tilde{W}_t + \tilde{U}\tilde{W}_{\tilde{x}} + \tilde{W}\tilde{W}_{\tilde{z}}\right) &= -\tilde{P}_{\tilde{z}} + \tilde{W}_{\tilde{x}\tilde{x}} + \tilde{W}_{\tilde{z}\tilde{z}} - \varepsilon_l^2 \mathrm{St}, && (5.105)\\
\tilde{U}_{\tilde{x}} + \tilde{W}_{\tilde{z}} &= 0, && (5.106)
\end{aligned}$$

in the gas, which now occupies the region above, below and in front the jet. The dimensionless parameters Re_l, Re_g, Fr^2 are defined as in §5.3 and $\mathrm{St} = \rho_g g L^2/(\mu_g U_s)$ is the Stokes number in the gas.

We continue to consider the free surfaces as $\tilde{H}(\tilde{x}, t)$ and $\tilde{H}(\tilde{x}, t)+\tilde{h}(\tilde{x}, t)$ separately, although by definition they join at the tip. The kinematic conditions are

$$\begin{aligned}
\tilde{w} &= \varepsilon_l\tilde{H}_t + \tilde{u}\tilde{H}_{\tilde{x}} && \text{on} \quad \tilde{z} = \tilde{H}, && (5.107)\\
\tilde{W} &= \varepsilon_l\tilde{H}_t + \tilde{U}\tilde{H}_{\tilde{x}} && \text{on} \quad \tilde{z} = \tilde{H}, && (5.108)\\
\tilde{w} &= \varepsilon_l\left(\tilde{H}_t + \tilde{h}_t\right) + \tilde{u}(\tilde{H}_{\tilde{x}} + \tilde{h}_{\tilde{x}}) && \text{on} \quad \tilde{z} = \tilde{H} + \tilde{h}, && (5.109)\\
\tilde{W} &= \varepsilon_l\left(\tilde{H}_t + \tilde{h}_t\right) + \tilde{U}(\tilde{H}_{\tilde{x}} + \tilde{h}_{\tilde{x}}) && \text{on} \quad \tilde{z} = \tilde{H} + \tilde{h}, && (5.110)
\end{aligned}$$

and the continuity of velocity conditions give

$$\tilde{u} = \tilde{U},\ \tilde{w} = \tilde{W} \quad \text{on} \quad \tilde{z} = \tilde{H},\ \tilde{H} + \tilde{h}. \tag{5.111}$$

The normal stress condition on $\tilde{z} = \tilde{H}$ is given by

$$\begin{aligned} \tilde{p} - \frac{\mu}{\varepsilon_l \mathrm{Re}_l}\tilde{P} &= \gamma\kappa + \frac{2}{\varepsilon_l \mathrm{Re}_l(1+\tilde{H}_{\tilde{x}}^2)}\Big[\tilde{H}_{\tilde{x}}^2(\tilde{u}_{\tilde{x}} - \mu\tilde{U}_{\tilde{x}}) + \\ &\qquad \tilde{w}_{\tilde{z}} - \tilde{W}_{\tilde{z}} - \tilde{H}_{\tilde{x}}(\tilde{u}_{\tilde{z}} + \tilde{w}_{\tilde{x}} - \mu(\tilde{U}_{\tilde{z}} + \tilde{W}_{\tilde{x}}))\Big], \end{aligned} \tag{5.112}$$

and on $\tilde{z} = \tilde{H} + \tilde{h}$ by

$$\begin{aligned} \tilde{p} - \frac{\mu}{\varepsilon_l \mathrm{Re}_l}\tilde{P} &= -\gamma\kappa + \frac{2}{\varepsilon_l \mathrm{Re}_l(1+(\tilde{H}_{\tilde{x}} + \tilde{h}_{\tilde{x}})^2}\Big[(\tilde{H}_{\tilde{x}} + \tilde{h}_{\tilde{x}})^2(\tilde{u}_{\tilde{x}} - \mu\tilde{U}_{\tilde{x}}) + \\ &\qquad \tilde{w}_{\tilde{z}} - \tilde{W}_{\tilde{z}} - (\tilde{H}_{\tilde{x}} + \tilde{h}_{\tilde{x}})(\tilde{u}_{\tilde{z}} + \tilde{w}_{\tilde{x}} - \mu(\tilde{U}_{\tilde{z}} + \tilde{W}_{\tilde{x}}))\Big], \end{aligned} \tag{5.113}$$

where, for convenience, we have used the curvature, $\kappa = -\nabla \cdot \mathbf{n}$, where $\mathbf{n}$ is the outward-pointing unit normal to the free surface. The tangential stress condition on $\tilde{z} = \tilde{H}$ is given by

$$\begin{aligned} &2\tilde{H}_{\tilde{x}}\left(\tilde{u}_{\tilde{x}} - \tilde{w}_{\tilde{z}}\right) + \left(\tilde{H}_{\tilde{x}}^2 - 1\right)\left(\tilde{u}_{\tilde{z}} + \tilde{w}_{\tilde{x}}\right) \\ &\qquad = \mu\left[2\tilde{H}_{\tilde{x}}\left(\tilde{U}_{\tilde{x}} - \tilde{W}_{\tilde{z}}\right) + \left(\tilde{H}_{\tilde{x}}^2 - 1\right)\left(\tilde{U}_{\tilde{z}} + \tilde{W}_{\tilde{x}}\right)\right], \end{aligned} \tag{5.114}$$

and on $\tilde{z} = \tilde{H} + \tilde{h}$ by

$$\begin{aligned} &2\left(\tilde{H}_{\tilde{x}} + \tilde{h}_{\tilde{x}}\right)\left(\tilde{u}_{\tilde{x}} - \tilde{w}_{\tilde{z}}\right) + \left(\left(\tilde{H}_{\tilde{x}} + \tilde{h}_{\tilde{x}}\right)^2 - 1\right)\left(\tilde{u}_{\tilde{z}} + \tilde{w}_{\tilde{x}}\right) \\ &\qquad = \mu\left[2\left(\tilde{H}_{\tilde{x}} + \tilde{h}_{\tilde{x}}\right)\left(\tilde{U}_{\tilde{x}} - \tilde{W}_{\tilde{z}}\right) + \left(\left(\tilde{H}_{\tilde{x}} + \tilde{h}_{\tilde{x}}\right)^2 - 1\right)\left(\tilde{U}_{\tilde{z}} + \tilde{W}_{\tilde{x}}\right)\right]. \end{aligned} \tag{5.115}$$

Finally, the no-slip, no-flux conditions on the solid substrate are given by

$$\tilde{U} = -1,\ \tilde{W} = 0 \quad \text{on} \quad z = 0. \tag{5.116}$$

In the far field in the jet, we must have

$$\tilde{u} \to 0,\ \tilde{h} \to 1 \quad \text{as} \quad x \to -\infty, \tag{5.117}$$

and in the gas, the flow must be quiescent far from the jet, except for $0 < \tilde{z} < \tilde{H}$ as $\tilde{x} \to -\infty$, where we must match to the solution in region II.

One thing that is immediately apparent is that, to leading order in ε_l and $\varepsilon_l^2\mathrm{Re}_g$, the tip region problem is quasi-steady. However, it is nontrivial to find solutions to the problem. Nevertheless, one matching condition drops out of our scalings in this

region. The pressure scaling in the gas in the tip region is $O(1/\ell)$ smaller than the gas pressure scaling in the bulk region. Therefore, at the tip in region II, we require

$$P(t,t) = 0, \tag{5.118}$$

which is physically intuitive since the high-pressure gas under the jet is flowing out into a large, quiescent region of gas. Further matching conditions do not come so readily.

When $\gamma = O(1)$, surface tension enters the leading-order tip region problem and (5.118) is a sensible matching condition to use in solving the bulk region model[3]. If γ is small, surface tension does not come into the leading-order problem in the tip region, which is slightly counter-intuitive in light of the rounded tips typically seen on lamellae and splash jets in experiments. Since small-γ is commonly the physically relevant limit, we might conjecture that if the curvature becomes large anywhere in the 'inner' tip region, an 'inner-inner' region would exist on an even finer lengthscale to bring the curvature terms back into the dynamic boundary condition. A thorough analysis of the inner region solution is needed to determine whether the curvature becomes large, and such an analysis, appears, unfortunately, to only be possible numerically, even in the limit in which γ is small. We would expect the correction described by such an 'inner-inner' region to be local and the flow to cause a lower-order perturbation in the 'inner' tip region we have just described (which acts as an intermediate region). Thus, we conjecture that (5.118) is the appropriate matching condition even in the limit in which γ is small.

In line with §5.3.2, in region II, we assume that $\varepsilon_l \ll 1$, $\mu/(\varepsilon_l \mathrm{Re}_l) = O(\varepsilon_l^3)$ and $\mu \ll 1$. Therefore, under these assumptions, all the gas terms drop out of the stress conditions (5.112)–(5.115) in the tip region to leading order. Thus, it appears that the only coupling at leading order between the jet and gas flows in the tip region is through the continuity of velocity conditions (5.111). Despite this and the fact the tip region is quasi-steady over the timescale we consider here, analytic progress is far from simple and we will not attempt anything further here. Fortunately, it transpires that when surface tension is small, (5.118) is the only matching condition that we require to solve the bulk region problem, as we shall now describe.

[3]Although this can only be confirmed with a thorough matched asymptotic analysis, which we do not pursue here.

5.5.2 Bulk region

In summary and for convenient reference in the following section, in region II, $H(x,t)$ and $P(x,t)$ satisfy

$$H_t + \frac{H_x}{2} = \frac{1}{12}\left(H^3 P_x\right)_x, \tag{5.119}$$

$$\left(1-\beta^2\right) H_{xx} + 2H_{xt} + H_{tt} = \lambda P, \tag{5.120}$$

for $0 < x < t$. Note that we have introduced $\beta^2 = 2\gamma$ for notational convenience and, for simplicity, we have assumed that $1/(\varepsilon_l \mathrm{Fr}^2) \ll 1$. Throughout this section we will assume that $0 \leq \beta < 1$. When $\beta = 1$, the problem is degenerate and needs to be studied in more detail. When $\beta \gg 1$, surface tension dominates the system, which is not the physically-relevant limit.

In order to consider what initial and boundary conditions we require, we write (5.119)–(5.120) as a system of five first-order partial differential equations by defining $P_x = Q$, $H_x = R$ and $H_t = V$. The characteristics of this system for $0 \leq \beta < 1$ are given by

$$\frac{\mathrm{d}t}{\mathrm{d}x} = 0\ (\times 3), \quad \frac{\mathrm{d}t}{\mathrm{d}x} = \frac{1}{\beta+1}, \frac{\mathrm{d}t}{\mathrm{d}x} = \frac{1}{1-\beta}. \tag{5.121}$$

Although we cannot say much about the system classification – although it is certainly not hyperbolic due to the repeated characteristics – there is clearly a change of behaviour when $\beta = 0$ because the fourth and fifth sets of characteristics coincide, with $\mathrm{d}t/\mathrm{d}x = 1$. These characteristic families also coincide with the jet tip at $x = t$. When $0 < \beta < 1$, one of the families of characteristics is entering the fluid domain from the tip, so we would expect to have to impose an additional condition at the jet tip when surface tension is not negligible.

To see this more clearly, we consider each of (5.119) and (5.120) in turn. If we know $H(x,t)$, then (5.119) is simply a second-order ordinary differential equation for $P(x,t)$. Therefore, we require two conditions on the pressure to solve the equation.

Now, suppose $P(x,t)$ is known, so that we can view (5.120) as a second-order, linear, constant-coefficient partial differential equation for $H(x,t)$. The characteristics of this equation are given by

$$(1-\beta^2)\dot{t} - 2\dot{t}\dot{x} + \dot{x}^2 = 0, \tag{5.122}$$

where a dot indicates differentiation with respect to τ, which measures distance along a characteristic.

When $\beta = 0$, (5.120) is parabolic, with repeated characteristic family $x - t = \text{const}$. Therefore, if we reduce (5.120) to canonical form by writing $\xi = x - t$, $\eta = t$,

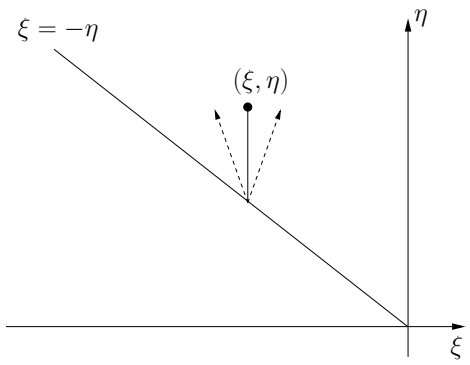

Figure 5.11: Domain of definition in the frame fixed with the jet tip, (ξ, η). The solid line indicates the lines of constant ξ which we must integrate along to solve (5.123), while the dashed arrows indicate the characteristics when β is nonzero.

$H(x,t) = \hat{H}(\xi,\eta)$, $P(x,t) = \hat{P}(\xi,\eta)$, we deduce that

$$\hat{H}_{\eta\eta} = \lambda \hat{P}. \tag{5.123}$$

We can solve this equation by integrating along lines of constant ξ, as depicted by the solid line in Figure 5.11. Therefore, we require two boundary conditions at the inlet on $\xi = -\eta$.

When $\beta > 0$, (5.120) is a hyperbolic equation for $H(x,t)$ if $P(x,t)$ is assumed to be known. Then, after moving to the domain fixed with the jet tip as in the parabolic case, we have

$$-\beta^2 \hat{H}_{\xi\xi} + \hat{H}_{\eta\eta} = \lambda \hat{P}, \tag{5.124}$$

where the characteristics of the equation are $\xi = \pm\beta\eta + \text{const}$. Therefore, as depicted by the dashed arrows in Figure 5.11, the family $\xi = \beta\eta + \text{const}$ will hit the boundary at $\xi = 0$. Therefore, we expect to apply a further boundary condition when β is nonzero.

Both of the arguments we have given suggest that we should consider the zero surface tension, $\beta = 0$, and nonzero surface tension, $0 < \beta < 1$, cases separately. Clearly there are further interesting limits of (5.119)–(5.120), for example the degenerate cases in which $\beta = 1$ and $\beta \to \infty$, but we leave these for future work.

Where do we prescribe the boundary conditions? We have already stated in §5.5.1 that matching with the tip region gives us a condition on P, so that

$$P(t,t) = 0 \tag{5.125}$$

We have shown that we require a second condition at the tip when the surface tension is nonzero, but we can say very little about this since we could not solve the tip region

problem. At the nozzle, physically we expect to be able to specify the height and angle at which we shoot the jet out. Furthermore, we would also expect there to be no flux of gas back underneath the nozzle. Hence, after returning to (x,t) coordinates, we specify

$$H(0,t) = a(t), \quad \left.\frac{\partial H}{\partial x}\right|_{(0,t)} = b(t), \quad \left.\frac{\partial P}{\partial x}\right|_{(0,t)} = \frac{6}{a(t)^2} \tag{5.126}$$

at the inlet.

We now have enough information to solve the growing jet problem for $\beta = 0$ numerically. However, in order to start the numerical schemes we develop in §5.5.3.2, we shall first perform a small-time analysis of (5.119)–(5.120) subject to (5.125)–(5.126).

5.5.3 Zero surface tension: $\beta = 0$

Recall that if we choose independent characteristic variables $\xi = x - t$, $\eta = t$, we reduce (5.120) to (5.123). This needs to be solved in the domain $-\eta < \xi < 0$, $\eta > 0$ as depicted in Figure 5.11. At the jet inlet, we know that

$$\hat{H}(-\eta,\eta) = a(\eta), \quad \left.\frac{\partial \hat{H}}{\partial \xi}\right|_{(-\eta,\eta)} = b(\eta). \tag{5.127}$$

We can differentiate the thickness condition with respect to η to deduce that

$$\frac{\partial \hat{H}}{\partial \eta} = \dot{a}(\eta) + b(\eta) \quad \text{on} \quad \xi = -\eta, \tag{5.128}$$

where a dot indicates differentiation with respect to argument. By integrating along lines of constant ξ, it is simple to solve (5.123), viz:

$$\hat{H}(\xi,\eta) = a(-\xi) + (b(-\xi) - \dot{a}(-\xi))\,(\eta+\xi) + \lambda \int_{-\xi}^{\eta}\int_{-\xi}^{s} P(\xi,\tau)\,\mathrm{d}\tau\,\mathrm{d}s, \tag{5.129}$$

or, after changing the order of integration,

$$\hat{H}(\xi,\eta) = a(-\xi) + (b(-\xi) - \dot{a}(-\xi))\,(\eta+\xi) + \lambda \int_{-\xi}^{\eta} (\eta-\tau) P(\xi,\tau)\,\mathrm{d}\tau. \tag{5.130}$$

In canonical variables, (5.119) is given by

$$\frac{\partial \hat{H}}{\partial \eta} - \frac{1}{2}\frac{\partial \hat{H}}{\partial \xi} = \frac{1}{12}\frac{\partial}{\partial \xi}\left(\hat{H}^3 \frac{\partial \hat{P}}{\partial \xi}\right), \tag{5.131}$$

with boundary conditions

$$\left.\frac{\partial \hat{P}}{\partial \xi}\right|_{(-\eta,\eta)} = \frac{6}{a(\eta)^2}, \quad \hat{P}(0,\eta) = 0. \tag{5.132}$$

We can integrate (5.131) along lines of constant η to deduce that

$$\hat{P}(\xi,\eta) = 12\int_0^\xi \frac{1}{\hat{H}(s,\eta)^3}\frac{\partial}{\partial\eta}\int_{-\eta}^{s}\hat{H}(\tau,\eta)\,\mathrm{d}\tau\,\mathrm{d}s - 6\int_0^\xi \frac{1}{\hat{H}(s,\eta)^2}\,\mathrm{d}s. \tag{5.133}$$

Thus, we have a pair of integral equations (5.129), (5.133) or differential equations (5.123), (5.131) for $\hat{H}$, $\hat{P}$. This gives us the basis of an iterative scheme to solve numerically for the gas layer thickness and gas pressure. To do so, we need a small-time solution of (5.123), (5.131).

5.5.3.1 Small-time solution

We now consider (5.123), (5.131) for small time. Let $0 < \epsilon \ll 1$. We suppose that $(\xi,\eta) = \epsilon(\bar{\xi},\bar{\eta})$ and write $\hat{H} = \epsilon^r\bar{H}$, $\hat{P} = \epsilon^s\bar{P}$. Note that we require time to be small, but we are still assuming that time is large enough that our large-aspect-ratio assumption is valid in the jet and gas layer (i.e. that the jet has formed). Then, assuming $a(0) \neq 0$, to retain a balance in (5.127), we must pick $r = 0$. Therefore, to retain the pressure at leading order in (5.123), we set $s = -2$. Hence, dropping the bars:

$$\epsilon^3\left(\frac{\partial H}{\partial\eta} - \frac{1}{2}\frac{\partial H}{\partial\xi}\right) = \frac{1}{12}\frac{\partial}{\partial\xi}\left(H^3\frac{\partial P}{\partial\xi}\right), \tag{5.134}$$

$$\frac{\partial^2 H}{\partial\eta^2} = \lambda P, \tag{5.135}$$

$$H(-\eta,\eta) = a(\epsilon\eta), \tag{5.136}$$

$$\left.\frac{\partial H}{\partial\xi}\right|_{(-\eta,\eta)} = \epsilon b(\epsilon\eta), \tag{5.137}$$

$$\left.\frac{\partial P}{\partial\xi}\right|_{(-\eta,\eta)} = \epsilon^3\left(\frac{6}{a(\epsilon\eta)^2}\right), \tag{5.138}$$

$$P(0,\eta) = 0. \tag{5.139}$$

We perform an asymptotic expansion in powers of ϵ, viz:

$$\begin{aligned} H &\sim H_0 + \epsilon H_1 + \epsilon^2 H_2 + \epsilon^3 H_3, \\ P &\sim P_0 + \epsilon P_1 + \epsilon^2 P_2 + \epsilon^3 P_3. \end{aligned}$$

The $O(1)$-, $O(\epsilon)$- and $O(\epsilon^2)$-solutions give

$$P_0 = 0, \quad H_0 = a(0), \tag{5.140}$$

$$P_1 = 0, \quad H_1 = \dot{a}(0)\eta + b(0)(\xi+\eta), \tag{5.141}$$

$$P_2 = 0, \quad H_2 = -\frac{\xi^2}{2}\ddot{a}(0) - \xi^2\dot{b}(0) - \left(\dot{b}(0) + \ddot{a}(0)\right)\xi\eta. \tag{5.142}$$

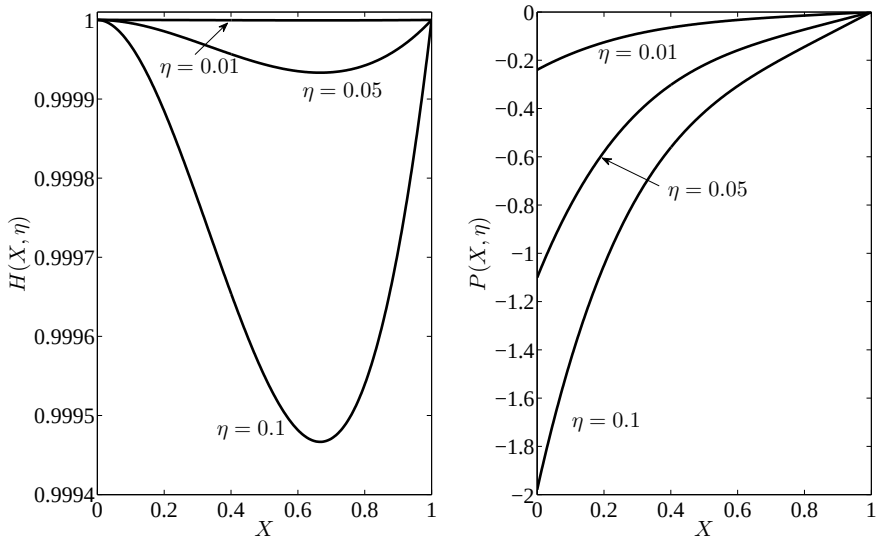

Figure 5.12: Small-time solution of (5.123)–(5.131) where $a(\eta) = 1$ and $b(\eta) = 0$.

Thus, solving (5.134) at $O(\epsilon^3)$, we find the leading-order solution for P_3, given by

$$P_3 = \frac{6\xi}{a(0)^2} \tag{5.143}$$

This can then be used along with (5.135) to deduce

$$H_3 = \left(\frac{6\lambda}{a(0)^2} + \frac{\dddot{a}(0)}{2} + \frac{\ddot{b}(0)}{2}\right)\xi^2\eta + \left(\frac{3\lambda}{a(0)^2} + \frac{\dddot{a}(0)}{3} + \frac{\ddot{b}(0)}{2}\right)\xi^3 + \frac{3\lambda}{a(0)^2}\xi\eta^2. \tag{5.144}$$

We can continue this process to find the correction to the leading-order linear form of $\hat{P}$. However, the algebra is quite involved and we do not produce it here.

When the splash jet is shot horizontally over the solid substrate, that is when $a(\eta) = 1$, $b(\eta) = 0$, the small-time solutions for $H(\xi, \eta)$ and $P(\xi, \eta)$ are plotted in figure 5.12. For ease of viewing we have mapped the domain $-\eta \leq \xi \leq 0$, $\eta > 0$ onto the domain $0 \leq X \leq 1$ where $\xi = (X - 1)\eta$. , the pressure in the gas layer sucks the jet toward the solid surface. The natural question is whether the jet can be induced to touch down by this gas layer. We investigate this numerically.

5.5.3.2 Numerical solution of the zero surface tension problem

We have developed two numerical schemes to solve (5.123) and (5.131) subject to (5.127), (5.128) and (5.132). The first is a Newton iterative solver based on an implicit discretization of the problem. This scheme is advantageous because it is

simple to implement and use, but its drawbacks are that it is not readily adaptable to the problem in which $\beta > 0$, and that for the very fine resolution needed as the thickness of the gas layer becomes small, the code takes in extraordinary amount of time to run. The second numerical scheme is a finite element solver, which while more difficult to develop (particularly in the case where $\beta = 0$), should extend readily to the $\beta > 0$ problem. This code was developed by Jon Whiteley using the PETSc libraries.

We shall almost exclusively use the Newton solver in this thesis, except in §5.5.3.3, where the higher resolution of the finite-element code is required. We will not describe the finite-element code in detail, but we will compare its output to the small-time asymptotics and the results produced by the Newton solver to verify that it is producing the correct solution.

Implicit Newton solver

In order to solve (5.123) and (5.131) subject to (5.127), (5.128) and (5.132), we will define (after dropping carets on the variables H and P),

$$V = \frac{\partial H}{\partial \eta}, \quad Q = \frac{H^3}{12}\frac{\partial P}{\partial \xi}. \tag{5.145}$$

Let the time be $\eta = \eta_n$ and discretise the domain of definition at this time by $-\eta_n = \xi_1 < \xi_2 < ... < \xi_M = 0$, where the uniform spacing is given by $\Delta\xi$ and M is a positive integer. Suppose we know H_j^n, P_j^n, V_j^n, Q_j^n for $j = 1, ..., M$. Then, if we increase the time to $\eta_{n+1} = \eta_n + \Delta\eta$, with $\Delta\eta = \Delta\xi$, the length of the domain increases by $\Delta\xi$. We denote the new gridpoint by $\xi_0 = \xi_1 - \Delta\xi$. We can evaluate the variables at the next time step by discretising (5.123), (5.131) and (5.145) as follows:

$$V_j^{n+1} = \frac{H_{j+1}^n - H_j^n}{\Delta\xi}, \tag{5.146}$$

$$\lambda P_j^{n+1} = \frac{V_j^{n+1} - V_j^n}{\Delta\xi}, \tag{5.147}$$

$$Q_j^{n+1} = \frac{(H_j^{n+1})^3}{12}\frac{P_{j+1}^{n+1} - P_j^{n+1}}{\Delta\xi}, \tag{5.148}$$

$$V_j^{n+1} - \frac{H_{j+1}^{n+1} - H_j^{n+1}}{2\Delta\xi} = \frac{Q_j^{n+1} - Q_j^{n+1}}{\Delta\xi}, \tag{5.149}$$

for $j = 0, ..., M$ and we have the boundary conditions

$$H_0^{n+1} = a(\eta_{n+1}), \quad V_0^{n+1} = b(\eta_{n+1}) + \dot{a}(\eta_{n+1}), \quad Q_0^{n+1} = \frac{a(\eta_{n+1})}{2}, \quad P_M^{n+1} = 0. \tag{5.150}$$

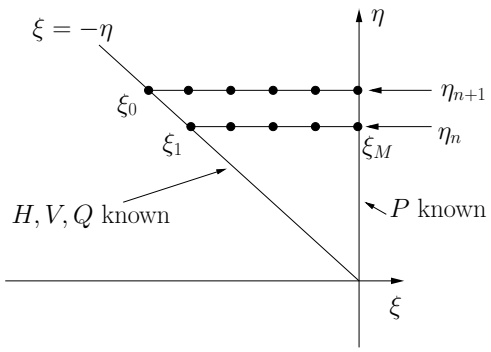

Figure 5.13: Discretization and solution procedure for the $\beta = 0$ problem.

The numerical iteration and discretization is depicted in Figure 5.13.

If the initial time, η_0, is suitably small, we can use our small-time solution to set the code running, using Newton iterations to solve the problem to a given tolerance at each value of $\eta_n > \eta_0$. This procedure can be repeated until the value of H becomes very small (and P, accordingly becomes large), where the code loses its accuracy.

Accuracy and convergence of the Newton solver

In order to check that the Newton solver is accurate and converges as we refine the time/space steps, we consider a specific example in which the jet is shot horizontally over the substrate, so that

$$a(\eta) = 1, \; b(\eta) = 0 \quad \text{for} \quad \eta > 0 \tag{5.151}$$

We start the code running at $\eta_0 = 0.01$ and use 100 gridpoints, so that $\Delta\xi = 0.0001$. To check the code is converging to the correct solution, we compare the results for H, P at $\eta = 0.05$, 0.1 and 0.2 against the small-time solution. The results are shown in Figure 5.14, where we have again plotted on the rescaled axis so that the jet is fixed on $0 \leq X \leq 1$, where $X = \xi/\eta + 1$. We see very good comparison between the numerical solution and the asymptotics, even up to $\eta = 0.2$. We have also plotted (dashed curve) the results at time $\eta = 0.2$ from the finite-element code run from $\eta_0 = 0.1$ with time-steps of size 0.01. We see good agreement between both codes and the asymptotic solution.

As well as checking the validity of our numerical solution against our asymptotic results, we need to confirm that the Newton code is converging by reducing the time/space steps. In Figure 5.15 we depict the gas layer thickness and pressure calculated from the Newton solver at time $\eta = 7$ for various values of $\Delta\xi$ varying from 0.01 to 0.001. We see that the results are virtually identical, even given the

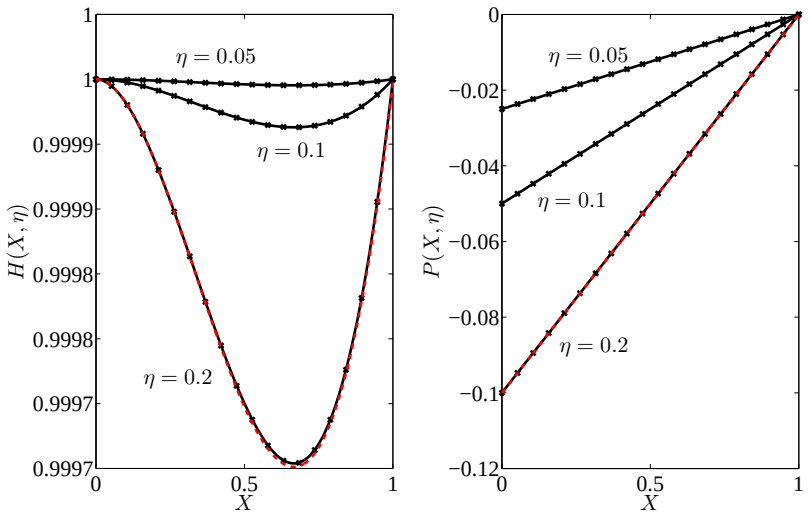

Figure 5.14: Comparison between the numerical (solid curves) and asymptotic (crosses) solutions of the $\beta = 0$ equation at various times, η. In this example $a(\eta) = 1$ and $b(\eta) = 0$. At time $\eta = 0.2$ we also include the results from the finite-element code (red dashed line).

order of magnitude change in the size of the time/space step. This is very good indication that the code is converging. Moreover, we have plotted (dashed pink curve) the corresponding solution from the finite-element code run from initial time $\eta_0 = 0.01$ with time-steps of size $\Delta\eta = 0.01$. The finite-element results almost exactly agree with the Newton solver solutions.

In Figure 5.16 we show the difference between the results for H and P produced at larger time/space steps to those produced when $\Delta\xi = 0.0001$. The convergence to this fine grid solution appears to be linear with $\Delta\xi$, although the error in the pressure solution is larger than that in the solution for H. As we shall see shortly, the difference in accuracy is due to the large pressure peaks that form when the jet gets close to touchdown on the substrate. Nonetheless, the results in Figures 5.15–5.16, coupled with the good comparison to the asymptotics for small η in Figure 5.14, are enough to conclude that our code is converging to the correct solution.

Results

We plot numerical solutions to the horizontal jet example, that is (5.123), (5.127), (5.131), (5.132) with (5.151). All of the results are calculated using the Newton solver. Our results are plotted in Figures 5.17-5.19. In the simulations, $\Delta\xi = 0.005$. In each

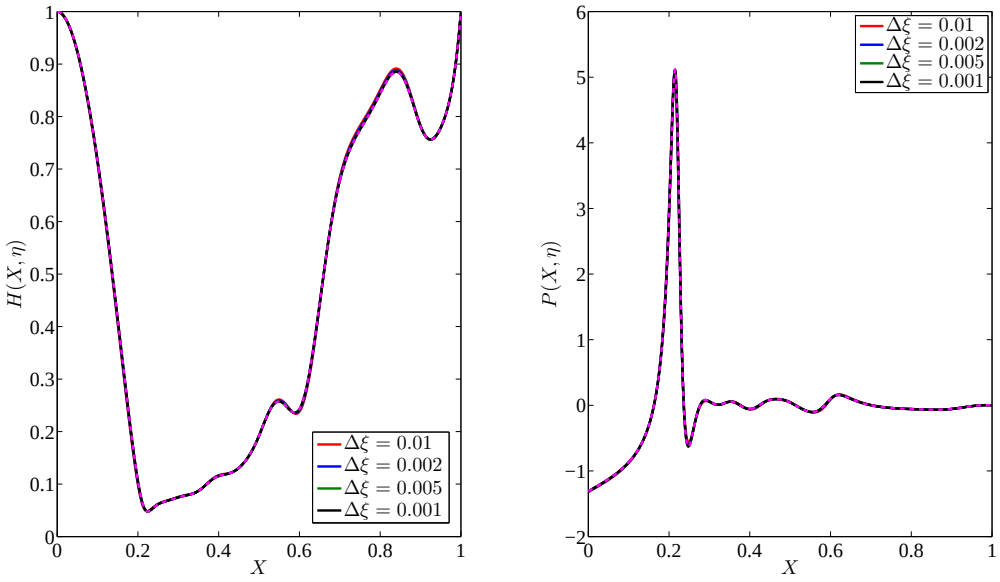

Figure 5.15: Comparison between the numerical solutions for H and P for $\Delta\xi = 0.01, 0.005, 0.002, 0.001$, where the final time is $\eta = 7$. The magenta dashed curve is the corresponding solution as found by the finite-element solver with timesteps of size 0.01. The curves are almost exactly on top of one another, giving good indication of convergence.

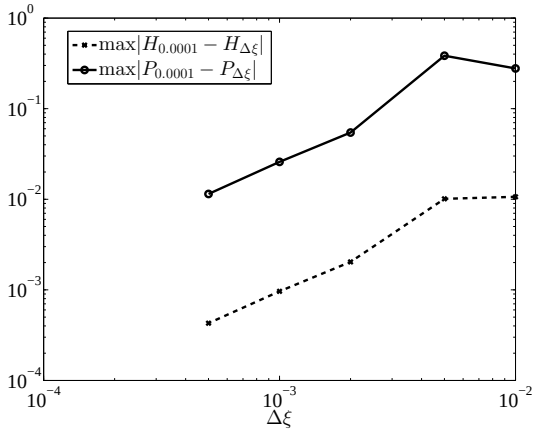

Figure 5.16: A log-log plot showing the convergence of H and P as we decrease $\Delta\xi = 0.01, 0.005, 0.002, 0.001, 0.0005$, to the solution $H_{0.0001}$, $P_{0.0001}$ for $\Delta\xi = 0.0001$ for time $\eta = 7$.

set of figures, we plot the gas layer thickness and the streamlines in the gas alongside the gas pressure. The streamlines are found from (5.39). We plot these variables against $X = \xi/\eta + 1$, where $0 < X < 1$.

In Figure 5.17, we plot the solution for $\eta = 2, 3, 4$. As the jet grows, the suction pressure in the gas causes a trough to form as the jet is displaced below its inlet height. While the gas upstream of this trough continues to pull the jet downwards, the flow downstream begins to flatten it out, slowing the speed at which the jet is pulled downwards. Recall that vertical velocity on $z = H$ is given by $W = H_\eta + ((1 - X)/\eta)H_X$. Let $X_m(\eta)$ denote the X-coordinate of the minimum of H. For $X < X_m$, $H_X < 0$, since we are on the downslope of the trough. Moreover, since the jet has been sucked down by the gas, $H_\eta < 0$ as well, so that $W < 0$ on the free surface and the jet continues to be pulled down. However, for $X > X_m$, $H_X > 0$, since we are on the upslope of the trough. Thus, eventually H_X is large enough to dominate $H_\eta < 0$ downstream of the trough, so W changes sign on the free surface downstream of the trough. This causes undulations downstream of the trough, as seen in the plot at $\eta = 4$.

We see these undulations grow in Figure 5.18 for $\eta = 5, 6, 7$, although the minimum of the gas layer thickness and the maximum pressure are still found at the original trough (smallest value of X for which there is a local minimum). As we increase time further in Figure 5.19, where $\eta = 8, 9, 10$ we see further local minima forming downstream of the original trough, and two in particular approach the original trough in magnitude. The width of these new troughs are much thinner than the original, that is $|H_X|$ is larger, and as a result they are pulled down more quickly by the sharp gradients in the gas pressure.

The code continues to run until $\eta = \eta_c \approx 10.548$, when it predicts that the layer thickness vanishes at $X \approx 0.661$. This is one of the new, narrower troughs downstream from the trough that corresponded to the global minimum in Figures 5.17–5.19 (which is at $X \approx 0.15$). We plot the 'touchdown' profile in Figure 5.20. Whether the jet as modelled by (5.123), (5.131) actually touches down in finite time or not is unclear, as the scales near touchdown are very fine and the numerics become unreliable. However, simulations using the finite-element method with a timestep of 10^{-7} still see touchdown, which is reasonable evidence that it does indeed occur.

Note that this idea of 'touchdown' is to be interpreted as touchdown away from the tip of the jet. Returning to original (x, t)-coordinates, if, say, we were to shoot the jet downwards, say $a(t) = 1$, $b(t) = -1/2$, the jet would certainly hit the solid surface at its tip. To see this, denote the thickness of the gas layer at the tip of the

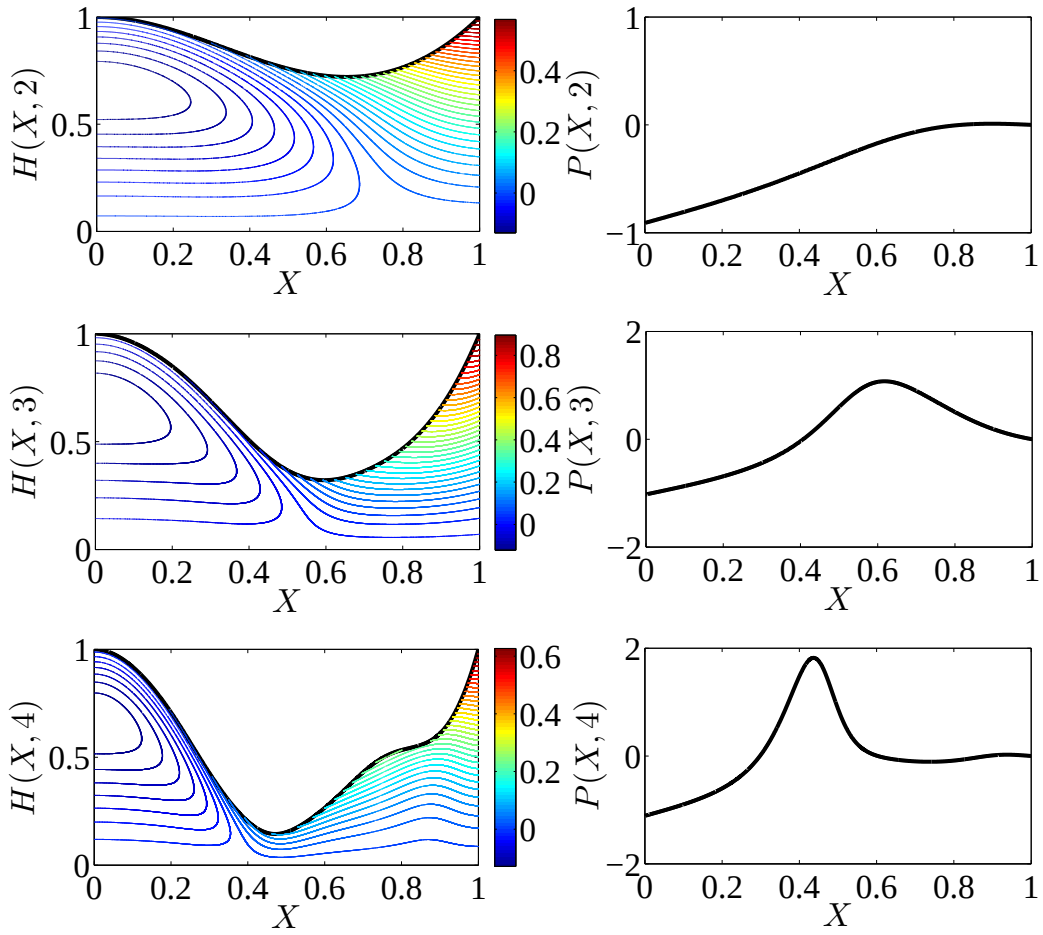

Figure 5.17: Solutions of the $\beta = 0$ problem for, from top to bottom, $\eta = 2, 3, 4$. On the left, we plot $H(X, \eta)$ along with the streamlines in the gas layer. On the right, we plot $P(X, \eta)$.

jet by $N(t) = H(t, t)$. Then,

$$\ddot{N}(t) = (H_{xx} + 2H_{xt} + H_{tt})|_{(t,t)} = \lambda P|_{(t,t)} = 0,$$

using the matching condition on the pressure (5.132). Hence $N(t) = At + B$. But using the small-time solution in §5.5.3.1, $H(0, 0) = 1$, $H_t(0, 0) = -1/2$, so that

$$N(t) = 1 - \frac{t}{2}. \tag{5.152}$$

Hence, we would expect touchdown of the jet by the latest time of $t = 2$ and possibly sooner if touchdown occurs away from the tip. We plot the numerical solution for

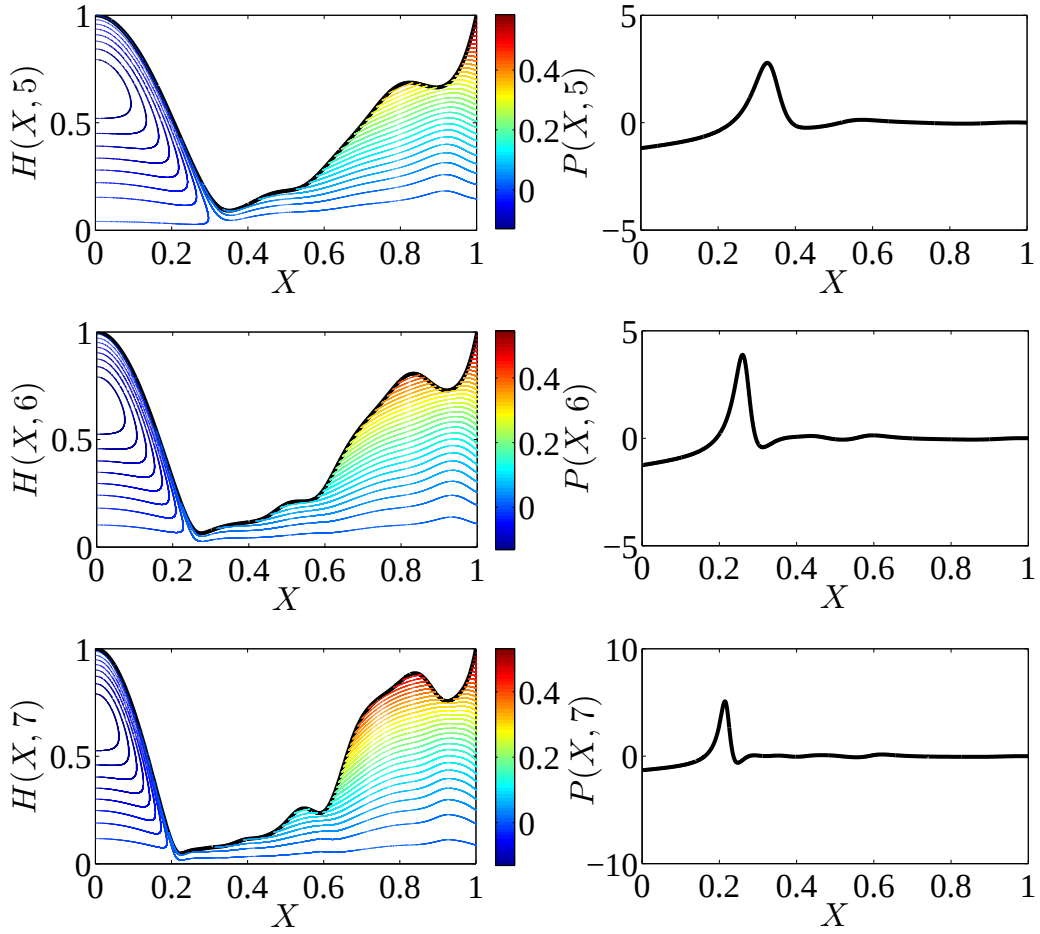

Figure 5.18: Solutions of the $\beta = 0$ problem for, from top to bottom, $\eta = 5, 6, 7$. On the left, we plot $H(X, \eta)$ along with the streamlines in the gas layer. On the right, we plot $P(X, \eta)$.

$a(t) = 1$, $b(t) = -1/2$ in Figure 5.21. Note that there is a singularity as the tip gets very close to touchdown; the tip region we discussed in §5.5.1 assumes that the gas layer thickness is the same order of magnitude as the splash jet. When the tip approaches touchdown, the gas layer thickness becomes vanishingly small, with the local pressure increasing accordingly. The singularity is clearly seen in the bottom-right plot in Figure 5.21.

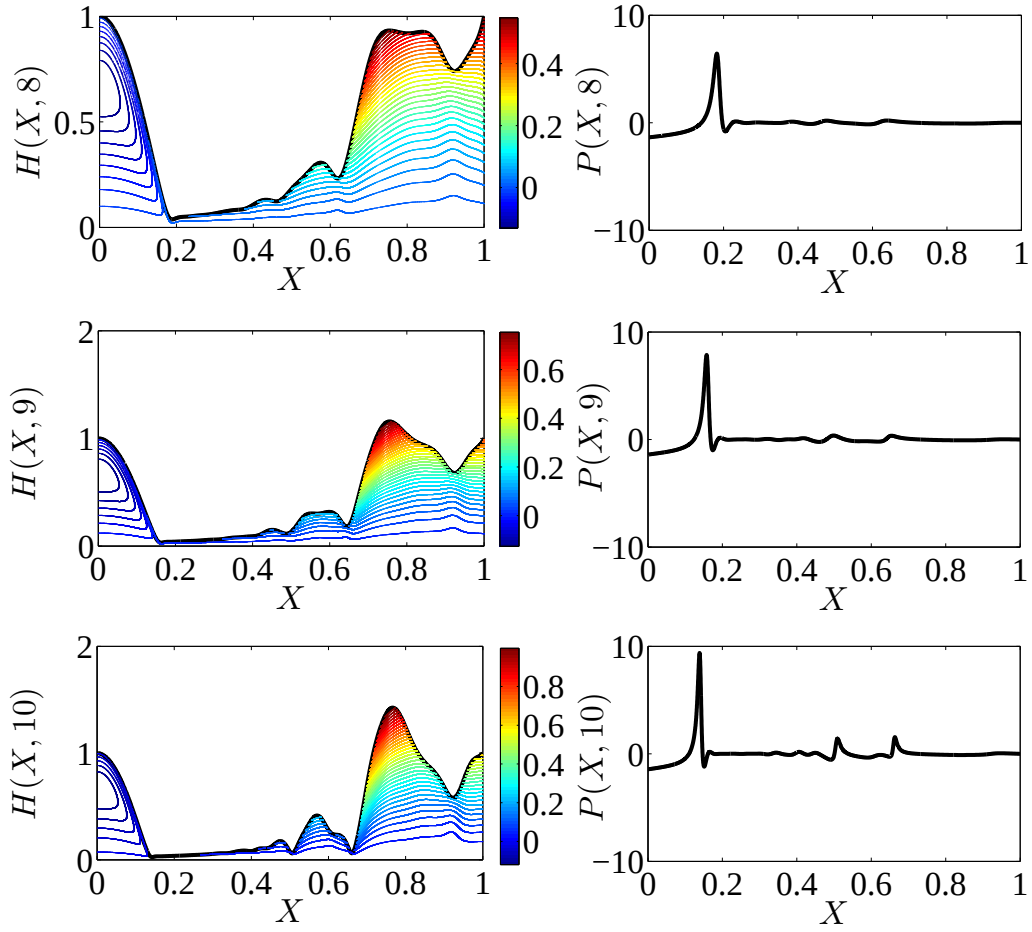

Figure 5.19: Solutions of the $\beta = 0$ problem for, from top to bottom, $\eta = 8, 9, 10$. On the left, we plot $H(X, \eta)$ along with the streamlines in the gas layer. On the right, we plot $P(X, \eta)$.

5.5.3.3 Conjectures on touchdown

We return to the case where $a(t) = 1$, $b(t) = 0$ and we conjecture that touchdown occurs away from the jet tip in finite time. If we consider, for example, Smith et al. (2003) or Purvis and Smith (2004), in such two-fluid problems it is common for there to be a similarity solution of the system (5.123), (5.131) as we approach touchdown. To investigate whether such a similarity solution is possible, in this section we will reconsider the problem in (x, t)-coordinates. We suppose that touchdown does occur in finite time, say at t_c at the point x_c. Define $\tau = t_c - t$ and let $x_m(\tau)$ be the

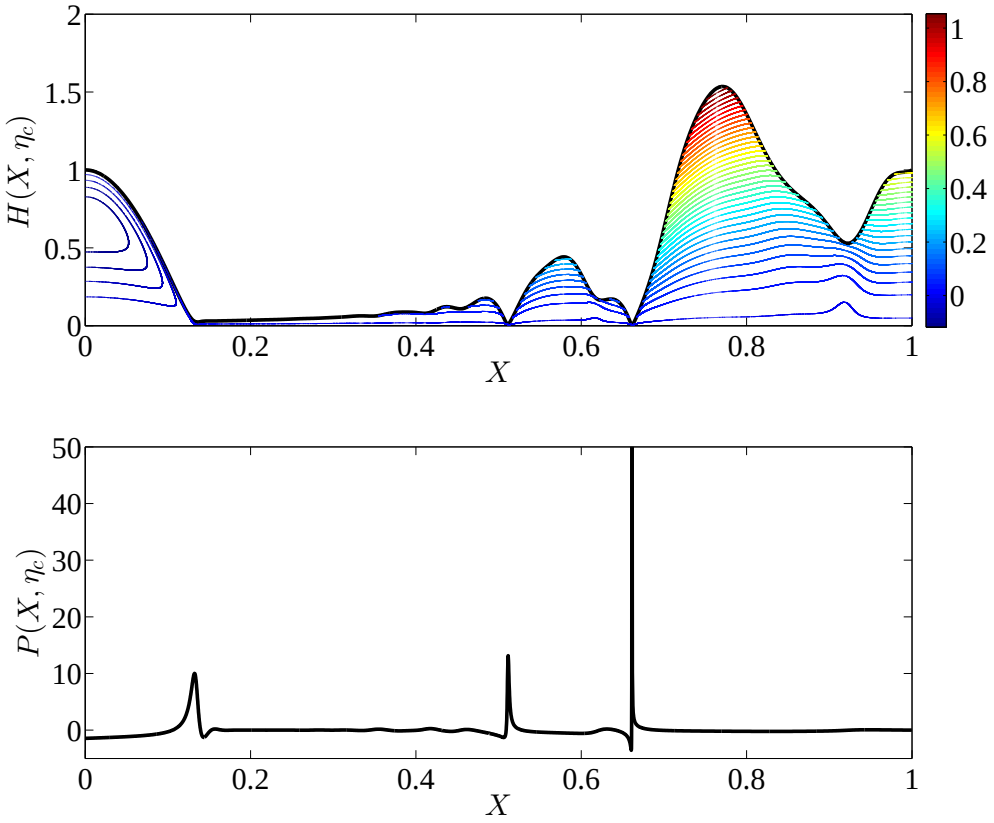

Figure 5.20: The code stops at time $\eta_c = 10.548$, when the minimum value of H reaches reaches zero.

x-coordinate of the minimum value of $H(x,\tau)$. We suppose that $x_m(\tau) \sim x_c + A\tau^\gamma$ as $\tau \to 0^+$ for some unknown γ, A. We conjecture that there exists a similarity solution to the problem of the form

$$H(x,t) = \tau^\alpha H^\dagger(\chi), \quad P(x,t) = \tau^\beta P^\dagger(\chi), \tag{5.153}$$

where α, β must be determined and the similarity variable is defined by

$$\chi = \frac{x - x_m(\tau)}{\tau^\delta}, \tag{5.154}$$

for some unknown power, δ. Upon substituting these scalings into (5.123), (5.131) and dropping the daggers, we deduce the similarity differential equations

$$\frac{\tau^{2\alpha+\beta-2\delta+1}}{12}(H^3P')' \;=\; \delta\chi H' - \alpha H + \frac{1}{2}\left(1 + 2A\gamma\tau^{\gamma-1}\right)\tau^{1-\delta}H', \tag{5.155}$$

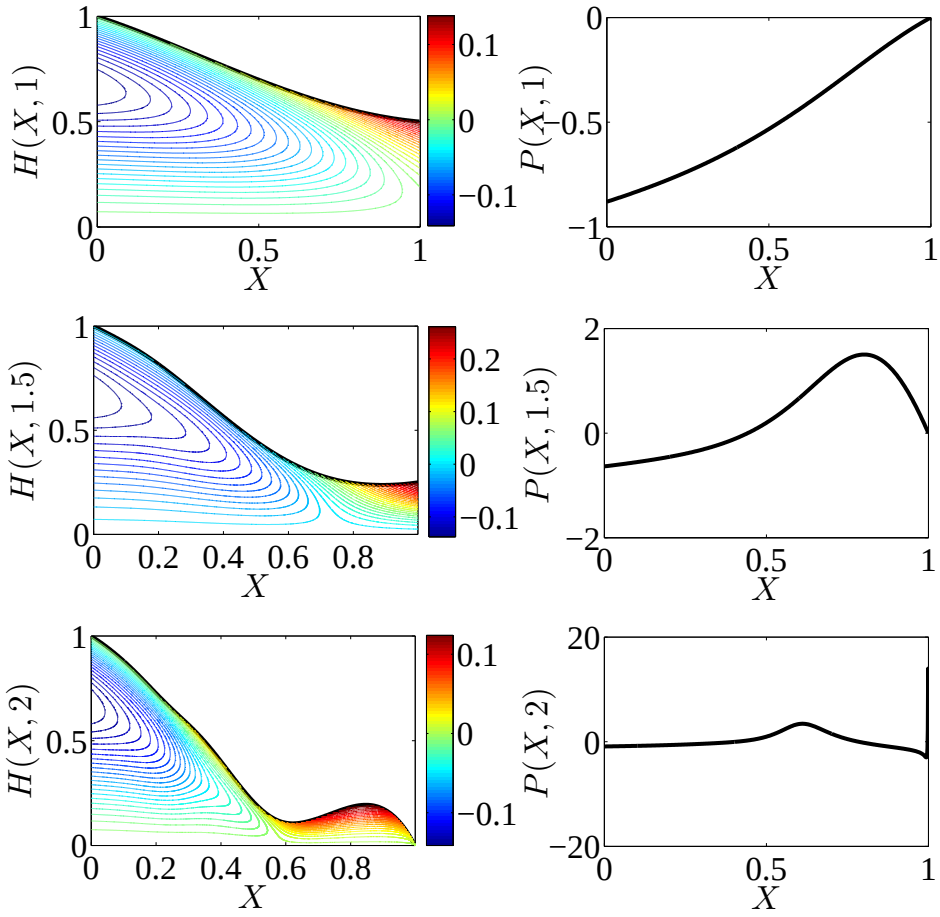

Figure 5.21: Touchdown at the tip at $\eta_c = 2$ for $a(t) = 1$, $b(t) = -1/2$.

$$\begin{aligned}\lambda\tau^{\beta}P &= (\alpha(\alpha-1)H - \delta(2\alpha-\delta-1)\chi H' + \delta^2\chi^2 H'')\tau^{\alpha-2} - \\ &\quad 2(A\gamma\tau^{\gamma-1}+1)((\alpha-\delta)H' - \delta\chi H'')\tau^{\alpha-\delta-1} + \\ &\quad (A\gamma\tau^{\gamma-1}+1)^2 H''\tau^{\alpha-2\delta} - A\gamma(\gamma-1)\tau^{\gamma-2+\alpha-\delta}H'. \qquad (5.156)\end{aligned}$$

In order to determine the unknown exponents α, β, γ and δ from the numerical solution, we use the finite-element code with very fine resolution near touchdown: the following results are run with timestep 10^{-7} and a variable grid-size, which reaches 10^{-6} near the touchdown region.

In Figures 5.22–5.23, we plot the minimum value of H, the maximum value of P and the corresponding x-coordinate. For $\tau = O(10^{-3} - 10^{-1})$, $\min(H)$ and $\max(P)$ scale approximately with $\tau^{3/2}$ and $\tau^{-3/2}$ respectively, although this behaviour tails off closer to touchdown. Whether this is as a result of a similarity formulation breaking

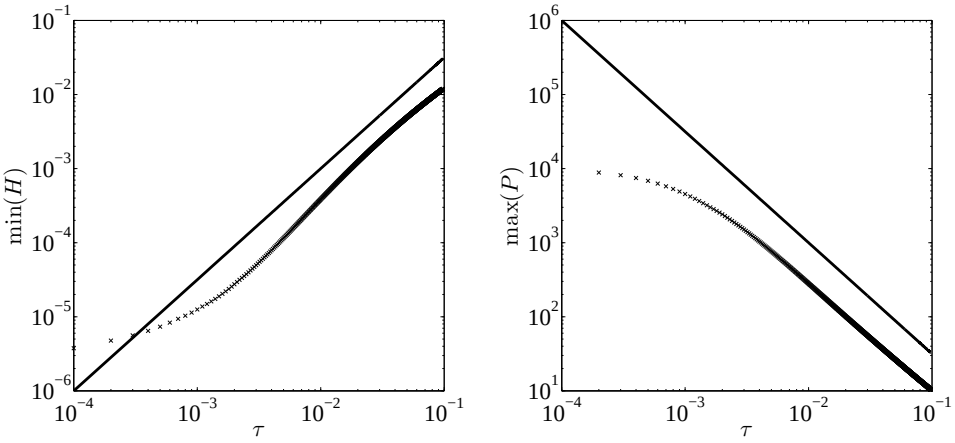

Figure 5.22: Log-log plots of the minimum thickness, $\min(H)$, and the maximum gas pressure, $\max(P)$ as a function of τ. The left-hand plot depicts $\min(H)$ and the guideline is $\tau^{3/2}$. The right-hand plot depicts $\max(P)$ and the guideline is $\tau^{-3/2}$. For larger τ we see good adherence to these scalings, but as we approach touchdown, there is significant deviation away from the proposed similarity form.

down or due to limitations of the numerical scheme is unclear. In Figure 5.23, we plot $x_m(\tau)$ along with a linear fit, suggesting that $\gamma \approx 1$ and $A = -0.55$.

With these estimates for α, β, γ, we must choose $\delta = 3/2$ in order to retain a leading-order balance in (5.155), giving

$$\frac{1}{12}(H^3P')' = \left(\frac{1}{2} + A\right)H' + \frac{3\tau^{1/2}}{2}(H - \chi H'), \tag{5.157}$$

$$\lambda P = (A+1)^2 H'' - 3\tau^{1/2}(A+1)\chi H'' + \frac{3\tau}{4}\left(H - \chi H' + 3\chi^2 H''\right), \tag{5.158}$$

so that for small τ, there is an approximate similarity solution satisfying

$$\Gamma(H^3 H''')' = H', \tag{5.159}$$

where $\Gamma = (\lambda(A+1)^2)/(6(1+2A)) < 0$, since $A < -1/2$.

Since $\tau^{1/2}$ is not particularly small for the range over which we see a good fit with these scaling laws, that is $\tau \approx 10^{-3} - 10^{-1}$, it is unclear whether this approximate

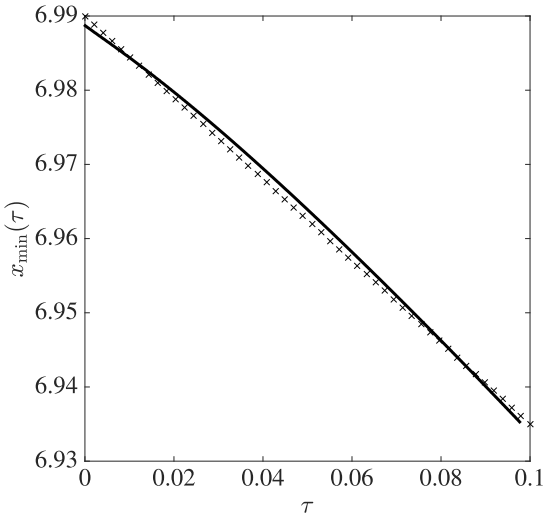

Figure 5.23: The x-coordinate of the minimum gas layer thickness, $x_m(\tau)$, plotted against τ (bold line). The crosses are a linear fit, as suggested in the text with, $\gamma = 1$ and $A = -0.55$.

similarity form is an appropriate model of behaviour close to touchdown. Further numerical analysis of the full problem is required; something, unfortunately, we do not have time for in this thesis. However, as any further work would need to investigate (5.159), we note that scaling H by $\Gamma^{2/3}$ and χ by Γ eliminates Γ from (5.159). Therefore, upon integrating once, we find that

$$H''' = \frac{1}{H^2} + \frac{B}{H^3}, \tag{5.160}$$

for some constant B. This equation occurs in applications of thin-film theory where similarity solutions can be found, for example in the thinning of a layer of paint, and has been studied in detail by Tuck and Schwartz (1990) and, in the particular case where $B = 0$, by Duffy and Wilson (1997). Note that we would need to use the numerical solution to provide appropriate boundary conditions for (5.160) for large χ.

5.5.4 Nonzero surface tension problem

Suppose surface tension is not negligible in the bulk region, and $0 < \beta < 1$. Then, if we view the gas pressure as a known function, the second-order linear, constant-coefficient, hyperbolic equation for the gas layer thickness is

$$(1 - \beta^2)\frac{\partial^2 H}{\partial x^2} + 2\frac{\partial^2 H}{\partial x \partial t} + \frac{\partial^2 H}{\partial t^2} = \lambda P, \tag{5.161}$$

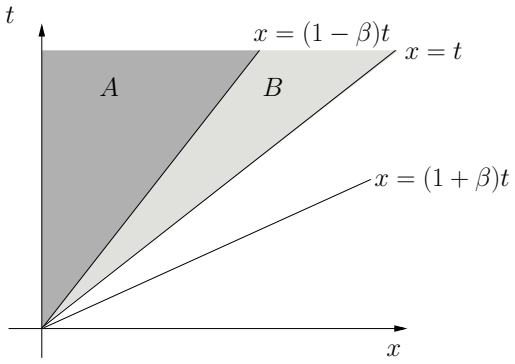

Figure 5.24: The two solution regions for the hyperbolic problem.

subject to

$$H(0,t) = a(t), \quad \left.\frac{\partial H}{\partial x}\right|_{(0,t)} = b(t) \tag{5.162}$$

plus a further condition at the tip which we must be found via matching, as discussed in §5.5.1. We shall for now prescribe H at $x = t$ by setting $H(t,t) = C(t)$, where C is a given function. We recall that, if we assume the pressure is a known function, the two families of characteristics associated with (5.161) are

$$x = (1 \pm \beta)t + \text{const.} \tag{5.163}$$

The jet tip is at $x = t$, and therefore, by our assumptions on β, the characteristic $x = (1-\beta)t$ divides the domain of definition of solutions to (5.161) into two regions: A and B, as depicted in Figure 5.24. Specifically,

$$\begin{aligned} A &= \{(x,t) \,|\, 0 < x < (1-\beta)t,\, t > 0\}, \\ B &= \{(x,t) \,|\, (1-\beta)t < x < t,\, t > 0\}. \end{aligned}$$

For $(\xi,\eta) \in A$, the solution is fed information from the boundary $x = 0$ by both families of characteristics, but for $(\xi,\eta) \in B$, the characteristic family $x - (1-\beta)t =$ const emanates from the tip of the jet, which is why we require a condition there. We will now solve the equation in each region separately and discern when the resulting solutions are continuous across the dividing characteristic, $x = (1-\beta)t$.

Let (ξ,η) be a point in region A and let D be the triangle bounded by the characteristics going through the point and the t-axis, as depicted in Figure 5.25. Define the integral of the pressure, $P(x,t)$, over the triangle by

$$I_p(\xi,\eta) = \lambda \iint_D P(x,t)\,\mathrm{d}x\,\mathrm{d}t. \tag{5.164}$$

Then, after integrating (5.161) over the triangle, we find that

$$I_p(\xi,\eta) = \iint_D \nabla\cdot\left((1-\beta^2)\frac{\partial H}{\partial x} + 2\frac{\partial H}{\partial t}, \frac{\partial H}{\partial t}\right)\mathrm{d}x\mathrm{d}t, \tag{5.165}$$

where ∇ is the gradient vector with respect to x and t. Thus, by the divergence theorem in the plane,

$$I_p(\xi,\eta) = \oint_{\partial D} (1-\beta^2)\frac{\partial H}{\partial x} + 2\frac{\partial H}{\partial t}\,\mathrm{d}t - \frac{\partial H}{\partial t}\,\mathrm{d}x. \tag{5.166}$$

Now, on a characteristic, $\mathrm{d}x = (1\pm\beta)\mathrm{d}t$. Hence

$$(1-\beta^2)\frac{\partial H}{\partial x} + 2\frac{\partial H}{\partial t}\,\mathrm{d}t - \frac{\partial H}{\partial t}\,\mathrm{d}x = (1\mp\beta)\,\mathrm{d}H.$$

Therefore, evaluating the right-hand side of (5.166), we find that

$$\begin{aligned} I_p(\xi,\eta) &= (1-\beta^2)\int_{\eta-\xi/(1+\beta)}^{\eta-\xi/(1-\beta)} \frac{\partial H}{\partial x}\,\mathrm{d}t + (1-\beta)H(0,\eta-\xi/(1-\beta)) - \\ &\quad (1+\beta)H(0,\eta-\xi/(1+\beta)) + 2\beta H(\xi,\eta), \end{aligned}$$

so that after using the boundary conditions and rearranging, we find that

$$\begin{aligned} H(\xi,\eta) &= \frac{1}{2\beta}\Bigg[I_p(\xi,\eta) + (1+\beta)a(\eta-\xi/(1+\beta)) \\ &\quad -(1-\beta)a(\eta-\xi/(1-\beta)) - (1-\beta^2)\int_{\eta-\xi/(1+\beta)}^{\eta-\xi/(1-\beta)} b(t)\,\mathrm{d}t\Bigg]. \end{aligned} \tag{5.167}$$

In the particular case where a and b are independent of time, the gas layer thickness is simply given by

$$H(\xi,\eta) = a + b\xi + \frac{\lambda}{2\beta}\iint_D P(x,t)\,\mathrm{d}x\,\mathrm{d}t. \tag{5.168}$$

Now let (ξ,η) be in region B. There are of course two characteristics that go through (ξ,η), but the one from the family $x-(1-\beta)t =$ constant intersects the jet tip at, $x = t$. Define this intersection to be the point E. Let D be the trapezium bounded by the two characteristics through (ξ,η), the t-axis and the characteristic of the family $x-(1+\beta)t =$ constant that meets $x = t$ at E. This trapezium is shown in Figure 5.26. Note that, relative to the origin, E has position vector

$$\frac{1}{\beta}\left(\xi-(1-\beta)\eta, \xi-(1-\beta)\eta\right).$$

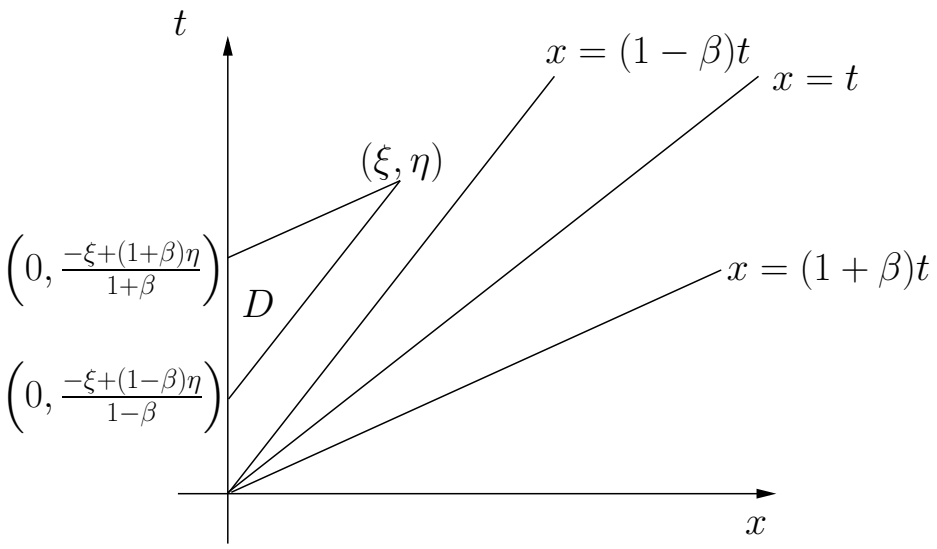

Figure 5.25: The triangle D.

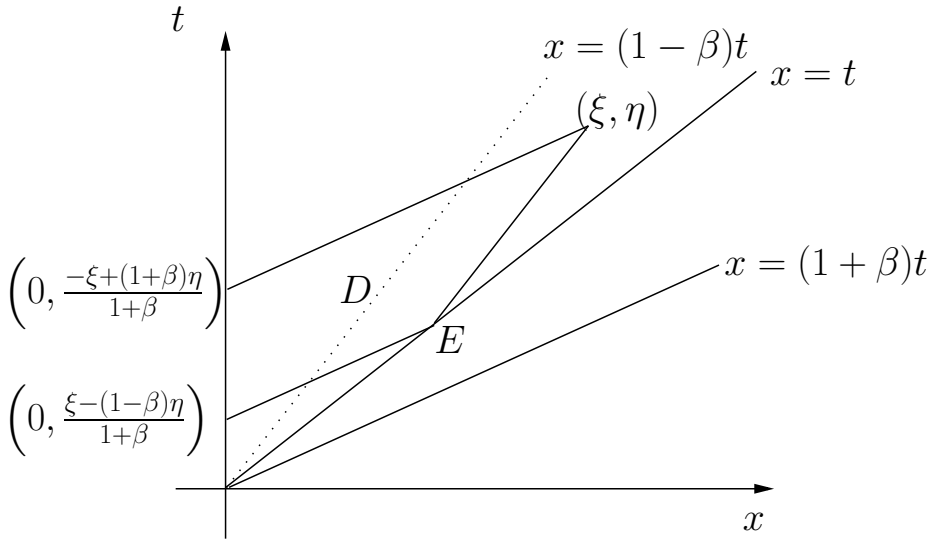

Figure 5.26: The trapezium D and the point of intersection, E.

Using a similar application of the divergence theorem as in region A, we find that the solution in region B is given by

$$H(\xi,\eta) = \frac{1}{2\beta}\Bigg[I_p(\xi,\eta) + (1+\beta)\left(a(\eta - \xi/(1+\beta)) - a((\xi-(1-\beta)\eta)/(1+\beta))\right) + 2\beta C\left(\frac{1}{\beta}(\xi-(1-\beta))\eta\right) - (1-\beta^2)\int_{\eta-\xi/(1+\beta)}^{(\xi-(1-\beta)\eta)/(1+\beta)} b(t)\,\mathrm{d}t\Bigg]. \quad (5.169)$$

In the particular example where a, b are constant, we find that

$$H(\xi,\eta) = C\left(\frac{1}{\beta}(\xi-(1-\beta)\eta)\right) - \frac{b}{\beta}(1-\beta)(\xi-\eta) + \frac{\lambda}{2\beta}\iint_D P(x,t)\,\mathrm{d}x\,\mathrm{d}t. \quad (5.170)$$

For the solution to be continuous - which we might expect since we do not see discontinuities in the jets and lamellae in experiments - we require (5.167), (5.169) to define a function that is continuous across the dividing characteristic, $x=(1-\beta)t$. Provided that the gas pressure is continuous across the characteristic, as we let (ξ,η) approach $x=(1-\beta)t$ in either region, the integral terms in (5.167), (5.169) will tend to the same value. Moreover, if we assume that $H(0,0)=a(0)$, $C\left((\xi-(1-\beta)\eta)/\beta\right)\to a(0)$ as we let $(\xi,\eta)\to((1-\beta)\eta,\eta)$. Hence, both (5.167) and (5.169) tend to the same value:

$$\begin{aligned} H^*(\eta) &= \frac{1}{2\beta}\Big[I_p((1-\beta)\eta,\eta) + (1+\beta)a(2\beta\eta/(1+\beta)) - \\ &\qquad (1+\beta)a(0) - (1-\beta^2)\int_{2\beta\eta/(1+\beta)}^{0} b(t)\,\mathrm{d}t\Big]. \end{aligned} \quad (5.171)$$

The second equation for H and P, (5.119), remains unchanged when $0<\beta<1$. Even though we will not attempt to provide one in this thesis, in order to initiate a numerical scheme to solve the problem for nonzero surface tension, we require a small-time solution to (5.119), (5.167) and (5.169), which we now compute.

5.5.4.1 Small-time solution

As in the zero surface tension case, we set

$$x=\epsilon\bar{x},\quad t=\epsilon\bar{t},\quad H=\bar{H},\quad P=\epsilon^{-2}\bar{P}.$$

Dropping the bar notation, we find

$$\epsilon^3\left(\frac{\partial H}{\partial t}+\frac{1}{2}\frac{\partial H}{\partial x}\right) = \frac{\partial}{\partial x}\left(\frac{H^3}{12}\frac{\partial P}{\partial x}\right), \quad (5.172)$$

along with

$$\begin{aligned} H(x,t) &= \frac{1}{2\beta}\Big[I_p(\epsilon x,\epsilon t) + (1+\beta)a(\epsilon(t-x/(1+\beta))) - \\ &\qquad (1-\beta)a(\epsilon(t-x/(1-\beta))) - \epsilon(1-\beta^2)\int_{t-x/(1+\beta)}^{t-x/(1-\beta)} b(\epsilon\tau)\,\mathrm{d}\tau\Big] \end{aligned} \quad (5.173)$$

in region A of Figure 5.25, and

$$\begin{aligned} H(x,t) = \frac{1}{2\beta}\Big[&I_p(\epsilon x,\epsilon t) + (1+\beta)\left(a(\epsilon(t-x/(1+\beta))) - a(\epsilon(x-(1-\beta)t)/(1+\beta))\right) \\ &+ 2\beta C\left(\frac{\epsilon}{\beta}(\xi-(1-\beta)\eta)\right) - \epsilon(1-\beta^2)\int_{t-x/(1+\beta)}^{(x-(1-\beta)t)/(1+\beta)} b(\epsilon\tau)\,\mathrm{d}\tau\Big] \end{aligned} \quad (5.174)$$

in region B of Figure 5.26. The boundary conditions on the gas pressure are given from (5.132) by

$$P(t,t) = 0, \quad \frac{\partial P}{\partial x} = \epsilon^3 \frac{6}{a(\epsilon t)^2}. \tag{5.175}$$

We note that, for $0 < \epsilon \ll 1$, $C\left(\epsilon/\beta(\xi - (1-\beta)\eta)\right) = H(\epsilon E)$ has the expansion

$$\begin{aligned} H(\epsilon E) \sim a(0) &+ \frac{\epsilon}{\beta}(x-(1-\beta)t)\left(H_x(0,0) + H_t(0,0)\right) + \\ &\frac{\epsilon^2}{2\beta^2}(x-(1-\beta)t)^2\left(H_{xx}(0,0) + 2H_{xt}(0,0) + H_{tt}(0,0)\right) + \\ &\frac{\epsilon^3}{6\beta^3}(x-(1-\beta)t)^3\left(H_{xxx}(0,0) + 3H_{xxt}(0,0) + 3H_{xtt}(0,0) + H_{ttt}(0,0)\right), \end{aligned}$$

since we assume $H(0,0) = C(0) = a(0)$ for continuity across the dividing characteristic. For brevity, we shall use the shorthand $H_i(E)$ to represent the coefficient of ϵ^i, $i \geq 1$ in the above expansion.

Therefore, expanding (5.172)–(5.174) for small ϵ, at $O(1)$, $O(\epsilon)$, $O(\epsilon^2)$, the gas pressure is zero, with corresponding layer thickness

$$\begin{aligned} H(x,t) \sim\ & a(0) + \epsilon\left(b(0)x + \dot{a}(0)t\right) + \frac{\epsilon^2}{4\beta}\left[\ddot{a}(0)\left((1+\beta)\left(t - \frac{x}{1+\beta}\right)^2\right.\right. \\ & \left. -(1-\beta)\left(t - \frac{x}{1-\beta}\right)^2\right) - (1-\beta^2)\dot{b}(0)\left(\left(t - \frac{x}{1-\beta}\right)^2\right. \\ & \left.\left. - \left(t - \frac{x}{1+\beta}\right)^2\right)\right], \end{aligned} \tag{5.176}$$

in region A, and

$$\begin{aligned} H(x,t) \sim\ & a(0) + \epsilon\left(\frac{(t-x)\dot{a}(0)}{\beta} - \frac{b(0)}{\beta}(1-\beta)(x-t) + H_1(E)\right) \\ & + \frac{\epsilon^2}{4\beta}\left[H_2(E) + (1+\beta)\ddot{a}(0)\left(\left(t - \frac{x}{1+\beta}\right)^2 - \left(\frac{x-(1-\beta)t}{1+\beta}\right)^2\right)\right. \\ & \left. - (1-\beta^2)\dot{b}(0)\left(\left(t - \frac{x}{1+\beta}\right)^2 - \left(\frac{x-(1-\beta)t}{1+\beta}\right)^2\right)\right], \end{aligned} \tag{5.177}$$

in region B.

At $O(\epsilon^3)$, (5.172) can be integrated directly. Upon applying the boundary conditions we find that

$$P_3(x,t) = \frac{6}{a(0)^2}(x-t). \tag{5.178}$$

We can evaluate the integral I_p in each of region A, B, but the algebra will not be produced here as it is very long-winded. Using (5.173), we find that

$$\begin{aligned} H_3(x,t) &= \frac{\dddot{a}(0)}{12\beta}\left((1+\beta)\left(t-\frac{x}{1+\beta}\right)^3-(1-\beta)\left(t-\frac{x}{1-\beta}\right)^3\right)- \\ &\quad \frac{(1-\beta^2)\,\ddot{b}(0)}{12\beta}\left(\left(t-\frac{x}{1-\beta}\right)^3-\left(t-\frac{x}{1+\beta}\right)^3\right)+ \\ &\quad \frac{\lambda}{a(0)^2\left(1-\beta^2\right)^2}\left(\left(3-\beta^2\right)x^3-3\left(1-\beta^2\right)x^2t\right) \end{aligned} \tag{5.179}$$

in region A, and using (5.174), we find that

$$\begin{aligned} H_3(x,t) &= H_3(E)+\frac{(1+\beta)\dddot{a}(0)}{12\beta}\left(\left(t-\frac{x}{1+\beta}\right)^3-\left(\frac{x-(1-\beta)t}{1+\beta}\right)^3\right)- \\ &\quad \frac{(1-\beta^2)\,\ddot{b}(0)}{12\beta}\left(\left(\frac{x-(1-\beta)t}{1+\beta}\right)^3-\left(t-\frac{x}{1+\beta}\right)^3\right) \\ &\quad +\frac{\lambda(x-t)}{\beta a(0)^2\left(1+\beta\right)^2}\left(2(\beta-1)t^2+2(2+\beta)xt-(2+\beta)x^2\right) \end{aligned} \tag{5.180}$$

in region B.

As an example, we consider a jet shot out at constant height, $a=1$, at zero angle, $b=0$, and assume that $C=1$. Then,

$$H(x,t)\sim 1+\epsilon^3\frac{\lambda}{(1-\beta^2)^2}\left((3-\beta^2)x^3-3(1-\beta^2)x^2t\right) \tag{5.181}$$

in region A, and

$$H(x,t)=1+\epsilon^3\frac{\lambda(x-t)}{\beta(1+\beta)^2}\left(2(\beta-1)t^2+2(2+\beta)xt-(2+\beta)x^2\right) \tag{5.182}$$

in region B. We plot the solution at times $t=0.05$, $t=0.1$ and $t=0.2$ in Figure 5.27. We have chosen $\lambda=1$ and $\beta=0.7$. We see similar behaviour to the zero surface tension case in that a small initial perturbation grows as the gas sucks the jet downwards.

5.5.5 Summary of the growing-jet model

We have developed a preliminary model for the evolution of a splash jet that is shot from an inlet at constant speed and with constant thickness. After several simplifying assumptions, the jet motion breaks down into two regions: a 'bulk' region where the model developed in §§5.2–5.3 applies, and a 'tip' region. In this section we

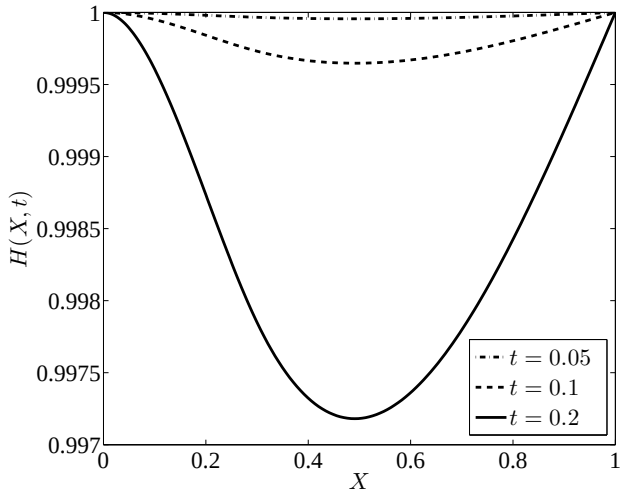

Figure 5.27: Small-time solution of the nonzero surface tension problem where $a(t) = 1$ and $b(t) = 0$. We have plotted the gas layer thickness against the scaled variable $X = x/t$.

concentrated on cases where the reduced Reynolds number in the gas is small in the bulk region, so that the air is viscous-dominated, while the Reynolds number in the jet is large, so that the jet motion is inertia-dominated.

We derived scalings for the tip region based on the assumption that the aspect ratio is of order unity in that region. Under the assumptions we made on the sizes of the gas/jet Reynolds numbers in the bulk region, the only way in which the gas and liquid flows couple in the tip region is through the continuity of velocity condition on the free boundary. Although the leading-order tip problem was intractable analytically, as a result of the pressure scalings, we were able to deduce a pressure-matching condition to apply at the tip in the bulk region.

In the bulk region, we argued via a numerical discretization and via a characterisation of the system that there is a change of behaviour in the system depending on whether the surface tension is zero or nonzero. We concluded that we would require an additional boundary condition at the tip to solve the problem when surface tension is nonzero.

When surface tension is zero, we derived the small-time asymptotic behaviour of the jet. We presented a simple implicit Newton solver for the system and ran several numerical simulations. The resulting numerics were compared to the small-time asymptotics and found to match well. For larger times, the jet buckles under the high pressures in the gas layer and the lower free surface of the jet was shown

to approach touchdown on the substrate. It is not clear whether touchdown actually occurs in this regime; our numerics become unreliable as H gets very small. We briefly considered the behaviour of H and P close to touchdown and commented on possible similarity behaviour, but were not able to make significant progress on our speculations.

Since we require a second matching condition with the tip region to supplement the pressure-matching condition when surface tension is nonzero, we were unable to make as much progress in this regime. Nonetheless, we derived the solution for H in terms of P analytically by including an unknown function at the tip. We used this solution to derive the small-time behaviour under the assumption that the jet tip moves with constant velocity.

Naturally, as a preliminary model, there are several limitations and assumptions in our the model. Nonetheless, it is a useful first step for future models or simulations of an evolving splash jet.

5.6 Outstanding problems and extensions

Much of the work in this chapter has been focused on deriving the splash jet model and exploring its underlying properties, so there is still much work to be done. Thoraval et al. (2012) claim that the bending, knuckling and touchdown of a splash jet are likely the result of changes in the angle at which the splash jet is emitted. While this may contribute to these phenomena, we have shown that a thin jet of liquid that is shot over a thin layer of gas is inherently unstable, particularly in light of the large Weber numbers that are commonplace in impact problems. Moreover, even a splash jet that is shot out of a fixed-height inlet parallel to a substrate can bend and eventually rupture the gas layer.

Certainly there needs to be a more in-depth numerical analysis of our model. In particular, it is crucial to determine what the second matching condition to the tip region is, as well as investigating the phenomenon of touchdown more carefully. Despite the weak evidence for a partial similarity solution at times close to touchdown, there was significant evidence that this form breaks down when the dimensionless time-to-touchdown is $O(10^{-3})$. Moreover, in light of the analysis in Purvis and Smith (2004) in regards to the touchdown of an impacting drop, it is highly likely that surface tension will play a crucial role as the jet nears touchdown: in Purvis and Smith (2004) surface tension inhibits touchdown entirely.

Moreover, most of the work in this chapter has concentrated on one particular limit of our model; that of a viscous gas layer and a constant-speed, constant-thickness jet.

There are a whole wealth of further regimes we could investigate; we attempted to suggest some of these cases in §§5.3.1-5.3.4, but naturally there are many more we could consider. For example, how do the model predictions change if we let the gas layer be much thinner than the jet or vice versa? What happens if we let surface tension dominate the leading-order equations? If the Reynolds number in the liquid is of order unity, (5.53)–(5.54) are the equations of extensional flow, which may make a significant change to our predictions regarding the growth of the jet.

Furthermore, we have made several simplifying assumptions in the course of the chapter, which need to be looked at more carefully. The role of the nozzle and unbounded air regions (I and IV in Figure 5.10) have not been taken into account. Furthermore, there are several open questions regarding the tip region.

Perhaps the most obvious extension we can make to the theory is to extend it to three-dimensions. All of the experimental motivation we used at the start of the chapter was for three-dimensional droplet impact. The bubble entrapment in Thoroddsen et al. (2010) occurs in rings, so it is likely that three-dimensional instabilities are important in touchdown of the lamellae depicted in Figure 4.2. To this end, we state the three-dimensional equations in Appendix C for future reference.

Chapter 6

Summary and conclusion

Although we have provided summaries as we have progressed through this thesis, we shall conclude by giving an overarching conclusion and discussion of the findings of the previous chapters. We will finish by outlining what questions remain to be answered.

6.1 Summary

This thesis was primarily split into three parts, all of which are connected through their aim to model different aspects of impact problems and splash dynamics. We have extended the classical theory of water-entry to oblique impact problems and derived a new asymptotic model that incorporates the surrounding gas into Wagner theory. Moreover, we have developed a new set of models for the dynamics of the splash jets that are ubiquitous in these impact problems.

After briefly motivating the thesis and discussing why modelling splashing is a difficult challenge – not only analytically, but also numerically and experimentally – in Chapter 1, we moved on to a review of classical normal-impact water-entry theory in Chapter 2. In the so-called Wagner limit in which the deadrise angle of the rigid impactor is small, we presented the leading-order matched-asymptotic solution for both two- and three-dimensional bodies under the assumptions that the liquid is ideal and incompressible, and that surface tension, gravity and the ambient air are all negligible. In the review on Wagner theory, we described the local-in-space-and-time stability analysis of Wilson (1989) and Gillow (1998), which shows that the leading-order-outer problem in two-dimensional Wagner theory is unstable to out-of-plane perturbations if the turnover points are not advancing.

Our first novel work took place in Chapter 3 where we extended the asymptotic theory to oblique impacts in both two and three dimensions. While the discovery

that the oblique component of impact velocity must be on the order of the inverse of the deadrise angle to enter the leading-order-outer theory and the use of the displacement potential in solving the outer problem are not new ideas, the use of a coordinate transformation to a fixed domain to reduce the problem to its normal-impact counterpart is original. We were able to do this because the leading-order displacement potential problem does not contain any time derivatives.

The transformation allows us to write down the solution of any oblique problem provided we know the corresponding normal-impact solution and we used this knowledge to study the effects of the oblique impact velocity on the validity of Wagner theory and, in particular, on the pressure on the impactor. We concluded that for nonzero oblique velocities there is the possibility that one of the turnover points stops advancing in two dimensions or for the outward-normal velocity of the turnover curve to vanish at a point in three dimensions, which leads to the instability described by Wilson (1989). For self-similar impacts, such as the constant-speed entry of a wedge or a cone, Wagner theory breaks down above a critical value of the oblique impact speed, whereas for the constant-speed impact of blunt bodies, such as a parabola, the theory becomes invalid for any oblique speed after a critical time.

Not only does breakdown lead to an instability in the leading-order-outer problem, but there is also a breakdown in the asymptotic structure of the problem, as the coefficient of the inverse square-root singularities in the expansions of the leading-order-outer pressure and velocity at the turnover point/curve vanish at the point of breakdown.

Prior to breakdown, we showed for several examples in both two- and three-dimensions that negative pressure forms on the impactor. Although we discussed the possibility of cavitation occurring on the impactor due to this negative pressure, we did not propose any models for it. Despite the change in the pressure on the impactor, we deduced that the normal-component of force on the impactor is unchanged from its value in vertical entry, a conclusion which is supported by several results in the literature.

We found that the oblique component of velocity had a profound effect on the motion of the splash jets in two dimensions and sheets in three dimensions. In the direction opposite the motion, the splash is inhibited, but the splash is accentuated in the direction of oblique motion. At the point of breakdown, fluid stops entering the splash jet/sheet and the Wagner solution breaks down.

In Chapter 4 we returned to vertical water-entry, but incorporated the surrounding air into the Wagner asymptotic structure. We neglected all influence of the air before impact and assumed that the impact initiated at a point. The key parameter

bringing the air into the leading-order-outer problem was the ratio of the air/liquid density ratio to the deadrise angle. We wrote down the leading-order solution in the small-deadrise limit assuming that this parameter was at most order unity and then performed an expansion for the physically-relevant limit in which it is small. This analysis was performed in both two- and three-dimensions, and the introduction of the air has some surprising results.

In the two-dimensional impact of a parabola, the air displaced the turnover points further from the apex of the impactor due to the suction caused by a source in the far-field of the outer air flow. The air layer cushioned the impactor, reducing the leading-order force from its Wagner value. We matched the leading-order-outer solution for the parabola to the impact of a solid cylinder into a liquid half-space.

For a wedge impact, we showed that the introduction of the air layer can introduce a source in the far-field of the liquid flow. As a result, we identified a far-field nonuniformity in our asymptotic analysis, which we did not attempt to resolve.

The modelling in three-dimensions was more difficult. However, in the axisymmetric case, we were able to reduce the leading-order-outer problem in the liquid to Titchmarsh-type dual integral equations, which we then solved. However, this method had its limitations and we showed that it breaks down completely for the impact of a cone, as the singularity in the far-field of the air flow is even stronger than a source. However, for impactors that grow at least as quickly as a paraboloid in the far-field, the method is valid. For the example of paraboloid impact, we found that the turnover curve was displaced further from the Wagner solution, although the outward-normal speed of the turnover curve remained unchanged. Although we concluded that there could be no source in the far-field of the liquid, we still found a singularity in the far-field solution of the free surface profile for paraboloid impact, which, again, we did not attempt to resolve.

We adopted a completely different track in Chapter 5, in which we developed a set of simple models that describe the motion of a splash jet, or indeed any thin layer of fluid, in the presence of a thin gas layer trapped between the jet and a solid substrate. This model was not directly inspired by Wagner theory and in fact incorporated elements from extensional flows and lubrication theory. We worked in two dimensions. Our primary aim was to develop a model that could perhaps be used to explain the instability, bending and touchdown of splash jets. Our initial model neglected the influence of the tip of the jet and the jet-root. We considered four separate regimes for various asymptotic limits of the reduced Reynolds numbers in the jet and gas. In each of the regimes we showed that a jet of constant speed and thickness is unstable provided that surface tension is sufficiently small, suggesting

that small perturbations may grow and eventually rupture the thin gas layer.

Using this knowledge and after making some simplifying assumptions about the flow near the nozzle, we attempted to derive a model for a growing jet, where the majority of the jet is governed by the small-aspect-ratio model we had already derived, with an inner region local to the jet tip where the aspect ratio is of order unity. Under the same parameter limits we used in the derivation of the bulk model, we were unable to solve the tip region problem analytically, although we were able to deduce a pressure-matching condition based on scaling arguments.

We moved on to consider the constant-speed, constant-thickness jets that we saw in some of the literature. In this limit, the system reduced to a second-order partial differential equation for the gas pressure and gas layer thickness, coupled with either the lubrication equation or plug flow equations in the gas. We used a numerical and analytical argument to show the system had a change of behaviour depending on whether surface tension can be neglected or not. This change of behaviour means that we require a further boundary condition to solve the problem when surface tension is nonzero.

Although explicit analytic solutions were not found when surface tension is negligible, we presented the asymptotic solution for small time. We were able to solve the zero surface tension problem using an implicit Newton solver. The resulting numerical simulations matched well with the small-time asymptotics and were shown to converge as the grid size was refined. For a jet shot out at a constant height, parallel to the solid surface, the numerical solution predicted that the jet would bend due to a reduced pressure in the gas layer and eventually approach touchdown in finite time. Unfortunately, since our numerics are unreliable when the gas pressure becomes very large, we were not able to investigate this touchdown in more detail, although we did propose a conjecture on the possibility of a partial similarity solution close to touchdown.

In the limit in which surface tension is not negligible, the system is much less tractable. We were forced to leave an unknown function in our analytic solution since we required a further matching condition with the tip region. This remains an open problem.

6.2 Outstanding questions and future directions

When our theory breaks down or more work needs to be done in certain parts of our analysis, we have attempted to highlight the problem in the text and propose how we might attempt to rectify it. However, for ease of reference, we will now review these

outstanding questions in this conclusion.

Chapter 3

- In §3.1.3 and §§3.2.2.3–3.2.2.4 we showed that the pressure on an obliquely impacting body can become negative *before* the breakdown of Wagner theory. There are two schools of thought as to what could happen. It is possible that cavitation occurs prior to breakdown, in which case a revised outer model, such as that we present in Appendix B, would hold. However, if fluid is moving sufficiently quickly through this region, it is possible that cavitation does not occur and ventilation along the trailing edge of the impactor rectifies this low pressure once breakdown occurs. This is considered in detail in Reinhard et al. (2012).

- It is unknown what happens after the breakdown of Wagner theory. We showed extensively in Chapter 3 that the general asymptotic structure breaks down when the turnover point (curve) stops advancing. However, as we also suggested, there is naturally a nonuniformity in our asymptotic expansion as we approach the critical oblique speed or critical time at which breakdown occurs. At this nonuniformity the speed of the trailing turnover point (curve) is on the same order of the deadrise angle, which impacts the matching and boundary conditions in the inner and jet regions. It is unclear what the inner region looks like this close to breakdown.

Chapter 4

- Both the two-dimensional and three-dimensional model for air-cushioning have a nonuniformity in the small-λ expansion when time is small. In each case we would need to give careful consideration to the initial conditions in the air, perhaps considering the impulsive motion we give the body in more detail.

- There is a singularity in the far-field of the leading-order wedge solution in §4.2.8.3 as $\lambda \to 0$. The matching to an 'outer-outer' region appears to be quite subtle and needs to be done carefully. A similar analysis is also required for the paraboloid example in §4.3.6.

- Naturally, we need to work out how to adapt the solution method for three-dimensional impactors in §4.3.2.2 so that it does not break down for a cone. We

postulate that this will involve finding an eigensolution that has the same far-field behaviour as $\hat{\mathcal{G}}_r$ and subtracting this from the leading-order (in ε) problem. Unfortunately, such an eigensolution escaped us.

Chapter 5

- There are a whole host of open questions in Chapter 5. Of most importance is perhaps the availability of experimental data for the thickness of gas layers and jets seen in droplet impacts and spreading lamellae so that we can convince ourselves that the regimes we presented in §§5.3.1-5.3.4 are applicable to a variety of physical scenarios. We gave some justification that this is indeed the case, but further comparison is needed. Moreover, it would be useful to compare the wavelengths that we found for the most unstable modes in our stability analysis to the wavelengths of the bubble ring patterns in lamella touchdown reported in, for example, Thoroddsen et al. (2010) and Palacios et al. (2012) to see if we have a possible mechanism for this phenomenon.

- It would be useful to derive a similar set of models as in §§5.3.1-5.3.4 for the case where the jet is shot over a bulk fluid as opposed to a solid substrate. This may be more applicable to some experimental configurations.

- In §5.5, a rigorous analysis of the small-time jet-growth problem is required, in which the jet length is comparable to its thickness.

- Numerical analysis of the tip region is required in order to ascertain the correct matching conditions in our growing jet model in §5.5.

- A closer look is needed at the region near the nozzle, which we neglected in our analysis in §5.5.

- A more thorough investigation of touchdown in §5.5.3.3 is clearly necessary. Although we have good numerical evidence that touchdown eventually occurs, we certainly need to back this up with some theory. There was some evidence of similarity behaviour close to touchdown - this also requires more investigation. It is also plausible that further physical effects will become important as the jet gets closer to the solid substrate.

- It would be prudent to consider how the models in §5.5 change when we do not assume the simple constant-speed, constant-thickness motion of the jet. It might be possible that the jet is destabilised by the air layer to such a degree

that disintegration occurs prior to the touchdown of the jet. This could be a mechanism distinguishing between 'prompt' and 'regular' splashing in experiments, as discussed by, for example, Latka et al. (2012).

- Further work is needed on the three-dimensional version of our splash jet model in Appendix C.

There is clearly a lot more research to be done and there are certainly further extensions we could consider that are not directly outstanding questions from this thesis. It would be interesting to incorporate our analysis in Chapter 4 into that in Chapter 3 to see how air-cushioning affects oblique impact and its breakdown. Furthermore, we could look at regimes in which the air layer in Chapter 4 is better modelled by a viscous fluid, comparing the results to post-impact lubrication theory as seen in Purvis and Smith (2004). There is clearly a wealth of work we could do with the model in Chapter 5. For example, we could use inlet conditions based on data from droplet impact experiments to compare our simulations to the pictures in, for example, Thoraval et al. (2012).

Splashing and impact theory is an exciting area in applied mathematics and there are many open problems to get to grips with. We hope that the analysis in this thesis has contributed in some way to helping understand these problems.

Appendix A

Splash sheet equations for an accelerating body

In Wagner theory, the leading-order splash jet or splash sheet equations are derived by transforming the equations of motion and boundary conditions to local curvilinear coordinates based on the impactor. For an accelerating body profile, we must consider whether such a transformation changes the leading-order splash jet/sheet problems in §3.1.5 and §3.2.4. We briefly discuss the three-dimensional case here, the two-dimensional case is a straightforward extension.

In dimensionless coordinates, the Cartesian frame fixed at the initial point of impact has origin O and orthogonal axes x, y, z. We consider a frame moving with the minimum of the rigid impactor. We denote its origin at the minimum by O', and denote the orthogonal axes by ξ, η, ζ.

If a particle P has position $\mathbf{R} = (\xi, \eta, \zeta)$ in the moving frame and position $\mathbf{r} = (x, y, z)$ in the fixed frame, we must have

$$\mathbf{r} = \mathbf{R} + \mathbf{q},$$

where $\mathbf{q} = (X(t)/\varepsilon, Y(t)/\varepsilon, t)$. Hence, if differentiation with respect to t is denoted by a dot on a variable, the velocities and accelerations in the two frames must satisfy

$$\dot{\mathbf{r}} = \dot{\mathbf{R}} + \dot{\mathbf{q}}, \quad \ddot{\mathbf{r}} = \ddot{\mathbf{R}} + \ddot{\mathbf{q}}$$

respectively.

Therefore, if the velocity and pressure of the fluid in the moving frame are defined by $\mathbf{U}(\xi, \eta, \zeta, t)$ and $P(\xi, \eta, \zeta, t)$ respectively, Euler's equations in the moving frame are given by

$$\ddot{\mathbf{q}} + \frac{\partial \mathbf{U}}{\partial t} + (\mathbf{U} \cdot \nabla)\,\mathbf{U} = -\nabla P \tag{A.1}$$

$$\nabla \cdot \mathbf{U} = 0, \tag{A.2}$$

where the gradient operator, ∇, is defined with respect to the moving frame.

The fluid in the fixed frame is initially irrotational and thus by Kelvin's theorem, always irrotational. Moreover, as the moving frame is not rotating, the fluid in the moving frame must also be irrotational and hence we must have

$$\nabla \wedge \mathbf{U} = 0. \tag{A.3}$$

In the splash sheet region, we would now define a curvilinear coordinate system based on the impactor. However, as the principal radii of curvature of the body are much larger than the extent of the splash sheet, to leading-order, such a curvilinear coordinate system can be approximated by (ξ, η, ζ), with $\zeta = 0$ representing the impactor. Hence, scaling ξ, η, ζ, U, V, W, P with $1/\varepsilon$, $1/\varepsilon$, ε, $1/\varepsilon$, $1/\varepsilon$, ε and $1/\varepsilon^2$ respectively, and expanding (A.1)-(A.2) in asymptotic series in powers of ε, to leading-order we find that

$$\ddot{X} + \frac{\partial U}{\partial t} + U\frac{\partial U}{\partial \xi} + V\frac{\partial U}{\partial \eta} + W\frac{\partial U}{\partial \zeta} = -\frac{\partial P}{\partial \xi}, \tag{A.4}$$

$$\ddot{Y} + \frac{\partial V}{\partial t} + U\frac{\partial V}{\partial \xi} + V\frac{\partial V}{\partial \eta} + W\frac{\partial V}{\partial \zeta} = -\frac{\partial P}{\partial \eta}, \tag{A.5}$$

$$0 = -\frac{\partial P}{\partial \zeta}, \tag{A.6}$$

$$\frac{\partial U}{\partial \xi} + \frac{\partial V}{\partial \eta} + \frac{\partial W}{\partial \zeta} = 0, \tag{A.7}$$

provided that $\ddot{X}$, $\ddot{Y}$ are at most order unity as $\varepsilon \to 0$. At leading order, the condition of irrotational flow reduces to

$$\frac{\partial U}{\partial \zeta} = 0, \quad \frac{\partial V}{\partial \zeta} = 0, \quad \frac{\partial U}{\partial \eta} = \frac{\partial V}{\partial \xi}. \tag{A.8}$$

The no-flux condition on the impactor is simply given by

$$W = 0 \ \text{ on } \ \zeta = 0. \tag{A.9}$$

Let the free surface of the jet be given by $\zeta = h(\xi, \eta, t)$. Therefore, to leading order, the kinematic and dynamic boundary conditions on the free surface are given by

$$W = \frac{\partial h}{\partial t} + U\frac{\partial h}{\partial \xi} + V\frac{\partial h}{\partial \eta}, \tag{A.10}$$

$$P = 0, \tag{A.11}$$

on $\zeta = h(\xi, \eta, t)$.

It is straightforward to integrate (A.6) with respect to ζ and, on applying (A.11), we deduce that $P = 0$ at leading order. Hence, by (A.4)–(A.5),

$$\ddot{X} + \frac{\partial U}{\partial t} + U\frac{\partial U}{\partial \xi} + V\frac{\partial U}{\partial \eta} = 0, \tag{A.12}$$

$$\ddot{Y} + \frac{\partial V}{\partial t} + U\frac{\partial V}{\partial \xi} + V\frac{\partial V}{\partial \eta} = 0, \tag{A.13}$$

where we have used (A.8) on the left-hand side.

Moreover, from (A.8) we know that $U = U(\xi, \eta)$, $V = V(\xi, \eta)$. Hence, upon integrating the continuity equation (A.7) with respect to ζ and applying (A.9) and (A.10) we deduce that

$$\frac{\partial h}{\partial t} + \frac{\partial}{\partial \xi}(Uh) + \frac{\partial}{\partial \eta}(Vh) = 0. \tag{A.14}$$

Clearly, (A.12)-(A.14) are the shallow water equations with the addition of acceleration terms from the moving frame.

Making the change of variables

$$\xi = x - X(t), \quad \eta = y - Y(t), \quad U = u - \dot{X}(t), \quad V = v - \dot{Y}(t),$$

back to the frame fixed at the initial point of impact (subject to the rescaling we made to move to the jet region), (A.12)–(A.14) reduce to

$$\frac{\partial u}{\partial t} + u\frac{\partial u}{\partial x} + \frac{\partial u}{\partial y} = 0, \tag{A.15}$$

$$\frac{\partial v}{\partial t} + u\frac{\partial v}{\partial x} + \frac{\partial v}{\partial y} = 0, \tag{A.16}$$

$$\frac{\partial h}{\partial t} + \frac{\partial}{\partial x}(uh) + \frac{\partial}{\partial y}(vh) = 0. \tag{A.17}$$

Hence, the zero-gravity shallow-water model for the splash sheet evolution for normal impact as derived in §2.3.5 can also be applied in the case where the body profile has an oblique component of impact velocity provided that $\ddot{X}$, $\ddot{Y}$ are at most of order unity as $\varepsilon \to 0$. This justifies the spray sheet equations we gave in §3.2.4.

Appendix B

A model for cavitation

Reinhard et al. (2012) present three possible models of the non-Wagner stage after breakdown for the two-dimensional oblique impact of a parabola. They suggest that ventilation of the trailing side of the parabola occurs when the point of zero pressure on this trailing side reaches the turnover point[1]. However, they can only speculate on the location of the point where the free surface separates from the impactor. They give various possibilities based on energy arguments or applications of the Brillouin-Villat condition. We do not discuss the possibility of ventilation any further here, but instead consider the case where the negative pressure on the impactor prior to breakdown causes cavitation to occur before the non-Wagner stage applies. Our model is based on that we proposed in Moore et al. (2012) and is presented in three dimensions, the two-dimensional equivalent being a simple extension.

The pressure required for cavitation to occur is given by $p_c < p_{\text{atm}}$ in dimensional coordinates, where p_{atm} is the atmospheric pressure and we assume that the pressure in any cavity takes the value p_c. Therefore, provided that

$$\varepsilon T^2 \frac{(p_c - p_{\text{atm}})}{\rho_l L^2} \ll 1, \tag{B.1}$$

the pressure in any cavity is given by $p = 0$ in outer variables at leading order. Hence, when the leading-order-outer pressure becomes negative in a subset of the contact region, we assume that a *patch cavity* forms on the impactor about the region of negative pressure. The dynamics of patch cavities is discussed in Howison et al. (1994), but the model we propose here is an adaptation of the discussion in Korobkin (2003) about a decelerating, normal, two-dimensional impact, to the oblique impact of the body profile $z = f(x - X(t), y - Y(t)) - t$.

[1]This is what happens according to Wagner theory, as we showed in Chapter 3, provided that no cavitation occurs prior to breakdown.

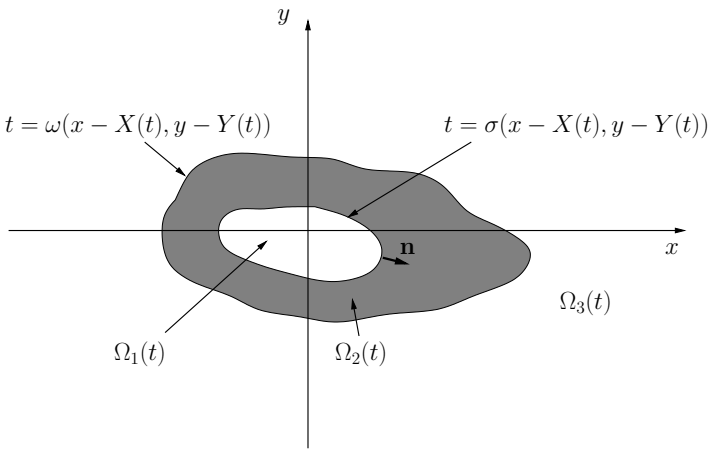

Figure B.1: The three regions of the leading-order outer problem with the introduction of a patch cavity on the impactor. $\Omega_1(t)$ represents the cavity, $\Omega_2(t)$ defines the remainder of the contact set and $\Omega_3(t)$ defines the non-contact set. The outward-pointing normal to the cavity is denoted by $\mathbf{n}$. This figure is based on one in Moore et al. (2012).

At the first instance the pressure on the impactor becomes negative, say at $t = t_c$, we assume that a cavity grows from a single point. The cavity is assumed to be thin in the sense that its thickness is an order of magnitude smaller than its extent in the x- and y-directions. Thus, in the leading-order-outer problem, the cavity boundary conditions linearise onto the plane $z = 0$. We sketch the key regions in the leading-order outer problem in Figure B.1. We denote the leading-order turnover curve by $t = \omega(x - X(t), y - Y(t))$ and the leading-order edge of the cavity by $t = \sigma(x-X(t), y-Y(t))$. The region $\Omega_1(t)$ defines the cavity on the impactor, that is (x, y) such that $t > \sigma(x - X(t), y - Y(t))$. The region $\Omega_2(t)$ defines the rest of the contact set, that is (x, y) such that $\omega(x-X(t), y-Y(t)) < t < \sigma(x-X(t), y-Y(t))$. Finally, $\Omega_3(t)$ defines the non-contact set, that is (x, y) such that $t < \omega(x - X(t), y - Y(t))$. Note that $\Omega_1(t)$ does not necessarily contain the minimum of the impactor.

Therefore, in the outer region, the leading-order velocity potential in the fluid, $\phi(x, y, z, t)$, leading-order free surface elevation, $h(x, y, t)$, and leading-order cavity thickness, $H(x, y, t)$, satisfy:

$$\nabla^2\phi = 0 \quad \text{in} \quad z < 0, \tag{B.2}$$

subject to

$$\phi = 0 \qquad \text{on} \quad z = 0, (x, y) \in \Omega_3(t), \tag{B.3}$$

$$\frac{\partial \phi}{\partial z} = \frac{\partial h}{\partial t} \qquad \text{on} \quad z = 0, (x, y) \in \Omega_3(t), \tag{B.4}$$

$$\frac{\partial \phi}{\partial z} = -1 - \dot{X} f_{,1} - \dot{Y} f_{,2} \qquad \text{on} \quad z = 0, (x, y) \in \Omega_2(t), \tag{B.5}$$

$$\frac{\partial \phi}{\partial z} = -1 - \dot{X} f_{,1} - \dot{Y} f_{,2} - \frac{\partial H}{\partial t} \qquad \text{on} \quad z = 0, (x, y) \in \Omega_1(t), \tag{B.6}$$

with the initial conditions $h(x, y, t_c) = h_c(x, y)$, $\omega(x, y) = \omega_c(x, y)$ and $\sigma(x, y) = 0$ at $t = t_c$, where $h_c(x, y)$ and $\omega_c(x, y)$ are given by the Wagner solution. The far-field conditions are

$$\phi = O(1/R^2) \quad \text{as} \quad R = \sqrt{x^2 + y^2 + z^2} \to \infty, \tag{B.7}$$

$$h = O(1/r^2) \quad \text{as} \quad r = \sqrt{x^2 + y^2} \to \infty. \tag{B.8}$$

Provided that the patch cavity is not within $O(\varepsilon)$-distance of the turnover curve, the inner region problem still follows as in §2.3.3. Therefore, we still require the velocity potential to have square-root behaviour in distance from the turnover curve as we approach it in any perpendicular plane. Moreover, the Wagner condition still holds at the turnover curve, as given by (3.81).

In addition to this, we require two further pieces of information to determine the location and size of the cavity. As described above, provided that (B.1) holds, we must also have $p(x, y, 0, t) = 0$ at leading-order for $(x, y) \in \Omega_1(t)$. As in Korobkin (2003), to determine a second condition, we say that the pressure close to the edge of the cavity is continuously differentiable (that is we seek the solution with minimal singularity). Hence, we require that $\partial p/\partial n \to 0$ as we approach the cavity boundary, $t = \sigma(x - X(t), y - Y(t))$. Here $\partial/\partial n$ is the normal derivative along the wetted surface normal to the edge of the cavity. Note that this forces $\partial^2 H/\partial t^2$ to be bounded at the cavity edge.

It is evident that the introduction of a patch cavity makes analysis of the leading-order-outer problem much more complicated. Moreover, changing to the displacement potential form of the problem does not appear to give any direct benefits. The solution of the patch cavity model we have presented here is an open problem.

Appendix C

Three-dimensional splash sheet model

It is an exercise in algebra to extend our model for two-dimensional jets in §5.2 to three dimensions since the arguments generalise directly. We consider a liquid splash sheet of density ρ_l and viscosity μ_l bounded by the free surfaces $z^* = H^*(x^*, y^*, t^*)$ and $z^* = H^*(x^*, y^*, t^*) + h^*(x^*, y^*, t^*)$ being shot between two gas layers of density ρ_g and viscosity μ_g. The lower gas layer is bounded by a solid wall at $z^* = 0$ and the surface $z^* = H^*(x^*, y^*, t^*)$, while the flow in the gas above the splash sheet is neglected throughout. For the purposes of our analysis, we assume that we are able to neglect the flow near the point of ejection of the sheet and the flow near the rim of the sheet. Hence, we let the sheet extend to infinity in the x^*-, y^*-directions.

Let the splash sheet have typical thickness ℓ and we are interested in deviations due to the pressure jump across this thin sheet, which occur on a typical lengthscale, L. For simplicity, we shall also assume that the gas layer has typical thickness, ℓ. The aspect ratio of the splash sheet and gas layer is defined to be $\varepsilon_l = \ell/L$. We assume that the sheet is moving with a typical speed, U_s. As in §5.2, we define the dimensionless parameters

$$\mathrm{Re}_l = \frac{\rho_l L U_s}{\mu_l}, \quad \mathrm{We} = \frac{\rho_l L U_s^2}{\sigma}, \quad \mathrm{Fr} = \frac{U_s}{\sqrt{gL}}, \quad \mu = \frac{\mu_g}{\mu_l}, \quad \lambda = \frac{\rho_g}{\varepsilon_l^4 \rho_l \mathrm{Re}_g}. \tag{C.1}$$

We will restrict our analysis to the case in which $\varepsilon_l \ll 1$, $\varepsilon_l^2 \mathrm{Re}_g \ll 1$ and $\mathrm{Re}_l = \infty$. Moreover, we assume that $\mathrm{Fr}^2 = O(1/\varepsilon_l)$, $\mathrm{We} = O(1/\varepsilon_l)$, $\mu \ll 1$ and $\lambda = O(1)$. With this choice of λ, L is given as in (5.33). Under these assumptions, the leading-order equations for the x- and y-components of the sheet velocity, u_0, v_0, the sheet

thickness, h_0, the gas layer thickness, H_0 and the gas pressure, P_0, are

$$u_{0t} + u_0 u_{0x} + v_0 u_{0y} = 0, \tag{C.2}$$

$$v_{0t} + u_0 v_{0x} + v_0 v_{0y} = 0, \tag{C.3}$$

$$h_{0t} + (u_0 h_0)_x + (v_0 h_0)_y = 0, \tag{C.4}$$

$$H_{0t} + \frac{1}{2}\left[\left(u_0 H_0 - \frac{H_0^3 P_{0x}}{6}\right)_x + \left(v_0 H_0 - \frac{H_0^3 P_{0y}}{6}\right)_y\right] = 0, \tag{C.5}$$

along with the three-dimensional generalisation of the pressure-jump equation (5.56), given by

$$\begin{aligned} h_0\left[H_{0tt} + 2u_0 H_{0xt} + 2u_0 v_0 H_{0xy} + 2v_0 H_{0yt} + u_0^2 H_{0xx} + v_0^2 H_{0yy}\right] = \\ \lambda P_0 - h_0^2\left(u_{0x}^2 + u_{0x}v_{0y} + u_{0y}v_{0x} + v_{0y}^2\right) + 2\gamma\left(H_{0xx} + H_{0yy}\right) + \\ \left(h_{0xx} + h_{0yy}\right) - h_0 \mathrm{Fr}^*, \end{aligned} \tag{C.6}$$

where $\mathrm{Fr}^* = 1/(\varepsilon_l \mathrm{Fr}^2)$ and $\gamma = 1/(\varepsilon_l \mathrm{We})$.

In the particular case where we make the further assumption that everything is axisymmetric, the model for the radial sheet velocity $u(r,t)$, sheet thickness $h(r,t)$, gas pressure $P(r,t)$ and gas layer thickness $H(r,t)$ is given by

$$(rh)_t + (rhu)_r = 0, \tag{C.7}$$

$$u_t + uu_r = 0, \tag{C.8}$$

$$(rH)_t + \frac{1}{2}\left(uH - \frac{H^3 P_r}{6}\right) = 0, \tag{C.9}$$

$$\begin{aligned} h\left(H_{tt} + 2uH_{rt} + u^2 H_{rr}\right) = \lambda P + \frac{\gamma}{r}\left(2(rH_r)_r + (rh_r)_r\right) - \\ \mathrm{Fr}^* h - h^2\left(u_r^2 + \frac{uu_r}{r} + \frac{u^2}{r^2}\right). \end{aligned} \tag{C.10}$$

The axisymmetric equations do not lend themselves to a simple linear stability analysis as we saw in §5.4. In particular, the base state is non-trivial due to the final terms on the right-hand side of (C.10). Certainly $u = \text{const}$, $rh = \text{const}$ are trivial solutions to (C.7)–(C.8), but it is unclear what the resulting solutions for H, P are. This is an open problem.

Bibliography

J.-L. Armand and R. Cointe. Hydrodynamic impact analysis of a cylinder. *ASME J. Offshore Mech. Arc. Eng.*, 111:109–114, 1987.

N. G. Asryan. Solid plate impact on surface of incompressible fluid in the presence of a gas layer between them (in Russian). *Izv. Akad. Nauk. Arm. SSR Mekh.*, 25: 32–49, 1979.

R. J. Astley. An idealised model for flat bottomed ship slamming. In *Proc. 5th Aus. Con. Hydraul. Fluid. Mech.*, 1974.

D. Battistin and A. Iafrati. Hydrodynamic loads during water entry of two-dimensional and axisymmetric bodies. *J. Fluids Struct.*, 17(5):643–664, 2003.

J. C. Bird, S. S. H. Tsai, and H. A. Stone. Inclined to splash: triggering and inhibiting a splash with tangential velocity. *New J. Phys.*, 11:063017, 2009.

G. Birkhoff and T. E. Caywood. Fluid flow patterns. *J. App. Phys.*, 20:646–659, 1949.

G. Birkhoff and E. Zarantonello. *Jets, wakes, and cavities.* Academic Press, 1957.

E. F. Campana, A. Caracterra, E. Ciappi, and A. Iafrati. Parametric analysis of slamming forces: compressible and incompressible phases. In *Proc. 3rd Int. Con. Hydrodyn., South Korea*, pages 167–172, 1998.

G. F. Carrier, M. Krook, and C. E. Pearson. *Functions of a complex variable.* McGraw-Hill, New York, 1966.

B. S. Chekin. The entry of a wedge into an incompressible fluid. *J. App. Math. Mech.*, 53(3):300–307, 1989.

S.-L. Chuang. Experiments on slamming of wedge-shaped bodies. *J. Ship Res.*, 11 (3):190–198, 1967.

C. Clanet, F. Hersen, and L. Bocquet. Secrets of successful stone-skipping. *Nature*, 427(6969):29–29, 2004.

R. Cointe. Two-dimensional water-solid impact. *J. Offshore Mech. Arc. Eng.*, 111 (2):109–114, 1989.

E. Cumberbatch. The impact of a water wedge on a wall. *J. Fluid Mech.*, 7(3): 353–373, 1960.

J. T. Czaykowski. Some unsteady problems in fluid dynamics. *DPhil Thesis, University of Oxford*, 1970.

N. de Divitiis and M. L. de Socio. Impact of floats on water. *J. Fluid Mech.*, 471: 365–379, 2002.

J. de Ruiter, J. M. Oh, D. van den Ende, and F. Mugele. Dynamics of collapse of air films in drop impact. *Phys. Rev. Lett.*, 108(7):074505, 2012.

J. N. Dewynne, J. R. Ockendon, and P. Wilmott. A systematic derivation of the leading-order equations for extensional flows in slender geometries. *J. Fluid Mech.*, 244:323–338, 1992.

J. N. Dewynne, P. D. Howell, and P. Wilmott. Slender viscous fibres with inertia and gravity. *Quar. J. Mech. App. Math.*, 47(4):541–555, 1994.

Z. N. Dobrovol'skaya. On some problems of similarity flow of fluid with a free surface. *J. Fluid Mech.*, 36(04):805–829, 1969.

N. Dombrowski and P. C. Hooper. The effect of ambient density on drop formation in sprays. *Chem. Engg. Sci.*, 17(4):291–305, 1962.

A. Driscoll and A. Lloyd. Slamming experiments- description of facilities and details of impact pressure results. *Report AMTE (H) R82002*, 53, 1982.

M. M. Driscoll and S. R. Nagel. Ultrafast interference imaging of air in splashing dynamics. *Phys. Rev. Lett.*, 107(15):154502, 2011.

M. M. Driscoll, C. S. Stevens, and S. R. Nagel. Thin film formation during splashing of viscous liquids. *Phys. Rev. E*, 82(3):036302, 2010.

L. Duchemin and C. Josserand. Curvature singularity and film-skating during drop impact. *Phys. Fluids*, 23:091701, 2011.

B. R. Duffy and S. K. Wilson. A third-order differential equation arising in thin-film flows and relevant to tanner's law. *Appl. Math. Lett.*, 10(3):63–68, 1997.

J. Eggers and E. Villermaux. Physics of liquid jets. *Rep. Prog. Phys.*, 71(3):036601, 2008.

E. V. Ermanyuk and N. V. Gavrilov. Experimental study of disk impact onto shallow water. *J. App. Math. Tech. Phys.*, 52(6):889–895, 2011.

E. V. Ermanyuk and M. Ohkusu. Impact of a circular disk on shallow water. *J. Fluids Struc.*, 20:345–357, 2005.

A. G. Fabula. Ellipse-fitting approximation of two-dimensional, normal symmetric impact of rigid bodies on water. In *Proc. 5th Midwestern Con. Fluid Mech.*, pages 299–315, 1957.

O. M. Faltinsen. Water entry of a wedge with finite deadrise angle. *J. Ship Res.*, 46 (1):39–51, 2002.

L. E. Fraenkel and J. B. McLeod. Some results for the entry of a blunt wedge into water. *Phil. Trans. Roy. Soc. London Ser. A*, 355(1724):523–535, 1997.

I. Frankel and D. Weihs. Stability of a capillary jet with linearly increasing axial velocity (with application to shaped charges). *J. Fluid Mech.*, 155:289–307, 1985.

I. Frankel and D. Weihs. Influence of viscosity on the capillary instability of a stretching jet. *J. Fluid Mech.*, 185:361–383, 1987.

F. D. Gakhov. *Boundary Value Problems*. Pergamon, 1966.

P. R. Garabedian. Oblique water entry of a wedge. *Comm. Pure App. Math.*, 6(2): 157–165, 1953.

K. Gillow. Codimension-two free boundary value problems. *DPhil Thesis, University of Oxford*, 1998.

J. M. Gordillo and M. Perez-Saborid. Aerodynamic effects in the break-up of liquid jets: on the first wind-induced break-up regime. *J. Fluid Mech.*, 541:1–20, 2005.

M. Greenhow. Wedge entry into initially calm water. *Appl. Ocean Res.*, 9:214–223, 1987.

W. W. Hagerty and J. F. Shea. A study of the stability of plane fluid sheets. *J. Appl. Mech*, 22(3):509–514, 1955.

K. Hagiwara and T. Yuhara. Fundamental study of wave impact loads on ship bows. *J. Soc. Naval. Arch. Japan*, 135:181–189, 1974.

I. J. Hewitt, N. J. Balmforth, and J. N. McElwaine. Continual skipping on water. *J. Fluid Mech.*, 669:328–353, 2011.

P. D. Hicks and R. Purvis. Air cushioning and bubble entrapment in three-dimensional droplet impacts. *J. Fluid Mech.*, 649(1):135–163, 2010.

P. D. Hicks and R. Purvis. Air cushioning in droplet impacts with liquid layers and other droplets. *Phys. Fluids*, 23(6):062104, 2011.

P. D. Hicks and F. T. Smith. Skimming impacts and rebounds on shallow liquid layers. *Proc. Roy. Soc. A*, 467(2127):653–674, 2011.

P. D. Howell. Extensional thin layer flows, 1994.

S. D. Howison, J. R. Ockendon, and S. K. Wilson. Incompressible water-entry problems at small deadrise angles. *J. Fluid Mech.*, 222:215–230, 1991.

S. D. Howison, J. D. Morgan, and J. R. Ockendon. Patch cavitation in flow past a rigid body. *Bubble Dyn, Interface Phen.*, 23:219–226, 1994.

S. D. Howison, J. D. Morgan, and J. R. Ockendon. A class of codimension-two free boundary value problems. *SIAM Review*, 39:221–253, 1997.

S. D. Howison, J. R. Ockendon, and J. M. Oliver. Deep-and shallow-water slamming at small and zero deadrise angles. *J. Engg. Math.*, 42(3):373–388, 2002.

S. D. Howison, J. R. Ockendon, and J. M. Oliver. Oblique slamming, planing and skimming. *J. Engg. Math.*, 48:321–337, 2004.

S. D. Howison, J. R. Ockendon, J. M. Oliver, R. Purvis, and F. T. Smith. Droplet impact on a thin fluid layer. *J. Fluid Mech.*, 542:1–24, 2005.

S.D. Howison and J. M. Oliver. A free boundary problem arising in a model for shallow water entry at small deadrise angles. *Eur. J. App. Math.*, 15:839–851, 2004.

O. F. Hughes. Solution of the wedge entry problem by numerical conformal mapping. *J. Fluid Mech.*, 56:173–192, 1972.

A. Iafrati. Hydrodynamics of asymmetric wedges impacting the free surface. In *Eur. Congr. Comp. Methods Appl. Sci. Eng, Barcelona*, pages 1–13, 2000.

G. B. Jeffery. On a form of the solution of Laplace's equation suitable for problems relating to two spheres. *Proc. Roy, Soc. A*, 87(593):109–120, 1912.

C. Josserand and S. Zaleski. Droplet splashing on a thin liquid film. *Phys. Fluids*, 15 (6):1650–1657, 2003.

C. Judge, A. Troesch, and M. Perlin. Initial water impact of a wedge at vertical and oblique angles. *J. Engg. Math.*, 48(3):279–303, 2004.

G. Keady and N. D. Fowkes. The vertical entry of a wedge into water: integral equations and numerical results. In *Third Biennial Engg. Math. App. Con. Adelaide*, volume 1, pages 277–81, 1998.

J. B. Keller and I. Kolodner. Instability of liquid surfaces and the formation of drops. *J. App. Phys.*, 25(7):918–921, 1954.

J. B. Keller, S. I. Rubinow, and Y. O. Tu. Spatial instability of a jet. *Phys. Fluids*, 16:2052, 1973.

T. I. Khabakhpasheva and A. A. Korobkin. Oblique impact of a smooth body on a thin layer of inviscid fluid. *Proc. Roy. Soc. A*, 469:20120615, 2013.

J. M. Kolinski, S. M. Rubinstein, S. Mandre, M. P. Brenner, D. A. Weitz, and L. Mahadevan. Skating on a film of air: Drops impacting on a surface. *Phys. Rev. Lett.*, 108:074503, 2012.

A. A. Korobkin. Formulation of penetration problem as a variational inequality. *Din. Sploshnoi Sredy*, 58:73–79, 1982.

A. A. Korobkin. Initial asymptotics of solution of three-dimensional problem on a blunt body penetration into ideal liquid. *Doklady Akademii Nauk SSSR*, 283: 838–842, 1985.

A. A. Korobkin. Inclined entry of a blunt profile into an ideal fluid. *Fluid Dynamics*, 23(3):443–447, 1988.

A. A. Korobkin. Impact of two bodies one of which is covered by a thin layer of liquid. *J. Fluid Mech.*, 300:43–58, 1995.

A. A. Korobkin. Water impact problems in ship hydrodynamics. In *Water Impact Prob. Ship Hydrodyn.: Comp. Mech. Pub.*, pages 323–371, 1996a.

A. A. Korobkin. Acoustic approximation in the slamming problem. *J. Fluid Mech.*, 318:165–188, 1996b.

A. A. Korobkin. Asymptotic theory of liquid-solid impact. *Phil. Trans. Math. Phys. Eng. Sci.*, 35:507–522, 1997.

A. A. Korobkin. Cavitation in liquid impact problems. *Fifth Intl. Symp. on Cavitation, Osaka*, 2003.

A. A. Korobkin. A linearized model of water exit. *J. Fluid Mech.*, 737:368–386, 2013.

A. A. Korobkin and V. V. Pukhnachov. Initial asymptotics in contact hydrodynamics problems. *4th Intl Con Numer. Ship Hydrodyn.*, pages 138–151, 1985.

A. A. Korobkin and Y.-M. Scolan. Three-dimensional theory of water impact. Part 2. Linearized Wagner problem. *J. Fluid Mech.*, 549:343–374, 2006.

A. A. Korobkin, A. S. Ellis, and F. T. Smith. Trapping of air in impact between a body and shallow water. *J. Fluid Mech.*, 611:365–394, 2008.

A. Latka, A. Strandburg-Peshkin, M. M. Driscoll, C. S. Stevens, and S. R. Nagel. Creation of prompt and thin-sheet splashing by varying surface roughness or increasing air pressure. *Phys. Rev. Lett.*, 109(5):054501, 2012.

L. J. Leng. Splash formation by spherical drops. *J. Fluid Mech.*, 427:73–105, 2001.

G. R. G. Lewison. On the reduction of slamming pressures. *Pub. Roy. Inst. Naval Arch.*, 112(3), 1970.

G. R. G. Lewison and W. M. Maclean. On the cushioning of water impact by entrapped air. *J. Ship Res.*, 12(2):116–130, 1968.

A. G. Mackie. The water entry problem. *Qua. J. Mech. App. Math.*, 22(1), 1969.

S. Mandre and M. P. Brenner. The mechanism of a splash on a dry solid surface. *J. Fluid Mech.*, 690:148, 2012.

S. Mandre, M. Mani, and M. P. Brenner. Precursors to splashing of liquid droplets on a solid surface. *Phys. Rev. Lett.*, 102:134502, 2009.

M. Mani, S. Mandre, and M. P. Brenner. Events before droplet splashing on a solid surface. *J. Fluid Mech.*, 647:163–185, 2010.

A. May. The cavity after vertical water entry. Technical report, U.S. Naval Ordnance Laboratory, Maryland, 1968.

A May. Water entry and the cavity-running behavior of missiles. Technical report, NAVSEA Hydroballistics Advisory Committee, Maryland, 1975.

V. Mehdi-Nejad, J. Mostaghimi, and S. Chandra. Air bubble entrapment under an impacting droplet. *Phys. Fluids*, 15(1):173–183, 2003.

T. Mikami, R. G. Cox, and S. G. Mason. Breakup of extending liquid threads. *Int. J. Multiphase Flow*, 2(2):113–138, 1975.

T. Miloh. On the oblique water-entry problem of a rigid sphere. *J. Engg. Math.*, 25 (1):77–92, 1991a.

T. Miloh. On the initial-stage slamming of a rigid sphere in vertical water entry. *App. Ocean Res.*, 13(1):43–48, 1991b.

M. Moghisi and P. T. Squire. An experimental investigation of the initial force of impact on a sphere striking a liquid surface. *J. Fluid Mech.*, 1981.

M. R. Moore and J. M. Oliver. On air-cushioning in axisymmetric impacts. *IMA. J. App. Math.*, 79(4):661–690, 2014.

M. R. Moore, S. D. Howison, J. R. Ockendon, and J. M. Oliver. Three-dimensional oblique water-entry problems at small deadrise angles. *J. Fluid Mech.*, 711:259–280, 2012.

M. R. Moore, S. D. Howison, J. R. Ockendon, and J. M. Oliver. A note on oblique water-entry. *J. Engg. Math.*, 81:67–74, 2013a.

M. R. Moore, J. R. Ockendon, and J. M. Oliver. Air-cushioning in impact problems. *IMA J. App. Math.*, 78:818–838, 2013b.

S. Muzaferija, M. Peric, P. Sames, and T. Schellin. A two-fluid Navier-Stokes solver to simulate water entry. In *Proc. 22nd Symp. Naval Hydrodyn. Washington D.C.*, pages 638–651, 1998.

W. C. E. Nethercote, M. Mackay, and B. Menon. Some warship slamming investigations. *DREA Tech. Mem.*, page 86/206, 1986.

J. M. Oliver. Water entry and related problems. *DPhil Thesis, University of Oxford*, 2002.

J. M. Oliver. Second-order wagner theory for two-dimensional water-entry problems at small deadrise angles. *J. Fluid Mech.*, 572:59–85, 2007.

J. Palacios, J. Hernández, P. Gómez, C. Zanzi, and J. López. On the impact of viscous drops onto dry smooth surfaces. *Exp. Fluids*, 52(6):1449–1463, 2012.

B. Peseux, L. Gornet, and B. Donguy. Hydrodynamic impact: numerical and experimental investigations. *J. Fluids Struct.*, 21:277–303, 2005.

V. V. Pukhnachov and A. A. Korobkin. Initial asymptotic in problem of blunt body entrance into liquid. In *Proc. 3rd Inter. Con. Numer. Ship Hydrodyn.*, pages 579–591. Paris, France, 1981.

R. Purvis and F. T. Smith. Air-water interactions near droplet impact. *Eur. J. App. Math.*, 15(6):853–871, 2004.

D. Quéré. Fluid dynamics: Impact on everest. *Nature*, 435(7046):1168–1169, 2005.

Lord Rayleigh. On the instability of jets. *Proc. London Math. Soc*, 1(1):4–13, 1878.

M. Rein and J.-P. Delplanque. The role of air entrainment on the outcome of drop impact on a solid surface. *Acta Mech.*, 201:105–118, 2008.

M. Reinhard, A. A. Korobkin, and M. J. Cooker. The bounce of a blunt body from a water surface at high horizontal speed. *Proc. 27th Intern. Workshop on Water Waves and Floating Bodies, Copenhagen, Denmark*, pages 153–156, 2012.

M. Reinhard, A. A. Korobkin, and M. J. Cooker. Water entry of a flat elastic plate at high horizontal speed. *J. Fluid Mech.*, 724:123–153, 2013.

L. Rosellini, F. Hersen, C. Clanet, and L. Bocquet. Skipping stones. *J. Fluid Mech.*, 543:137–146, 2005.

C. Schmieden. Der Aufschlag von Rotationskörpern auf eine Wasseroberfläche. *Z. angew. Math. Mech.*, 33(4):147–151, 1953.

R. D. Schroll, C. Josserand, S. Zaleski, and W. W. Zhang. Impact of a viscous liquid drop. *Phys. Rev. Lett.*, 104(3):034504, 2010.

Y.-M. Scolan and A. A. Korobkin. Three-dimensional theory of water impact. Part 1. Inverse Wagner problem. *J. Fluid Mech.*, 440:293–326, 2001.

Y.-M. Scolan and A. A. Korobkin. Hydrodynamic impact (Wagner) problem and Galin's theorem. In *Proc. 27th Intern. Workshop on Water Waves and Floating Bodies, Copenhagen, Denmark*, pages 165–168. 2012.

Y. A. Semenov and A. Iafrati. On the nonlinear water entry problem of asymmetric wedges. *J. Fluid Mech.*, 547:231–256, 2006.

Y. A. Semenov and B.-S. Yoon. Onset of flow separation for the oblique water impact of a wedge. *Phys. Fluids*, 21:1121031–11, 2009.

M. Shiffman and D. C. Spencer. The force of impact on a sphere striking a water surface. *AMP Rep. 42 2B AMG-NYU No. 133*, 1945.

M. Shiffman and D. C. Spencer. The force of impact on a cone striking a water surface (vertical entry). *Comm. Pure App. Math.*, 4(4):379–417, 1951.

H. Sirringhaus, T. Kawase, R. H. Friend, T. Shimoda, M. Inbasekaran, W. Wu, and E. P. Woo. High-resolution inkjet printing of all-polymer transistor circuits. *Science*, 290(5499):2123–2126, 2000.

F. T. Smith, L. Li, and G. X. Wu. Air cushioning with a lubrication/inviscid balance. *J. Fluid Mech.*, 482:291–318, 2003.

I. N. Sneddon. *Mixed Boundary Value Problems in Potential Theory.* North-Holland, 1966.

H. B. Squire. Investigation of the instability of a moving liquid film. *Brit. J. App. Phys.*, 4(6):167, 1953.

A. M. Sterling and C. A. Sleicher. The instability of capillary jets. *J. Fluid Mech.*, 68(3):477–495, 1975.

S. L. Sun and G. X. Wu. Oblique water entry of a cone by a fully three-dimensional nonlinear method. *J. Fluids Struc.*, 42:313–332, 2013a.

S. L. Sun and G. X. Wu. Oblique water-entry of non-axisymmetric bodies at varying speed by a fully nonlinear method. *Quar. J. Mech. App. Math.*, 66(3):366–393, 2013b.

O. Tammisola, A. Sasaki, F. Lundell, M. Matsubara, and L. D. Söderberg. Stabilizing effect of surrounding gas flow on a plane liquid sheet. *J. Fluid Mech.*, 672:5–32, 2011.

G. I. Taylor. The formation of a blast wave by a very intense explosion. i. theoretical discussion. *Proc. Roy. Soc. London. Ser. A*, 201(1065):159–174, 1950.

G. I. Taylor. The dynamics of thin sheets of fluid. ii. waves on fluid sheets. *Proc. Roy. Soc. London Ser. A*, 253(1274):296–312, 1959.

T. J. Tharakan, K. Ramamurthi, and M. Balakrishnan. Nonlinear breakup of thin liquid sheets. *Acta Mech.*, 156(1-2):29–46, 2002.

M.-J. Thoraval, K. Takehara, T. G. Etoh, S. Popinet, P. Ray, C. Josserand, S. Zaleski, and S. T. Thoroddsen. Von Kármán vortex street within an impacting drop. *Phys. Rev. Lett.*, 108:264506, 2012.

S. T. Thoroddsen. The ejecta sheet generated by the impact of a drop. *J. Fluid Mech.*, 451:373–382, 2002.

S. T. Thoroddsen, T. G. Etoh, and K. Takehara. Air entrapment under an impacting drop. *J. Fluid Mech.*, 478:125–134, 2003.

S. T. Thoroddsen, T. G. Etoh, K. Takehara, N. Ootsuka, and Y. Hatsuki. The air bubble entrapped under a drop impacting on a solid surface. *J. Fluid Mech.*, 545: 203–212, 2005.

S. T. Thoroddsen, T. G. Etoh, and K. Takehara. High-speed imaging of drops and bubbles. *Ann. Rev. Fluid Mech.*, 40:257–285, 2008.

S. T. Thoroddsen, K. Takehara, and T. G. Etoh. Bubble entrapment through topological change. *Phys. Fluids*, 22:051701, 2010.

S. T. Thoroddsen, M. J. Thoraval, K. Takehara, and T. G. Etoh. Droplet splashing by a slingshot mechanism. *Phys. Rev. Lett.*, 106(3):34501, 2011.

L. A. Tkacheva. Impact of a body with a plane bottom on a thin liquid layer at a small angle. *Fluid Dyn.*, 48(13):352–365, 2013.

L. M. Trefethen and R. L. Panton. Some unanswered questions in fluid mechanics. *Appl. Mech. Rev.*, 43(8):153–170, 1990.

F. T. Trouton. On the coefficient of viscous traction and its relation to that of viscosity. *Proc. Roy. Soc. London. Ser. A*, 77(519):426–440, 1906.

E. O. Tuck. On planing. *Private communication*, 1994.

E. O. Tuck and L. W. Schwartz. A numerical and asymptotic study of some third-order ordinary differential equations relevant to draining and coating flows. *SIAM Rev.*, 32(3):453–469, 1990.

D. B. van Dam and C. Le Clerc. Experimental study of the impact of an ink-jet printed droplet on a solid substrate. *Phys. Fluids*, 16(9):3403–3414, 2004.

B. W. van de Fliert, P. D. Howell, and J. R. Ockendon. Pressure-driven flow of a thin viscous sheet. *J. Fluid Mech.*, 292:359–359, 1995.

J.-M. Vanden-Broeck and J. B. Keller. Pouring flows with separation. *Phys. Fluids*, 1(1):156–159, 1989.

J.-M. Vanden-Broeck and F. T. Smith. Surface tension effects on interaction between two fluids near a wall. *Quart. J. Mech. App. Math.*, 61(2):117–128, 2009.

J. H. G. Verhagen. The impact of a flat plate on a water surface. *J. Ship Res*, 11(4): 211–223, 1967.

T. von Kármán. The impact of seaplane floats during landing. *NACA TN 321*, 1929.

H. Wagner. Über Stoß- und Gleitvorgänge an der Oberfläche von Flüssigkeiten. *Z. angew. Math. Mech.*, 12:193–215, 1932.

S. Watanabe. Resistance of impact on water surface. Part I. *Inst. Phys. Chem. Res.. Tokyo Sci. Papers*, 12:251–267, 1930.

S. K. Wilson. The mathematics of ship slamming. *DPhil Thesis, University of Oxford*, 1989.

S. K. Wilson. A mathematical model for the initial stages of fluid impact in the presence of a cushioning fluid layer. *J. Engg Math.*, 25(3):265–285, 1991.

G. D. Xu, W. Y. Duan, and G. X. Wu. Numerical simulation of water entry of a cone in free-fall motion. *Quar. J. Mech. App. Math.*, 64(3):265–285, 2011.

L. Xu, W. W. Zhang, and S. R. Nagel. Drop splashing on a dry smooth surface. *Phys. Rev. Lett.*, 94(18):184505, 2005.

L. V. Zhang, J. Toole, K. Fezzaa, and R. D. Deegan. Evolution of the ejecta sheet from the impact of a drop with a deep pool. *J. Fluid Mech.*, 690(5), 2012a.

L. V. Zhang, J. Toole, K. Fezzaa, and R. D. Deegan. Splashing from drop impact into a deep pool: multiplicity of jets and the failure of conventional scaling. *J. Fluid Mech.*, 703:402–413, 2012b.

R. Zhao and O. Faltinsen. Water entry of two-dimensional bodies. *J. Fluid Mech.*, 246(1):593–612, 1993.

R. Zhao, O. Faltinsen, and J. Aarsnes. Water entry of arbitrary two-dimensional sections with and without flow separation. In 21^{st} *Symp. Naval Hydrodyn.*, 1997.